Department of Physics
University of Fribourg (Switzerland)

The Muonic Hydrogen Lamb Shift Experiment: Lifetime and Population of the μp($2S$) State

Inaugural Dissertation

submitted to the Faculty of Sciences of the
University of Fribourg (Switzerland)
in conformity with the requirements for the degree of
Doctor rerum naturalium

by

Dr. Livia Ludhova

from Bratislava (Slovakia)

October 2005

Thesis Nr. 1489

Paul Scherrer Institut Druckerei

2005

Accepted by the Faculty of Sciences of the University of Fribourg (Switzerland) on the recommendation of:
Prof. Dr. Jean–Claude Dousse, University of Fribourg (Jury President)
Prof. Dr. Lukas Schaller, University of Fribourg (Ph.D. Supervisor)
Dr. Franz Kottmann, ETH Zürich (Advisor)
Prof. Dr. Françoise Mulhauser, University of Illinois at Urbana–Champaign, USA (Advisor)
Dr. Jean–Pierre Egger, University of Neuchâtel (External Advisor)

Fribourg, October 2005

Ph.D. Supervisor:

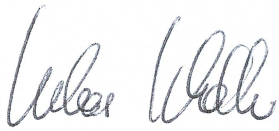

Prof. Dr. Lukas Schaller

Faculty Dean:

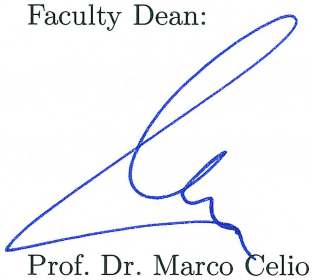

Prof. Dr. Marco Celio

It was that kind of comfortable persons which decided to write on the maps: "Hic Sunt Leones", here are the lions. As an explanation, an apology or as an excuse, and as a warning that it is not recommended to go there, that those places have to remain forever unknown and left to lions. But that other kind of people goes just there. Attracted, may be, by the eagerness to find that unknown, may be they like to fight for some comfort or against the fear, or, may be, they desire just one thing: to see the lions.

MIROSLAV HORNÍČEK
(Czech actor and writer)

To my father who taught me the desire to go and to see the lions. To my mother for making me feel always on the safe side. To those special ones having a reserved place somewhere deep in my heart.

Acknowledgments

I would like to thank

- Prof. Lukas Schaller for giving me the opportunity to join the μp($2S$) Lamb shift collaboration, as well as for his constant support whenever it was needed and for his advices when writing this thesis.
- Dr. Franz Kottmann for his infinite support and patience. He taught me a lot while guiding me through the major part of the analysis. His scientific approach to every problem and excellent self–organization remain as an example for me.
- Dr. Françoise Mulhauser for her constant help with everything. It was a pleasure to work with her on an every–day basis when she gave me the possibility to learn a lot from her. Her friendship helped me a lot to find my way in Switzerland. Special thanks also for her help with editing the final version of this thesis.
- Dr. Paul Knowles for his unique approach with which he taught me a lot of things about physics and experiments. His many "little tricks" from the lab and from behind the computer are of a great value for an experimental physicist. Special thanks for final English corrections in this thesis.
- Dr. Randolf Pohl for his help during and after the data taking period. He wrote the code for the wave–form–digitizer analysis which was a great tool for the major part of the analysis presented in this work. His advice on "how to use it" and "how to change it" were invaluable.
- Dr. David Taqqu for the discussions full of ideas leading to solutions of many problems and for his interest in every new result from the analysis.
- Aldo Antognini for being a great co–graduate student of the experiment ready to help and discuss any problem.
- "The group from the laser hut", the group from LKB Paris (Dr. François Nez, Prof. Lucile Julien, Prof. François Biraben, Dr. Paul Indelicato, Dr. Catherine Schwob) and Dr. Andreas Dax. Dr. Yi-Wei Liu also participated in the experiment.
- The Coimbra University group specialized in x–ray detectors for being of a great help especially during the data taking period (Prof. Joaquim dos Santos, Dr. João Veloso, Fernando Amaro, Cristina Monteiro, Daniel Covita, Prof. Carlos Conde). Special thanks go to Dr. Luis Fernandes ready to share his experience from the tests and measurements with the LAAPDs.
- Olivier Huot for his help with the electronics and many technical details.
- Dr. João Cardoso who provided us with the computer code for the wave–form–digitizer allowing us "to see on–line" the measured data.
- Prof. P. Rabinowitz for providing us with the Raman laser.
- Prof. T.W. Hänsch for his constant support of our experiment.
- Dr. Thomas Jensen for providing the results of his cascade calculations adjusted to experimental conditions.
- Dr. Leo Simons and Bruno Leoni for their help with the cyclotron trap.
- Dr. Satish Dhawan for the newly developed wave–form–digitizers.

- The staff at PSI: the accelerator group for providing us with an excellent beam, the workshop for building important parts of our setup (gas target included), and the Hallendienst for helping us to put everything together and to take it apart again.
- The workshop at Fribourg University who built some important parts of our setup.

Summary

This thesis is dedicated to the muonic hydrogen (μp) Lamb shift experiment being performed at the Paul Scherrer Institute, Switzerland. Its goal is to measure the $2S-2P$ energy difference in μp atoms by infrared laser spectroscopy and to deduce the proton root–mean–square (rms) charge radius $r_{\rm p}$ with 10^{-3} precision, an order of magnitude better than presently known. This radius is a basic property of the simplest nucleus, the proton, and treated in the recently published 2002–CODATA adjustment as a fundamental physical constant. The CODATA value $r_{\rm p} = (0.8750 \pm 0.0068)$ fm originates mainly from a comparison of the $1S$–Lamb shift measured in normal hydrogen atoms (2×10^{-6} relative accuracy) with the calculated value which depends on *bound–state quantum electrodynamics* (QED) ($\sim 10^{-6}$ theoretical uncertainty) and the radius r_p.

Precise knowledge of r_p from an independent experiment would make it possible to test bound–state QED on the level of the quoted experimental and theoretical uncertainties. However the only presently available independent, *i.e.*, non–spectroscopic, $r_{\rm p}$–value originates from electron scattering experiments. Its uncertainty is still as large as 2%, limiting the calculation of the $1S$–Lamb shift and hence the test of bound–state QED to a precision level of 6×10^{-6}.

Muonic hydrogen atoms are best suited for a precise determination of $r_{\rm p}$ because the relative contribution of the proton size to the muonic Lamb shift is 1.8 percent, two orders of magnitude more than for normal hydrogen. The recent breakthrough in bound–state QED calculations of the hydrogen $1S$–Lamb shift, together with the prospect of more precise data from hydrogen spectroscopy in the near future, increased the interest in the muonic Lamb shift experiment. A determination of $r_{\rm p}$ with 10^{-3} precision would lead to a test of bound–state QED on a level of a few times 10^{-7} and to an improved determination of the Rydberg constant. Alive interest in a precise $r_{\rm p}$–value comes also from the QCD community, since it would serve as an important benchmark for new effective–field and lattice theory calculations.

The principle of our experiment is to measure the energy difference between the $2S^{F=1}_{1/2} - 2P^{F=2}_{3/2}$ atomic levels in μp atoms to a precision of 30 ppm, using a pulsed laser tunable at wavelengths around 6 μm. Negative muons from a unique low–energy muon beam are stopped at a rate of ~ 100 s^{-1} in 0.6 hPa of H_2 gas. Highly excited μp atoms are formed, and most of them de–excite to the $1S$ state within ~ 100 ns. There is a probability of about 1% that long–lived μp($2S$) atoms with a lifetime of 1.3 μs are populated. An incoming muon triggers a pulsed multi–stage laser system which delivers 0.2 mJ per pulse at $\lambda \approx 6$ μm. The laser pulse has a delay of about 1.5 μs with respect to the "prompt"

muon cascade. If the laser is on resonance, it induces $\mu p(2S) \rightarrow \mu p(2P)$ transitions. The subsequent de–excitation to the $\mu p(1S)$ state emits a 1.9 keV K_α x ray which is detected by Large Area Avalanche Photodiodes (LAAPDs). The resonance frequency, and hence the Lamb shift and r_p, are determined by measuring the intensity of these x rays as a function of the laser wavelength.

All parts of the system operated during an engineering run in late 2002. Several problems appeared and an intense effort was invested to solve them for the 2003–beam time. The whole setup could be tested and optimized with beam in the second half of 2003. A search for the $2S - 2P$ resonance line in which a broad range of laser frequencies was scanned, corresponding to proton radii between 0.85 and 0.91 fm, took place in November 2003. A new sophisticated method to analyze the data, in particular the LAAPD pulse shapes, was developed in 2004. The result of the data analysis is that no significant $2S - 2P$ resonance was observed. The negative result is with high probability due to the low statistics. The QED calculations of the $\mu p(2S - 2P)$ energy difference as well as the hydrogen ground–state Lamb shift (resulting in the CODATA value for r_p) were remarkably improved over the last 5 years, which makes it unlikely that the search was performed in a wrong range of laser wavelengths.

There are three main reasons why the rate of expected laser–induced events is less than what was foreseen. A factor 2 was lost because a lithium foil had to be installed in front of the LAAPDs in order to protect them against alpha particles emitted by the ThF_4 dielectric coating of the laser cavity mirrors. Another loss–factor of 2 was caused by the too long internal delay of the excimer laser. In addition, only recently it was found by a Monte Carlo simulation that the $\mu p(2S)$ atoms have a much higher probability than previously assumed to drift out of the laser–irradiated volume before the laser pulse arrives. These effects reduced the rate of expected laser–induced events from 4/hour to 0.7/hour which is too low for the limited measuring time of $5 - 10$ hours per wavelength.

More than 10^6 x rays from μp K_α, K_β, and K_{rest} transitions (at 1.898, 2.249, and ~ 2.46 keV, respectively) were detected in total. This represents at least two orders of magnitude more than in any previous muonic hydrogen experiment performed at ultra–low densities. The laser was fired for $\sim 30\%$ of these events. Additional events were measured between two laser pulses, during the dead time of the laser system. A detailed analysis of all data, with and without firing the laser, brought several interesting results.

First, the muon–stop distribution along the beam axis in the hydrogen target was determined. It was found that a gold surface (present at the end of the muon stop volume) is a good reflector for muons with kinetic energies of a few keV. The effective length of the gas target is thus doubled and the rates of muons stopping in the low–density gas and forming μp atoms correspondingly increased.

Second, the cascade time, *i.e.*, the time difference from atomic capture of the muon until emission of a K–series x ray, could be measured for the first time in μp atoms. A small admixture of N_2 and O_2 gases (at a total level of 0.4%) due to an air–leak in our system was found in the data analysis. The 3.1 keV x rays from $\mu N(5 - 4)$ transitions turned out to be absolutely essential to determine the muon stop time distribution without the contribution of the μp cascade time. In addition, coincident low–energy x rays from

successive radiative transitions in μN, as well as in μO, were found which allow us to extract valuable information how to calibrate the x–ray times and energies measured in the LAAPDs, and to obtain an efficiency curve for x–ray energies between 1.3 and 9 keV. A detailed analysis of the three x–ray time spectra from μp K_α and $K_{\rm rest}$ and μN$(5-4)$ transitions was performed by simultaneously optimizing the parameters of the corresponding three highly–correlated fit functions. The exponential decay time of the μp cascade turns out to be $\tau_{\rm cas}^{\mu p} = (28 \pm 5)$ ns. This value is in contradiction with the most recent cascade calculations giving a value of about 70 ns for $\tau_{\rm cas}^{\mu p}$.

Third, collision–induced radiative decays of the so called "fast" component of metastable μp$(2S)$ atoms were detected, also for the first time. The corresponding delayed K_α transitions are present in the μp K_α time spectrum, but absent in the $K_{\rm rest}$ and μN spectra. The resulting lifetime and relative population (with respect to the number of μp atoms) are $\tau_{\rm 2S}^{\rm fast} = (148 \pm 22)$ ns and $P_{\rm 2S}^{\rm fast} = (1.02 \pm 0.21)\%$, respectively. These results agree with the values expected from calculations performed for collisions of μp$(2S)$ with H–atoms, if the density of H–atoms is assumed to be approximately 1.8 times the density of H_2 molecules.

The "fast" $2S$ component corresponds to μp$(2S)$ atoms with kinetic energies above the $2S-2P$ energy threshold of 0.31 eV in the laboratory frame. Collisional excitation to the $2P$ state is thus allowed, followed almost immediately by a K_α transition to the ground state. About half of the μp$(2S)$ atoms are decelerated by elastic collisions below the 0.31 eV threshold, forming the "slow" $2S$ component with a relative population $P_{\rm 2S}^{\rm slow}$. Collisional $2P$ excitation is energetically forbidden for this component which was found in previous experiments to de–excite via resonant formation of excited muonic molecules and subsequent non–radiative dissociation to the ground state. The sum $P_{\rm 2S}^{\rm fast} + P_{\rm 2S}^{\rm slow}$ of both $2S$ populations has to be equal to the initial relative μp$(2S)$ population, deduced from the well known μp K–series x–ray yields to be $P_{\rm 2S} = (2.49 \pm 0.17)\%$ at 0.6 hPa. A new independent value $P_{\rm 2S}^{\rm slow} = P_{\rm 2S} - P_{\rm 2S}^{\rm fast} = (1.47 \pm 0.27)\%$ can thus be deduced for the population of the "slow" $2S$ component, on which our laser experiment is based. The new result agrees with the value $P_{\rm 2S}^{\rm slow} = (1.1 \pm 0.2)\%$ previously obtained in a direct measurement of the "slow" component.

Zusammenfassung

Die vorliegende Arbeit befasst sich mit dem Lambshift–Experiment an myonischem Wasserstoff (μp), welches am Paul Scherrer Institut in Villigen durchgeführt wird. Es hat zum Ziel, die $2S-2P$ Energiedifferenz in μp–Atomen zu messen und daraus den mittleren quadratischen Ladungs–Radius des Protons (rms–Radius r_{p}) mit einer Genauigkeit von 1 Promille zu bestimmen, d.h. um eine Grössenordnung besser als bisher. Dieser Radius wird mehr und mehr als eine der grundlegenden Eigenschaften des einfachsten Atomkerns, also des Protons, aufgefasst und dementsprechend als neue fundamentale physikalische Konstante in der kürzlich publizierten CODATA–2002 Zusammenstellung aufgeführt. Der dort angegebene Wert $r_{\mathrm{p}} = (0.8750 \pm 0.0068)$ fm ergibt sich hauptsächlich aus dem Vergleich der in normalen Wasserstoffatomen gemessenen $1S$–Lamb–Verschiebung mit dem berechneten Wert, der von der Quantenelektrodynamik (QED) gebundener Zustände sowie vom Radius r_{p} abhängt. Die experimentelle Genauigkeit beträgt 2×10^{-6} (relativ), die theoretische Unsicherheit der QED–Rechnungen $\sim 10^{-6}$.

Falls r_{p} aus einem unabhängigen Experiment genau bekannt wäre, könnte die *QED gebundener Zustände* auf dem Niveau der angeführten experimentellen bzw. theoretischen Genauigkeiten getestet werden. Gegenwärtig stammt aber der einzige unabhängige, also nicht von spektroskopischen Messungen hergeleitete Wert für r_{p} aus Elektronenstreuexperimenten, mit einem relativ grossen Fehler von 2%. Für die rechnerisch vorhergesagte $1S$–Lamb–Verschiebung und damit auch für den QED–Test in gebundenen Systemen folgt daraus eine relativ grosse Unsicherheit von 6×10^{-6}.

Myonische Wasserstoffatome eignen sich bestens für eine präzise Bestimmung von r_{p}, weil der Protonenradius einen verhältnismässig grossen Anteil von 1.8 Prozent an der myonischen Lamb–Verschiebung hat, zwei Grössenordnungen mehr als beim normalen Wasserstoff. Kürzlich erfolgte ein Durchbruch in der Berechnung höherer QED–Korrekturterme für die $1S$–Lamb–Verschiebung im normalen Wasserstoff, und neue hochpräzise Wasserstoff-Spektroskopiedaten dürften auch bald anstehen, was das Interesse an der Messung der myonischen Lamb–Verschiebung noch vergrössert. Eine Bestimmung von r_{p} mit einer Genauigkeit von 10^{-3} wird es ermöglichen, die Theorie der QED für gebundene Systeme im Genauigkeitsbereich von 10^{-7} zu testen, und die Rydbergkonstante kann ebenfalls wesentlich präziser festgelegt werden. Ein präziserer r_{p}–Wert interessiert aber auch die QCD–Spezialisten, da dieser ein wichtiger Meilenstein für neue Berechnungen effektiver Feldtheorien und Gittereichrechnungen darstellt.

Im hier beschriebenen Experiment geht es darum, die Energiedifferenz zwischen den $2S^{F=1}_{1/2}$ und $2P^{F=2}_{3/2}$–Zuständen im μp–Atom mit Hilfe eines gepulsten Lasers, der bei

einer Wellenlänge von 6 μm abgestimmt werden kann, auf 30 ppm genau zu bestimmen. Dabei werden negative Myonen, welche aus einem neuartigen, sehr niederenergetischen Myonenstrahl stammen, in einer Wasserstoff–Gaszelle bei niedrigen Drücken (0.6 hPa) mit einer Rate von ca. 100/s gestoppt. Es werden hochangeregte μp–Atome gebildet, von denen die meisten innerhalb von $\sim$ 100 ns zum $1S$–Grundzustand herunter kaskadieren. Mit etwa 1% Wahrscheinlichkeit werden langlebige $\mu\mathrm{p}(2S)$–Zustände mit einer mittleren Lebensdauer von 1.3 μs bevölkert. Das einfallende Myon liefert das Startsignal (Trigger) für ein gepulstes mehrstufiges Lasersystem, welches 0.2 mJ Pulsenergie bei einer Wellenlänge von $\lambda \approx 6$ μm liefert. Der Laserpuls weist eine zeitliche Verzögerung gegenüber der "prompten" Myonenkaskade von rund 1.5 μs auf. Hat der Laser die korrekte Frequenz, induziert er resonante Übergänge vom $\mu\mathrm{p}(2S)$ zum $\mu\mathrm{p}(2P)$–Niveau. Die nachfolgende myonische Abregung in den $\mu\mathrm{p}(1S)$–Zustand liefert Röntgenstrahlung der Energie 1.9 keV, welche mit grossflächigen Lawinen–Photodioden (LAAPDs) gemessen wird. Die Resonanzfrequenz, und somit auch Lambshift und r_p–Radius, werden dann durch die Intensitätsmessung dieser Röntgenstrahlung als Funktion der Laserwellenlänge bestimmt.

Alle Systemkomponenten konnten erstmals während eines längeren "Testruns" im Herbst 2002 eingesetzt werden. Dabei traten verschiedene Probleme auf, welche mit einigem Aufwand bis zur nächsten Strahlperiode gelöst werden konnten. Der gesamte apparative Aufbau konnte dann in einer weiteren Strahlperiode im zweiten Halbjahr 2003 getestet und optimiert werden. Im November 2003 schliesslich wurde die $2S - 2P$ Resonanz über ein breites Spektrum von Laserfrequenzen abgesucht, entsprechend r_p–Werten im Bereich zwischen 0.85 und 0.91 fm. Eine aufwändige Auswertung der Daten, insbesondere der für jedes Röngtenquant einzeln gemessenen LAAPD–Pulszüge, wurde im Jahre 2004 durchgeführt, aber die gewünschte $2S - 2P$ Resonanz konnte nicht gefunden werden. Dieses negative Resultat beruht sehr wahrscheinlich auf der zu geringen Statistik der Messdaten. Es ist unwahrscheinlich, dass die Resonanzsuche bei falschen Laserwellenlängen durchgeführt wurde, da sowohl die QED–Rechnungen der $\mu\mathrm{p}(2S - 2P)$ Energiedifferenz als auch jene der $1S$–Lamb–Verschiebung im H–Atom in den letzten fünf Jahren bemerkenswert verbessert worden sind (und damit auch die Voraussagen für den Protonenradius).

Spezifisch gibt es 3 Hauptgründe, warum die Anzahl laserinduzierter Ereignisse tiefer ausfiel als erwartet. Ein erster Faktor 2 ging verloren, weil vor den LAAPDs noch Lithiumfolien eingebaut werden mussten, um diese Detektoren gegen Alphateilchen zu schützen, welche aus den dünnen dielektrischen ThF_4 Schichten der Laserkavitätsspiegel austraten. Ein weiterer Verlustfaktor 2 wurde durch die (zu) lange interne Zeitverzögerung des Excimerlasers verursacht. Schliesslich ergaben neue Monte–Carlo Rechnungen, dass die $\mu\mathrm{p}(2S)$–Atome mit erheblich grösserer Wahrscheinlichkeit als bislang angenommen aus dem laserbestrahlten Targetvolumen herausdriften, bevor der mit dem gestoppten Myon korrelierte Laserpuls eintrifft. Diese drei Effekte reduzierten die Ereignisrate von den ursprünglich erhofften 4/h auf 0.7/h, was bei der beschränkten Messdauer von 5–10 Stunden pro Laserwellenlänge zu wenig ist, um eine signifikante Statistik zu erreichen.

Insgesamt konnten mehr als 10^6 Röntgenquanten von μp K–Serieübergängen mit Energien von 1.898 keV (K_α), 2.249 keV (K_β) und $\sim$ 2.46 keV (K_rest) gemessen werden.

Diese Zahl ist um mindestens zwei Grössenordnungen höher als bei früheren myonischen Wasserstoffexperimenten, welche bei ähnlich tiefen Gasdichten durchgeführt worden sind. Etwa 30% aller Ereignisse wurden *mit Laser* gemessen, der Rest während der Lasertotzeit zwischen zwei Laserpulsen. Eine detaillierte Analyse all dieser Daten, sowohl mit als auch ohne Laser, lieferte verschiedene interessante Resultate.

Erstens konnte die Stoppverteilung der Myonen entlang der Strahlachse bestimmt werden. Dabei zeigte sich, dass die Goldoberfläche am Ende des Myonenstoppvolumens ein guter Reflektor für Myonen mit kinetischen Energien von ein paar keV ist. Die wirksame Länge der Gaszelle wurde dadurch praktisch verdoppelt, und die Rate der bei niedriger Gasdichte gestoppten Myonen und folglich die Rate gebildeter μp–Atome fielen entsprechend höher aus.

Zweitens konnte erstmals die Kaskadenzeit in μp–Atomen gemessen werden, definiert als Zeitdifferenz vom atomaren Einfang freier Myonen bis zur Emission eines Röntgenquants der K–Serie. Zunächst trat in der Datenanalyse eine Beimischung von total 0.4 Volumenprozent der Gase N_2 und O_2 zu Tage, offensichtlich wegen eines kleinen Luftlecks im Gassystem. In der Folge stellte sich heraus, dass die resultierenden μN(5–4) Röntgenübergänge bei 3.1 keV es überhaupt erst ermöglichten, die Myonenstoppzeitverteilung *ohne* den Beitrag der μp–Kaskadenzeit zu bestimmen. Ausserdem wurden koinzidente Röntgenquanten verschidener übergänge in μN beziehungsweise μO Atomen bei niedrigen Energien gemessen, was eine verfeinerte Eichung der in den LAAPDs gemessenen Energie- und Zeitspektren ermöglichte. Zudem konnte deren Detektionseffizienz im Energiebereich 1.3 bis 9 keV bestimmt werden. Schliesslich wurden die drei Zeitspektren der μp K_α und $K_{\rm rest}$ sowie μN(5–4) Röntgenübergänge eingehend untersucht. Die entsprechenden drei Fitfunktionen wurden entwickelt und die untereinander stark korrelierten Parameter optimiert. Daraus resultiert eine μp–Kaskadenzeit von $\tau_{\rm cas}^{\mu p} = (28 \pm 5)$ ns, was im Gegensatz zu neuen Kaskadenrechnungen steht, welche ein $\tau_{\rm cas}^{\mu p}$ von etwa 70 ns liefern.

Drittens wurde — ebenfalls erstmals — die lange gesuchte so-genannte "schnelle" Zerfallskomponente der metastabilen μp$(2S)$–Atome experimentell nachgewiesen. Hervorgerufen durch Kollisionen treten verzögerte $2P-1S$ Röntgenübergänge auf, die im μp K_α Zeitspektrum, nicht hingegen in den $K_{\rm rest}$ und μN Spektren nachweisbar sind. Die resultierende Lebensdauer und Population (relativ zur Anzahl gebildeter μp–Atome) betragen $\tau_{\rm 2S}^{\rm fast} = (148 \pm 22)$ ns und $P_{\rm 2S}^{\rm fast} = (1.02 \pm 0.21)\%$. Diese Resultate stimmen mit den berechneten Werten überein, die sich für Kollisionen von μp$(2S)$ mit H–Atomen ergeben, sofern eine Dichte von etwa 1.8 H–Atomen pro H_2–Molekül angenommen wird.

Die "schnelle" $2S$–Komponente ergibt sich für μp$(2S)$–Atome mit kinetischen Energien oberhalb der $2S-2P$ Energieschwelle von 0.31 eV im Laborsystem, wo Übergänge zum $2P$–Zustand energetisch erlaubt sind. Dieser zerfällt dann beinahe instantant in den Grundzustand, unter Aussendung eines K_α–Quants. Ungefähr die Hälfte aller μp$(2S)$–Atome werden durch elastische Stösse unter die 0.31 eV–Schwelle herabgebremst, woraus sich die "langsame" $2S$–Komponente mit einer relativen Population von $P_{\rm 2S}^{\rm slow}$ ergibt. Übergänge zum $2P$–Zustand sind für diese Komponente energetisch verboten. Hingegen weiss man aus früheren Experimenten, dass diese Komponente via resonanter Bildung myonischer Moleküle mit anschliessender Dissoziation *strahlungsfrei* zum Grundzustand

übergehen kann. Die Summe $P_{2S}^{fast}+P_{2S}^{slow}$ beider $2S$–Populationen muss gleich der relativen $2S$–Anfangspopulation sein, die sich aus den ziemlich genau gemessenen Strahlungsausbeuten der μp K–Übergänge zu $P_{2S} = (2.49 \pm 0.17)\%$ bei 0.6 hPa ergibt. Daraus lässt sich ein neuer unabhängiger Wert von $P_{2S}^{slow} = P_{2S} - P_{2S}^{fast} = (1.47 \pm 0.27)\%$ für die Population der "langsamen" $2S$–Komponente bestimmen, worauf unser Laserexperiment beruht. Das neue Ergebnis stimmt mit dem früher bestimmten Wert von $P_{2S}^{slow} = (1.1 \pm 0.2)\%$ überein, der sich aus direkten Messungen der "langsamen" Komponente ergab.

Contents

List of Figures

List of Tables

Introduction

The collaboration of the muonic hydrogen Lamb shift experiment consists of 28 physicists from ten institutes and seven countries. I became a member of the collaboration as a graduate student in September 2001.

Until July 2003 I was based at the Physics Department of Fribourg University working with the group of Medium Energy Physics. My work was mainly devoted to the study of the Large Area Avalanche Photodiodes (LAAPDs) used as 2 keV x–ray detectors. In late 2002 I took part at the engineering run at the Paul Scherrer Institute (PSI) and worked on the analysis of the collected data. In the period July–December 2003 I participated at the latest beam–time and data taking period at PSI. Since then, I was based at PSI, working full–time on the data analysis.

The thesis is divided in seven main chapters. Chapter 1 introduces the Lamb shift. The energy levels in ordinary and muonic hydrogen are compared there and the advantage of the muonic hydrogen atom (μp) for the rms proton–radius determination is explained. Chapter 2 briefly summarizes the goal, motivation and principle of the muonic hydrogen Lamb shift experiment. In Chapter 3 some key points of the physics of low–Z muonic atoms are introduced as far as this experiment is concerned. The terminology used throughout the thesis concerning the muonic cascade, the muon transfer and the μp($2S$) state is given there.

Chapter 4 describes the main parts of the experimental setup. The last part of this section is a published paper dedicated to a detailed study of the LAAPDs behaviour:

> L. Ludhova et al., *Planar LAAPDs: Temperature Dependence, Performance, and Application in Low Energy X-ray Spectroscopy*, Nucl. Instrum. Methods Phys. Res. A **540** (2005) 169–179.

Chapter 5 describes the logic of the electronic scheme used in the data acquisition and explains its main features important for the understanding of the analysis procedure. The main types of the data sets are given here.

The sizable Chapter 6 is dedicated to the description of the methods used in the data analysis. In seven sections, the details of the LAAPD pulse–shape analysis, the terminology and definitions used throughout the thesis, the methods employed for time and energy calibration, and for determining the x–ray detection efficiency, as well as the study of electron spectra and the x–ray energy–spectra background are given.

The last Chapter 7 gives the results deduced from the data. It is divided into three sections, each one dedicated to a different type of analysis. Section 7.1 describes the muon stop–time distribution dominated by the processes of the muon slowing down in hydrogen gas and by its reflection at a gold surface. Section 7.2 describes the search for the μp($2S-2P$) resonance and discusses the probable reasons why no resonance signal was observed. Section 7.3 is dedicated to the analysis of the μN and μp x–ray time distributions. As new results, the μp cascade time $\tau_{\rm cas}^{\mu p}$ is obtained and the first direct

observation of the μp($2S$) fast component is described; its population $P_{2S}^{\rm fast}$ and lifetime $\tau_{2S}^{\rm fast}$ are also given. The summary of the abbreviations is given in Appendix A.

Chapter 1

Lamb shift in hydrogen and muonic hydrogen atoms

The hydrogen atom has played a key role in the history of modern physics. Measurements revealing its discrete electron energy levels triggered the development of quantum mechanics (QM). Experiments investigating properties of the hydrogen spectrum were and still are a driving force for fundamental physical theories, from QM to refined quantum electrodynamics (QED). In the past few decades other kinds of hydrogen–like atoms, so called exotic hydrogen atoms, appeared on the scene of physics research. Their study, which is closely connected with that of ordinary hydrogen, allows us to probe various basic aspects of modern physics.

This Chapter aims to recall what the Lamb shift is and what contributes mainly to it. The formulas are written in a general way, valid for both ordinary hydrogen (ep) and muonic hydrogen (μp) atoms. The standard notation used throughout this Chapter is given in Table 1.1. Energy levels and main QED corrections in ep and μp atoms are compared. Values of the main contributions to the $\mu\mathrm{p}(2S_{1/2})$ Lamb shift, important for the $\mu\mathrm{p}(2S)$ Lamb shift experiment (Chapter 2), are summarized.

From the point of view of non–relativistic QM, the energy levels are split only according to n. The radial part of the Schrödinger equation written in spherical coordinates and including the static Coulomb potential in the Hamiltonian (point nucleus with infinite mass and charge Ze) has the form

$$\frac{1}{r^2}\frac{d}{dr}\left(r^2\frac{dR}{dr}\right)+\frac{2m}{\hbar^2}\left(E_n+\frac{Z\alpha}{r}\hbar c-\frac{\hbar^2}{2m}\frac{l(l+1)}{r^2}\right)R=0\,, \tag{1.1}$$

and results in the energy levels

$$E_n=-\frac{mc^2(Z\alpha)^2}{2}\,\frac{1}{n^2}\qquad n=1,2,3,\ldots \tag{1.2}$$

An effort to join QM with relativistic kinematics led to the formulation of the Dirac equation, requiring the existence of electron (muon) spin. The energy levels are slightly modified and become dependent on the total angular momentum j:

$$E_{nj}=\frac{mc^2}{\sqrt{1+\left(\frac{Z\alpha}{n-\varepsilon_j}\right)^2}}-mc^2\,, \tag{1.3}$$

Table 1.1: Summary of the notation introduced in this Chapter.

Abbreviation	Meaning
e, μ, p	electron, negative muon, proton
Z	nuclear charge
e	elementary charge
m	mass of the orbiting (lighter) particle
m_e	electron mass = 0.511 MeV/c^2
m_μ	muon mass = 105.6 MeV/c^2
M	nuclear mass (for proton m_p = 938.3 MeV/c^2)
n	principal quantum number
l	orbital quantum number
S, P, D	states defined by $l = 0$, 1, 2, respectively
s	spin of the orbiting particle (1/2 for electron and muon)
$\oplus$	quantum sum
j	total angular momentum of the orbiting (lighter) particle $j = s \oplus l$
I	spin of the nucleus (1/2 for proton)
F	total angular momentum of the hydrogen–like atom $F = j \oplus I$
F_z	z–component of F
E_b	binding energy of the state defined by quantum number(s) b
r, θ, ϕ	spherical coordinates
R	radial part of the wave–function in spherical coordinates
fs	fine splitting
hfs	hyperfine splitting
m_r	reduced mass
α	fine structure constant
c	speed of light in vacuum
h	Planck constant
$\hbar$	$\hbar = h/2\pi$
δ_{ij}	Kronecker symbol

where

$$\varepsilon_j = j + \frac{1}{2} - \sqrt{\left(j + \frac{1}{2}\right)^2 - (Z\alpha)^2}\,. \tag{1.4}$$

Therefore, the Dirac equation removes a part of the n–state degeneracy, Eq. (1.2), predicted by the Schrödinger equation. In the Dirac spectrum, energy levels with the same principal quantum number n but different j are split into n components of the fine structure (fs). However, states with the same n and j remain degenerate. For example the $2S_{1/2}$ and $2P_{1/2}$ states (both having $n = 2$, $j = 1/2$) have the same binding energy, independent of the l–value, but different from the energy of the $2P_{3/2}$ ($n = 2$, $j = 3/2$) state. When E_{nj} is expanded in powers of $(Z\alpha)$, the relation with E_n becomes evident:

$$E_{nj} = E_n \left[1 + \frac{(Z\alpha)^2}{n}\left(\frac{1}{j+\frac{1}{2}} - \frac{3}{4n}\right) + \ldots\right]. \tag{1.5}$$

The hyperfine splitting (hfs) of energy levels results from an interaction between the angular momentum j and the nuclear spin I. In a naive picture, an orbiting charged

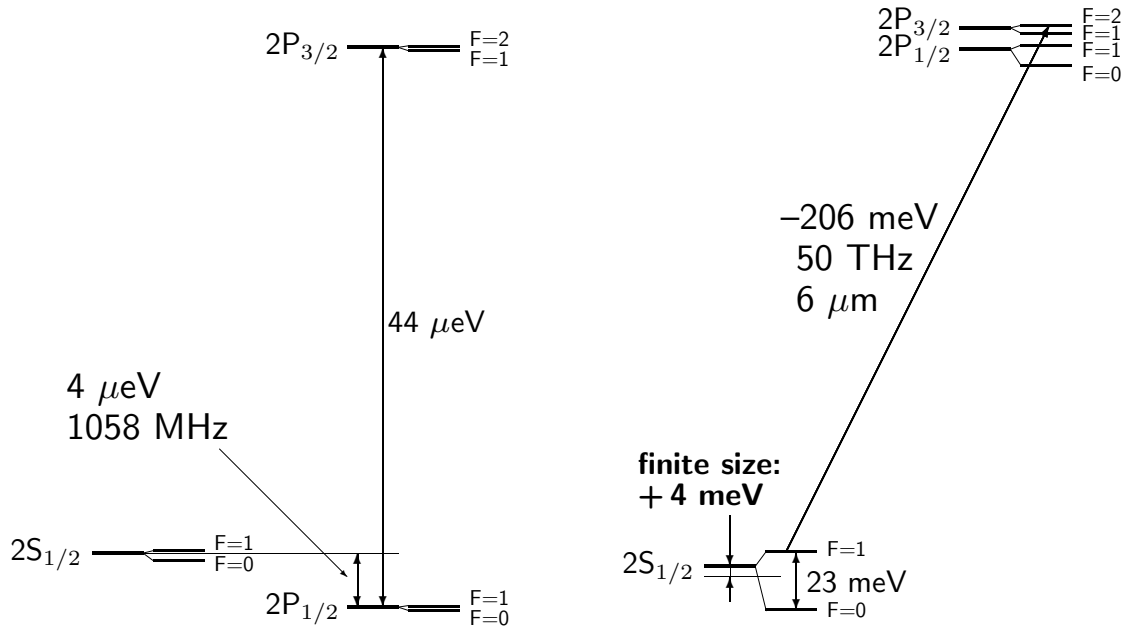

*Figure 1.1: Comparison of the $n = 2$ energy levels in normal hydrogen (*ep *atom left) and in muonic hydrogen (μp *atom right). Note the different energy scales in the two atoms (μeV in the* ep *and meV in the* μp*). The indicated 4 μeV energy difference between the* ep$(2S_{1/2})$ *and* ep$(2P_{1/2})$ *states was discovered by the famous Lamb experiment in 1947 and is dominated by the electron self–energy correction. In the* μp *atom, on the other hand, the $2S$ level lies ∼200 meV below both $2P$ levels due to the dominant vacuum polarization correction. The arrow shows the* μp$(2S^{\mathrm{F}=1}_{1/2} \rightarrow 2P^{\mathrm{F}=2}_{3/2})$ *transition (6 μm wavelength) used in the* μp$(2S)$ *Lamb shift experiment (Chapter 2). The nuclear finite size correction of ≈4 meV represents about 2% of the* μp$(2S)$ *Lamb shift.*

particle induces a magnetic field which interacts with the magnetic moment of the nucleus. The energy of this interaction causes an additional splitting of each energy level. The energy difference between the hyperfine levels with different $F = j \oplus I$ becomes

$$\Delta E_{\mathrm{hfs}} = \frac{8}{3}\,\frac{A}{n^3}\,\frac{F(F+1) - I(I+1) - j(j+1)}{j(j+1)(2l+1)}\,, \tag{1.6}$$

where A is the splitting between the hyperfine levels $F = 1$ and $F = 0$ of the $1S_{1/2}$ state. The $1S_{1/2}$ hyperfine splitting in the ep atom is one of the most accurately measured quantities in physics: $A = 1420.405\ 751\ 766\ 7(9)$ MHz, as given in Ref. [1]. The "center of gravity" of the split levels remains E_{nj} (Eq. (1.5)) and the total splitting ΔE_{hfs} is shared between hyperfine levels according to their population. In the case of the $1S_{1/2}$ state, the $F = 1$ and $F = 0$ states are, respectively, a triplet ($F_z = +1, 0, -1$) and a singlet ($F_z = 0$). The shift of the energy level of the $F = 1$ state is $+1/(1+3) \cdot \Delta E_{\mathrm{hfs}}$, while the shift of the $F = 0$ level is $-3/(1+3) \cdot \Delta E_{\mathrm{hfs}}$.

In 1947, the experiment of Lamb and Retherford discovered a splitting between the $2S_{1/2}$ and the $2P_{1/2}$ energy levels in the ep atom [2], which according to Dirac theory are degenerate. This energy splitting (Fig. 1.1, which will be discussed in detail below) amounts to 4 μeV (1058 MHz), which represents a relative correction of 10^{-6} to the $2S_{1/2}$ binding energy. In the same year Bethe explained this splitting by the electron self–interaction [3]. This was the first QED correction. Since then QED made enormous progress in the study of subtle energy corrections, even those which are up to six orders

of magnitudes smaller than the energy splitting discovered by Lamb [4]. These additional contributions to the energy levels result from the interaction of the quantized electromagnetic field. The corrections are divided in four main classes [5]:

1. two–body recoil
2. radiative
3. radiative–recoil
4. nuclear size and structure

The **recoil corrections** take the nucleus motion into account and reflect a deviation from the theory with an infinitely heavy nucleus. They depend on the mass ratio m/M and $(Z\alpha)$. They describe contributions to the energy levels [5] which cannot be taken into account with the help of the reduced mass $m_{\rm r}$

$$m_{\rm r} = \frac{m\,M}{m+M}\,. \tag{1.7}$$

Besides the simple reduced mass correction

$$\Delta E^1(\text{reduced mass}) = -\frac{m}{m+M}\;E_{nj}\,, \tag{1.8}$$

there is a second reduced mass correction

$$\Delta E^2(\text{reduced mass}) = -\frac{(m_{\rm r}c)^2}{M+m}\;\frac{(Z\alpha)^4}{8n^4}\,. \tag{1.9}$$

The original Lamb experiment [2] measured the energy splitting $\Delta E(2S_{1/2} - 2P_{1/2})$, which is an experimental observable defined independently of any theory [5]. Modern high–precision experiments require an extended, unambiguous definition of the Lamb shift. There emerged an almost universally adopted convention to call as Lamb shift all deviations from the Dirac energy ΔE_{nj}, with the exception of both reduced mass corrections and hyperfine splitting:

$$E = \Delta E_{nj} + \Delta E^1(\text{reduced mass}) + \Delta E^2(\text{reduced mass}) + \Delta E(\text{Lamb shift})\,. \tag{1.10}$$

In practice, the Lamb shift of P states is much smaller than those of S states, since the P state wave–function is equal to zero at the origin.

The leading recoil correction of order $(Z\alpha)^4(m/M)^n$, *i.e.*, the term ΔE^2(reduced mass) together with the spin–orbit correction

$$\Delta E(\text{spin-orbit}) = \frac{(m_{\rm r})^3c^2}{M^2}\;\frac{(Z\alpha)^4}{2n^3}\;\left[\frac{1}{j+\frac{1}{2}} - \frac{1}{l+\frac{1}{2}}\right](1-\delta_{l0}) \tag{1.11}$$

represent the one photon exchange between the nucleus and the orbiting particle. These corrections may still be taken into account with the help of the effective Dirac equation in the external field (the Hamiltonian containing the Breit effective potential and the kinetic energy of the nucleus [6]), which is not possible for the higher order corrections [5]. The two– and three–photon exchanges are the recoil corrections of order $(Z\alpha)^5(m/M)m$ and $(Z\alpha)^6(m/M)m$ [5], respectively.

The **radiative corrections** consider the changes of the electromagnetic potential seen by the orbiting particle. They depend on the parameters α and $(Z\alpha)$, but do not depend on the recoil parameter m/M [5]. Powers in α arise only from the QED loops, and all

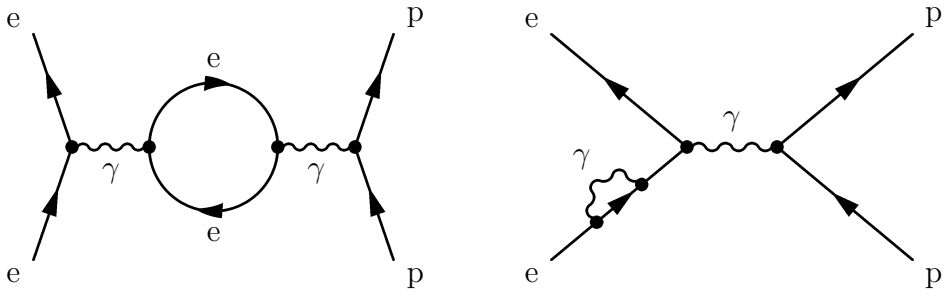

Figure 1.2: Feynman diagrams of the e^+e^- vacuum polarization (left) and the electron self–energy (right) corrections to the energy levels in an ep *atom. Analogous diagrams are valid for the* μp *atom; the electron has to be replaced by the muon (excluding the e^+e^- loop).*

associated corrections have a quantum field theory nature. These corrections are the dominant contributions to the Lamb shift for both ep and μp atoms. There are two main types of radiative corrections, the electron (muon) self–energy and the vacuum polarization (VP). The Feynman diagrams for the one–loop electron VP and the electron self–energy corrections in the ep atom are shown in Fig. 1.2.

The electron (muon) self–energy corrections are due to the emission and re–absorption of virtual photons [7] and as a result its electric charge is spread over a finite volume instead of being point–like [5]. Thus, the orbiting particle acquires form factors and no longer behaves precisely as a point–like Dirac particle. An experimental consequence of this fact is, *e.g.*, the anomalous magnetic moment of the electron (muon). Since the electron (muon) charge is on the average more spread around the Coulomb source than in the case of a point-like particle, the binding is weaker and the energy level lies higher [5].

The VP corrections results in a modification of the photon propagator due to a virtual e^+e^- pair production and re-annihilation; this leads to a modification of Coulomb's law at distances small compared to the electron Compton wavelength. The bound particle, which has penetrated in the polarization cloud near the nucleus, sees effectively a larger charge and experiences a stronger binding force, which lowers the energy level [5].

The one–loop radiative correction $\Delta E^1_{\rm rad}$, including both self–energy and VP can be expressed [6, 8] by

$$\Delta E^1_{\rm rad} = \frac{mc^2}{n^3}\,\frac{\alpha}{\pi}\,(Z\alpha)^4\,F_n(Z\alpha)\,, \tag{1.12}$$

where $F_n(Z\alpha)$ is a complex expansion in terms of $(Z\alpha)$ and $\ln(Z\alpha)^{-2}$; its coefficients include the famous one–loop Bethe logarithm whose precise evaluation required more than three decades [4].

The two–loop radiative corrections $\Delta E^2_{\rm rad}$ can be expressed in an analogous way, where the $F_n(Z\alpha)$ expansion is replaced by the $H_n(Z\alpha)$ expansion with coefficients B_{ij}:

$$\begin{aligned} H_n(Z\alpha) =& B_{40} + (Z\alpha)B_{50} + \\ &+ (Z\alpha)^2\{B_{63}\ln^3(Z\alpha)^{-2} + B_{62}\ln^2(Z\alpha)^{-2} + B_{61}\ln(Z\alpha)^{-2} + B_{60}\} + \dots\,, \end{aligned} \tag{1.13}$$

where i is the total order in $(Z\alpha)$ and j is the order in $\ln(Z\alpha)^{-2}$. The coefficient B_{60} is the two–loop Bethe logarithm calculated only recently [4].

A special case of the VP correction is due to the virtual $\mu^+\mu^-$ pair creation. As a consequence of the large muon mass, this correction is suppressed by a factor $(\frac{m_e}{m_\mu})^2$

with respect to the e^+e^- vacuum polarization [5]. The contribution of virtual hadronic states, *i.e.*, the hadronic VP is obtained from the total cross section $e^+e^- \to$ hadrons; it is suppressed by a factor 0.66 with respect to the $\mu^+\mu^-$ vacuum polarization [7].

Radiative–recoil corrections are the expansion terms which depend simultaneously on the parameters α, $(Z\alpha)$ and m/M [5]. The largest radiative–recoil correction $\Delta E_{\rm rr}$ which is not included in the corrections described above is of order $(Z\alpha)^5$ and contributes only to S states

$$\Delta E_{\rm rr} = -1.364\,49(1)\ \alpha\ \frac{(Z\alpha)^5}{n^3}\ \frac{m}{M}\ mc^2\ \delta_{l0}\,. \tag{1.14}$$

The most important contributions to the last class of corrections are the **finite nuclear size** and the **nuclear polarization**. The finite nuclear size considers the spatial distribution of the nucleus. For spherically symmetric charge distributions with a root–mean–square charge radius $\langle r^2\rangle^{1/2}$, one obtains [9]

$$\Delta E_{\rm FS} = \frac{mc^2}{(\hbar/mc)^2}\ \frac{2}{3n^3}\ (Z\alpha)^4\ \langle r^2\rangle\ \delta_{l0}\,. \tag{1.15}$$

The $\Delta E_{\rm FS}$ contributes only to S states. This correction is very sensitive to the orbiting–particle mass, being proportional to m^3. Naively speaking, the heavier the particle, the smaller the Bohr radius of the atom, so that the energy levels are correspondingly more sensitive to the nucleus (proton) finite size. The nuclear polarization accounts for the nuclear excitation to virtual excited states and its precise calculation is still a challenge.

The ratio of the μp and ep reduced masses has the large value of 186 and is the main cause of differences in the structure of the ep and μp energy levels. The binding energy of a muon is therefore 186 times higher than that of an electron in the same quantum state, and the μp Bohr radius is 186 times smaller with respect to a normal hydrogen atom. Binding energies in the ep atom are in the eV region, in the μp atom in the keV region. In particular, the K_α lines in the ep and μp atoms have energies of 10 eV and 1.9 keV, respectively.

From the point of view of the μp$(2S)$ Lamb shift experiment it is important to point out the differences between the $n = 2$ energy levels in the ep and μp atoms (Fig. 1.1). The main contribution to the ep$(2S)$ Lamb shift is the electron–self energy correction of $\sim$4 μeV (a 10^{-6} effect on the $2S$ binding energy). The VP is about 40 times weaker and has a negative sign. In contrast, the μp$(2S)$ Lamb shift is dominated by the VP, since the μp atom dimensions ($2S$ Bohr radius $= a_{2S}^{\mu\rm p} = 1139$ fm) are comparable with the electron Compton wavelength ($\lambda\!\!\!^{-}_{\rm e} = 386$ fm). The μp$(2S)$ VP correction is -206 meV (3.3×10^{-4} relative to its binding energy). Hence, it shifts the $2S$ level well below both the $2P_{1/2}$ and $2P_{3/2}$ states. In the μp atom the muon self–energy correction is $+0.7$ meV, *i.e.*, $\sim$300 times smaller than the VP.

The S states of the muonic atom overlap considerably with the nuclear volume and their energy is therefore much more sensitive to the finite size of the proton. The corresponding shift $\Delta E_{\rm FS}$ represents about 2% of the μp$(2S)$ Lamb shift, *i.e.*, two orders of magnitude more than in the ep atom. This makes the μp atom an excellent tool for studying the proton structure by measuring the $(2S - 2P)$ shift, in particular $\Delta E(2S^{\rm F=1}_{1/2} - 2P^{\rm F=2}_{3/2})$ (Chapter 2).

Several precise calculations of $\Delta E(2S^{\rm F=1}_{1/2} - 2P^{\rm F=2}_{3/2})$ in the μp atom have been made in the last few years [5, 6, 10–15]. They include contributions on the level of some ppm, like three–loop vacuum polarization (0.008 meV) [11] and hadronic vacuum polarization (0.011 meV) [16]. A summary of the different contributions is given in Table 1.2. The

Table 1.2: Summary of all contributions to the energy difference $-\Delta E(2S^{\mathrm{F}=1}_{1/2} - 2P^{\mathrm{F}=2}_{3/2})$ *in the* μp *atom. The total energy difference as well as the precision goal of the* μp$(2S)$ *Lamb shift experiment are indicated. The finite size corrections are given for* $r_{\mathrm{p}} = 0.8750(68)$ *fm (Ref. [22] adopted). The relevant references are [5, 6, 10–15]. The values for the (estimated) uncertainties are given only when they exceed 0.0002 meV. The values denoted by* $*$ *are dominated by the* r_{p} *uncertainty.*

Contribution	[meV]	Uncertainty [meV]
Leading order VP	205.0074	
Relativistic correction to VP	0.0169	
Double VP	0.1509	
Two–loop VP	1.5079	
Three–loop VP	0.0076	
Muon self energy and muon VP	-0.6677	
Muon self energy and electron VP	-0.0055	0.0010
Hadronic VP	0.0108	0.0004
Recoil of order $(Z\alpha)^4$	0.0575	
Recoil of order $(Z\alpha)^n$	-0.0445	0.0010
Radiative-recoil	-0.0095	
Proton self energy	-0.0099	
Wichmann–Kroll	-0.0010	
Virtual Delbrück	0.0013	
e–loop in the radiative photon, $\alpha^2(Z\alpha)^4$	-0.0016	
Finite size of order $(Z\alpha)^4$, -5.1974 r_{p}^2	-3.9793	$*$
Finite size of order $(Z\alpha)^5$, 0.0363 r_{p}^3	0.0243	$*$
Finite size of order $(Z\alpha)^6$	-0.0009	0.0003
VP with finite size, -0.0282 r_{p}^2	-0.0216	$*$
Radiative correction to finite size	0.0005	
Proton polarizability	0.0157	0.0040
Fine structure $\Delta E(2P_{1/2} - 2P_{3/2})$	8.3520	0.0010
$2P^{\mathrm{F}=2}_{3/2}$–hfs, $3.393 \times 3/(3+5)$	1.2724	0.0005
$2S^{F=1}_{1/2}$–hfs, $-22.8148 \times 1/(1+3)$	-5.7037	0.0020
Total $209.9566 - 5.2256 r_{\mathrm{p}}^2 + 0.0363 r_{\mathrm{p}}^3$	205.9800	
Experimental goal of 30 ppm precision	± 0.0062	

$2S$–hfs was recently investigated by Martynenko [15], reducing the uncertainty due to the proton structure (Zemach correction) to 0.008 meV for the $2S$–hfs which corresponds only to 0.002 meV for the $2S^{\mathrm{F}=1}_{3/2}$ state. Disregarding terms which depend on the proton radius, the calculated $\Delta E(2S^{\mathrm{F}=1}_{1/2} - 2P^{\mathrm{F}=2}_{3/2})$ value is finally limited to the 10–20 ppm precision level by the present uncertainty in the calculated proton polarization shift (0.013 meV [17], 0.012(2) meV [18], 0.017(4) [19], 0.016 meV [20]). In Table 1.2, an average value of 0.0157 meV was adopted for this proton polarizability. Relatively large uncertainties stem from yet uncalculated light–by–light scattering terms, as discussed in Refs. [12] and [14]. However, a calculation of these terms seems feasible, as it was done, *e.g.*, for muonic helium [21].

Chapter 2

Muonic hydrogen Lamb shift experiment: what, why, and how

The goal of the muonic hydrogen Lamb shift experiment going on at the Paul Scherrer Institute (PSI), *i.e.*, which quantity will be measured with which precision, is discussed in this Chapter together with an overall picture of the basic principle of the experiment. The importance of our measurement in the framework of theory and other experiments is demonstrated here.

Our experiment aims to measure the energy difference between the $2S^{\mathrm{F}=1}_{1/2}$ and $2P^{\mathrm{F}=2}_{3/2}$ energy levels in the μp atom (Fig. 1.1) by means of laser spectroscopy to a precision of 30 ppm ($\sim$10% of the natural line width which is determined by the $2P$ state lifetime). Such a precision allows us to determine the root–mean–square (rms) charge radius of the proton, r_{p}, with 10^{-3} relative accuracy (20 times more precise than presently known from non–spectroscopic experiments), according to the relation (resulting from Table 1.2)

$$\Delta E(2S^{\mathrm{F}=1}_{1/2} - 2P^{\mathrm{F}=2}_{3/2}) = 209.957(5) - 5.226\ r_{\mathrm{p}}^2 + 0.036\ r_{\mathrm{p}}^3 \qquad [\mathrm{meV}]\,, \tag{2.1}$$

where r_{p} is given in fm. In terms of frequency this energy splitting is about 50 THz, corresponding to a wavelength $\lambda \approx 6$ μm.

Many physical constants are known with high precision, *e.g.*, fractions of ppm. The proton is the lightest and the simplest stable hadronic system, and to understand its properties is of fundamental importance. However, such a basic property as its size, expressed by r_{p}, is known only at the precision level of a few percent. The present knowledge of the proton charge radius comes from two independent sources, namely from electron scattering experiments and from precision spectroscopy of normal hydrogen atoms (Fig. 2.1).

The analysis of experiments measuring cross sections versus momentum transfer q of electron scattering on protons faces many problems, and the resulting r_{p} values are in contradiction with each other. A recent re–evaluation of all available electron scattering data [23] takes Coulomb distortion of the electron wave–function into account and introduces a new parametrization allowing proper treatment of data at higher momentum transfer. However, the resulting value, $r_{\mathrm{p}} = 0.895(18)$ fm, has still a relative uncertainty of 2%.

A slightly more precise r_{p}–value can be obtained via the determination of the $1S$ Lamb shift in ep atoms by means of laser spectroscopy. The most precise value considers all measurements of the $1S$–$2S$ and $2S$–nD transitions in hydrogen and deuterium and results in an uncertainty of the order of 2 ppm [24]. This $1S$ Lamb shift value yields an independent value for r_{p}, assuming that the bound–state QED calculations are precise.

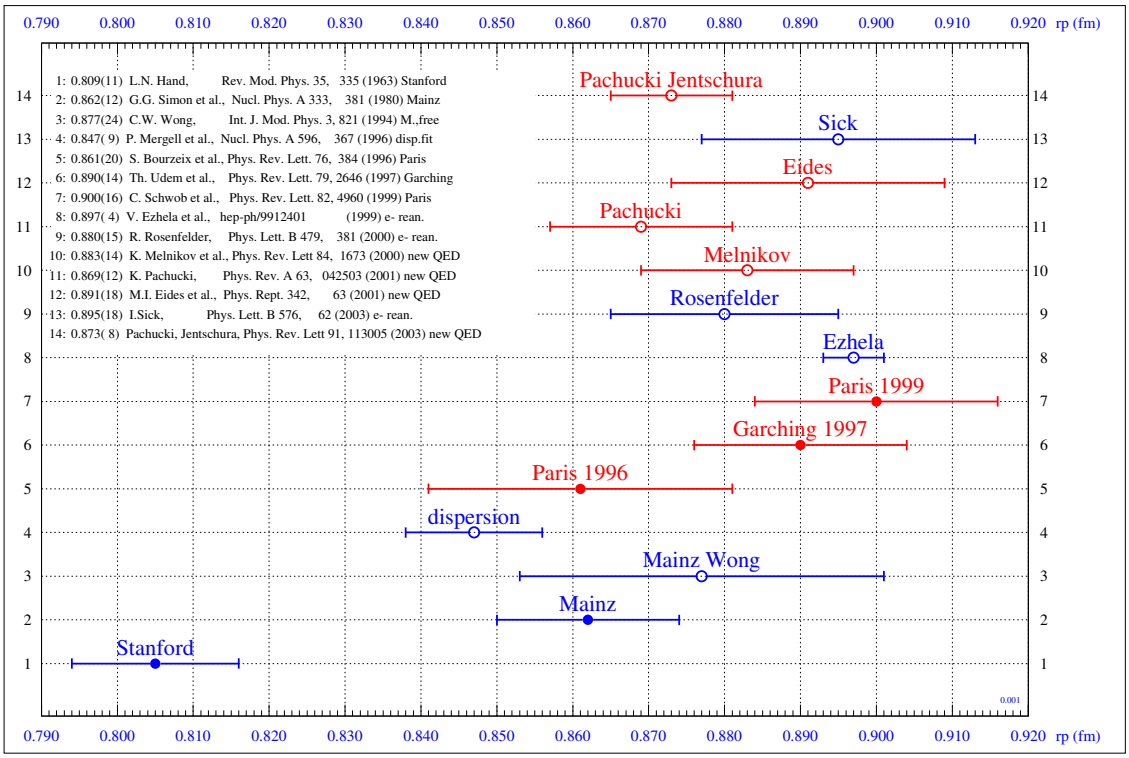

Figure 2.1: Proton charge radius r_p as a result of different experiments and calculations (the references are given in the top left corner; each number corresponds to the y–coordinate of the relevant point). The most recent values are shown at the top. Blue and red points stand for electron scattering and hydrogen spectroscopy experiments, respectively. Full points show the results of the original experiments, while empty points are the results of later re–evaluations of older data.

The recently published r_p–value from the 2002–CODATA adjustment [22] considers all data from electron scattering and hydrogen spectroscopy, resulting in r_p= 0.8750(68) fm (0.8% precision), but it is practically dominated by the measurements and calculations of the ep($1S$) Lamb shift.

The steady progress in the measurements of the Lamb shift in hydrogen and hydrogen–like atoms stimulated improvements in the methods of its calculation [5], and vice versa [24]. In particular, the first calculation of all terms given in Eq. (1.13) of the problematic two–loop self–energy contribution was published only recently [4]. The quoted precision of the calculated $1S$ Lamb shift is 0.25 ppm, when terms depending on the r_p are neglected. Further calculations of this two–loop contribution were performed by other authors, using different methods [25]. They confirm the previous result on the level of 1 ppm which can now be considered as a conservative estimate of the theoretical uncertainty for the $1S$ Lamb shift. However, this uncertainty becomes six times bigger, *i.e.*, 6 ppm, when the large r_p uncertainty determined by the only independent method (electron scattering) is considered. Therefore it is now mainly the r_p uncertainty which limits the comparison of theory with experiment at the 6 ppm level (3 times worse than the 2 ppm precision of the experiments). And from the point of view of the r_p value itself: since bound–state QED cannot be tested at the 2 ppm level, the r_p value calculated from the experimental results assuming QED validity at the same precision needs another independent confirmation.

An r_p determination from an independent source is therefore highly desirable. Such an independent source is precisely the μp atom where the finite size contribution to the

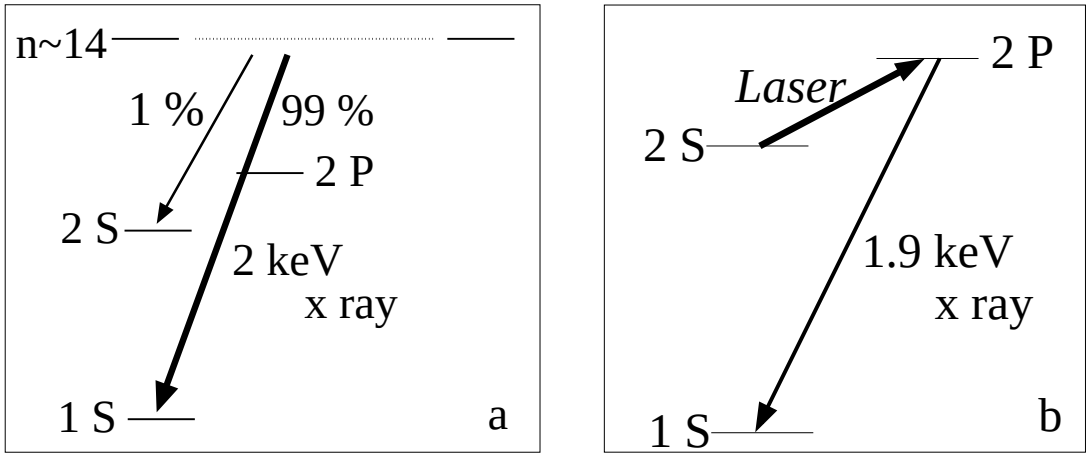

Figure 2.2: (a) A very simple sketch of the muon cascade in a μp atom. The muon is captured into a highly excited state ($n \approx 14$). With a high ($\sim$ 99%) probability the muon de–excites to the $1S$ state emitting a 1.9 keV x ray. Only $\sim$ 1% of the stopped muons end in a long–lived metastable $\mu p(2S)$ state ("slow" $2S$ component) having a lifetime of about 1.3 μs at 0.6 hPa H_2 gas pressure. The existence of a "fast" decaying $2S$ component is neglected here.
(b) The basic idea of the $\mu p(2S)$ Lamb shift experiment. A short laser pulse, which is in resonance with the $2S$–$2P$ energy difference, excites the muon from the metastable $2S$ state to a short lived $2P$ state. The emitted 1.9 keV K_α x ray will be delayed with respect to the muon stop time, but coincident with the laser.

$\Delta E(2S - 2P)$ is as large as 1.8%, two orders of magnitude more than for the ep atom. Therefore, a μp–experiment with 30 ppm precision can be used to determine r_p with 10^{-3} precision. This is exactly the aim of our experiment, as stated at the beginning of this Chapter. Measuring the $\mu p(2S)$ Lamb shift and combining it with precision hydrogen spectroscopy will then lead to a test of bound–state QED at a precision level of a few times 10^{-7} [4], and also to an improved value of the Rydberg constant. This would again stimulate higher–order correction calculations and higher precision measurements.

A full understanding of the quark interactions at low energies would allow us to predict the proton charge radius. Therefore, there is an additional strong interest in the r_p value also from the QCD community side, since a precise, experimentally known value can be a guide and a test for lattice and effective–field theory calculations.

The principle of our $\mu p(2S)$ Lamb shift experiment is now summarized as follows: Negative muons are stopped in low pressure H_2 gas where highly excited μp atoms are formed (§3.1). Most of them de–excite within ~100 ns to the ground state emitting K–series x rays with an energy around 2 keV (Fig. 2.2 a). Only about 1% of the stopped muons form long–lived $\mu p(2S)$ atoms with a lifetime of 1.3 μs at 0.6 hPa gas pressure [26]. A short laser pulse with a wavelength tunable around $\lambda \approx 6$ μm is sent into a mirror cavity surrounding the muon stop volume. The laser pulse is delayed by $\sim$ 1.5 μs with respect to the muon stop. A shorter delay of a few hundred ns would be optimum, but the present value is given by the internal delay of the laser. The laser pulse induces the $2S$–$2P$ transition (Fig. 2.2 b). The short–lived $2P$ state (8.6 ps lifetime) de–excites radiatively to the $1S$ state emitting a 1.9 keV K_α x ray. In contrast to the K_α x rays from the direct cascade, these x rays are $\sim$ 1.5 μs delayed and are in coincidence with the laser (Fig. 2.3). The $\Delta E(2S^{F=1}_{1/2} - 2P^{F=2}_{3/2})$ energy difference is directly determined from the laser wavelength which is in resonance with the $2S^{F=1}_{1/2} - 2P^{F=2}_{3/2}$ transition. A resonance

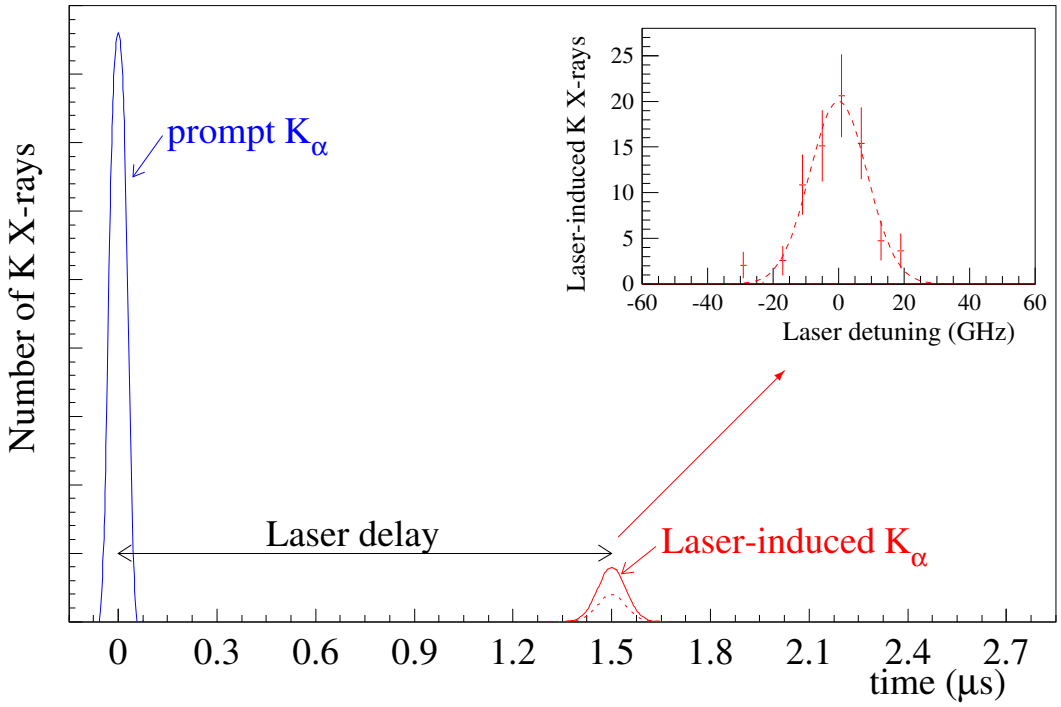

Figure 2.3: A cartoon of the time spectrum of the μp K_α x rays. The high intensity peak at early times is due to the x rays from the direct muon cascade (Fig. 2.2 a). A smaller peak centered at 1.5 μs, i.e., at the time of the laser arrival to the muon stop volume, is due to the laser–induced x rays (Fig. 2.2 b). The smaller plot at the top right corner represents a resonance curve resulting from measurements at different laser frequencies, i.e., the intensity of the delayed, laser–induced K_α peak as a function of the laser frequency (0 represents the resonance frequency).

curve is obtained by measuring at different laser wavelengths the number of laser induced K_α x rays which occur in time coincidence with the laser pulse.

It is obvious that a detailed knowledge about lifetime and population of the metastable $\mu p(2S)$ state is important for the Lamb shift experiment. It is known from previous experimental work [27] that the $2S$ state is initially populated with more than 2% probability. The kinetic energies of the $\mu p(2S)$ atoms are broadly distributed around a few eV. About half of them make collision–induced Stark transitions to the $2P$ state where they radiatively decay to the ground state ("fast" $2S$ component). The other half is elastically slowed–down to near–thermal energies, well below the $2S-2P$ energy threshold (0.31 eV), and there is only a non–radiative $2S-1S$ decay channel open, resulting in the before mentioned much longer $2S$–lifetime ("slow" $2S$ component).

The fast radiative $2S$ component was searched for without success in previous experiments [28, 29], but observed for the first time in the data obtained here for our laser experiment. A detailed analysis and discussion of the population and lifetime of this fast $2S$ component is one of the main topics of this thesis, together with the first direct measurement of the μp cascade time. The laser experiment itself is based on the slow $2S$ component, but the new results about the fast component give also an independent confirmation of the value previously determined for the population of the slow $2S$ component.

Chapter 3

Muonic atoms

Exotic atoms are atoms where an electron is replaced by another negatively charged particle, like a μ^-, π^-, K^-, or $\bar{p}$. In a more general way, any electromagnetically bound state of one negatively and one positively charged particle is considered as an exotic atom, like *e.g.*, muonium μ^+e^- or positronium e^+e^-. The muonic atoms μZ (where Z stands for any nucleus with charge Z) are one representation of the family of exotic atoms.

This Chapter introduces the key points of the physics of muonic atoms, necessary to understand the following parts of this work. Section 3.1 concerns the most elementary case, the muonic hydrogen (μp) atom. Section 3.1.1 describes the μ^- slowing down in H_2 gas preceding an eventual formation of an excited $(\mu p)^*$ atom. The characteristics of the muonic cascade in μp atoms, *i.e.*, of the de–excitation to the ground state, are given in §3.1.2. A crucial item for the $\mu p(2S)$ Lamb shift experiment is the existence of a metastable $2S$ state, to which §3.1.3 is dedicated.

The x–ray energy spectra measured in our experiment are dominated by the μp K–series x rays. However, transitions from other muonic atoms have also been identified in the spectra. Their basic properties are given in §3.2. The muon in the μp atom can be transferred to another higher Z atom. The most intense "background" in our energy spectra (at times delayed with respect to the μp formation) is due to x rays from μC atoms, having their origin in the muon transfer to a carbon atom in the polypropylene ($\approx (CH_2)_n$) foils placed in front of the x–ray detectors (§6.7.2).

A detailed analysis of our x–ray spectra proved the existence of a small air leak in our setup (see Appendix B). Therefore, there is a small probability (of order 10^{-2}) that a muon is captured by a N_2 or O_2 molecule and forms a muonic nitrogen (μN) or a muonic oxygen (μO) atom. μN and μO transitions can then be recognized in our x–ray energy spectra due to the large statistics collected in our measurements ($\sim 10^6$ μp x rays). Although such an air leak is an imperfection of our setup, the existence of muonic transitions at various energies helped us to identify some particular effects important for the energy and time calibration of our x–ray detectors (§§6.4 and 6.3, respectively). Moreover, the μN x ray time distribution is an important cornerstone for the analysis of the μp cascade time and the $\mu p(2S)$ lifetime (§7.3). Finally, no μN and μO x rays are emitted at delayed times where our search for laser induced μp K_α x rays is performed. Therefore, these x rays do not represent a source of "dangerous" background, in particular since the air concentration in hydrogen gas was at the level of 0.4%. The corresponding absolute partial air pressure of $\sim 2 \times 10^{-3}$ hPa is low enough that x rays after muonic transfer, *e.g.* $\mu p \rightarrow \mu N$, are emitted at negligibly small rates (of order 10 s^{-1}) for transition energies below 10 keV. The $\mu p(2S)$ lifetime is also not affected on any relevant level by this admixture.

3.1 Muonic hydrogen

3.1.1 Slowing down of μ^- and formation of a $(\mu p)^*$ atom

The slowing down of negative muons in hydrogen was studied both theoretically and experimentally, and similarities with antiprotons were stressed [30–35]. Negative muons and antiprotons with the same velocity v have approximately the same stopping power S. The stopping power, often given in units $\frac{\text{eV}}{\text{atoms/cm}^2}$, can be expressed as a function of the projectile energy. Knowing the stopping power S, both the energy loss in a gas with atomic density n is:

$$\frac{dE}{dx} = -nS\,, \tag{3.1}$$

$$\frac{dE}{dt} = v\,\frac{dE}{dx} = -vnS\,. \tag{3.2}$$

By integrating Eqs. (3.1) and (3.2), a mean range $R(E_i)$ and a mean slowing down time $T(E_i)$ can be obtained:

$$R(E_i) = \int_{E_{\text{cap}}}^{E_i} \frac{1}{-\frac{dE}{dx}} dE = \frac{1}{n}\int_{E_{\text{cap}}}^{E_i} \frac{1}{S(E)} dE\,, \tag{3.3}$$

$$T(E_i) = \int_{E_{\text{cap}}}^{E_i} \frac{1}{-\frac{dE}{dt}} dE = \frac{1}{n}\int_{E_{\text{cap}}}^{E_i} \frac{1}{vS(E)} dE\,, \tag{3.4}$$

where E_i stands for the initial projectile energy and E_{cap} for the energy when it is captured and an exotic atom is formed. The instantaneous velocity v can be expressed as a function of the kinetic energy E:

$$v(E) = \sqrt{\frac{2}{mc^2}}\, c\sqrt{E}\,, \tag{3.5}$$

where m is the projectile mass and c the speed of light.

For the stopping power S we use the form

$$\frac{1}{S} = \frac{1}{S_{\text{low}}} + \frac{1}{S_{\text{high}}} \tag{3.6}$$

first suggested by Varelas and Biersack [36]. S_{low} dominates at low energies and S_{high}, well described by the Bethe formula, at high energies. The stopping power for muons is not known with the same precision as for antiprotons. Therefore, we adopted the parametrization published for antiprotons in H_2 gas with energies above 0.5 keV in Ref. [32], where the similarity with the measured muon stopping power [31] down to muon energies of about 100 eV is pointed out. Rescaling in–between the muon and the antiproton can easily be done, considering that at the same velocity the relation between the muon energy E_μ and the antiproton energy $E_{\bar{p}}$ is

$$E_\mu = E_{\bar{p}}\frac{m_\mu}{m_{\bar{p}}}\,, \tag{3.7}$$

where m_μ and $m_{\bar{p}}$ are the muon and antiproton masses, respectively. We then obtain for muons

$$S_{\text{low}} = 0.30 E_\mu^{0.3} \times 10^{-15} \qquad \left[\frac{\text{eVcm}^2}{\text{atoms}}\right], \tag{3.8}$$

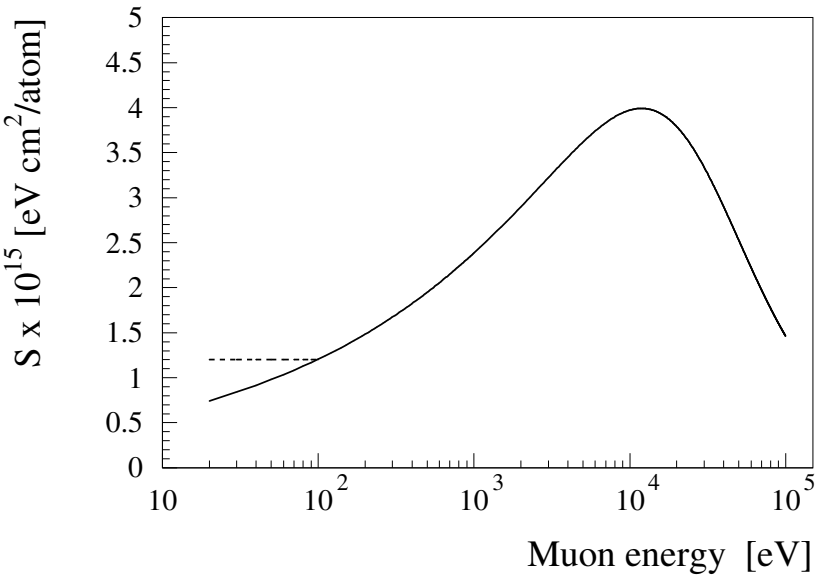

Figure 3.1: The stopping power S for negative particles in H_2 gas deduced from $\bar{p}$ data [32], as a function of muon energy (solid line). The dashed line represents a constant stopping power S_0 which is in better agreement with the μ^- data of Ref. [31] at energies below 100 eV.

$$S_{\rm high} = \frac{27414}{E_\mu}\ \ln\left(1 + \frac{4.52\times10^7}{E_\mu} + 1.026\times10^{-3}E_\mu\right) \qquad \left[\frac{\rm eVcm^2}{\rm atoms}\right], \tag{3.9}$$

where E_μ is given in eV. The resulting muon stopping power S is shown in Fig. 3.1. $S_{\rm low}$ deviates from S by less than ∼10% for muons with energies lower than ∼ 6000 eV.

Based on the experimental results shown in Ref. [31], the muon stopping power at energies below ∼200 eV is nearly constant, namely $S_0 = 1.2\times10^{-15}\ \frac{\rm eVcm^2}{\rm atoms}$. Therefore, at muon energies below 100 eV, where the parametrization shown above yields a stopping power below this value, the parametrized stopping power is replaced by the constant value S_0. In Fig. 3.1, S_0 is represented by the dashed line.

Knowing the stopping power S, the mean range R and the mean slowing down time T can be calculated for different initial muon energies by means of Eqs. (3.3) and (3.4). For a muon slowing down in hydrogen, $E_{\rm cap}$ was calculated to be about 15 eV [30]. The dependency of T versus R shown in Fig. 3.2 is calculated for muons with initial energies E_i ranging from 16 to 10^4 eV, slowing down in 0.6 hPa of hydrogen ($n = 3.0\times10^{16}$ atoms cm^{-3} at 290 K). Note that dT/dR decreases with increasing range (energy).

As can be seen in Fig. 3.2, it takes a few hundred ns to slow down a muon with a kinetic energy of a few hundred eV. Such a time scale is consistent with the muon stop time distribution observed in our x–ray time spectra, as will be discussed in detail in §7.1. A muon slowed down to the energy $E_{\rm cap}$ can be captured by a hydrogen molecule. The $(pp\mu e)^*$ complex initially formed has an uniform energy distribution in the interval from 0 to 0.92 eV [37]. The upper part of the cascade is assumed to be dominated by de–excitation through dissociation and ro–vibrational excitations of the H_2 molecule [38]. Based on the H_2 dissociation energy of 4.7 eV, it is usually assumed that the $(\mu p)^*$ atom gets an initial kinetic energy around 1 eV [39]. The question of the initial n level ($n_{\rm i}$) is not yet completely solved. A rule of thumb, *i.e.*, $n_{\rm i} = \sqrt{m_{\rm r}(\mu p)/m_{\rm r}({\rm ep})} \approx 14$, corresponds to an optimum overlap of muonic and electronic wave functions. However, there are indications both

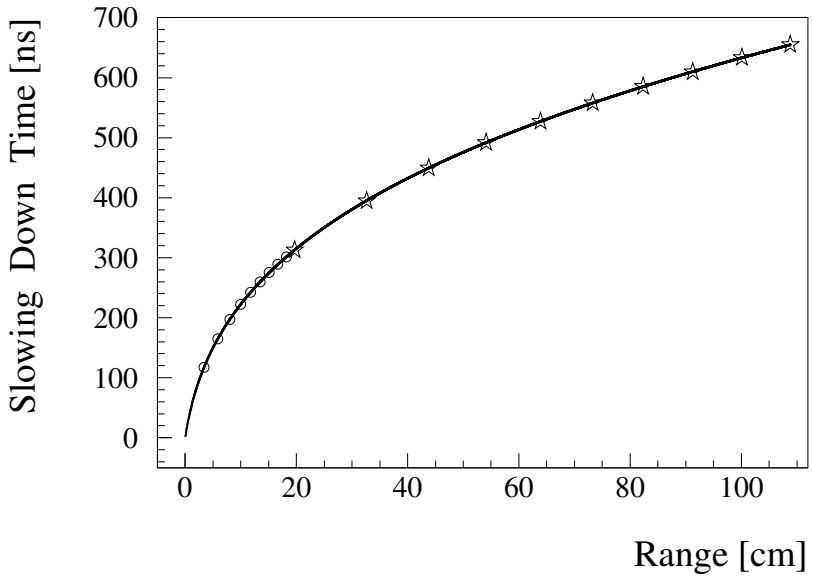

Figure 3.2: Mean slowing down time T versus mean range R for muons with energies from 16 to 10^4 eV slowing down in 0.6 hPa of hydrogen (a pressure used in the 2003 data taking period of the μp$(2S)$ Lamb shift experiment). Muons with initial energies in the range from 10 to 900 eV, in steps of 100 eV, are represented by circles, while those with initial energies in the range from 1 to 10 keV, in steps of 1 keV, are shown by stars.

from theory and experiments that the $n_{\rm i}$ values are larger and distributed at $n_{\rm i} \geq 14$ with probabilities proportional to n^{-3} [37].

3.1.2 Muon cascade after the formation of a μp atom

The formation of a μp atom is followed by a so called atomic cascade, *i.e.*, a number of transitions until the $1S$ ground state or the metastable $2S$ state are reached (in the following text this process is referred to as the *direct cascade*). Several cascade mechanisms are essential for a basic understanding of the atomic cascade:

1. *Coulomb de–excitation:*
   Represents a collisional type of de–excitation. A μp atom is about 200 times smaller compared to an ep atom. Due to its electroneutrality, it can approach the proton of an H_2 molecule, the field of which causes mixing between different nl states of the μp atom. From this point of view, Coulomb and Stark mixing (see below) are similar. In order to mix states with different values of n, as is the case for Coulomb de–excitation
   $$(\mu{\rm p})_{n_i} + p \rightarrow (\mu{\rm p})_{n_f} + p \tag{3.10}$$
   (where the final–state n_f is smaller than the initial–state n_i), a much stronger field is needed than in the case of mixing of nearly degenerate l sub-states with the same n (Stark mixing). The Coulomb de–excitation rates increase with n, dominate at high n states relative to other de–excitations and are proportional to $1/\sqrt{E_k}$ [40], where E_k is the kinetic energy of the μp atom. A significant part of the released binding energy is converted into μp kinetic energy, *i.e.*, the Coulomb de–excitation causes an acceleration of the μp atom. It is thus responsible for the so called high–energy component of the μp kinetic energy distribution.

2. *External Auger effect:*
   De–excites a μp atoms via ionization of neighboring H_2 molecules,

$$(\mu p)_i + H_2 \rightarrow (\mu p)_f + H_2^+ + e^- \,. \tag{3.11}$$

   The external Auger transition is only weakly dependent on E_k [40]. In contrast to the Coulomb de–excitation, nearly all the transition energy is carried away by the released electron, so that the recoil energy of the μp atom is rather small. The Auger cross section has its maximum at a critical level $n_c = 7$ above which only $\Delta n > 1$ transitions are energetically possible (the H_2 ionization potential being 15.4 eV) and the cross section decreases with n. Below n_c, $\Delta n = 1$ transitions are possible, and the Auger rate falls rapidly with decreasing n as the size of the μp atom becomes much smaller than the electron Bohr radius.
3. *Stark mixing transitions:*
   Represent the fastest collisional processes with the cross section determined by the size of the ep atom [40]. When a small electroneutral μp atom crosses an ep atom, the electric field mixes the l sub-levels with the same n (linear Stark effect)

$$(\mu p)_{nl_i} + H \rightarrow (\mu p)_{nl_f} + H \,. \tag{3.12}$$

   The Stark transitions affect the population of the l sub-levels, having a strong effect on the rates of processes allowed only from certain l sub-levels. The Stark rates are monotonically increasing functions of the kinetic energy E_k and of n.
4. *Radiative transitions:*
   Are dominated by $E1$ electric dipole transitions with the selection rule $\Delta l = \pm 1$

$$(\mu p)_i \rightarrow (\mu p)_f + x \,. \tag{3.13}$$

   The emitted x rays are the most important observables for a thorough study of the cascade process. The radiative rates strongly increase with decreasing n. Below a specific density–dependent n value, the radiative transitions dominate the cascade, and the kinetic energy E_k remains more or less unchanged. This cut–off–n increases with lower hydrogen density, so that measurements of the kinetic energy distribution at low pressures provide relevant information on the n–dependence of the collisional effects. Some possible radiative transitions in a μp atom are schematically shown in Fig. 3.3. The most probable transitions, with the highest yields are the so called *circular transitions*, *i.e.*, transitions between the highly populated sub-levels with $l = n - 1$, thus characterized by $\Delta n = \Delta l = 1$. The *circular transitions* are the most important source feeding the $1S$ ground state. The non–circular transitions partially feed the ground state, and exclusively the metastable $2S$ state. The radiative–transition yields depend on the H_2 gas pressure, being a consequence of the density dependence of the cut–off–n.
5. *Elastic scattering:*
   This process between μp and ep atoms,

$$(\mu p)_{nl} + H \rightarrow (\mu p)_{nl} + H \,, \tag{3.14}$$

   is a deceleration mechanism for a μp atom changing its kinetic energy but not its quantum state. The elastic scattering does not dominate the evolution of the energy distribution, and the atoms are far from being thermalized at the end of the cascade [40]. The elastic–scattering rates have the same $1/\sqrt{E_k}$ energy dependence as the Coulomb de–excitation [40].

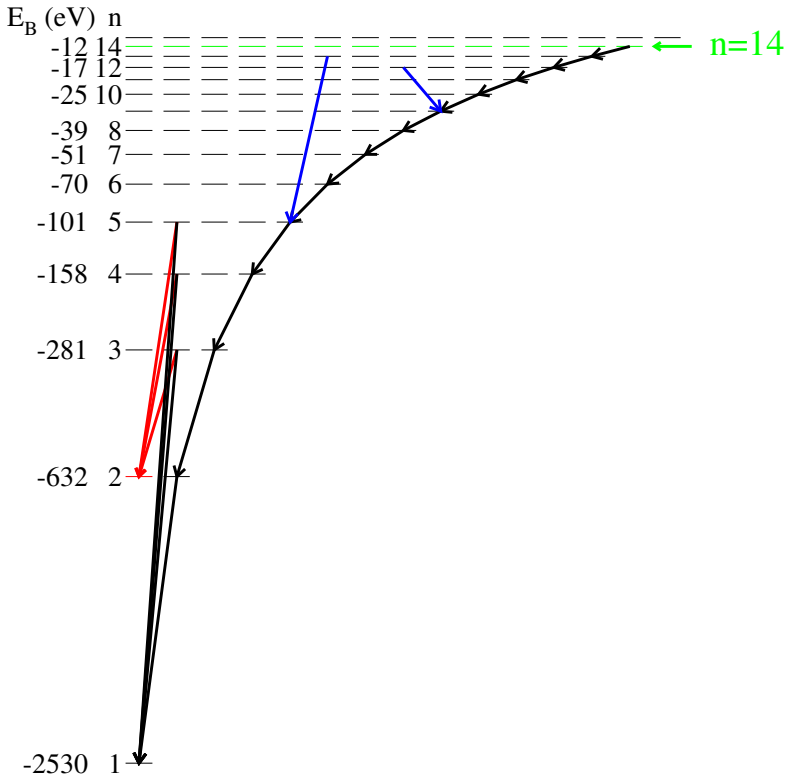

Figure 3.3: Scheme of the energy levels in the μp atom. The negative numbers on the left are the binding energies in electronvolts. The initial n_i is about 14. The arrows illustrate possible radiative transitions. The arrows at the very right represent the circular transitions between the $l = n - 1$ sub-levels, characterized by $\Delta n = \Delta l = 1$ and feeding the $1S$ ground state. The metastable $2S$ state is exclusively populated by non–circular transitions.

In the last four decades different cascade models have been developed. The so–called "minimum cascade model" (or "standard cascade model") considers the external Auger effect, Stark mixing and radiative transitions [39, 41, 42]. No energy evolution of the μp kinetic energy is taken into account in this model. The constant kinetic energy is a free model parameter chosen in order to fit the experimental data (usually it is around 1 eV). The minimum cascade model is of limited validity as soon as the kinetic energy distribution is concerned. However, it is widely used because it successfully describes the most important observable, the x–ray intensities.

The "extended cascade model", considering also the kinetic energy evolution, Coulomb transitions and elastic scattering, was introduced by V. Markushin [40, 43] and further developed by the extensive work of T. S. Jensen [38] treating the higher n domain by a classical–trajectory approach. This model was a breakthrough for understanding the pressure–dependent kinetic energy distributions. One of its limits is that it does not take into account the resonant formation of molecular states between the μp atom and H_2 molecule which play an important role at low n levels, in particular $n = 2$ (§3.1.3).

An important input and a cross-check for the cascade models come from measurements of the kinetic energies and yields over a wide range of H_2 gas pressures. The distribution

Table 3.1: Energies and measured relative yields (interpolated for 0.6 hPa) of the μp K–series [27, 47, 48]. K_α and K_β are the $2P \to 1S$ and $3P \to 1S$ transitions, respectively. K_{rest} represents the sum of all transitions from nP states with $n > 3$ down to the $1S$ state. Y_{tot} is the total K–yield, $Y_{tot} = Y_{K_\alpha} + Y_{K_\beta} + Y_{K_{rest}} \leq 1$.

Transition		Energy [keV]	Relative yield Y_K/Y_{tot}
$2 \to 1$	K_α	1.898	0.821(12)
$3 \to 1$	K_β	2.249	0.061(9)
$(> 3) \to 1$	K_{rest}	2.45(2)	0.118(11)

of the μp kinetic energies was first measured at gas pressures between 50 to 750 hPa [1] [44] and then investigated in more detail between 0.0625 hPa and 16 hPa [45, 46]. It was shown that the average kinetic energy of the μp($1S$) atoms increases from 1.3 ± 0.8 eV at 0.0625 hPa to 6.0 ± 0.5 eV at 16 hPa [26]. The K–series x–ray yields were measured between 0.33 hPa and liquid hydrogen density [27, 47, 48]. All measured yields and kinetic energies are quite well reproduced by the extended cascade model [46]. The relative yields of the μp K–series interpolated from theses data for 0.6 hPa H_2 gas pressure (used in the 2003 data taking period of the μp($2S$) Lamb shift experiment) are summarized in Table 3.1, together with the corresponding transition energies.

At low gas densities there are other important observables such as the time distributions of the K–series x rays. The shape of the measured x–ray time spectrum is the result of an interplay between the muon stop–time distribution and the cascade time distribution and can be described by a convolution of the corresponding two functions (§6.3). In the present experiment, the cascade time distributions could be clearly disentangled from the stop time distribution for the first time. Figure 3.4 shows the distributions of the μp direct cascade times calculated for K_α, K_β, and K_{rest} at 0.6 hPa H_2 gas pressure [46, 49] considering different $n_i = 12$, 14, and 16. The time zero is defined by the muon–capture time. The following characteristics of these time distributions are important for the analysis of the data described in §7.3:

1. Apart from the first few tens of ns, the calculated K_α, K_β, and K_{rest} time distributions can be described by a simple exponential function characterized by the same decay constant $\tau_{cas}^{\mu p}$ for all three cases. If such an exponential function is fitted to these time distributions (for times from 150 to 500 ns), the resulting $\tau_{cas}^{\mu p}$ is about 50, 70, and 80 ns for $n_i = 12$, 14, and 16, respectively.
2. There is no indication that the ratio of the K_{rest} and K_β intensities is significantly changing in time (apart from a small effect at early times).
3. The K_α time distribution increases during the first few tens of ns. If only a simple exponential function is used to fit the measured K_α time spectrum (which is further smeared out by the stop–time distribution), this "build–up" character would result in a positive time offset (with respect to the muon capture time) and a widening (with respect to the K_{rest} time distribution) of the K_α x–ray time spectrum.
4. The K_{rest} time distribution has a steep slope within the first ≈10 ns. If only a simple exponential function is used to fit the corresponding data, this different shape at early times would result in a negative time offset with respect to the muon capture time.

[1] 100 Pa = 1 hPa ≅ 1 mbar = 5.0 $\times 10^{16}$ atoms/cm^3 at T = 290 K; liquid hydrogen density = 4.25 $\times 10^{22}$ atoms/cm^3.

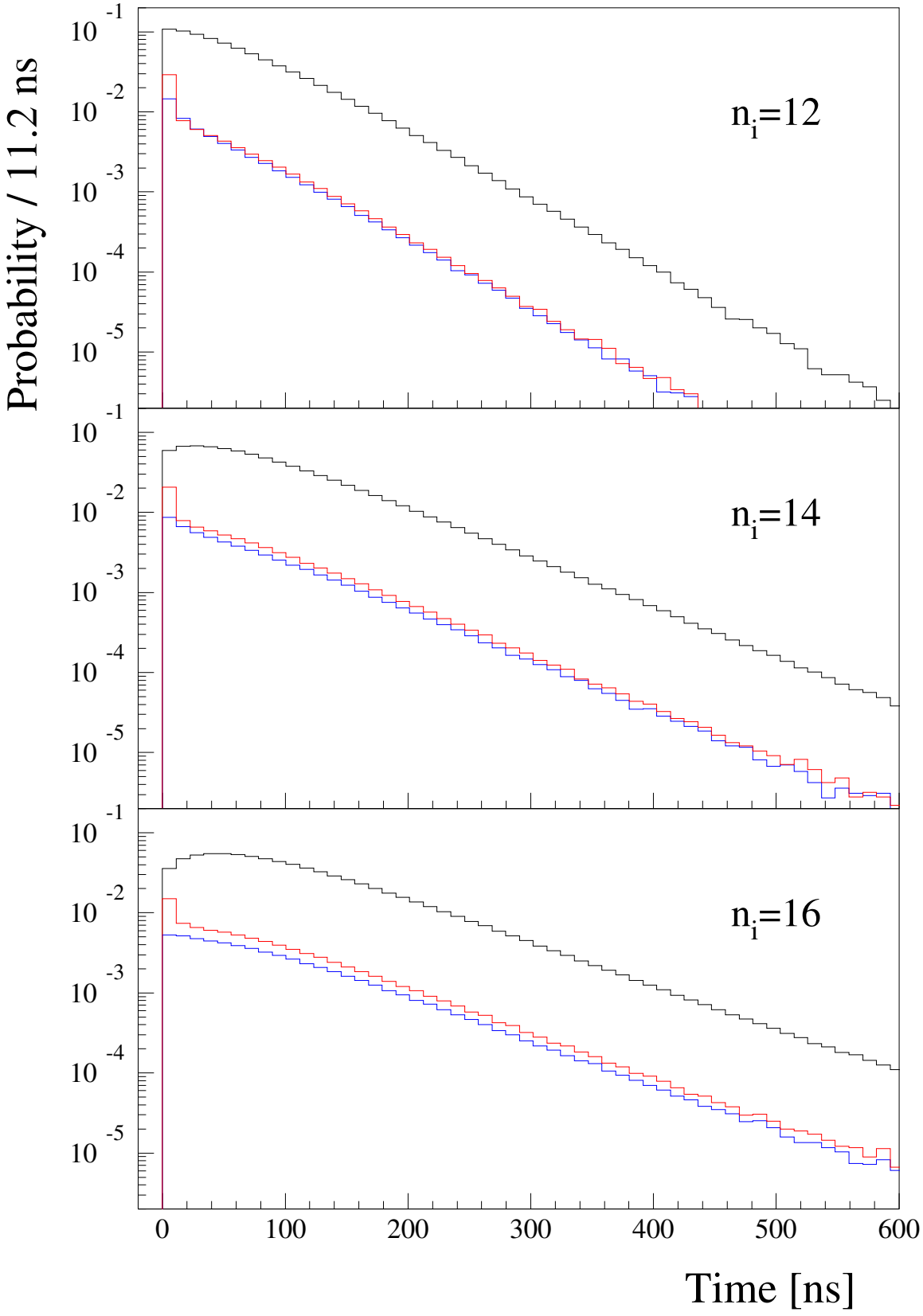

Figure 3.4: Time distributions of the μp direct–cascade K–series intensities calculated for 0.6 hPa H_2 gas pressure [49]. The highest intensity corresponds to the K_α transition. K_{rest} and K_β are plotted in red and blue, respectively. The top, middle, and bottom parts consider different initial n states (n_i = 12, 14, and 16, respectively). Time zero is defined by the muon capture time.

3.1.3 Characteristics of the metastable μp($2S$) state

The metastability of the μp($2S$) state is due to the fact that the one–photon $E1$ decay channel to the $1S$ level is forbidden ($\Delta l = 0$), and that the spontaneous two–photon decay [50] occurs with a rate of $\sim 1.5 \times 10^3$ s^{-1} which is small compared to the muon decay rate $\lambda_\mu = 4.55 \times 10^5$ s^{-1} (the inverse of the lifetime $\tau_\mu = 2.197$ μs). The $2S$ state is initially populated via non–circular radiative transitions from higher n levels. Population by non–radiative transitions is totally negligible at hPa gas pressures. Since these levels also feed the $1S$ ground state via the K$_\beta$ and K$_{\rm rest}$ transitions (see Fig. 3.3), there is a relation between the measured K–series x–ray yields Y_K and the fraction $P_{\rm 2S}$ of muons initially populating the $2S$ state. Radiative yields $Y_{\rm K}/Y_{\rm tot}$ are obtained from the measured energy spectra, but the small deviation of the total K–yield from unity due to non–radiative $2S$–decay can be estimated, as demonstrated below. Using the calculated branching ratios $\Gamma_{\rm rad}(3P \to 2S)/\Gamma_{\rm rad}(3P \to 1S) = 0.134$ and $\Gamma_{\rm rad}(n_{>3} \to 2S)/\Gamma_{\rm rad}(n_{>3} \to 1S) = 0.144$ for radiative transitions in the μp atom one obtains [27, 51]

$$P_{\rm 2S} = 0.134\ Y_{\rm K_\beta} + 0.144\ Y_{\rm K_{rest}}\ , \tag{3.15}$$

where the yields $Y_{\rm K_\beta}$ and $Y_{\rm K_{rest}}$ are by definition normalized to the number of all μp atoms, *i.e.*, the sum $N_{1S} + N_{2S}$ of μp atoms reaching the 1S or 2S state. This normalization guarantees that $P_{\rm 2S}$ corresponds to its definition

$$P_{\rm 2S} = \frac{N_{2S}}{N_{1S} + N_{2S}}\ . \tag{3.16}$$

Figure 3.5 shows $P_{\rm 2S}$ calculated from the measured x–ray yields at a wide range of H$_2$ gas pressures. As will be discussed below, there are two classes of μp($2S$) atoms, a "fast" component which has a population $P_{\rm 2S}^{\rm fast}$ and decays within ~150 ns (at 0.6 hPa) via emission of a (delayed) K$_\alpha$ x ray, and a "slow" component with population $P_{\rm 2S}^{\rm slow}$ and ~1.3 μs lifetime, decaying non–radiatively to the $1S$–state. These populations are again normalized to $N_{1S} + N_{2S}$, and therefore

$$P_{\rm 2S} = P_{\rm 2S}^{\rm slow} + P_{\rm 2S}^{\rm fast}\ . \tag{3.17}$$

In practice, the fast component is included in the measured relative yield $Y_{\rm K_\alpha}/Y_{\rm tot}$, whereas the slow component does not contribute to the total K–yield:

$$Y_{\rm K_\alpha} + Y_{\rm K_\beta} + Y_{\rm K_{rest}} = Y_{\rm tot} = 1 - P_{\rm 2S}^{\rm slow}\ . \tag{3.18}$$

For hPa gas pressures [45, 46], $P_{\rm 2S}^{\rm slow}$ was measured to be about 1%. By multiplying the measured relative yields $Y_{\rm K_\beta}/Y_{\rm tot}$ and $Y_{\rm K_{rest}}/Y_{\rm tot}$ (Table 3.1) with $Y_{\rm tot} \approx 0.99$, we get the absolute yields needed in Eq. (3.15) and hence

$$P_{\rm 2S} = (2.49 \pm 0.17)\% \quad (0.6\ {\rm hPa})\,. \tag{3.19}$$

The intrinsic lifetime of the $2S$ state is essentially given by the muon lifetime. In a gaseous environment however, the interactions with the surrounding molecules have to be taken into account, because collisional quenching may de–excite the μp($2S$) atom. As shown in Fig. 1.1 on page 5, the $2S$ level is shifted (mainly due to the attractive vacuum polarization correction) by ≈ 200 meV below the $2P$ levels. In H$_2$ gas, μp($2S$) atoms with center of mass (CM) energies above and below this threshold undergo different processes.

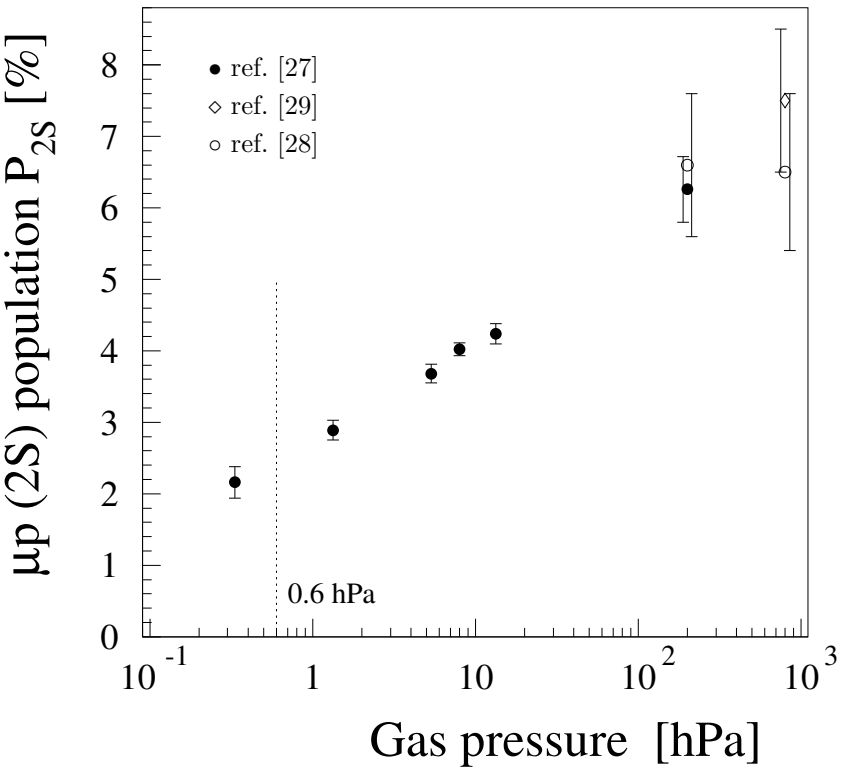

Figure 3.5: Fraction P_{2S} of muons reaching the $2S$ state versus gas pressure as obtained from measurements of muonic hydrogen K–series x–ray yields. The vertical dotted line represents the gas pressure used in our 2003 data taking period of the $\mu p(2S)$ Lamb shift experiment.

The $\mu p(2S)$ atoms with a kinetic energy of more than 0.31 eV in the laboratory frame (LAB), equivalent to 0.2 eV CM–energy, can be excited to the $2P$ state (10^{-11} s lifetime) if the collision is non–adiabatic, which is very likely at energies above $\sim$1 eV. Therefore, the original $\mu p(2S)$ atom can be radiatively quenched to the ground state via the fast $2P \rightarrow 1S$ transition:

$$\mu p(2S) + H_2 \rightarrow \mu p(2P) + H_2 \rightarrow \mu p(1S) + H_2 + K_\alpha \,. \tag{3.20}$$

This quenching of energetic $\mu p(2S)$ atoms characterizes the short–lived, so–called "fast component" of the total fraction P_{2S}. The corresponding cross sections $\sigma_{\rm quench}$ were calculated for collisions with H atoms, $\mu p(2S) + H \rightarrow \mu p(2P) + H$, to be of order of the atomic size, *i.e.*, $\sigma_{\rm quench} \approx \pi\, a_o^2$ [52–54].

Towards lower kinetic energies, this cross section $\sigma_{\rm quench}$ at kinetic energies around 1 eV decreases. Below 1 eV kinetic energy, the elastic–collision cross section $\sigma_{\rm elastic}$ (Eq. (3.14)), where the μp atom is slowed down but remains in the $2S$ state, starts to dominate. At kinetic energies below 0.31 eV (LAB), $\sigma_{\rm quench}$ is zero because $2P$–excitation is energetically forbidden. All $\mu p(2S)$ atoms which are either initially created at kinetic energies below 0.31 eV or survive the process of slowing down, will form the long–lived, so–called "slow" $2S$–component.

The cascade calculations show that the kinetic energy distribution of the $\mu p(2S)$ atoms does practically not differ from the one of the $\mu p(1S)$ atoms. At pressures below a few hPa the cascade process is predominantly radiative for low n numbers, and at higher n–

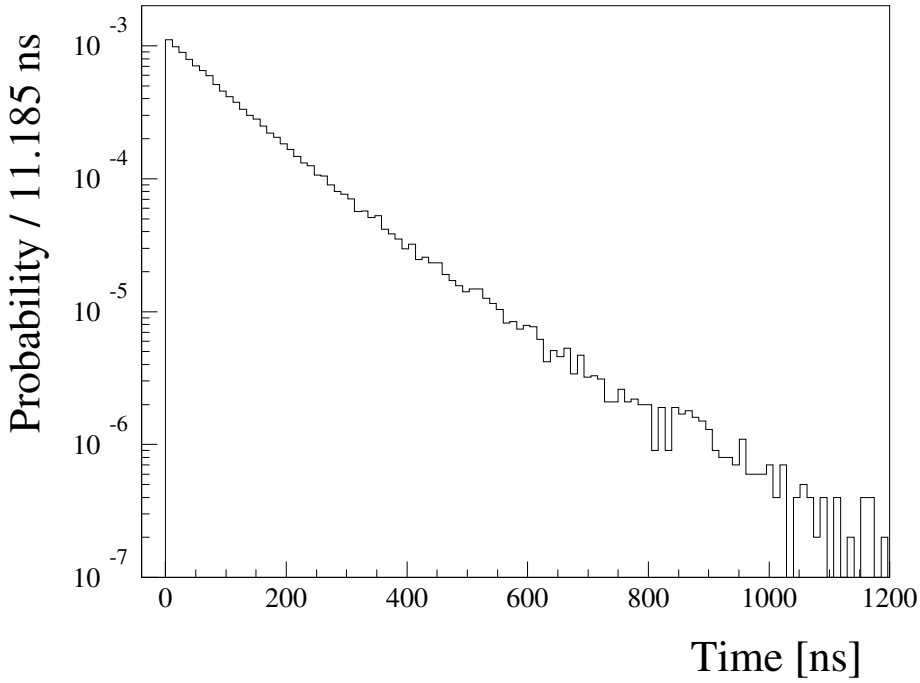

Figure 3.6: Time distribution of the delayed K_α *x rays due to radiative quenching of the* $\mu p(2S)$ *fast–component calculated for 0.6 hPa [49]. Time zero is defined as muon "arrival" time to the* $2S$ *state. The* H_2 *molecule is treated as two H atoms,* $n_i = 14$*. The fit of a simple exponential function (in time interval from 200 to 700 ns) yields the lifetime* $\tau_{2S}^{fast} \sim 120$ *ns. The same value is obtained also for distributions calculated for* $n_i = 12$ *and 16.*

values, where the μp kinetic energy can be changed by collisional transitions, the Stark mixing of the l–states smears out possible differences in the cascade history of $\mu p(1S)$ and $\mu p(2S)$ atoms [45]. The σ_{quench} and $\sigma_{elastic}$ cross sections are strongly energy dependent. By measuring the $\mu p(1S)$ kinetic energy distribution, one can determine the relative population P_{2S}^{slow} of the long–lived $\mu p(2S)$ atoms (slow component), normalized to the total number of formed μp atoms. Using this method, P_{2S}^{slow} was determined to be about 1% at the H_2 pressures in an interval from 0.0625 hPa to 16 hPa [45, 46].

The dominant quenching channel for the slow $\mu p(2S)$ component is the resonant formation of an excited muonic molecule which dissociates within 10^{-12} s

$$\mu p(2S) + H_2 \rightarrow \{[(pp\mu)^+]^* pee\}^* \rightarrow \mu p(1S) + p + \cdots , \tag{3.21}$$

as theoretically described in Refs. [55, 56] and experimentally confirmed in Ref. [26]. In this process, the $2S-1S$ energy difference of 1.9 keV is shared among the $\mu p(1S)$ atom and one proton, resulting in $\mu p(1S)$ atoms with kinetic energies of 900 eV. The measurement of such a hot component in the $\mu p(1S)$ kinetic energy distribution was the first direct observation of the slow $\mu p(2S)$ component.

Radiative quenching of thermalized $\mu p(2S)$ atoms due to Stark mixing *during* a collision,

$$\mu p(2S) + H_2 \rightarrow [\mu p\ (\alpha\,|2S\rangle + \beta\,|2P\rangle) + H_2] \rightarrow \mu p(1S) + H_2 + K_\alpha \tag{3.22}$$

was discussed a long time ago [57–59]. The calculated cross section ($\sigma \sim 10^{-18}$ cm^2) is however much smaller than the one measured for the process (3.21) ($\sigma \sim 10^{-16}$ cm^2 per molecule, at thermal energies). This also explains why the early experiments [60] did not

Table 3.2: Energies [61] and yields of radiative transitions after muon transfer to a μC atom. The yields are calculated [62] based on the cascade model and program given in Refs. [63, 64], respectively.

Transition	Energy	Yield	
	[keV]	$n_i = 5$	$n_i = 4$
$5 \to 4$	2.26	0.005	0
$4 \to 3$	4.89	0.035	0.039
$3 \to 2$	13.97	0.20	0.22
$2 \to 1$	75.25	0.41	0.44
$3 \to 1$	89.21	0.30	0.34

succeed to see any delayed K_α x rays, although the population of the thermalized $\mu p(2S)$ atoms is sufficiently high at about 1%. The determination of the P_{2S}^{slow} population from the fraction of the hot component in the $\mu p(1S)$ kinetic energy distribution is in agreement with the P_{2S}^{slow} determination from the total $\mu p(1S)$ kinetic energy distribution. The lifetime of the $\mu p(2S)$ slow component at our H_2 gas pressure of 0.6 hPa is $\tau_{2S}^{slow} \approx 1.3$ μs.

As discussed above, the initial population P_{2S} of $\mu p(2S)$ atoms is $P_{2S} = (2.49 \pm 0.17)\%$ at 0.6 hPa H_2 gas pressure. The slow $\mu p(2S)$ component P_{2S}^{slow} was measured to be $(1.1 \pm 0.2)\%$ [45]. The first experimental observation of the P_{2S}^{fast} population and its lifetime τ_{2S}^{fast} is presented in this work (§7.3). Thus, a new independent value $P_{2S}^{slow} = P_{2S} - P_{2S}^{fast} = (1.47 \pm 0.27)\%$ can be deduced for the population of the "slow" $2S$ component, on which our laser experiment is based. The time distribution of the P_{2S}^{fast} population calculated for 0.6 hPa by T.S. Jensen [49] is shown in Fig. 3.6.

3.2 Other muonic atoms: muonic nitrogen, oxygen, and carbon

3.2.1 Muon transfer to μC

Muon transfer can occur when a μp atom approaches another atom with atomic number $Z > 3$

$$\mu p + Z \to (\mu Z)^* + p\,. \tag{3.23}$$

In our experiment, the most intense x–ray background at delayed times is due to muon transfer to a C atom present in the polypropylene foils placed in front of the x–ray detectors. Reaction (3.23) then occurs for as much as half of all μp atoms. Table 3.2 summarizes the energies and yields of radiative transitions after transfer to a μC atom. There is no experimental information available indicating if this transfer reaction produces in the $n = 5$ or $n = 4$ state of the μC atom. The contribution of different transitions to the background will be discussed in §6.7.2.

3.2.2 Direct muon capture into μN and μO

As discussed in Appendix B, the H_2 target gas contained 0.4% air admixture and therefore μN and μO atoms were created. X–ray energies and yields of radiative transitions in these two exotic atoms are summarized in Table 3.3. As will be discussed in §7.3, the times when

*Table 3.3: Energies and measured yields of selected radiative transitions in μN and μO atoms. The measurements were performed in N_2 and O_2 gases, both at a pressure of 13.3 hPa [66, 67]. The yields marked by a * are calculated values.*

	μN		μO	
Transition	Energy [keV]	Yield	Energy [keV]	Yield
Circular and other $\Delta n = 1$ transitions				
$7 \rightarrow 6$	1.01	0.639*	1.32	0.545*
$6 \rightarrow 5$	1.67	0.621(56)	2.19	0.654(50)
$5 \rightarrow 4$	3.08	0.708(35)	4.02	0.661(33)
$4 \rightarrow 3$	6.65	0.766(25)	8.69	0.740(25)
$3 \rightarrow 2$	19.00	0.834(9)	24.85	0.801(24)
$2 \rightarrow 1$	102.3	0.927(8)	133.4	0.888(10)
Non–circular transitions ($\Delta n = 2$)				
$7 \rightarrow 5$	2.68	0.090(12)	3.50	0.080(11)
$6 \rightarrow 4$	4.75	0.069(10)	6.21	0.079(9)
$5 \rightarrow 3$	9.73	0.044(8)	12.72	0.044(7)
Non–circular transitions ($\Delta n = 3$)				
$7 \rightarrow 4$	5.76	0.038(7)	7.53	0.050(7)
$6 \rightarrow 3$	11.40	0.019(6)	14.90	0.024(7)

muons are captured and form μp atoms are similar to the time distribution of μN($5 \rightarrow 4$) transition x rays.

This statement is based on the two assumptions that

1. the kinetic energies where muons are captured and form μp and μN atoms do not differ substantially;
2. the μN cascade time is negligibly small compared to the μp cascade time.

There is no indication against the validity of the first assumption. The μN atomic cascade is dominated at high n levels by internal Auger transitions and by radiative transitions at lower n levels. The resulting cascade time is of the order of 10^{-10} [65], *i.e.*, negligibly small compared to the μp cascade time.

Chapter 4

Experimental setup of the μp Lamb shift experiment

The μp Lamb shift experiment takes place at the Paul Scherrer Institute (PSI) at Villigen, in the PSI πE5 area. Almost 2 mA of protons are accelerated to 590 MeV and produce pions and muons after collision with a carbon target. Details about the PSI accelerators are found in Ref. [68].

The experiment consists of stopping muons in a low pressure hydrogen target (0.6 hPa) to produce long–lived metastable μp($2S$) atoms. Section 4.1 describes the muon beam line which allows us to obtain very low energy muons stopping in hydrogen. Interactions between muons and the apparatus are measured using various detectors, which are detailed in §4.2. The Lamb shift measurement requires a very complex laser system. The whole system is not commercially available and is described in §4.3 (further details can be found in Ref. [69]).

Section 4.4 is dedicated to a detailed study of the Large Area Avalanche Photodiodes (LAAPDs). This section is a reprint of the paper published in Nucl. Instrum. Methods A **540** (2005) 169–179. There, results concerning the temperature dependence of their behaviour and particularities of their application as low–energy x–ray detectors in our experiment are given. Characteristics and choices of the various electronics modules have been performed at the University of Fribourg and are reported in an internal report [70].

4.1 Muon beam line

The laser experiment requires to create μp atoms in the metastable $2S$ state. Time–separation of the few laser–induced $2S \rightarrow 2P \rightarrow 1S$ transitions from the large number of "prompt" $2P \rightarrow 1S$ transitions (last stage of the direct muonic cascade) can only be achieved at low H_2 gas pressures, in the hPa region, because collisional quenching shortens the μp($2S$)–lifetime too much at higher densities. In our case, the limiting factor is the long delay of the excimer laser (§4.3) forcing us to work at a very low H_2 pressure (0.6 hPa). A beam of unprecedentedly low–energy negative muons is required so that their stopping range in the gas matches the length of a reasonably sized target vessel. Single muons have to be detected in order to trigger the laser and data acquisition systems. After detection, the muon should still have enough energy to cross the muon entrance window separating the H_2 gas from the beam line vacuum, but has to be stopped and captured by a hydrogen molecule. This molecule will then dissociate, and the highly excited μp atom ($n \sim 14$) will cascade to the $1S$ ground state, or, with much lower probability, to the metastable

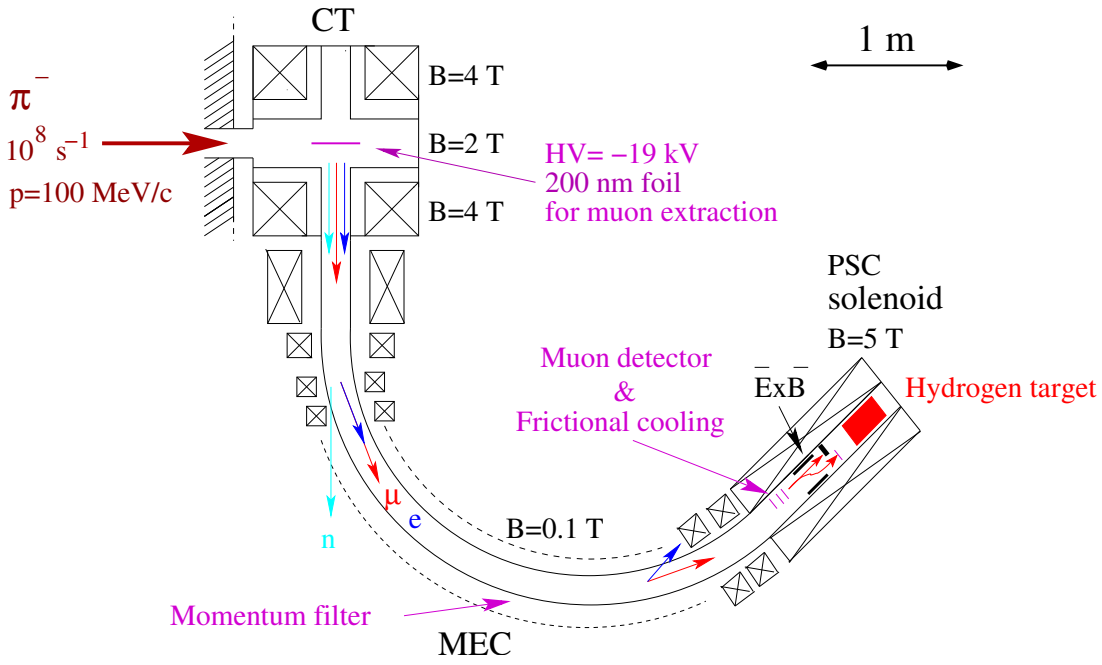

Figure 4.1: Lay–out of the PSI πE5 area with Cyclotron Trap CT, muon extraction channel MEC, and PSC solenoid ($B = 5$ Tesla).

$2S$ state.

Figure 4.1 shows the specifically designed low–energy negative–muon beam line which yields an order of magnitude more muon stops in a small low–density gas volume than a conventional muon beam line. It consists of the so–called cyclotron trap (CT) [71], the muon extraction channel (MEC) [72], and the 1 m long PSC–solenoid[1] [73] with the gas target and two transmission detectors for the muons. A photo of the PSI πE5 area with the mounted experimental setup is shown in Fig. 4.2. About 10^8 π^-/s of 100 MeV/c momentum are injected from the πE5 beam into the CT which acts here as a magnetic bottle. The π^- spiral in the CT and decay in flight, producing μ^- with kinetic energies of a few MeV. These μ^- are decelerated to keV energies after crossing a few 100 times a foil of 200 nm thickness (17 cm diameter) placed in the center of the trap. This foil is at a high voltage of -19 kV producing an electric field which enhances muon extraction. The MEC is a long curved solenoid selecting low–energy muons and guiding them to the entrance of the PSC solenoid. Charged particles extracted from the CT follow the magnetic field lines inside the MEC which act as a momentum filter. This means that the relatively few μ^- with the desired energy are selected from the high flux of gammas, neutrons, electrons and more energetic muons which are present at the CT exit.

The detection of keV–muons is based on the system of frictional cooling [74] — that is cooling a beam of very low–energetic particles by moderation in matter and simultaneous acceleration in an electrostatic field — by means of a system of "stack" detectors S_1 and S_2 (Fig. 4.3). Each stack consists of several rings (Fig. 4.4) defining the "uphill" and "downhill" potential profiles smoothing the energy of the muons. Five rings of the S_1 stack and one ring of S_2 contain ultra–thin carbon foils (areal density (thickness) $\xi = 4$ μg/cm^2). A muon crossing a carbon foil can release an electron which is accelerated in the electric field of the stack. Electrons released from the S_1 foils in the forward direction are separated

[1] PSC stands for the Phase Space Compression as described in [73]

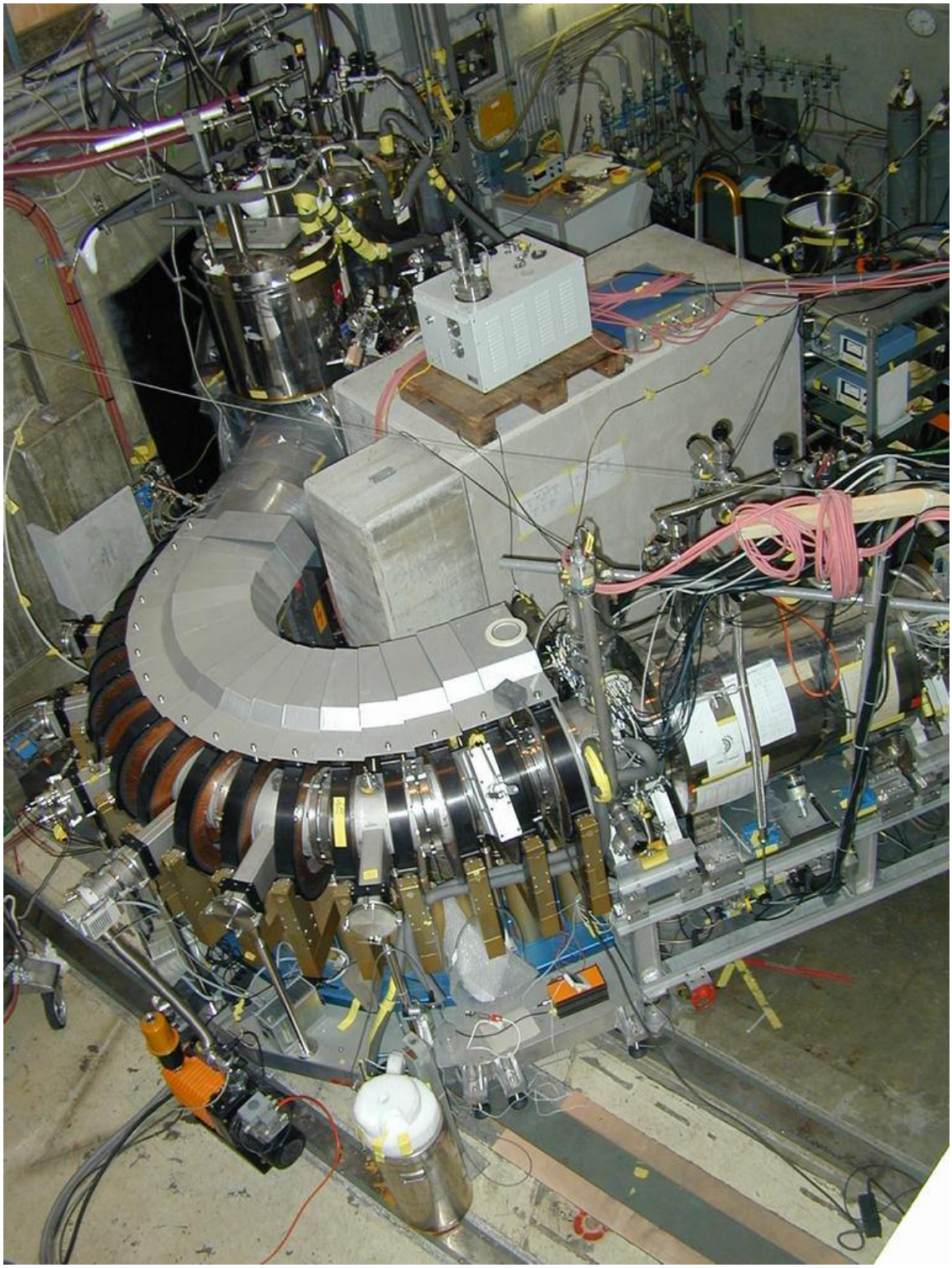

Figure 4.2: Photo of the PSI πE5 area. The metallic cylinder in the top–left corner is one liquid He vessel of the CT. The curved structure with coils is the MEC, connecting the CT with the PSC solenoid (metal cylinder in right front). The concrete blocks in the middle shield the setup inside the bore of the PSC solenoid from neutrons originating mainly from the region around the CT.

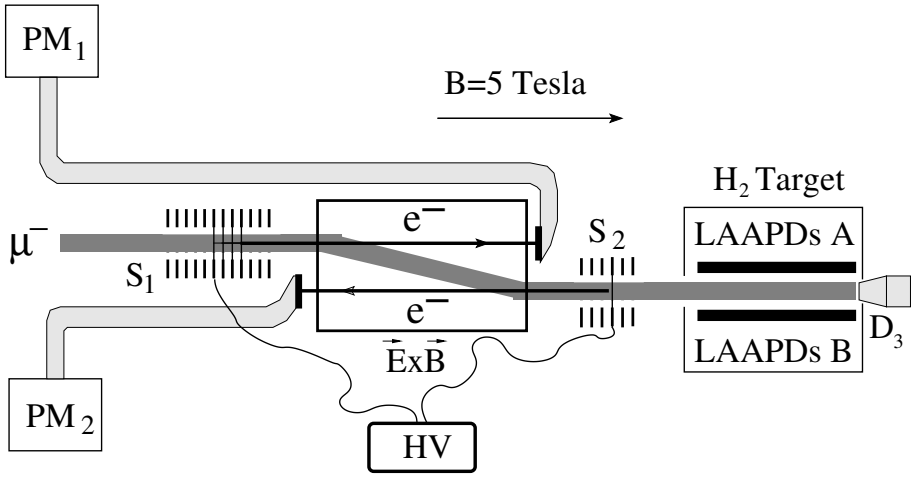

Figure 4.3: A sketch of the the central part of the apparatus kept at high vacuum inside the PSC solenoid providing an axial magnetic field of 5 Tesla. The picture is not in scale and represents approximately a side view. The muons enter from the left and cross two stacks of ultra–thin carbon foils, S_1 *and* S_2*, which act, together with plastic scintillators read by photomultipliers* PM_1 *and* PM_2*, as a muon detector. The* $\vec{E} \times \vec{B}$ *filter separates* μ^- *from* e^-*. The gas target is filled with 0.6 hPa* H_2 *gas. Detector* D_3 *indicates the muons which did not stop in the target. Two LAAPD arrays, A and B, are mounted above and below the muon stop volume, respectively. The laser cavity mirrors are placed sideways to the muon stop volume and hence are not shown.*

from muons in the $\vec{E} \times \vec{B}$ separator, which shifts the slow muons about 10 mm downwards whereas the faster electrons follow nearly the magnetic field lines. These electrons are then detected by a plastic scintillator which is read by the photomultiplier tube PM_1. For S_2, a backward–readout is introduced, *i.e.*, only electrons emitted by the foil in the anti–parallel direction with respect to the muon beam are detected by another plastic scintillator read by PM_2. This backward readout makes it possible to introduce an anti–detector D_3 at the end of the gas target for muons which did not stop in the gas. Such muons are stopped in the gold plated surface of a LYSO[2] scintillator crystal (with photomultiplier readout). Several μAu x ray transitions are then produced, resulting in a high probability to be detected in the LYSO scintillator (the x–ray attenuation length in LYSO is 1.15 cm at 511 keV). These x rays cannot be a source of potentially dangerous delayed background for the laser experiment, since the μAu atom lifetime is only 74 ns. The gold also acts as an efficient mirror for low–energy muons as found by the analysis described in §7.1. An arriving muon has to induce a signal in both S_1 and S_2 detectors with the correct time delay, *i.e.*, within the time–of–flight (TOF) interval which corresponds to axial kinetic energies of muons stopping in the gas. If, in addition, no signal is detected by D_3, the muon is accepted as a trigger for the pulsed laser and the data acquisition systems. In the following, S_1 and S_2 refer to the complete (stack S_1 plus PM_1) and (stack S_2 plus PM_2) systems, respectively.

The measured muon detection efficiencies are 87% for S_1 and 42% for S_2. A collimator restricts the beam size at the target entrance to 15×5 mm^2. The 5 Tesla B-field of the PSC solenoid keeps the transverse muon beam size to the value given by the collimator. The rate of muons detected in a time–of–flight coincidence between S_1 and S_2 is 320 s^{-1}.

[2]LYSO stands for Lutetium Yttrium Orthosilicate, a Cerium doped scintillator with high light output and fast response.

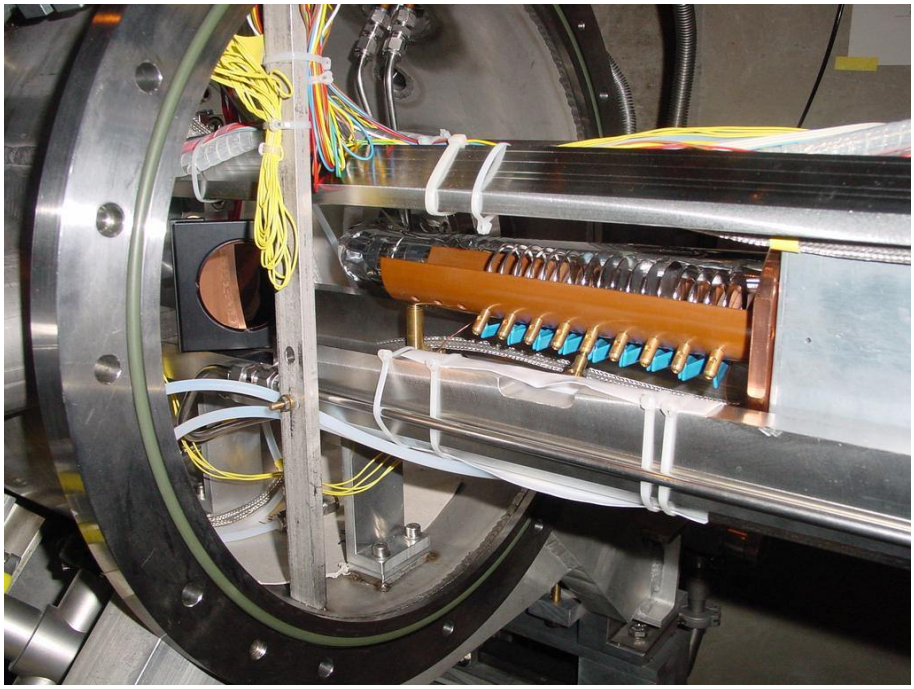

Figure 4.4: Upstream part of the setup placed in the PSC solenoid. Muons enter from the left side. The brown device is an isolator (vespel) holding the rings of the S_1 detector. The blue pieces below are high voltage resistors serving as a voltage divider. Behind the S_1 stack the PM_1 light guide wrapped in aluminum foil can be recognized. More downstream a part of the aluminum box containing the $\vec{E} \times \vec{B}$ separator is visible. The copper mirror at the left side of the picture (behind the vertical support rod) is used to deflect the 6 μm light towards the target cavity (which is located outside the picture). All components including the gas target are supported by the massive stainless steel beams seen above and below S_1. The multi-colored cables are part of the LAAPD heater and temperature measurement system.

It drops to 240 s^{-1} when the D_3 anti–coincidence is active. These $S_1 \cdot S_2 \cdot \bar{D}_3$ signals, properly anti–gated by the laser dead time, provide the trigger signal for the pulsed laser and the data acquisition system (Chapter 5). The resulting average laser repetition rate of ~ 50 s^{-1} is dominated by the dead time of the excimer lasers.

4.2 X–ray and electron detectors

Large Area Avalanche Photodiodes (LAAPDs) are used as x–rays detectors. Twenty LAAPDs, each with a sensitive area of 13.5 mm×13.5 mm, are mounted on top and bottom of the target vessel, in two face–to–face rows of 10 devices, at a vertical distance of only 8 mm from the muon beam center (Figs. 4.5, 4.6, 4.7, and 4.8). A detailed description of these LAAPDs and their performance is given in a reprint of the paper published in Nucl. Instrum. Methods A **540** (2005) 169–179 (§4.4). The following notation is used throughout this thesis:

1. A and B side LAAPDs refer to the arrays mounted above and below the muon stop volume, respectively.
2. The LAAPDs are numbered from 0 to 9 following the beam direction. Therefore, LAAPDs A0 and B0 are the ones closest to the muon entrance window, while A9

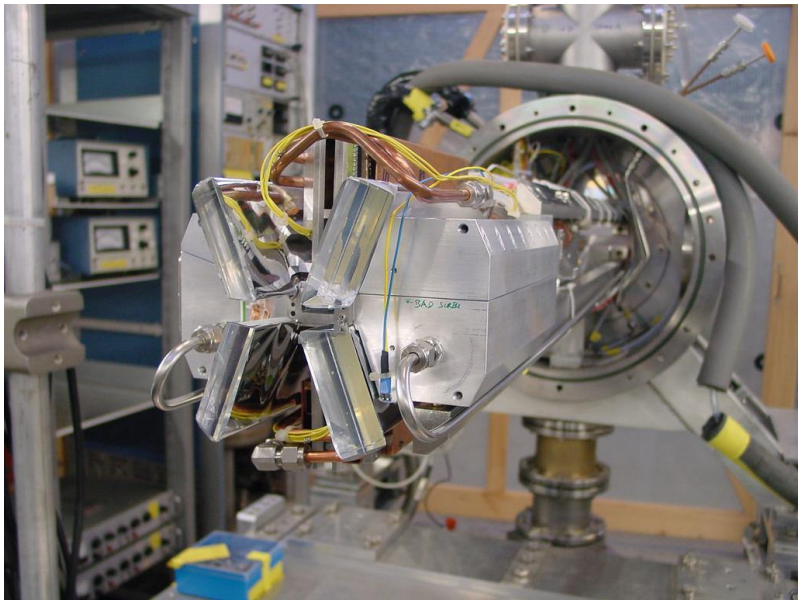

Figure 4.5: Downstream part of the setup placed in the PSC solenoid vacuum. Muons enter from behind (i.e., come out of the photo). The aluminum piece is the target chamber holding 0.6 hPa H_2 gas. Hydrogen is constantly flushed through the stainless steel tubes. The side parts of the target contain the laser mirrors and their mounts, while the muon stop volume is restricted to the pencil–shaped central part of the target. The X–shaped structure are the plastic scintillators of the EP_{left} and EP_{right} electron detectors having each an upper and a lower paddle. The copper housing of the LAAPD preamplifiers can be recognized in between the EP_{left} and EP_{right} paddles. The copper tubes are for the ethanol used to cool the LAAPDs. The yellow and blue wires belong to the temperature sensor and the heater of the target chamber.

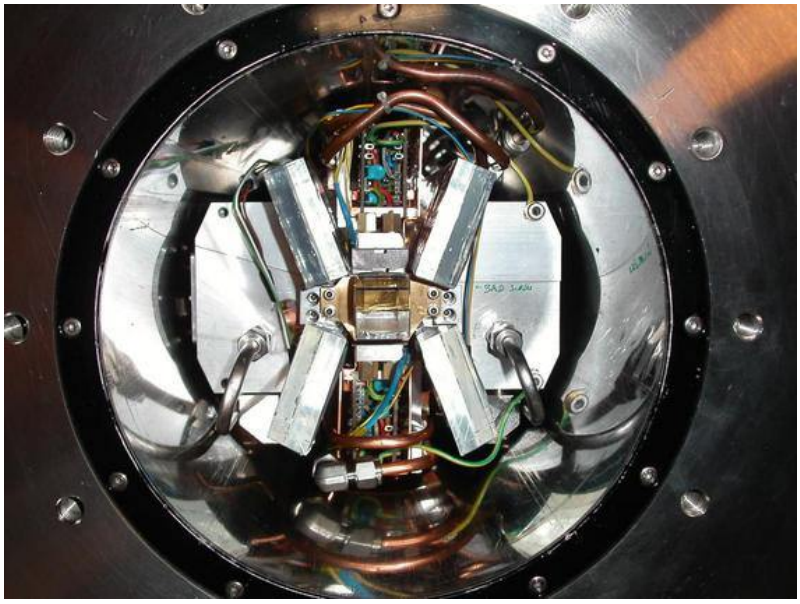

Figure 4.6: A view of the downstream opening of the PSC solenoid when the whole setup is placed inside the 20 cm diameter bore. The visible parts are the same as in Fig. 4.5. In addition, the LAAPD preamplifier boards above and below the muon stop volume are visible. The transparent piece in the middle is the D_3 scintillator (LYSO crystal) detecting the muons which did not stop in the target.

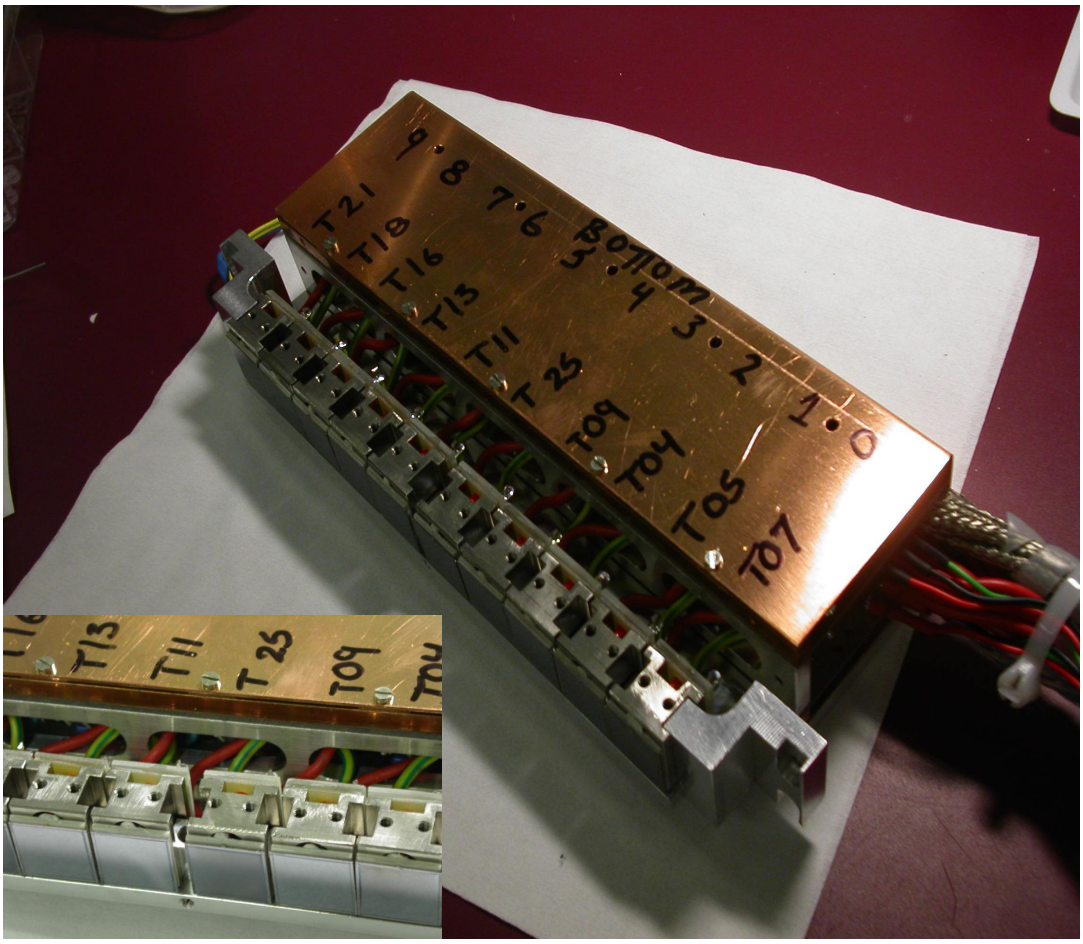

Figure 4.7: B–side LAAPD array which was mounted below (and analogously A–side array above) the muon stop volume. The wires at the right side contain the high voltage and signal cables and are connected to the vacuum feed-through when mounted. The picture at the lower left corner is a detailed view of the central part of the array. Each square (13.5 mm×13.5 mm) planar LAAPD is glued to a Ti holder. At the back side of each holder a pair of wires is visible (yellow/green is ground, red is the positive high voltage) leading to the 10 preamplifier boards covered by a copper shielding.

and B9 are the most distant ones. In some cases, the LAAPDs are labeled only with numbers ranging from 0 to 19, where 0 to 9 stand for A–side LAAPDs while 10 to 19 for B–side diodes.

3. The front side LAAPDs are the diodes which are close to the muon entrance window, *i.e.*, LAAPDs with labels X0 to X4 (X = A or B).
4. The backside LAAPDs are the diodes which are distant from the muon entrance window, *i.e.*, LAAPDs with labels from X5 to X9 (X = A or B).
5. The notation ABx (x = 0–9) means that the data in question are summed data from Ax and Bx.

For background suppression it is important to detect the muon–decay electrons (§6.2). Four BICRON BC–400 type plastic scintillator plates (so called electron paddles) mounted in an X–shape (Fig. 4.5) are dedicated to this purpose. The upper and the lower paddle at the left (right) side (from the muon beam point of view) are read out by the same

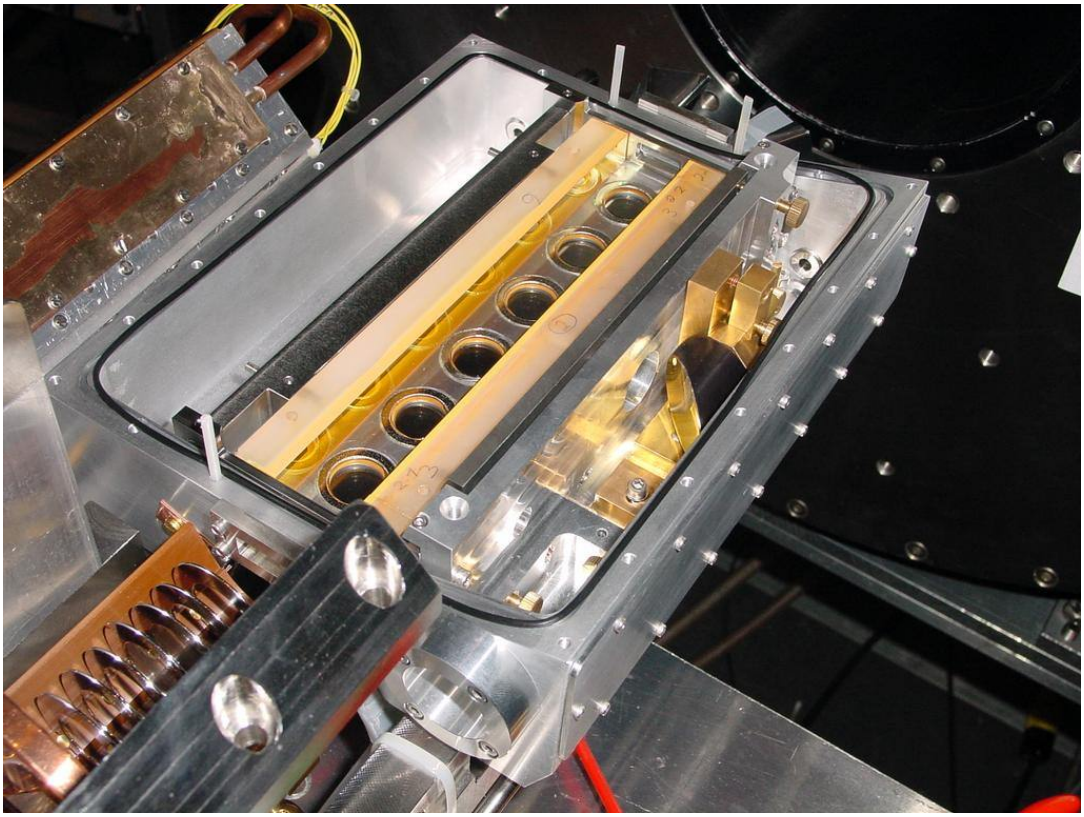

Figure 4.8: A view of the opened target chamber. Muons enter from the lower left after having passed the rings of the S_2 detector. Six beveled–edge LAAPDs (used in the earlier stages of the experiment) are visible from below facing the pencil–shaped muon stop volume. The 6 μm light enters through a window held by a cylindrical flange in the lower corner. The light is then reflected by an off–axis–parabolic mirror (black piece with a gold surface). Two mirrors left and right of the muon stop volume (long glass pieces with yellow coating) define the laser cavity. Through a small hole in the center of the right mirror, the light enters the cavity and is then reflected back and forth about 1700 times. The total illuminated volume is 170 mm (along the muon beam axis) x 25 mm (between the mirrors) x 7 mm (vertically).

phototube. In the following they are referred to as $\mathrm{EP_{left}}$ and $\mathrm{EP_{right}}$ detectors.

In addition, the D_3 scintillator can also be used for electron detection. The muon decay electrons deposit much more energy in D_3 than typical μAu x rays. Therefore, by applying a higher discriminator level, the D_3 signal is used for electron detection and is referred to as D_3^{hi}. As will be shown in Chapter 6, the LAAPDs can also be used for electron detection.

4.3 Laser system

The μp Lamb shift experiment puts severe requirements on its laser system. The most stringent one is caused by the time structure of the available muon beams. At PSI, there are only continuous muon beams, whereas pulsed muon sources available elsewhere are not intense enough. The laser has therefore to be triggerable on muons entering the apparatus at stochastic times, with a short delay of the order of the μp($2S$) lifetime (≈ 1.3 μs), and with a dead time between two shots as short as possible.

Table 4.1: Requirements on the laser system for the muonic hydrogen $2S-2P$ Lamb shift measurement.

Requirements		Comments
Frequency	50 THz	corresponding to $\lambda = 6\,\mu$m
Bandwidth	< 2 GHz	$\Gamma_{2S-2P} = 18$ GHz (FWHM)
Tunability	250 GHz	large uncertainty in $r_{\rm p}$, λ from 6.00 to 6.03 μm
Energy/pulse	$\gtrsim 0.2$ mJ	illuminated volume $25 \times 7 \times 170\,\mathrm{mm}^3$
Triggerability	stochastic	μp formation time is random
Repetition rate	100 s^{-1}	100 s^{-1} results in 1 event/hour
Delay	$< 1.5\,\mu$s	$1.3\,\mu$s lifetime of the $2S$ state
Reliability	10^8 shots	many days with 100 s^{-1} shots

The laser tunability of 250 GHz (corresponding to wavelengths from 6.00 to 6.03 μm), is determined by the uncertainty of the rms proton charge radius. The laser bandwidth has to be small compared to the natural linewidth of the $2S-2P$ transition of 18 GHz. A determination of the $2S-2P$ line position with 30 ppm precision corresponds to an accuracy of 1.5 GHz. An energy density of 16.5 mJ/cm^2 is required to saturate the $2S-2P$ transition, *i.e.*, to drive $(1-1/e)$ of the $2S$–population to the $2P$ level. This density is obtained in the mirror cavity ($25\times7\times170\mathrm{mm}^3$) where the μp atoms are formed (Fig. 4.8), if the 6 μm laser pulse has an energy of ≈ 0.2 mJ at the cavity entrance. Reliability of the whole system during the measuring time of several weeks is essential. The requirements on the laser system are summarized in Table 4.1.

No tunable and fast triggerable laser providing sufficient energy in the 6 μm region is commercially available. A home–built system was therefore developed whose main components are shown in Fig. 4.9. An excimer–pumped dye laser is used to drive a titanium sapphire (Ti:Sa) system whose wavelength is then shifted to 6 μm using a multipass Raman cell filled with hydrogen. The whole system was placed in a special isolated room, the so–called laser hut.

Two high power *Lambda Physik* series LPX 200 XeCl excimer lasers provide the pumping energy (320 mJ each) for the whole system and have a maximum repetition rate of 100 Hz, *i.e.*, a dead time of 10 ms. In practice, a longer dead time between shots of 14 ms was chosen in order to guarantee an optimum stability and beam quality of the excimer–pumped dye lasers. The internal delay from trigger to output signal is 1.2 μs. A dead time between shots of 14 ms combined with a muon trigger rate of 240 s^{-1} results in an average laser repetition rate of 55 $\mathrm{s}^{-1} \approx (1/240 + 0.014)^{-1}$ s^{-1}. This means that the laser is fired on average for every fourth detected muon entering the target.

Each of the two excimer lasers pumps its own dye laser oscillator–amplifier system converting 308 nm excimer pulses to 20 ns long green light pulses of 45 mJ at 540 nm. 30 liters of dye solution (Coumarin 153 dissolved in ethanol with addition of DABCO) were used per day of data taking. The light from the first and the second dye lasers was monitored by the diodes Dye_1 and Dye_2, respectively.

The dye lasers pump an injection–seeded oscillator–amplifier titanium–sapphire (Ti:Sa) laser delivering 6 ns long pulses of 12 mJ at 708 nm (red light). The wavelength tunability and bandwidth of the Ti:Sa oscillator, and therefore of the subsequent amplifier and 6 μm light, is controlled by a single–mode continuous wave (cw)–Ti:Sa laser stabilized on a

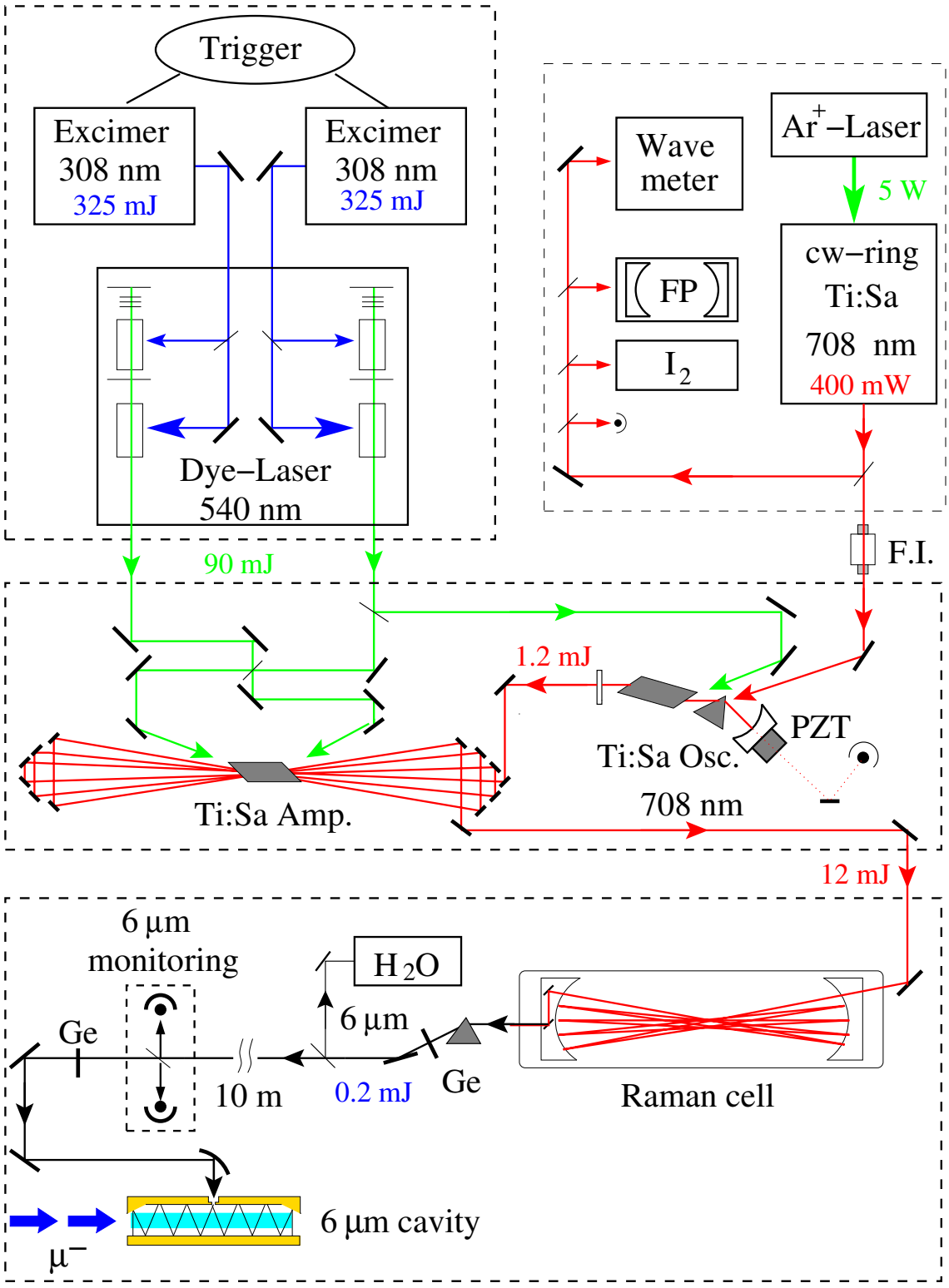

Figure 4.9: Schematic view of the laser system. The main components are a pulsed excimer–dye laser system, a tunable cw Ti:Sa laser, a pulsed oscillator–amplifier Ti:Sa laser, a Raman cell, and a 6 μm multipass mirror cavity with its diagnostic system. FP: Fabry–Perot, I_2: iodine absorption cell, H_2O: water absorption cell, PZT: piezo transducer, FI: Faraday isolator.

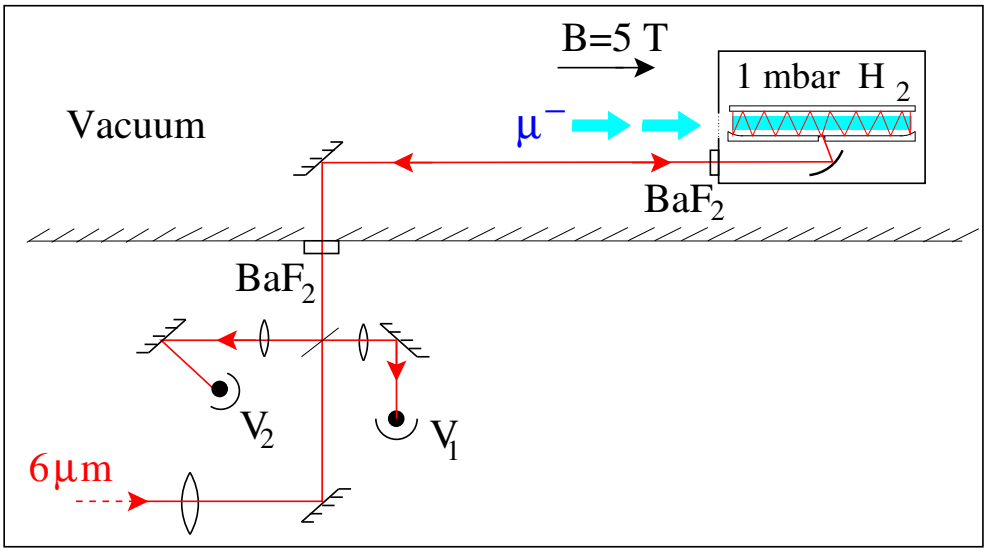

Figure 4.10: Monitoring system for the 6 μm cavity. Before entering the vacuum system, 5% of the 6 μm light is reflected by a 45° CaF_2 plate and focused on a fast infrared detector V_1. The transmitted pulse crosses the vacuum and target windows and enters the cavity. Part of the light escaping from the entrance hole travels back on the same axis as the incoming light and is detected with a second infrared detector V_2.

calibrated Fabry–Perot (FP) cavity. When searching the $2S-2P$ resonance the cw–Ti:Sa laser is locked on a particular transmission fringe of the FP. Laser light from the Ti:Sa oscillator and amplifier was monitored by the photo–detectors TiSa_osc and TiSa_amp, respectively.

The wavelength is further converted from the visible to the infrared using a third–Stokes Raman shifter operated with 14 bar H_2 gas [75]. The frequency of the 708 nm photons from the Ti:Sa laser is shifted three times via the excitation of H_2 molecules from their vibrational state $\nu = 0$ to $\nu = 1$. The Raman shifter produces 6 ns long pulses of 0.2 mJ at 6 μm for 12 mJ input pulses which is optimum for the search of the $2S$–$2P$ resonance.

The water molecule exhibits several ro-vibrational states with precisely known transition energies in the 6 μm region of our interest. Therefore, a precise calibration of the 6 μm light is performed by scanning over water absorption lines.

The infrared light is transported from the laser hut to the H_2 target inside the 5 Tesla solenoid via a 12 m long path. The 6 μm beam–line tube is flushed with dry N_2 gas to avoid absorption by water vapor. Before entering the vacuum system, about 5% of the 6 μm light is reflected by a 45° CaF_2 plate and focused on a fast infrared detector V_1 monitoring the entering light (Fig. 4.10). Two mirrors located on the left and right side of the muon stop volume form a non–resonant 6 μm multipass enhancement cavity. One of the mirrors has a hole of 0.63 mm diameter where the laser light enters and partially also exits the cavity. The light is reflected back and forth between the two mirrors, is spread out and almost homogeneously illuminates the whole μp stop volume. A part of the confined light is back–reflected, exits the cavity via the same entrance hole and is detected by a fast infrared photo–detector V_2. This provides diagnostics for the light circulation inside the multipass cavity (Fig. 4.10). The average lifetime of the light in the cavity is 145 ns corresponding to 1700 reflections between the two mirrors (Fig. 4.11).

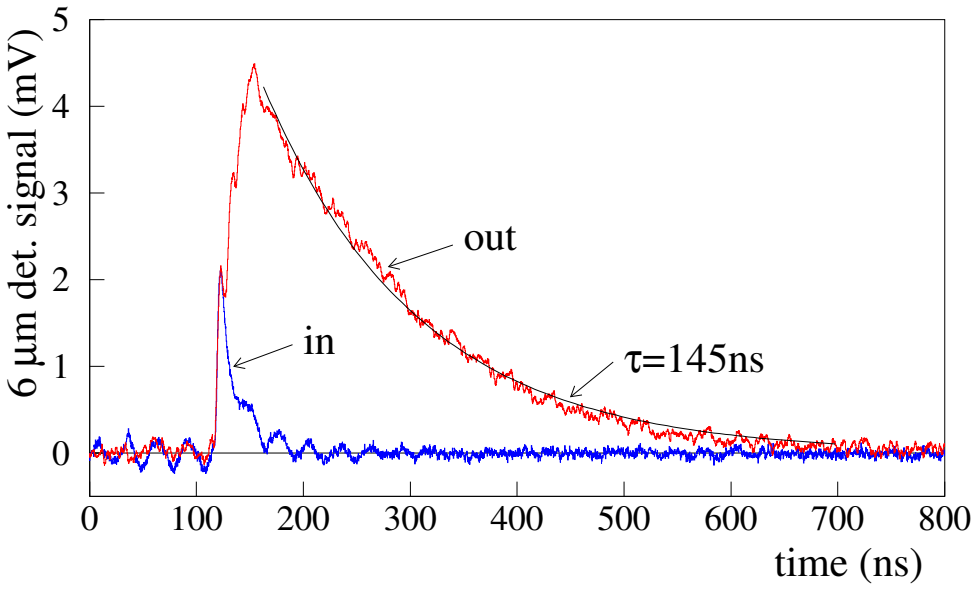

Figure 4.11: Signal detected by the V_1 *detector monitoring the 6* μm *light entering the mirror cavity (in). The lifetime of the laser light inside the cavity is measured by the* V_2 *detector (out) and amounts to* $\tau \approx 145$ *ns corresponding to 1700 reflections between the two mirrors.*

The total delay of the 6 μm pulse from the excimer laser trigger signal to the pulse arrival in the mirror cavity was in an interval from 1.52 to 1.72 μs. This value corresponds to the sum of the following delays: excimer–dye laser (from 1126 to 1326 ns), Ti:Sa oscillator (56 ns), Ti:Sa amplifier (45 ns), Raman cell (213 ns) and various beam paths (80 ns). The internal delay of the excimer laser was not stable during the measurement and varied typically by $\pm$50 ns on a long time scale. In addition, its mean delay was successfully shortened by $\sim$200 ns in the middle of the data taking period. The experimentally relevant time difference between a muon stop (or, more precisely, the emission of a direct–cascade μp K_α x ray) and the arrival of the laser pulse in the cavity was between 1.42 to 1.62 μs. This number is composed of the total laser delay (from 1.52 to 1.72 μs) and the time needed to generate the $S_1 \cdot S_2 \cdot \bar{D}_3$ trigger signal (0.4 μs), reduced by the slowing–down and cascade time of the muon ($\sim 0.5\,\mu$s).

4.4 Planar LAAPDs: Temperature Dependence, Performance, and Application in Low Energy X–ray Spectroscopy, Nucl. Instrum. Methods A 540 (2005) 169–179

L. Ludhova, F.D. Amaro, A. Antognini, F. Biraben, J.M.R. Cardoso, C.A.N. Conde, D.S. Covita, A. Dax, S. Dhawan, L.M.P. Fernandes, T.W. Hänsch, V.-W. Hughes, O. Huot, P. Indelicato, L. Julien, P.E. Knowles, F. Kottmann, J.A.M. Lopes, Y.-W. Liu, C.M.B. Monteiro, F. Mulhauser, F. Nez, R. Pohl, P. Rabinowitz, J.M.F. dos Santos, L.A. Schaller, D. Taqqu, and J.F.C.A. Veloso.

Available online at www.sciencedirect.com
SCIENCE DIRECT®
ELSEVIER
Nuclear Instruments and Methods in Physics Research A 540 (2005) 169–179
NUCLEAR INSTRUMENTS & METHODS IN PHYSICS RESEARCH Section A
www.elsevier.com/locate/nima

Planar LAAPDs: temperature dependence, performance, and application in low-energy X-ray spectroscopy

L. Ludhova[a,b,*], F.D. Amaro[c], A. Antognini[d], F. Biraben[e], J.M.R. Cardoso[c], C.A.N. Conde[c], D.S. Covita[c], A. Dax[f,1], S. Dhawan[f], L.M.P. Fernandes[c], T.W. Hänsch[d], V.-W. Hughes[f], O. Huot[a], P. Indelicato[e], L. Julien[e], P.E. Knowles[a], F. Kottmann[g], J.A.M. Lopes[c], Y.-W. Liu[h], C.M.B. Monteiro[c], F. Mulhauser[a,2], F. Nez[e], R. Pohl[b,d], P. Rabinowitz[i], J.M.F. dos Santos[c], L.A. Schaller[a], D. Taqqu[b], J.F.C.A. Veloso[c]

[a]*Département de Physique, Université de Fribourg, CH-1700 Fribourg, Switzerland*
[b]*Paul Scherrer Institut, CH-5232 Villigen PSI, Switzerland*
[c]*Departamento de Física, Universidade de Coimbra, PT-3000, Coimbra, Portugal*
[d]*Max-Planck Institut für Quantenoptik, D-85748 Garching, Germany*
[e]*Laboratoire Kastler Brossel, École Normale Supérieure et Université P. et M. Curie, F-75252 Paris, Cedex 05, France*
[f]*Physics Department, Yale University, New Haven, CT 06520-8121, USA*
[g]*Labor für Hochenergiephysik, ETH-Hönggerberg, CH-8093 Zürich, Switzerland*
[h]*Physics Department, National Tsing Hua University, Hsinchu 300, Taiwan*
[i]*Chemistry Department, Princeton University, Princeton, NJ 08544-1009, USA*

Received 1 November 2004; accepted 4 November 2004
Available online 16 December 2004

Abstract

An experiment measuring the 2S Lamb shift in muonic hydrogen (μ^-p) was performed at the Paul Scherrer Institute, Switzerland. It required small and compact detectors for 1.9 keV X-rays (2P–1S transition) with an energy resolution around 25% at 2 keV, a time resolution better than 100 ns, a large solid angle coverage, and insensitivity to a 5 T magnetic field. We chose Large Area Avalanche Photodiodes (LAAPDs) from Radiation Monitoring Devices as X-ray detectors, and they were used during the last data taking period in 2003. For X-ray spectroscopy applications, these LAAPDs have to be cooled in order to suppress the dark current noise; hence, a series of tests were performed to choose the optimal operation temperature. Specifically, the temperature dependence of gain, energy resolution, dark current,

*Corresponding author. Paul Scherrer Institut, CH-5232, Villigen PSI, Switzerland. Tel.: +41 56 310 3758; fax: +41 56 310 5230.
E-mail address: livia.ludhova@psi.ch (L. Ludhova).
[1]Present address: CERN, CH-1211 Geneva 23, Switzerland.
[2]Present address: University of Illinois at Urbana-Champaign, IL 61801, USA.

0168-9002/$ - see front matter
doi:10.1016/j.nima.2004.11.017

excess noise factor, and detector response linearity was studied. Finally, details of the LAAPDs application in the muonic hydrogen experiment as well as their response to α particles are presented.

PACS: 07.85.−m; 29.40.Wk; 85.60.Dw; 36.10.Dr

Keywords: Low-energy X-ray spectroscopy; Large Area Avalanche Photodiodes performance; Temperature dependence; Response to α particles

1. Introduction

An experiment measuring the 2S Lamb shift ΔE(2P–2S) in muonic hydrogen (μ^-p) by precision laser spectroscopy was being performed at the Paul Scherrer Institute (PSI), Switzerland [1]. The experiment required the detection of 1.9 keV X-rays from the muonic hydrogen K_α Lyman line. The apparatus was installed in a muon beam area at the PSI proton accelerator, an environment with a rather high level of neutron-induced radiative processes as well as electromagnetic and acoustic noise.

The 1.9 keV X-ray detector has to reach an energy resolution of ~25% and a time resolution better than 100 ns. To optimize the solid angle for X-rays, the detector has to be mounted as near as possible to the pencil-shaped volume where the μ^-p atoms are formed. There is space for two sets of X-ray detectors (with sensitive areas up to $\sim 2 \times 17\,cm^2$) at the top and bottom side of the gas target, which is mounted inside a solenoid with 20 cm inner diameter. The magnetic field of 5 T produced by the solenoid is another limitation for the detector choice. In addition, the whole target and detector setup is operated in vacuum.

The experiment was installed for the first time in the muon beam area during an engineering run in 2002. A second beam period followed in 2003 during which the apparatus was further improved. Valuable data were taken in the last few weeks of the 2003 run, with the aim to search for the 2P–2S resonance.

In 2002 we used Large Area Avalanche Photodiodes from Advanced Photonix Inc. [2] (API LAAPDs), a representative of the beveled-edge LAAPDs, reviewed, for example, in Ref. [3]. They are circular, with a 16 mm diameter active surface surrounded by an ~5 mm wide ring of inactive material (Fig. 1). Their behavior in high magnetic fields was studied in Refs. [4,5], while a systematic investigation of their low-temperature performance in X-ray and visible-light detection can be found in Ref. [6]. An example of their application to muonic atom spectroscopy during the first stages of our experiment is given in Ref. [7].

During the most recent measurements in 2003, we replaced the API diodes by LAAPDs from Radiation Monitoring Devices Inc. [8] (RMD LAAPDs). Two arrays of these detectors mounted below and above the pencil-shaped target have a considerably larger solid angle for X-ray detection due to the LAAPD square shape and better ratio of sensitive to total detector area (Fig. 1). The principle of the RMD LAAPDs, in particular their novel planar bevel fabrication process, is summarized in Ref. [9]. In Section 2 we describe these LAAPDs, their performance and the results of

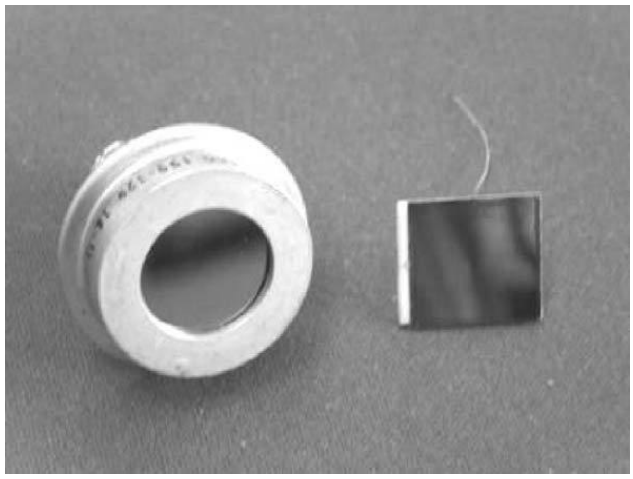

Fig. 1. Circular beveled-edge API LAAPD (left) with 16 mm diameter active surface area and square planar RMD LAAPD (right) with $13.5 \times 13.5\,mm^2$ active surface.

systematic tests. Section 3 contains some details about the RMD LAAPDs application in our experiment, in particular their response to α particles. A comparison with the previously used API LAAPDs is given in the conclusions.

2. Properties of the RMD LAAPDs

2.1. First tests

RMD LAAPDs, model S1315, are square planar devices with a 13.5 mm × 13.5 mm sensitive area surrounded by 1 mm wide borders of inactive material. The operational voltage indicated by the manufacturer is in the region from 1560 to 1765 V at 23°C. The first tests with a ^{55}Fe source emitting 5.9 keV X-rays performed at temperatures above 0°C have shown that these LAAPDs require cooling to temperatures well below 0°C in order to detect low-energy X-rays with an acceptable resolution. The main reason is a high dark current reaching 1 μA at 1620 V at room temperature; when cooled to 1°C, 1 μA is reached at 1710 V (Fig. 2).

At room temperature, the noise tail in the energy spectrum extends up to ~6 keV. By cooling below −20°C, satisfactory results were obtained not only for 5.9 keV X-rays, but also for 2.3 keV X-rays, for which an energy resolution of 26% FWHM was reached. The 2.3 keV X-rays were produced by sulfur fluorescing when irradiated by

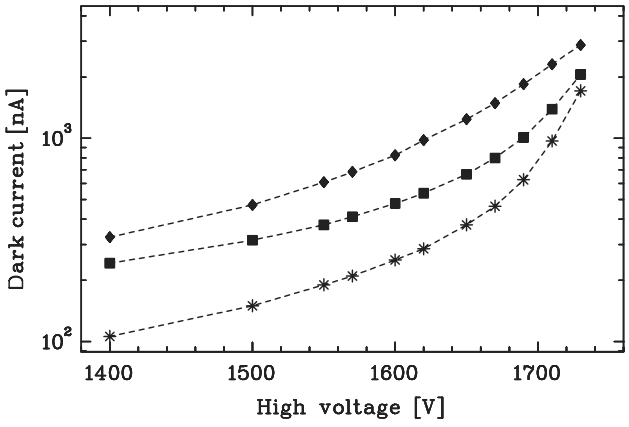

Fig. 2. LAAPD dark current versus high voltage measured at 1°C (∗), 10°C (■), and 23°C (◆).

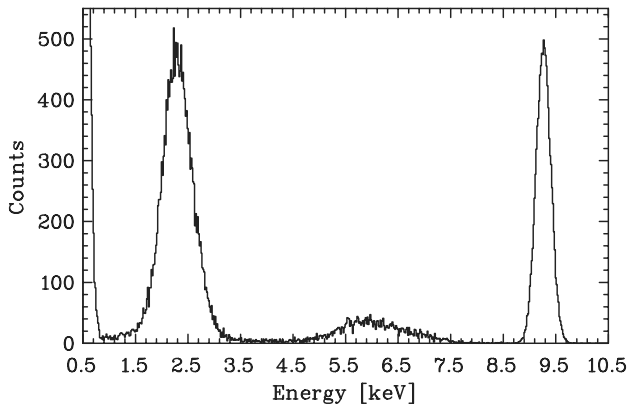

Fig. 3. LAAPD energy spectrum measured at −23°C with 2.3 and 5.9 keV X-ray peaks and a peak due to the test pulses from a pulse generator.

a strong ^{55}Fe source. An example of such a spectrum measured at −23°C is shown in Fig. 3, where 2.3 and 5.9 keV X-ray peaks, as well as a peak due to the test pulses from a pulse generator, which are fed directly to the preamplifier, are visible. The noise tail ends at 0.9 keV, which makes X-ray spectroscopy around 2 keV well feasible.

2.2. Experimental setup

In order to choose the optimal working temperature and to better understand the temperature dependence of the RMD LAAPD performance both for X-ray and visible-light detection, a series of tests were performed. X-rays with energies up to 15 keV from ^{54}Mn, ^{55}Fe, and ^{57}Co radioactive sources were used. Light pulses from a light emitting diode (LED) with a peak emission at 635 nm were carried by a light guide to the LAAPD surface. The LED light intensity was varied to achieve an energy equivalent (LAAPD pulse height) of 11–14.5 keV.

The LAAPDs were operated in a light-tight, thermally insulated box. A constant flow of cold nitrogen gas, regulated by a heater submerged in a container of liquid nitrogen, was used for LAAPD cooling with a temperature stabilization within ±0.5°C.

The LAAPD signals were fed into a low-noise charge-sensitive integrating RAL 108A preamplifier [10] followed by a linear amplifier HP 5582A, for which a gain between 16 and 128 as well as a

200 ns shaping time constant were used. A PC-based, 1024-channel analyzer Nucleus PCA II was used to record the energy spectra.

2.3. Gain measurements

Absolute gain measurements rely on the determination of unity gain, which was found by averaging the amplitudes of 100 ns visible-light LED pulses (635 nm wavelength) measured at a bias voltage in the range from 300 to 500 V. For bias voltages below 300 V the recombination of the primary electron–hole pairs plays an important role and the absolute gain is below one. Fig. 4 shows the relative amplitudes of the light pulses as a function of high voltage, together with the dark current observed during the measurement. A horizontal line shows the unity gain.

Assuming that the visible-light and the X-ray gains are equal at low LAAPD gains, the absolute gain for X-rays was determined with a ^{55}Fe source emitting 5.9 keV X-rays. Absolute X-ray gain versus high voltage, for the temperature range from −46°C to 17°C, is given in Fig. 5.

For a given bias voltage, the gain increases exponentially with decreasing temperature as seen in Fig. 6. The dependency is more pronounced for higher bias voltages and similar for both X-rays (solid lines) and visible light (dashed lines). Below a certain temperature the gain starts to increase even more rapidly, as is demonstrated in Fig. 6.

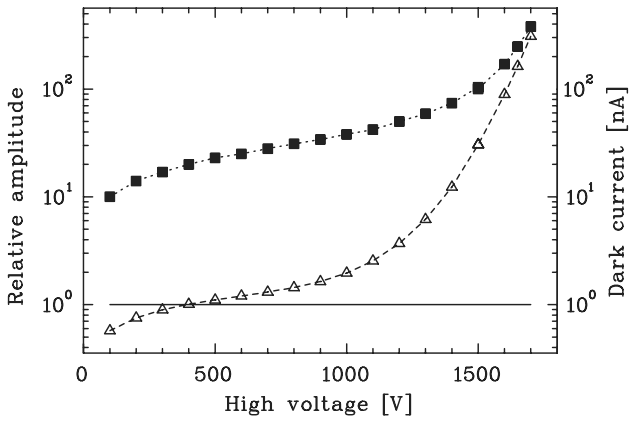

Fig. 4. LAAPD relative amplitude of the visible-light pulses (△) and the dark current (■) versus high voltage; measurement performed at 7°C. The horizontal line represents the unity gain.

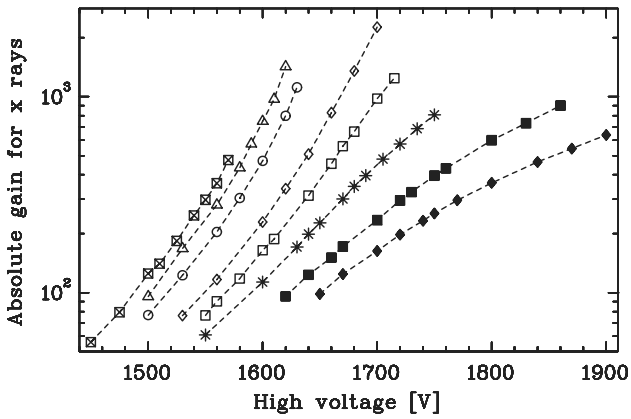

Fig. 5. LAAPD absolute X-ray gain versus high voltage measured at −46 (⊠), −40 (△), −33 (◯), −17 (◇), −8 (□), 0 (∗), 10 (■), and 17°C (◆).

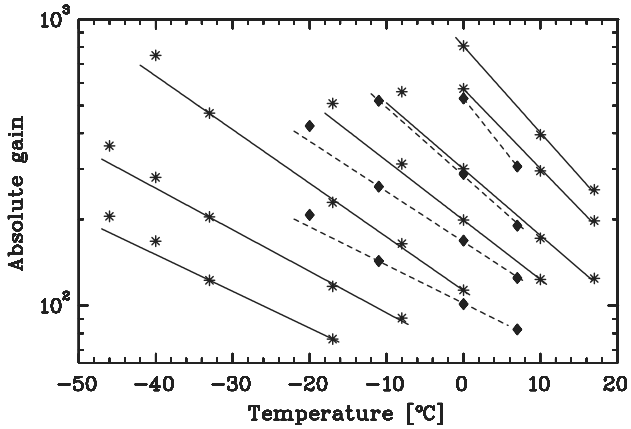

Fig. 6. LAAPD absolute X-ray (∗) and visible-light (◆) gain versus temperature. Measurements were performed at constant high voltages with X-rays (solid lines) at (from right to left) 1530, 1560, 1600, 1640, 1670, 1720, and 1750 V and with visible light (dashed lines) at 1590, 1625, 1660, and 1700 V.

2.4. Energy resolution

At low gain values the energy resolution improves with increasing gain. This trend continues up to a gain around 200 where the optimum is obtained, for both 5.9 keV X-rays (Fig. 7) and visible light (Fig. 8). This optimal gain value does not depend on the temperature. Higher gain increases the effect of spatial nonuniformity of the LAAPD gain. Due to the local character of the X-ray interaction with an LAAPD, this effect worsens the X-ray energy resolution. For light

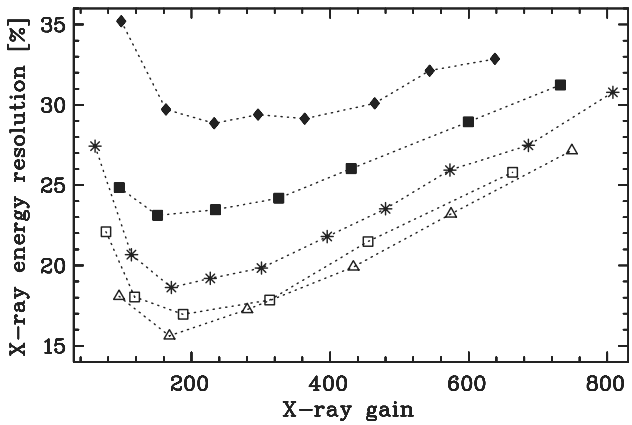

Fig. 7. LAAPD energy resolution for 5.9 keV X-rays versus gain measured at −40 (△), −8 (□), 0 (∗), 10 (■), and 17°C (◆).

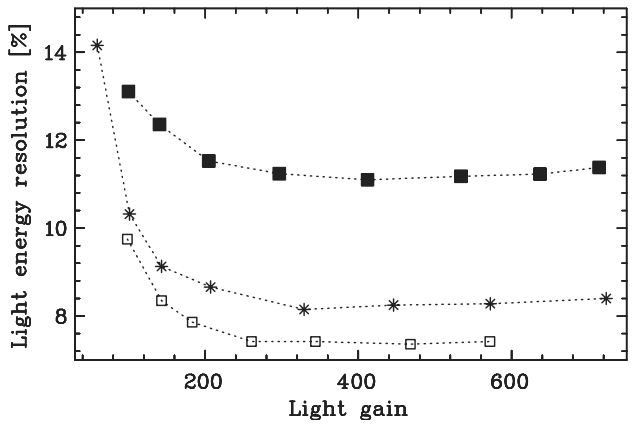

Fig. 8. LAAPD energy resolution for visible light versus gain measured at −12 (□), 0 (∗) and 10°C (■). The energy equivalent of the light pulses corresponds to 11–14.5 keV X-rays.

detection the whole illuminated area contributes to the output signal, averaging local gain variations [11]. Consequently and in contrast to the X-rays, the visible-light energy resolution remains constant at gains above 250.

Simultaneous measurements of 5.4 keV X-rays, visible-light pulses, and test signals from a pulse generator were made at different gains and temperatures. The energy calibration was determined by the X-ray peak and the LAAPD gain was deduced from the position of the visible-light peak. The position of the test-pulse peak does not depend on the LAAPD gain. Its width represents

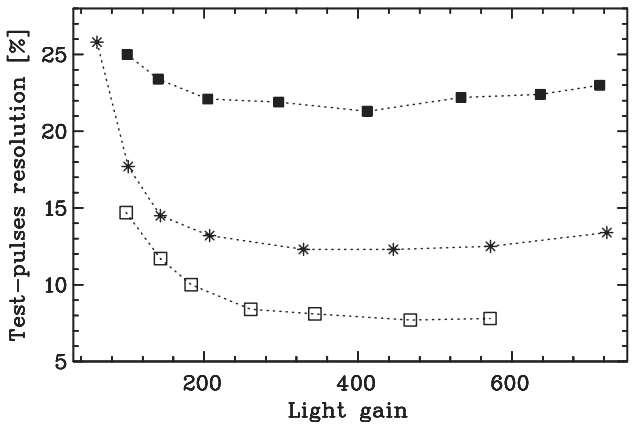

Fig. 9. LAAPD energy resolution for the test pulses versus gain, normalized to 5.9 keV. Measurements at −12 (□), 0 (∗), and 10°C (■).

the LAAPD dark current and preamplifier noise contributions to the overall resolution [3]. To express the test-pulse width as a relative energy resolution, it has to be normalized to a given energy which was chosen to be 5.9 keV, as shown in Fig. 9. Also here, the resolution reaches the minimum at a gain of about 200 and stabilizes for higher gains. The similar behavior of the visible-light and test-pulse resolutions is explained in Section 2.6.

2.5. Dark current

The dark current depends strongly on the temperature and LAAPD gain. At a given temperature it increases with gain and is reduced by an order of magnitude for each 20°C temperature decrease, as shown in Fig. 10. At −33°C and in the gain region below 800, the dark current is below 10 nA.

2.6. Excess noise factor

Measurements of the 5.4 keV X-rays from a ^{54}Mn source, visible-light, and test pulses were made simultaneously for different temperatures and different gains, allowing us to study the temperature dependence of the excess noise factor (F), defined [3] as

$$F = 1 + \sigma_A^2/M^2, \quad (1)$$

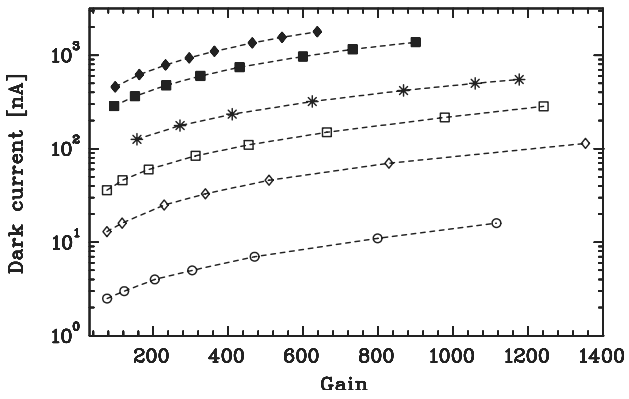

Fig. 10. LAAPD dark current versus gain measured at −33 (◯), −17 (◇), −8 (□), 0 (∗), 10 (■), and 17°C (◆).

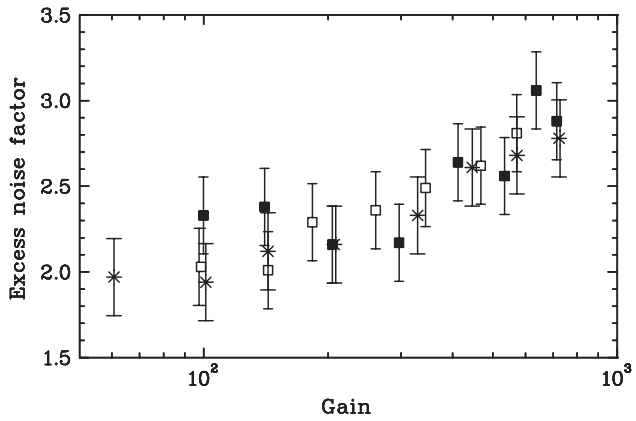

Fig. 11. LAAPD excess noise factor versus gain measured at −12 (□), 0 (∗), and 10°C (■).

where M is the LAAPD gain and σ_A its variance. Neglecting the small light-intensity fluctuations and considering that detector inhomogeneity contributions to the energy resolution are averaged out for the light measurements, the energy resolution ΔE (FWHM) of the light peak with a Gaussian shape can be described [3] as

$$\Delta E^2 = (2.355)^2 FE\varepsilon + \Delta^2_{\text{noise}}, \quad (2)$$

where E is the energy equivalent of the light peak, ε is the energy per electron–hole pair creation in Si (3.6 eV), and Δ^2_{noise} is the dark noise contribution of the diode–preamplifier system.

In the energy spectrum, the X-ray peak gives the energy calibration. The FWHM of the test pulses peak defines Δ^2_{noise}. The deduced value of F was found to be temperature independent and slowly increasing with the LAAPD gain (Fig. 11). A faster increase at gains above 300 reflects the contribution of holes to the amplification process [11]. Typical values were $F \approx 2.2$ at gain 200 and $F \approx 2.8$ at gain 600; this represents a 27% increase.

As given by Eq. (2), for light pulses with an energy equivalent E there are two contributions to the resolution ΔE. By cooling, the contribution from the dark current noise Δ^2_{noise} is suppressed (Fig. 9) and the contribution due to the temperature independent increase of the excess noise factor becomes relatively more significant. However, it is important to note that a 27% increase of F is accompanied by only a small increase of ΔE even at low temperatures. For light pulses with an energy equivalent in the range 11–14.5 keV, the corresponding ΔE increase is below 4%, 7%, and 10% at temperatures 10, 0, and −12°C, respectively. This also explains the similar behavior of the visible-light and test-pulse resolutions as functions of LAAPD gain, as was shown in Section 2.4 and in Figs. 8 and 9.

2.7. Nonlinearity

The use of the X-ray peak for the energy calibration of the light peak is correct only if the LAAPD response is perfectly linear, i.e., if the resulting signal amplitude is proportional to the initial number of electron–hole pairs. In reality, there is a well-known nonproportionality between the gains for X-ray and visible-light events, as well as between X-ray events with different energies [3,6,11–13]. In contrast to visible light, an X-ray interacting in the LAAPD produces high charge densities causing both a decrease of the local electric field and local heating. The effect is important at higher gains and causes the X-ray gain to be smaller than the visible-light gain.

The nonlinearity for X-rays with different energies was measured with a ^{57}Co source by comparing the relative positions of the 6.4 keV Fe K_α line and the 14.4 keV γ line. A comparison of three such spectra measured at different temperatures and different gains is presented in Fig. 12.

The amplitude ratio of the 14.4 and 6.4 keV X-ray signals versus gain, measured at −20 and 1°C,

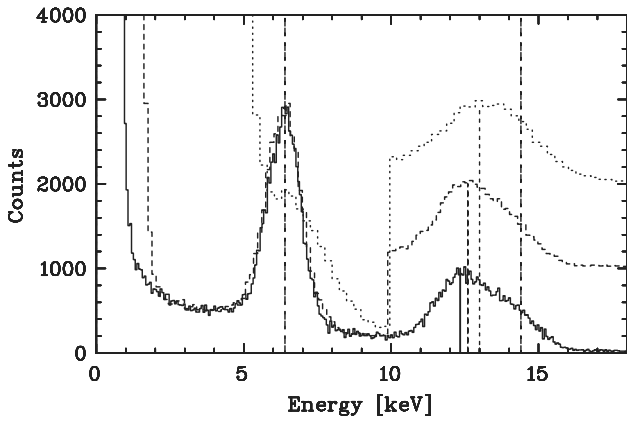

Fig. 12. LAAPD energy spectra from measurements of 6.4 keV X-rays and 14.4 keV γ rays from a ^{57}Co source, performed at -24°C (solid line), 1°C (dashed line), and 27°C (dotted line) at gains of 400, 350, and 200, respectively. Each spectrum was separately calibrated in energy such that the 6.4 keV peak occurs at the same position. The maxima of the 14.4 keV peaks are then at 12.4, 12.6, and 13.0 keV, respectively, due to the nonlinear LAAPD response. The parts of the spectra above 10 keV for the measurements at 1 and 27°C are shifted in the y direction by 1000 and 2000, respectively.

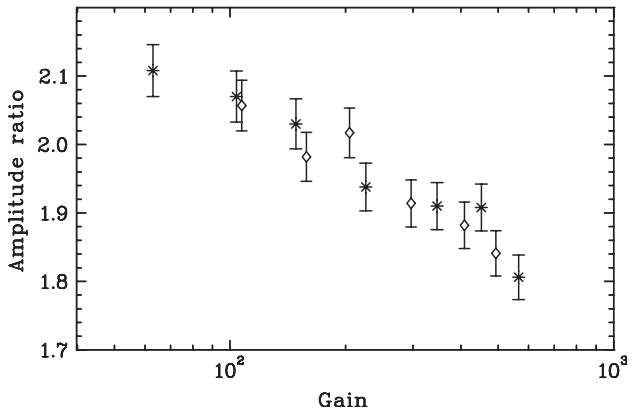

Fig. 13. Ratio of the amplitudes of 14.4 and 6.4 keV signals versus LAAPD gain, measured at -20 (◇) and 1°C (∗).

is shown in Fig. 13. The LAAPD nonlinear response for X-rays with different energies is temperature independent; normalized to the value for linear operation, 14.4/6.4, the nonlinear effect is 11% at gain 200 and 16% at gain 400.

The ratio of the X-ray to visible-light gains, shown in Fig. 14, was measured by a simultaneous

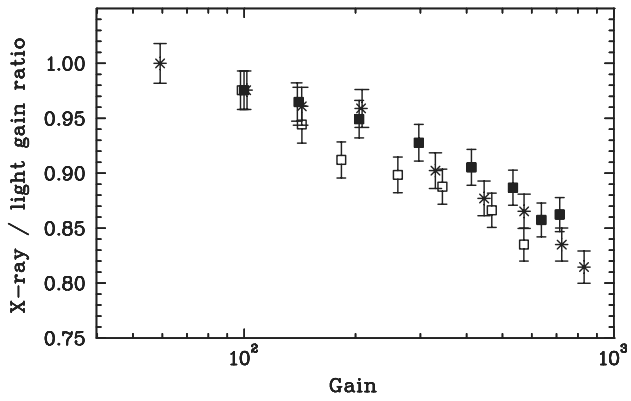

Fig. 14. Ratio of 5.4 keV X-ray to visible-light gains versus LAAPD gain, measured at -12 (□), 1 (∗), and 10°C (■).

illumination of the LAAPD by 5.4 keV X-rays and by visible-light pulses. A possible temperature dependence of this ratio, as was observed for the API LAAPDs [6], is not visible given our measurement uncertainty. The nonlinearity effect is 5% at a gain of 200, and reaches 10% at a gain of 400. Assuming that the LAAPD response to the light pulses with an energy equivalent of 11–14.5 keV is linear, one can consider the nonlinearity as an absolute nonlinearity for 5.4 keV X-rays.

Assuming that the nonlinearities for 5.4 and 6.4 keV X-rays are similar, the absolute nonlinearity for 14.4 keV X-rays can be estimated from the measurements shown in Figs. 13 and 14. It amounts to about 15% at a gain of 200 and to about 24% at a gain of 400.

The high local charge density created in the LAAPD by an interacting X-ray—the reason for the nonlinear LAAPD response—is proportional to the number of electron–hole pairs, and hence, at a given LAAPD gain, to the X-ray energy. It is thus reasonable to assume that the nonlinearity at a certain gain is, in first order, proportional to the X-ray energy. The ratio of the nonlinearities for 14.4 keV X-rays to 5.4(6.4) keV X-rays is 3.0 and 2.4 for gains 200 and 400, respectively. These ratios differ from the direct ratio of the energies $14.4/5.4(6.4) = 2.7(2.3)$ by less than 15%, an error introduced by the assumption of the same nonlinearity for 5.4 and 6.4 keV X-rays.

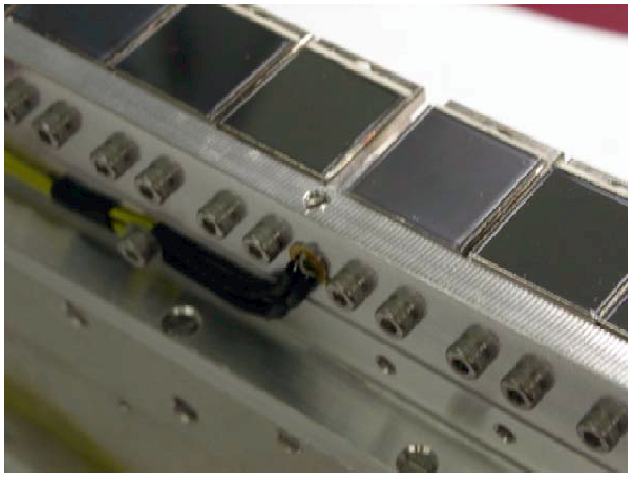

Fig. 15. Central part of one RMD LAAPD array. The wires are the thermometer leads electrical connections. High-voltage connections and preamplifiers are located on the backside of each LAAPD.

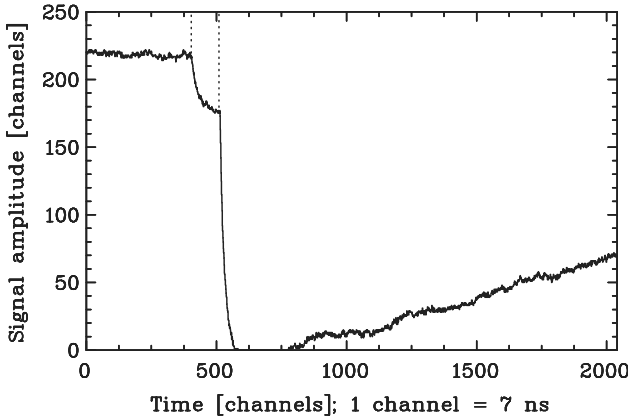

Fig. 16. A typical event with two superimposed LAAPD pulses ($\Delta t = 750$ ns) recorded by a wave-form digitizer. The pulses have negative amplitude. The small first pulse is a 1.9 keV X-ray signal and the second larger pulse is due to a muon-decay electron. The digitizer dynamic range is between 0 and 255, and hence the second pulse is saturated between channels 600 and 800 and only gives 0 as reading. The beginning of each signal is marked by a vertical dotted line.

3. LAAPD application in the muonic 2S Lamb shift experiment

3.1. LAAPD operation conditions

During the most recent data-taking period of the muonic 2S Lamb shift experiment in 2003, two face-to-face rows of ten RMD LAAPDs each were mounted around the target. Fig. 15 shows the central part of one row. The detector assembly was operated in a vacuum of 10^{-6} mbar and a magnetic field of 5 T.

For an optimal measurement of the 1.9 keV X-ray line, we cooled the whole mount to -30°C by circulating cold methanol through a small heat exchanger which was in thermal contact with the LAAPDs. The resolutions (FWHM) obtained for 5.9 keV X-rays varied for the 20 LAAPDs between 11% and 20%, with an average of about 15%. A tendency that LAAPDs with higher gain at a given high voltage have better resolution was observed.

The typical bias voltage was around 1600 V and the corresponding gain about 400, a value chosen for each LAAPD so that the amplitude of the 1.9 keV X-ray signal was sufficiently above the noise level without worsening the resolution. Based on the discussion in Section 2.7 the nonlinearity for X-rays with energies ~2 keV can be estimated to be about 3–4% at gain 400. The dark current was between 8 and 25 nA for the majority of the LAAPDs.

After the preamplifiers, the amplitude of a 1.9 keV X-ray signal was about 2 mV. The signal rise time for 25% of the detectors was below ~250 ns, for 50% was in the interval 300–450 ns and for 25% was above 450 ns. After further amplification, the negative amplitude signals were stored in an 8-bit wave-form digitizer [14] operated at 140 MHz, which allowed an optimal suppression of background signals with nonstandard shape and, in particular, permitted the separation of two consecutive, superimposed pulses. A typical event from one LAAPD is given in Fig. 16. The baseline noise fluctuations, although small, cannot be neglected in comparison with the amplitude of the 2 keV X-ray.

3.2. LAAPD response to α particles

In our experiment, the LAAPDs were exposed to α particles with kinetic energies from 2 to 9 MeV at a rate of about $5\,s^{-1}$. The α particles came from the dielectric coating of two high-reflectivity laser mirrors for 6 μm light which contain thorium. The mirrors were mounted only 1.5 cm away from the LAAPD surface.

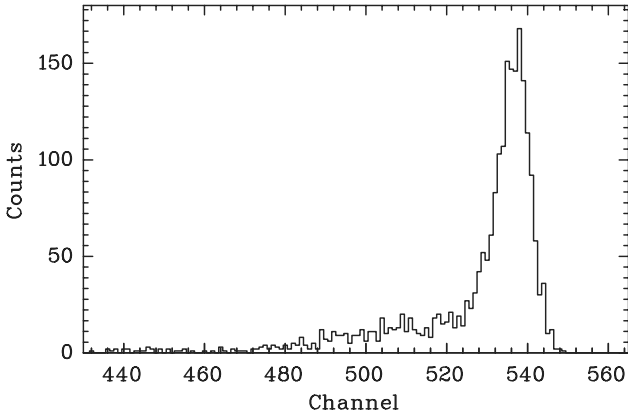

Fig. 17. LAAPD energy spectrum of the α particles from a ^{241}Am source measured at 600 V. Due to energy loss in the source, the spectrum has a low energy tail.

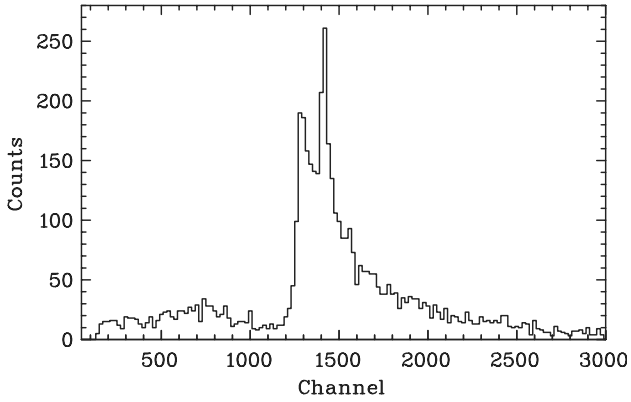

Fig. 18. LAAPD energy spectrum of the α particles as in Fig. 17, but measured at 1300 V. It corresponds to not saturated signals. Note the high-energy tail which is absent in Fig. 17.

The response of the API LAAPDs to α particles was studied with a collimated ^{241}Am α source (5.4 MeV) providing events at about 20 s^{-1}. Due to the high ionization density of α particles, they produce signals measurable in the LAAPD even at room temperature and without bias voltage. The signal has a long rise time of about 500 ns and becomes faster when bias voltage is applied. At 600 V the rise time is about 230 ns and a typical α spectrum with a low-energy tail, due to energy losses in the source, is observed (Fig. 17).

However, with a further high voltage increase a high-energy tail appears. In addition, at about 1300 V, huge pulses are observed which correspond to a LAAPD gain of order 10^5. The origin of these pulses is attributed to a plasma discharge in the avalanche region along the very high ionization density of an α particle trace [15]. These pulses cause saturation of the preamplifier and have a long recovery time. In addition, the presence of these signals gives rise to large fluctuations of the LAAPD dark current. In a spectrum measured at 1300 V (Fig. 18), one may recognize a peak due to some α particles which are not creating a plasma discharge. Not visible in Fig. 18 is the saturated signal peak from the plasma discharge signals.

With an oscilloscope probe sensor we studied the shape of the plasma discharge signals after the input coupling capacitor, while the preamplifier was removed. The LAAPD was operated at 1780 V. The saturated signal has a long relaxation time of 200 ms and a huge amplitude of 70 V. For comparison, a 6 keV X-ray produces a signal of $\sim 10^{-4}$ V in amplitude. Such a long recovery time represented an unacceptable dead time and the high amplitude was dangerous for the preamplifier.

Two high-conductance ultra fast diodes 1N4150 [16], chosen for their fast recovery time of around 5 ns, were installed at the input of the charge integrating RAL 108A preamplifier [10] to limit the amplitude of plasma discharge signals. To reduce the relaxation time, another input coupling capacitor was added and placed after the two diodes. Both input coupling capacitances were tuned in order to find an optimum between shortening the relaxation time and losing the charge sent to the preamplifier. A good compromise was found by using a first capacitance of 4.7 nF and a second of 2.2 nF. The electronic scheme in Fig. 19 represents the final arrangement of the preamplifier electronics. The recovery time was reduced by a factor of 10 to reach 20 ms, measured after the preamplifier.

At lower temperatures, the characteristics of plasma discharge signals did not change. The only difference was that they started to appear at lower voltages, since at lower temperatures a certain gain is reached already at a lower voltage.

In our application during the 2002 data-taking period, after having installed the laser mirrors and, hence, the α particles source, three out of the ten

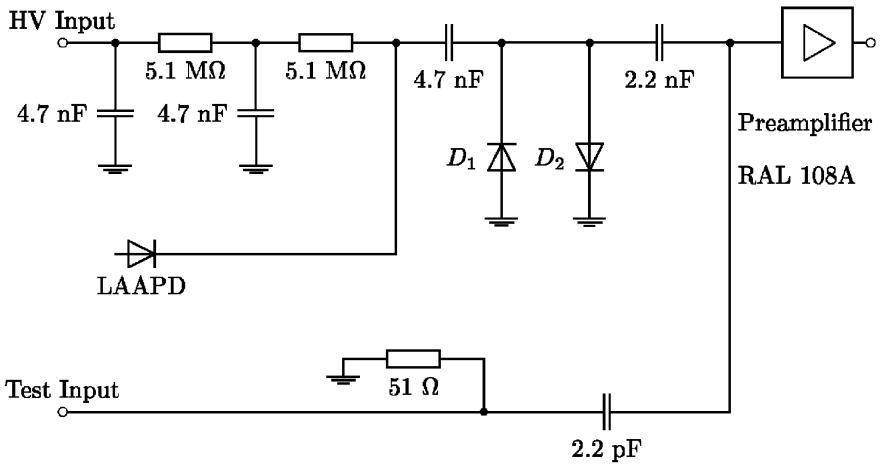

Fig. 19. Final electronic scheme of a preamplifier box used for each RMD LAAPD. Note the two input coupling capacitors (4.7 nF and 2.2 nF) with the two diodes (D_1, D_2) in between; for an explanation see text.

API LAAPDs were destroyed within a day. This happened after two weeks of perfect functioning, so there was a high probability that the API LAAPDs were destroyed by the α particles.

For the 2003 data-taking period we used RMD LAAPDs as X-ray detectors. Due to their rectangular shape and to only a thin border of inactive material, they covered a larger solid angle. With 20 LAAPDs we were able to cover an average solid angle of 30% compared to 17% obtained with the API LAAPDs. Unfortunately, when exposed to α particles, their response was very similar to that of the API LAAPDs. To avoid the risk of LAAPD damage or slow deterioration, during the final data taking we shielded the RMD LAAPDs with a 0.2 mm thick lithium sheet, absorbing all α particles below 9 MeV, but unavoidably also about 40% of the 1.9 keV X-rays.

4. Discussion and conclusions

The experiment measuring the 2S Lamb shift in muonic hydrogen, performed at the Paul Scherrer Institute in Switzerland, has demanding requirements for the 1.9 keV X-ray detectors. The beveled-edge API LAAPDs used in the initial stages of the experiment were replaced by the planar RMD LAAPDs for the latest data taking.

In our experiment the LAAPDs are exposed to α particles causing high-amplitude signals with a long recovery time and, with a high probability, detector damage or destruction. No significant difference in the detector response to α particles was found in between API and RMD LAAPDs.

The results of systematic tests studying the RMD LAAPDs performance at low temperatures were shown. In comparison, the API LAAPDs [6] show, in general, better performance and require less or no cooling, but the much higher solid angle coverage achievable with the RMD LAAPDs is an essential advantage for an application like ours.

In order to perform any reasonable soft X-ray spectroscopy measurements, the RMD LAAPDs have to be cooled. The dark current of RMD LAAPDs is of the order of a few μA at room temperature whereas values around 10 nA are reached at −30°C. In contrast, the dark current of the API LAAPDs is of the order of a few hundred nA at room temperature and can be reduced to 10 nA already at 0°C.

The RMD LAAPDs we used demonstrated worse energy resolution in comparison with the API LAAPDs. An 8% energy resolution for visible light with an energy equivalent of about 10 keV was obtained at room temperature with the API LAAPDs; to reach the same resolution with the RMD LAAPDs, they needed to be cooled to −10°C. With the API LAAPDs an energy resolution of 11% for 5.4 keV X-rays at room temperature was measured; with the RMD LAAPDs the

resolution of 11% for 5.9 keV X-rays was reached only at −30°C with the best LAAPDs.

The API LAAPDs operate with their optimal resolution at gain 50. At this gain the nonlinearity for 5.4 keV X-rays is negligible and at gain 200 it reaches only 1%. RMD LAAPDs have their best resolution at gain 200. At this gain the nonlinearity for 5.4 keV X-rays is about 5%, and at gain 400 reaches 10%. The relatively high nonlinearity of the RMD LAAPDs is not an essential problem for our experiment, because we are interested only in the intensity variation of the 1.9 keV X-rays as a function of the laser frequency. A higher gain achievable with the RMD LAAPDs in feasible X-ray spectroscopy measurements represents an advantage, especially for an experiment realized in a high-noise environment.

Our final data taking was performed at typical gains of 400 with a satisfactory energy resolution. All 20 RMD LAAPDs were operated for several weeks without any deterioration. At the end it was proved that the RMD LAAPDs are suitable for soft X-ray spectroscopy measurements.

Acknowledgements

Support is acknowledged from the Swiss National Science Foundation, the Swiss Academy of Engineering Sciences, from the Portuguese Foundation for Science and Technology (FCT) Lisbon, and FEDER through the Project POCTI/FNU/41720/2001, and the program PAI Germaine de Staël no. 07819NH du Ministère des Affaires Étrangères France. The project was in part supported by the US Department of Energy. Laboratoire Kastler Brossel is a Unité Mixte de Recherche du CNRS no. 8552. Financial support for this research was received from the Swedish Science Research Councils (VR).

The authors would like to thank L. Simons and B. Leoni for setting up the cyclotron trap. We also thank the PSI accelerator division, PSI Hallendienst, PSI and University Fribourg workshops, and other support groups for their valuable help.

References

[1] F. Kottmann, et al., Hyp. Interact. 138 (2001) 55.
[2] Advanced Photonix Inc., 1240 Avenida Acaso, Camarillo, CA 93012, USA.
[3] M. Moszynski, M. Szawlowsky, M. Kapusta, M. Balcerzyk, Nucl. Instr. and Meth. A 485 (2002) 504.
[4] L.M.P. Fernandes, et al., Nucl. Instr. and Meth. A 498 (2003) 362.
[5] M. Boucher, et al., Nucl. Instr. and Meth. A 505 (2003) 136.
[6] L.M.P. Fernandes, et al., IEEE Trans. Nucl. Sci. NS- 51 (4) (2004) 1575.
[7] L.M.P. Fernandes, et al., Spectro. Acta B 58 (2003) 2255.
[8] Radiation Monitoring Devices, Inc., 44 Hunt Street, Watertown, MA 02472, USA.
[9] R. Farrell, et al., Nucl. Instr. and Meth. A 442 (2000) 171.
[10] CLRC Rutherford Appleton Laboratory, Chilton, Didcot, Oxfordshire, OX11 0QX, UK.
[11] M. Moszynski, M. Kapusta, M. Szawlowski, D. Wolski, Nucl. Instr. and Meth. A 442 (2000) 230.
[12] J.P. Pansart, Nucl. Instr. and Meth. A 387 (1997) 186.
[13] M. Moszynski, M. Szawlowski, M. Kapusta, M. Balcerzyk, Nucl. Instr. and Meth. A 497 (2003) 226.
[14] S. Dhawan, Developed at Physics Department, Yale University, New Haven, CT 06520-8121, USA.
[15] R. Farrell, Radiation Monitoring Devices, Private communication.
[16] Fairchild Semiconductor Corporation, 82 Running Hill Road, South Portland, ME 04106, USA.

Chapter 5

Electronics and data sets

The electronics system used for the data acquisition of the μp Lamb shift experiment in 2003 is described here. The muons interact with the detectors in the PSI πE5 experimental area. Due to high radiation, it is not allowed to enter this zone when the measurement is in progress. Therefore, the signals from all detectors are brought to the counting room (CR) and some of them to the laser hut (LH). The CR, where all systems are ultimately controlled and measured, is about 40 m away from the zone; the corresponding cable length delayed all signals by about 200 ns. The laser beam is generated in the LH and then sent to the experimental area, separated from the LH only by the concrete–blocks shielding against radiation. The LH is about 10 m distant from the CR, which corresponds to about 50 ns cable delay.

The laser can operate at about 50 Hz maximum. Therefore, the time from muon detection to laser trigger must be minimized and the events which can be accompanied by a laser pulse are the priority. However, events without laser are needed for normalization and control.

The trigger system, divided in two parts (the LH– and the CR–trigger systems), is described in §5.1. The detector electronics is the topic of §5.2. Section 5.3 summarizes the type and quantity of data collected.

5.1 Trigger system

The main roles of the trigger system are

1. To recognize low–energy muons with a chance to stop in the gas target and to create a μp atom, and to decide if the laser and DAQ systems are ready to accept such an event;
2. To decide when to trigger the excimer lasers;
3. To decide if the detector signals (LAAPDs, electron detectors, laser detectors) following a muon stop signal should be read. This is a very important decision, since data reading and writing to the computer is a long process. Events without any interesting information should not be read and the system has to be reset to accept a new event as soon as possible.

The first two items are decided in the LH–trigger system located in the laser hut. The decision to fire a laser pulse has to be made as soon as possible and, the LH is the location which is closest to the experimental area. The third item is processed in the CR–trigger system placed in the counting room. The timing scheme of the main trigger signals is

shown in Fig. 5.1. A detailed scheme of the whole trigger system is shown in Fig. 5.2. Table 5.1 summarizes the key modules of the trigger system.

The signals from the S_1, S_2 and D_3 detectors are split in the zone and one part is sent to the LH. The S_1 signal with an amplitude above a set threshold opens the S1G gate of 80 ns. If a S_2 signal passes a discriminator level of S2D, a 10 ns wide signal is generated. If the S2D signal is within the S1G gate, the T1 coincidence is set under the condition that a pile–up gate PUG is not set on. The PUG is opened for 260 ns after each T1 signal and ensures that within this time T1 can be produced just once. The main purpose of this protection is to avoid after–pulses present on the S_2 signal faking a second muon. The width of the S1G gate corresponds to the time–of–flight (TOF) interval which limits the range of kinetic energies of the accepted muons. It has to be carefully set in order to trigger only on those muons which have a sufficient probability to be stopped in the gas target. A trigger signal sent to the CR is T$\bar{\text{B}}\bar{\text{I}}$_LH which is generated as a coincidence of

1. T1 coincidence,
2. Anti–INH and anti–DASTOP signals ensuring that the electronics and computers are ready to accept a new event,
3. Anti–LWI signal correlated with the laser status and described below.

The D_3 signal passing a threshold of the D3D discriminator opens a 230 ns wide gate. If this gate is not opened and the signal T1 is produced the MUON coincidence is set. The MUON represents the $S_1 \cdot S_2 \cdot \bar{D}_3$ signal described in §4.1. This signal sets a fire laser FL signal triggering both excimer lasers under the condition that the laser system is ready. This is ensured in a way that each FL signal opens a laser status LS gate of 14 ms. If this gate is on, it means that the laser is recovering from the previous shot and is not yet ready to produce another pulse. However, the long dead time of the laser can be used to detect muon stops without a laser shot (§5.3). This is ensured by two gates which divide the LS gate in two parts. For the first 11 ms, the "no–laser events" NLE gate is opened and within this time the electronics will accept muon stops (*i.e.*, the T$\bar{\text{B}}\bar{\text{I}}$_LH signal is allowed) knowing that there will be no laser shot. For the remaining $14 - 11 = 3$ ms the "laser wait inhibit", LWI, gate is on and inhibits production of the T$\bar{\text{B}}\bar{\text{I}}$_LH coincidence. This inhibit ultimately gives priority to muon stops with the possibility of laser interaction. If any muon stop would be accepted within the LWI gate, the laser is clearly not yet ready and cannot fire. But, in addition and in contrast to the events taken within the NLE gate, the data read–out would not yet be finished when the laser would again be ready and so a potential muon stop occurring soon after the laser became ready would be lost because the computer would still be reading the CAMAC.

The trigger parts described below are located in the counting room. There are two signals important for the trigger which are sent from the LH to the CR. The first one is the MUON, which is regenerated in the MUON_CR discriminator and opens the MUON_TRIG latch. The second one is the T$\bar{\text{B}}\bar{\text{I}}$_LH signal, regenerated in the CR by the T$\bar{\text{B}}\bar{\text{I}}$_CR discriminator. The T$\bar{\text{B}}\bar{\text{I}}$_CR trigger opens three important gates:

1. The event gate, EVG, opened for 12 μs. This gate defines the time after the arrival of the muon during which physics events are accepted from the detectors. If any LAAPD signal above threshold is detected within EVG, then the event is marked for read out.
2. The "event in progress", EIP, gate which is opened for a longer time than EVG, indicates that the electronics is processing an event. Another T$\bar{\text{B}}\bar{\text{I}}$_CR signal produced

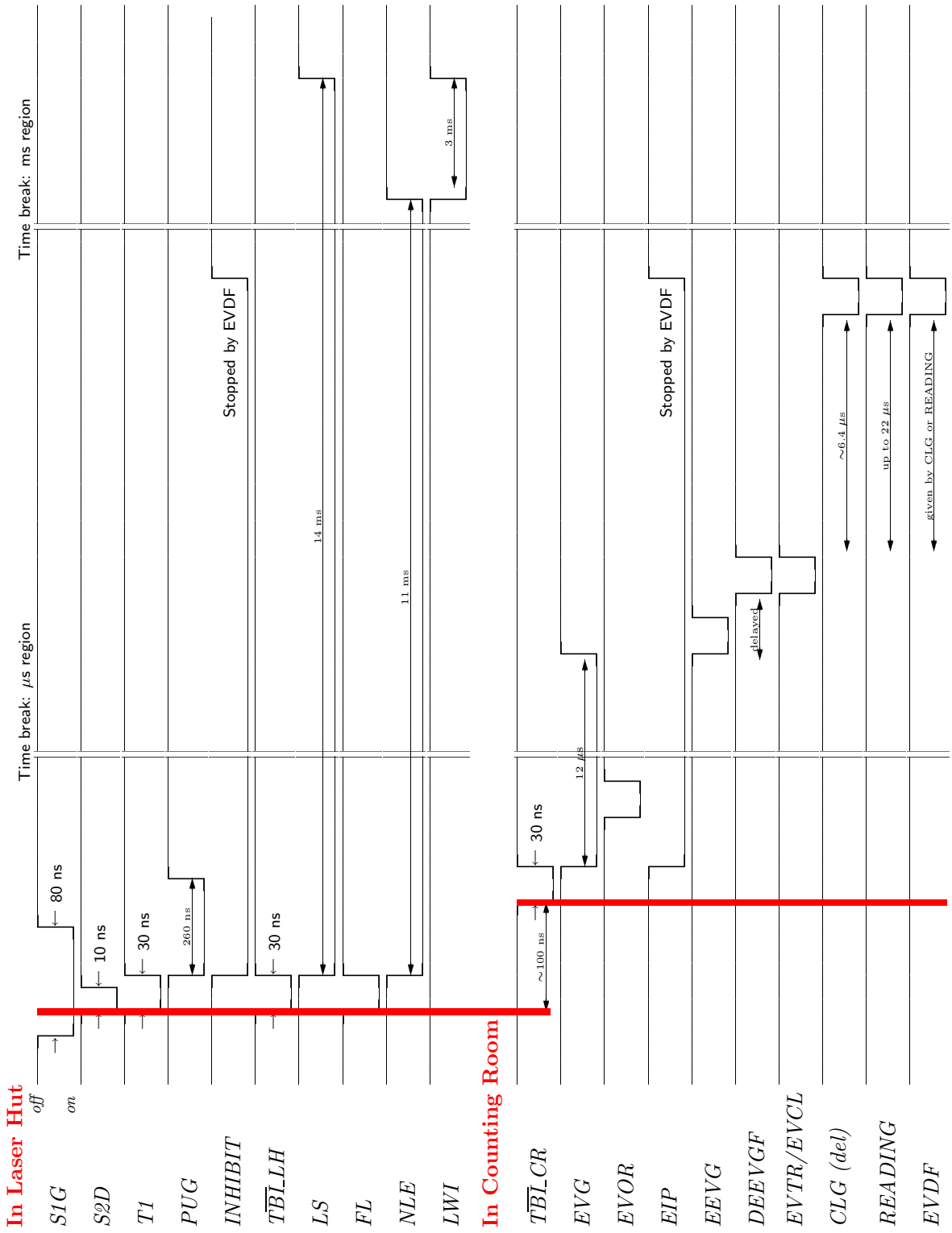

Figure 5.1: Relative timing of the main signals in the trigger system. The levels are NIM logic, i.e., 0 V = off = false, -0.8 V = on = true. The meaning of the abbreviations is explained in Table 5.1. For the position of the modules within the electronics scheme see Fig. 5.2.

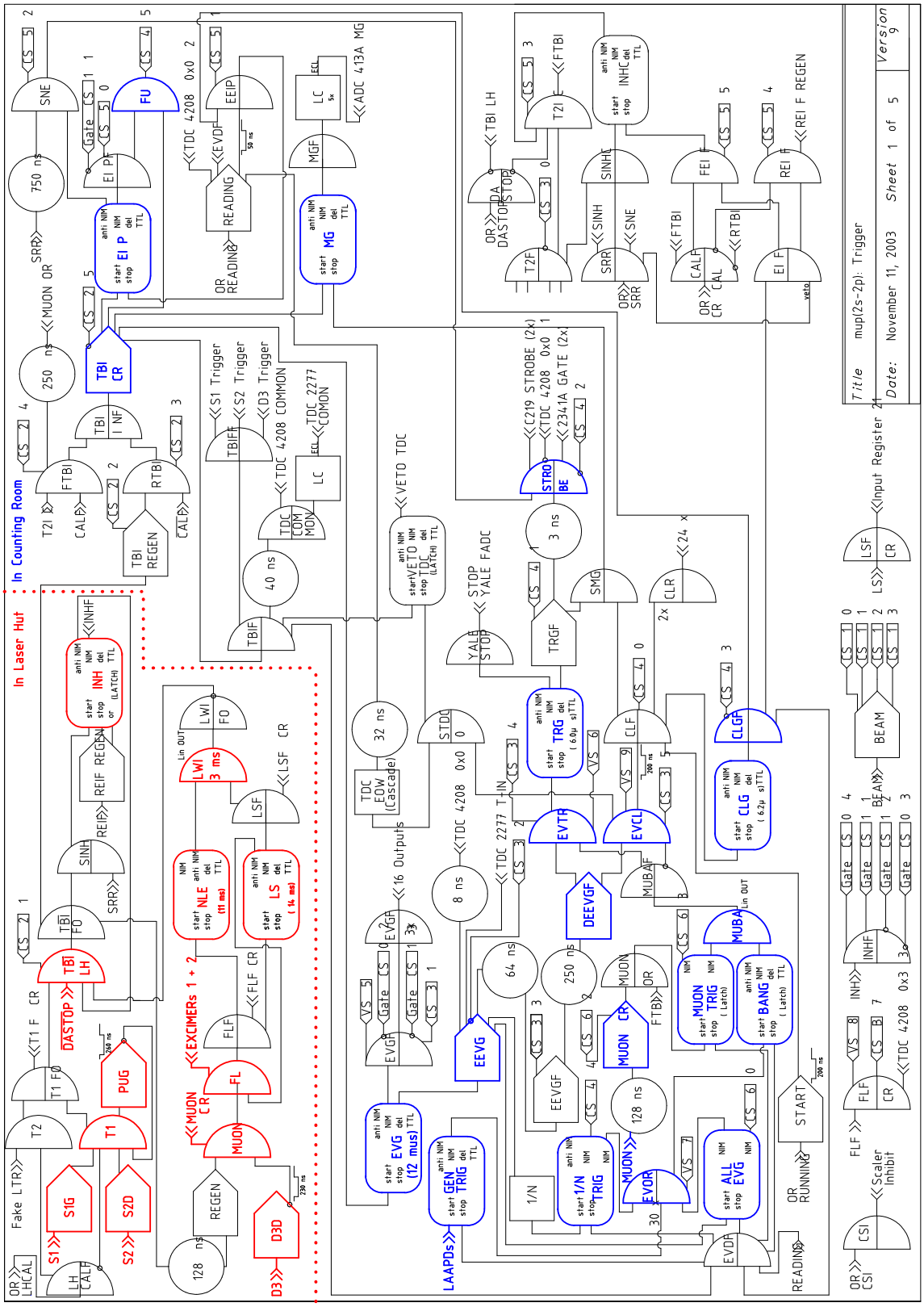

Figure 5.2: Scheme of the trigger system. The most important modules discussed in the text are marked in colours. The names of the modules receiving signals from the detectors (S_1, S_2, D_3, and LAAPDs) are also given in colours. The red dotted line separates the parts placed in the laser hut (red) and in the counting room (blue).

Table 5.1: Summary of the principal modules in the trigger part of the electronics scheme shown in Fig. 5.2.

Abbreviation	Full Name	Comments
modules in the laser hut LH		
S1G	S_1 gate	muon in stack S_1
S2D	S_2 discriminator	muon in stack S_2
T1	trigger 1	TOF coincidence of S_1 and S_2
PUG	pile–up gate	protection against muon pile–up
INH	inhibit latch	DAQ is busy to process an event
DASTOP	data acquisition stop	the data reading and storing is in progress
$T\bar{B}\bar{I}$_LH	T1 & anti–INH & anti–LWI in the LH	trigger sent to the CR
D3D	D_3 discriminator	muon in D_3
MUON	T1 & anti-D3D	muon did stop in the gas
FL	fire laser	trigger for both excimers
LS	laser status gate	laser is recovering after a shot
NLE	no–laser events gate	part of the LS where $T\bar{B}\bar{I}$ is allowed
LWI	laser wait inhibit	part of the LS where $T\bar{B}\bar{I}$ is not allowed
modules in the counting room CR		
$T\bar{B}\bar{I}$_CR	T1 & anti–INH & anti–LWI in the CR	trigger to open EVG and MG
MG	master gate	gate for ADCs 413A
EVG	event gate	x–ray and e^- signals accepted
EEVG	end of EVG	EVG was just closed
DEEVGF	delayed EEVG fan	distributes delayed EEVG signal
GEN_TRIG	generic trigger latch	20 gates, one for each LAAPD LAAPD detected x–ray or e^-
1/N_TRIG	1/N trigger latch	sampling of all EVGs
ALL_EVG	all EVG latch	each EVG triggers
EVOR	event or	any of GEN TRIG, 1/N TRIG or ALL EVG triggered
MUON_CR	MUON in CR	MUON from LH regenerated
MUON_TRIG	muon trigger latch	muon is detected
BANG	bang latch	opened by EVOR
MUBA	MUON & BANG	muon is detected and the event should be read
EVTR	event trigger	decision to read an event
EVCL	event clear	decision to clear an event
TRG	trigger gate	turns on the STROBE freezes the WFD spectra
STROBE	strobe	signal asking the computer to read the data
EIP	event in progress latch	event is under the process
FU	failed unit	$T\bar{B}\bar{I}$ during EIP
READING	reading	data read–out begins
CLG	clear gate	clearing is in the process
CLGF	clear gate fan	end of CLG gate
EVDF	event done fan	closes trigger latches

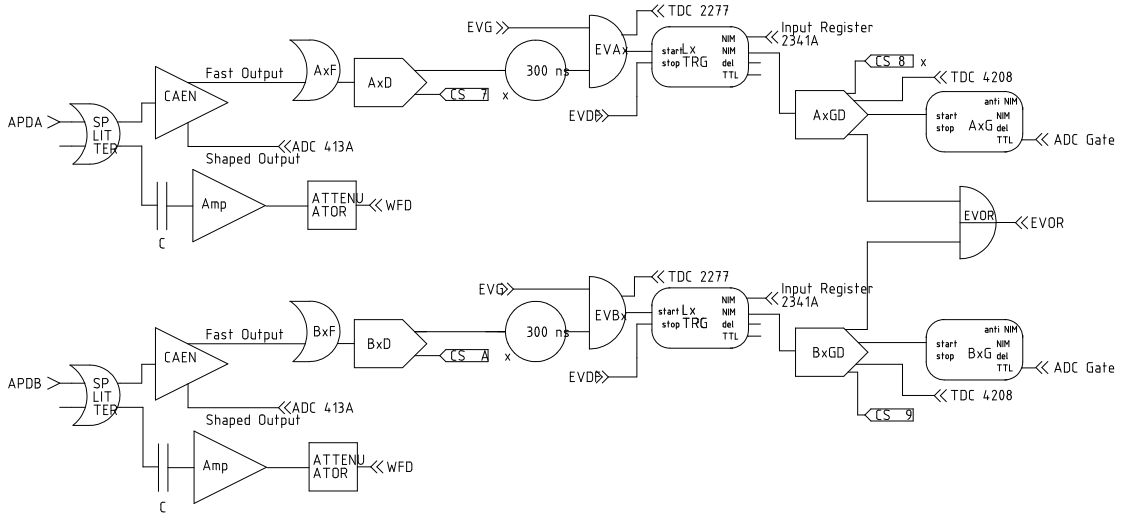

Figure 5.3: Scheme of the x–ray detectors electronics located in the counting room (here shown for one A–side LAAPD and one B–side detector). The capacitance C acts as a high–pass filter mainly to remove 50 Hz noise.

within this gate would indicate a serious failure in the trigger system and thus the flag "failed unit"(FU) was used to monitor for that case.

3. The "master gate" MG. Within this gate the amplitude–digital converters (ADCs) digitize signals from individual detectors (§5.2).

The end of the EVG is indicated by a 30 ns wide EEVG signal, which is renamed to DEEVGF when delayed by $\sim$ 300 ns. At that time the electronics decides to read or clear the event and thus the EVTR or EVCL signal is produced. The EVTR signal is produced if DEEVGF is in coincidence with the MUBA signal, meaning that both MUON_TRIG and BANG latches were true. As described above, MUON_TRIG means a $S_1 \cdot S_2 \cdot \bar{D}_3$ coincidence. The BANG latch is opened by the EVOR, which is enabled if any of the following latches are set:

1. The "generic trigger" GEN_TRIG latch. In reality this trigger is represented by 20 Lx_TRIG (x from 0 to 19) latches (Fig. 5.3), each one connected to one LAAPD. Lx_TRIG latch is set if the respective LAAPD did detect a signal above a certain, individually set threshold.
2. The 1/N_TRIG latch. This latch is set by the prescaled EEVG signal, therefore reading all detectors independently of the LAAPDs. For large N, the rate of good events with LAAPD signals is reduced only negligibly. On the other hand, one gains unbiased information about all categories of signals opening the EVG.
3. The ALL_EVG latch which is opened by every EVG. This mode corresponds to item 2 with N = 1. The probability to detect a 2 keV x ray when the μp atom is already created is only 10%. Therefore, this mode was only used for special calibration measurements.

The EVTR signal opens the TRG gate which stops the data collection by the wave–form digitizers (WFD) used for the LAAPDs (§4.4), and TiSa_osc, and V_2 signals (§§4.3 and 5.2). The TRG signal turns on the STROBE signal, indicating to the computer that the data accumulated by the electronics should be read. When the data read–out begins

(14 to 28 μs after the end of EVG), the computer generates the READING signal. After that, it takes up to a few ms until the data are stored in the computer and the new $\mathrm{T\bar{B}\bar{I}}$ trigger signal is allowed.

In case the event is not read but cleared, the EVCL signal opens the "clear gate" CLG at the end of which the CLGF signal is produced. Either READING or CLGF signals (OR'ed in the "event done fan" the EVDF module) resets the GEN_TRIG, 1/N_TRIG, ALL_EVG, MUON_TRIG, BANG, EIP, and INH latches.

The central components and signals of the trigger system described above are supplemented by many other components. Those parts which were not mentioned but can be seen in Fig. 5.2 are different fan-out units distributing the same signal to different modules, delays important for correct timing of the signals and components used in various calibration modes of the trigger. The labels CS x (x being a number) in Fig. 5.2 stand next to the modules whose rates are monitored via scalers. The timing of the different signals was regularly controlled, and in some most critical cases (as EEVG, STROBE, READING) the signals were fed to time–to–digital converters (TDCs) allowing strict event-by-event control offline.

5.2 Detector signal electronics

Timing and amplitude information of all detectors is required; specifically for S_1, S_2, D_3, D_3^{hi}, EP_{left}, EP_{right}, LAAPDs, Dye_1, Dye_2, TiSa_osc, TiSa_amp, V_1, V_2, and some other laser diodes monitoring the light quality. For this purpose different ADC and TDC modules are used, namely LeCroy [76] ADC 2249A, ADC 2249SG, ADC 2249W, ADC 2259B, TDC 4208, PTDC 2277, and Ortec [77] ADC413A. For both TDC and pipeline TDC (PTDC), the electronics principle is very similar. An analog signal from a detector is sent to a discriminator with a certain threshold, and if the signal amplitude is higher than this threshold, the discriminator sends a NIM signal to a TDC (PTDC) module which measures the timing of this signal. The difference is that while with a TDC only the first signal can be detected, the PTDC can detect up to 16 consecutive signals from the same detector. If the same signal is sent to both TDC and PTDC, the resulting time spectrum from the TDC and from the first hit of the PTDC have to be the same. The S_1 and S_2 PTDC signals are crucial for detecting so called second muon stops, as it will be described in detail in §6.2.

At the first stages of the experiment, the LAAPD signals were analyzed by the same means in order to have a reference for the new wave–form digitizers (WFD) [78] used in the final data–taking (§4.4). The WFDs were also used in the analysis of the TiSa_osc and V_2 signals (in addition to ADC and TDC).

The complexity of the electronics leading a detector analog signal to a TDC, PTDC, ADC or WFD input is demonstrated using the example of an LAAPD. After the RAL 108A preamplifier [79], the amplitude of a 1.9 keV x–ray signal was about 2 mV. This signal was inverted and 20 times amplified by the post–amplifiers placed in the experimental zone. After that the signal was sent by $\sim$ 40 m long cables (200 ns) to the CR where it was fed into the electronics shown in Fig. 5.3. There the analog signal was split. One part, after passing through another stage of amplification and attenuation, with the freedom to adjust the amplitude of the signal if necessary, was fed to the WFD. The second part of the split signal was passed to a CAEN N568BB spectroscopic amplifier [80]. The CAEN amplifier shaped output was sent to an Ortec ADC 413A in the initial stages of the experiment. The CAEN fast output was sent via a fan (enabling to watch and control the

signal at any time) to a discriminator whose rate was monitored by a scaler. If the fast signal was above a discriminator threshold and in coincidence with the EVG, it turned on the Lx_TRIG latch and a signal was sent to the PTDC. A NIM output of the Lx_TRIG latch was regenerated in another discriminator whose output was sent to regular TDC. In addition, this signal was sent to the EVOR module (§5.1), opened a gate for the ADC module, and its rate was monitored by a scaler. Identical signal treatment modules were built for each LAAPD.

5.3 Data sets

The experimental setup used for the latest data taking period, as described in Chapter 4, was installed and tested at the experimental site in the period from July to October 2003. The data analyzed in this work were taken within a four week period in November 2003. During this time the whole setup was maintained in good operating condition and no principal changes were made. All data are subdivided into so-called runs, where one run is stored in a single computer file and represents between 10 and 60 minutes of data. The main advantage of this data division is a better control of possible systematic drifts.

Laser maintenance times were used for taking L_{OFF} data. Naturally, L_{ON} data were taken with the laser functioning. Within a run of L_{ON} data there are L_{ON} events and L_{OFF} events. The L_{ON} events occur when the $S_1 \cdot S_2 \cdot \bar{D}_3$ trigger is accompanied by the fire laser FL signal.

In order to consider an event to be a L_{ON} event it is important to ensure that the laser

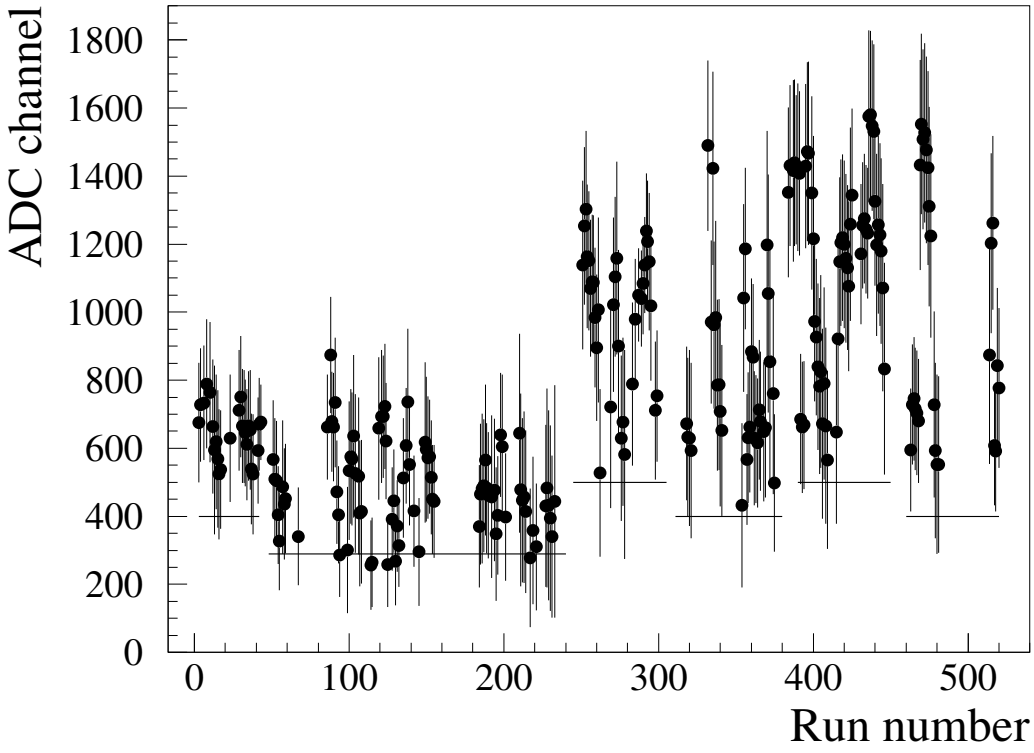

Figure 5.4: Amplitude of V_2 signals given in ADC channels as a function of run number. Each point represents a mean value for one run. Horizontal lines represent the minimal amplitudes required in order to accept an event as a L_{ON} one.

system received not only a FL trigger signal, but also that a good quality 6 μm pulse was produced. Therefore, each L_{ON} event requires that a V_2 diode detected a signal, the V_2 TDC was hit, and the V_2 ADC signal was above a certain threshold; only such events are analyzed in the search of the $2S - 2P$ resonance. Events which do not fulfill all these conditions but are accompanied by the FL signal are labeled as "strange L_{ON} events".

The V_2 ADC threshold was optimized for different data acquisition periods, as demonstrated in Fig. 5.4. This threshold was changed for different laser adjustments in order to correspond to comparable absolute levels of the laser pulse energy.

The L_{OFF} events within the L_{ON} data occur when the trigger signal $S_1 \cdot S_2 \cdot \bar{D}_3$ is not accompanied by a laser trigger FL, *i.e.*, the events taken within the NLE gate. The L_{OFF} events within the L_{ON} data were used to study the background of the laser induced events, as described in §7.2. The analysis presented in §§7.1 and 7.3 was performed without any distinction among the L_{ON} and L_{OFF} data or events.

A special type of data, L_{CAL}, is dedicated to the time calibration of the system. Part of the red light from the Ti:Sa oscillator was sent via a light guide directly to the target. The intensity of the red light was varied for several calibration measurements. The aim was to illuminate each LAAPD individually with such a light intensity that the amplitude of its output signal corresponded to the amplitude of a 2 keV x ray signal. The results are given in §6.3 dedicated to the time calibration.

Table 5.2 summarizes the amount and type of data taken. The total measuring time,

Table 5.2: Summary of the amount and type of the taken data. FP stands for Fabry–Perot fringe and λ for the laser wavelength.

Data type	Duration [s]	Duration hh:mm:ss	EVG # [$\times 10^6$]	TRIGGER # [$\times 10^3$]	CLEAR # [$\times 10^6$]	V_2 # [$\times 10^3$]
L_{OFF} data	185 611	51:33:31	39.086	3863.2	35.223	41.5
L_{ON} data	266 468	142:29:11	104.365	20205.1	94.042	21 374.8
FP	λ [nm]					
282000 +	7070 +					
794	9.90174	00:39:48	0.535	53.1	0.481	85.2
801	9.72649	05:39:10	4.476	442.6	4.033	770.3
808	9.55126	08:00:00	5.770	565.0	5.205	993.1
815	9.37603	15:15:07	11.185	1 098.0	10.087	2 008.2
822	9.20082	08:40:35	5.831	576.3	5.255	1 261.2
829	9.02561	08:51:00	6.393	625.7	5.768	1 261.4
836	8.85041	10:49:08	8.403	824.6	7.578	1 612.3
843	8.67522	13:03:53	10.111	999.2	9.112	2 076.3
850	8.50003	15:03:34	9.854	983.0	8.871	2 243.4
857	8.32486	14:02:59	10.536	1 064.7	9.471	2 272.0
860	8.24979	08:11:30	5.864	573.1	5.291	1 307.3
863	8.17472	08:11:21	5.874	581.8	5.292	1 360.9
869	8.02458	08:12:31	6.141	610.5	5.530	1 306.7
877	7.82441	06:31:35	4.231	421.2	3.810	1 011.8
884	7.64927	07:19:51	5.570	547.6	5.022	1 190.8
891	7.47414	03:31:32	2.797	279.6	2.518	480.5
934	6.39852	00:57:19	0.793	77.0	0.716	133.4

the number of EVG, event TRIGGERS and event CLEARS are given for all L_{OFF}, L_{ON} and L_{CAL} data. The L_{ON} data are subdivided according to the laser wavelength λ, dependent on the FP fringe number (§4.3). The L_{OFF} data should not contain any V_2 hits. However, about 0.1% of the L_{OFF} data is accompanied by a V_2 signal, due to some test laser triggers. This has no effect on the analysis results, since the L_{OFF} data were considered only for that part of the analysis, when the presence of a laser pulse is irrelevant.

Chapter 6

Data analysis

This chapter is dedicated to a detailed description of the data analysis. Section 6.1 describes the techniques with which the WFD data were processed. Section 6.2 defines the terminology connected with the analysis and used throughout the following text. Sections 6.3 and 6.4 are dedicated to the time and energy calibration, respectively. In §6.5 the LAAPD efficiency as a function of the incident x–ray energy is described. In §6.6 the LAAPD response to electrons is shown, as well as the electron spectra from the electron paddles and some particularities about the electron detection of our system. Section 6.7 introduces different types of the background used in the analysis of the x–ray energy spectra.

6.1 Analysis of the WFD signals

As described in §5.2, the LAAPD output signals were amplified in several stages and fed into the 8–bit WFD [78] operated at 140 MHz. Each of the 2048 WFD channels thus has a time width of about 7 ns and a dynamic range between 0 and 255. Each WFD record, referred to as "WFD spectrum", represents the evolution of a LAAPD output signal in time during ~ 14.3 μs. The WFD spectra should be clearly distinguished from the spectra which are the histograms of the parameters resulting from the analysis of many WFD spectra, such as the energy and time spectra described below. The diversity of the WFD spectra, demonstrated in Fig. 6.1, requires a complex analysis considering the variety of the shapes of LAAPD output signals and particularities of individual diodes. A function is fit to each measured WFD spectrum, depending on several parameters which have to be tuned individually for all 20 LAAPDs and whose stability throughout the whole data taking period has to be controlled. The LAAPD characteristics, *e.g.*, the noise level, the base line level and its fluctuation, and the sensitivity to charged particles, influence the optimal parameter values.

A WFD spectrum has a flat baseline with superimposed negative–going, single or multiple pulses (Fig. 6.1, (a) – (h)). An individual pulse in a WFD spectrum is mainly a response to an x ray or an electron. Since the LAAPD detection efficiency for high–energy x rays is small (§6.5), there is a trend that small amplitude pulses are due to x rays and large–amplitude pulses are due to electrons. The electron–signal amplitude is often out of the WFD dynamic range, as shown in Fig. 6.1 (d). Such signals will be referred to as "saturated signals". However, it should be emphasized that these saturated signals can also be due to high–energy x rays, and vice versa, *i.e.*, small–amplitude signals can also be due to electrons, as will be shown in Section 6.6.

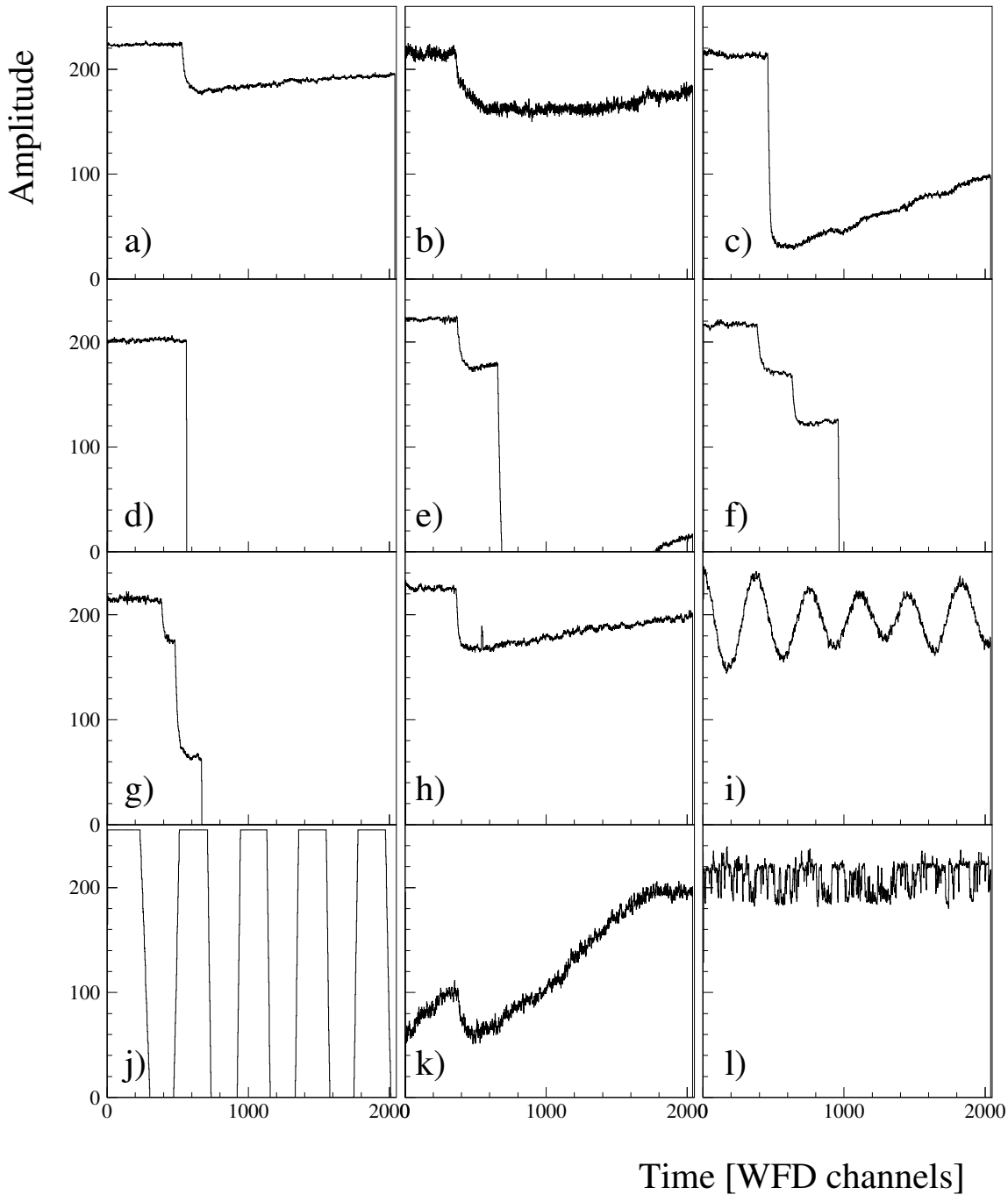

Figure 6.1: Examples of typical WFD spectra (7 ns/channel, total time range 14.3 μs). (a, b, c, d) Single pulse spectra: signals due to x rays with energy of ∼ 2 keV from (a) a high quality LAAPD and (b) from a noisy LAAPD; (c) higher–amplitude signal within the WFD dynamic range, (d) saturated high–amplitude signal out of this dynamic range, most probable from an electron. (e) Double pulse spectrum: first pulse from a 2 keV μp x ray, second pulse due to a muon–decay electron. (f, g) Triple pulse spectra: (f) two 2 keV μp x rays and an electron signal, (g) 2 keV μp x–ray signal followed by a delayed second pulse due to a 4.9 keV μC x ray and a third, muon–decay electron pulse. (h, i, j, k, l) Other types of WFD spectra, details in the text: (h) an overshoot due to crosstalk, (i, j) ringing, (k) pulse super-imposed over a steep baseline, (l) an example of an irregular structure.

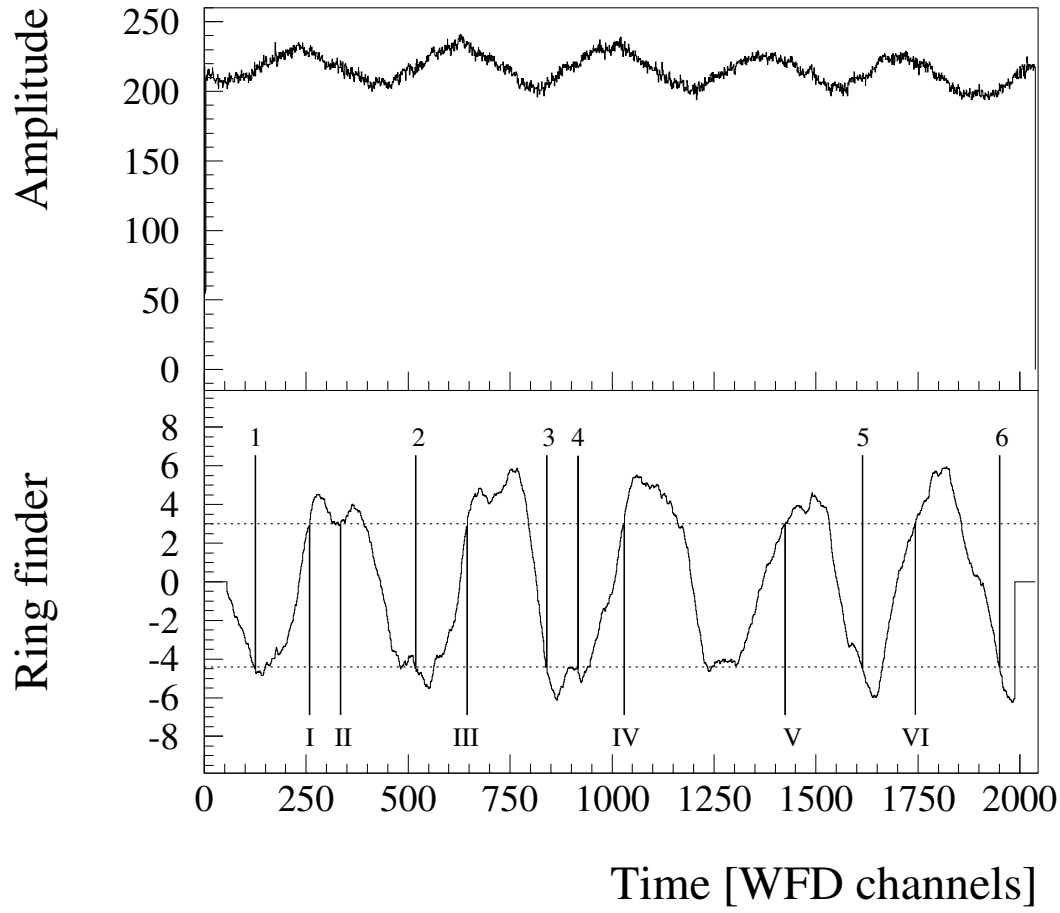

Figure 6.2: (Top) WFD spectrum classified as ringing. (Bottom) The result of the "ring finder" procedure for the spectrum shown above. For each channel, the difference between the integral of 50 channels before and 50 channels after this channel is calculated (and divided by 100). The dashed horizontal lines show the levels of Thr_pos and Thr_neg, being +3 and −4.4, respectively. Six negative–going (1–6) and six positive–going (I–VI) edges were identified. Thus, a ringing event is found and discarded.

The DC offset of each LAAPD output signal was tuned considering the baseline fluctuations, with the aim to detect the baseline of each pulse within the WFD dynamic range and to maximize the dynamic range remaining for the pulse itself. The signal amplification (as described in §5.2) was chosen so that the amplitude of a 2 keV x ray signal is ∼40. The signal amplitude is given as a unitless number between 0 and 255 (8–bit WFD). The full dynamic range available for the pulse corresponds to x–ray energies from 8 to 13 keV for various LAAPDs. Higher amplitude pulses are saturated as shown in Fig. 6.1 (d)–(g).

Apart from the relatively simple WFD spectra described above, there are also more complex ones (Fig. 6.1 (h) – (l)). The aim of the analysis is to identify them and to ensure that they do not fake the simple individual pulses. One feature observed in the WFD spectra is an overshoot, a positive–going slope, shown in Fig. 6.1 (h) resulting from crosstalk among LAAPDs. Such an overshoot in one LAAPD is present only in coincidence with a large amplitude pulse in another LAAPD. Ringing (Fig. 6.1 (i, j)) is usually present in several LAAPDs from the same side (A or B) and is attributed to a

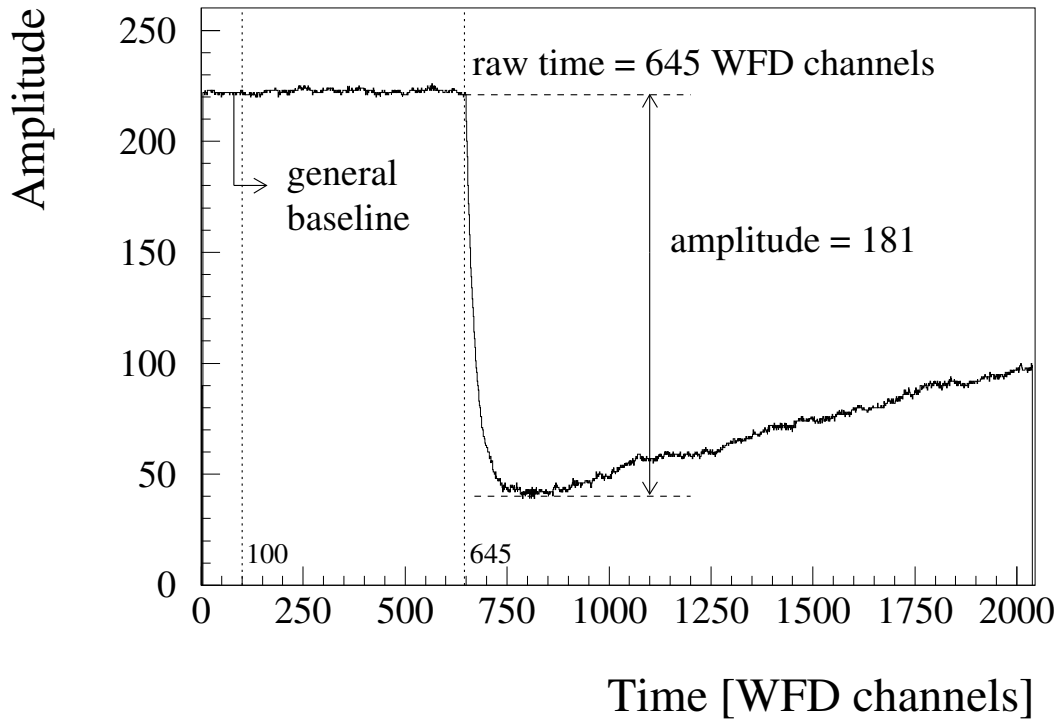

Figure 6.3: Details of a WFD spectrum. The meaning of the terms general baseline, raw time, and amplitude is shown here.

plasma discharge mainly originating from alpha particles (§4.4). The ringing occurs with a quite stable frequency with a period time of about 400 WFD channels. In some cases, however, a similar structure is also observed after a large amplitude (electron) signal. If this is the case, this structure is again present in several LAAPDs on the same side. Different disturbances can cause a real pulse to be superimposed over the more complicated baseline (Fig. 6.1 (k)). In several cases even more complicated and irregular structures are present, as shown in Fig. 6.1 (l).

The analysis of each WFD spectrum has several steps:

1. ringing detection,
2. edge identification,
3. χ^2 minimization, general baseline and standard pulse subtraction
4. repetition of steps 2 and 3 until no edge is found.

The analysis is either performed on all 2048 WFD channels, or it is stopped if and when the signal saturates. When saturation occurs in one WFD spectrum, the analysis of all spectra from the same event is stopped at the corresponding WFD channel, because there may be oscillations in several LAAPDs after a saturated signal in one diode. Here and in the following an *event* refers to all signals detected after a muon trigger, *i.e.*, within the same event gate (§5.1). This procedure is justified also by the fact that a high amplitude signal is mainly due to a muon–decay electron and after that no pulses of interest can occur. The last channel where the analysis is performed is defined as the *End_point*.

1. *Ringing detection:*
   Ringing detection and edge identification use the same procedure. The difference

between the integral of 50 channels before and 50 channels after a given channel is calculated and divided by 100. This means that for an ideal edge of amplitude 40 (typical 2 keV x ray pulse), a value $(40 \times 50)/100 = 20$ is obtained. This difference is calculated starting from channel 51 until channel (*End_point* – 50). If this difference is above a positive threshold *Thr_pos* for at least *Min_above* channels, a negative–going edge is identified and its position is defined tentatively at the first channel where the *Thr_pos* is crossed. If this difference is below a negative threshold *Thr_neg* for at least *Min_below* channels, a positive–going edge is identified and its position is defined at the first channel where the *Thr_neg* is crossed. This procedure is illustrated on an example of the ringing–detection result shown in Fig. 6.2.

The values of the parameters *Min_above* and *Min_below* are equal to 20 channels both for the ringing detection and the edge identification. In the case of ringing detection, the values of *Thr_pos* and *Thr_neg* for different LAAPDs are within the intervals from 3 to 8 and from -5 to -9, respectively (as a signal amplitude this number is also dimensionless). The optimization of these thresholds is based on the idea that their absolute value should be minimal to identify all ringing spectra, but has to be large enough that no normal pulses are considered to be ringing. A negative going edge corresponds to a normal pulse due to an x ray or an electron. The maximum possible number of pulses of our interest is three and corresponds to the physical case, that a 2 keV μp x ray, a delayed 4.9 keV μC x ray and a muon–decay electron are detected by the same LAAPD (Fig. 6.1 (g)). The maximum allowed number of positive–going edges is one, corresponding to a possible crosstalk (Fig. 6.1 (h)). Therefore, if the number of identified negative–going edges is bigger than three or the number of positive–going edges is bigger than one, the spectrum is identified as ringing and the whole event is discarded.

2. *Edge identification:*
   The next step is the edge identification, *i.e.*, a procedure to find the most probable position of a real pulse. In this case, the value of *Thr_pos* for different LAAPDs is within the interval from 7 to 12. A small value of this threshold, required for identification of pulses with minimal amplitude, is limited by the presence of irregular structures and fluctuations.

3. χ^2 *minimization, general baseline and standard pulse subtraction*

   For each edge found, a χ^2 minimization procedure is performed using a standard pulse for which optimal position and amplitude is searched. This procedure results in determination of (Fig. 6.3):

   - *raw time*, *i.e.*, the WFD channel where the pulse starts to deviate from the baseline level,
   - *raw energy*, *i.e.*, the pulse amplitude expressed by a number within the WFD dynamic range $(0 - 255)$.

   If the χ^2 minimum is found, a function composed of a "general baseline" and a "standard pulse" is subtracted from the data and the edge finding procedure is repeated. The cycle of edge identification, χ^2 minimization, and subtraction continues until no edge is found.

The general baseline is a linear function fitted to the first 100 channels of each WFD spectrum. As a standard pulse is used a standard wave form (SWF) which represents a typical LAAPD response to a 2 keV x ray. In order to construct the SWF, up to 120 clean, single 2 keV pulses were chosen for each LAAPD and for each run from a set of 27 runs spread throughout the whole data acquisition period. These pulses were aligned in time relative to each other and the contents of corresponding channels were averaged. From the averaged pulse, the SWF is produced and its amplitude is normalized to unity. The first bin of the SWF is defined as the WFD channel where the pulse amplitude starts to deviate from the baseline level. On average, this channel is ≈500, what is a typical raw time of the μp K_α x rays from the direct cascade (Fig. 6.1). The aim is, however, to define the SWF for all 2048 WFD channels. The missing channels are therefore defined by an extrapolation of the first ∼1500 channels resulting from the pulse averaging. The SWF for all 20 LAAPDs are shown in Fig. 6.4 in full size, while in Fig. 6.5 the first 100 channels are shown in detail.

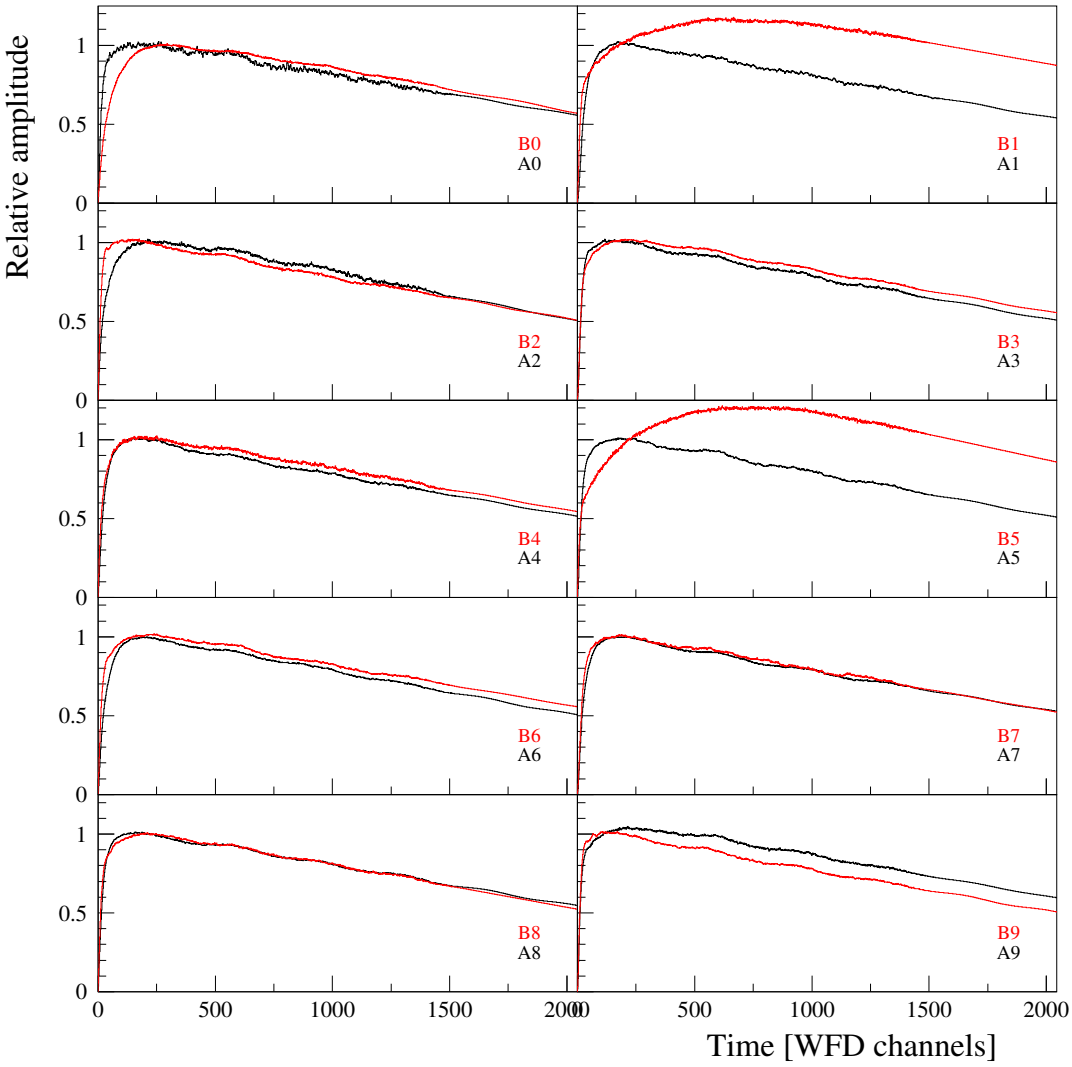

Figure 6.4: Standard wave forms for all 20 LAAPDs. The SWF is shown in all 2048 WFD channels (∼7 ns per channel).

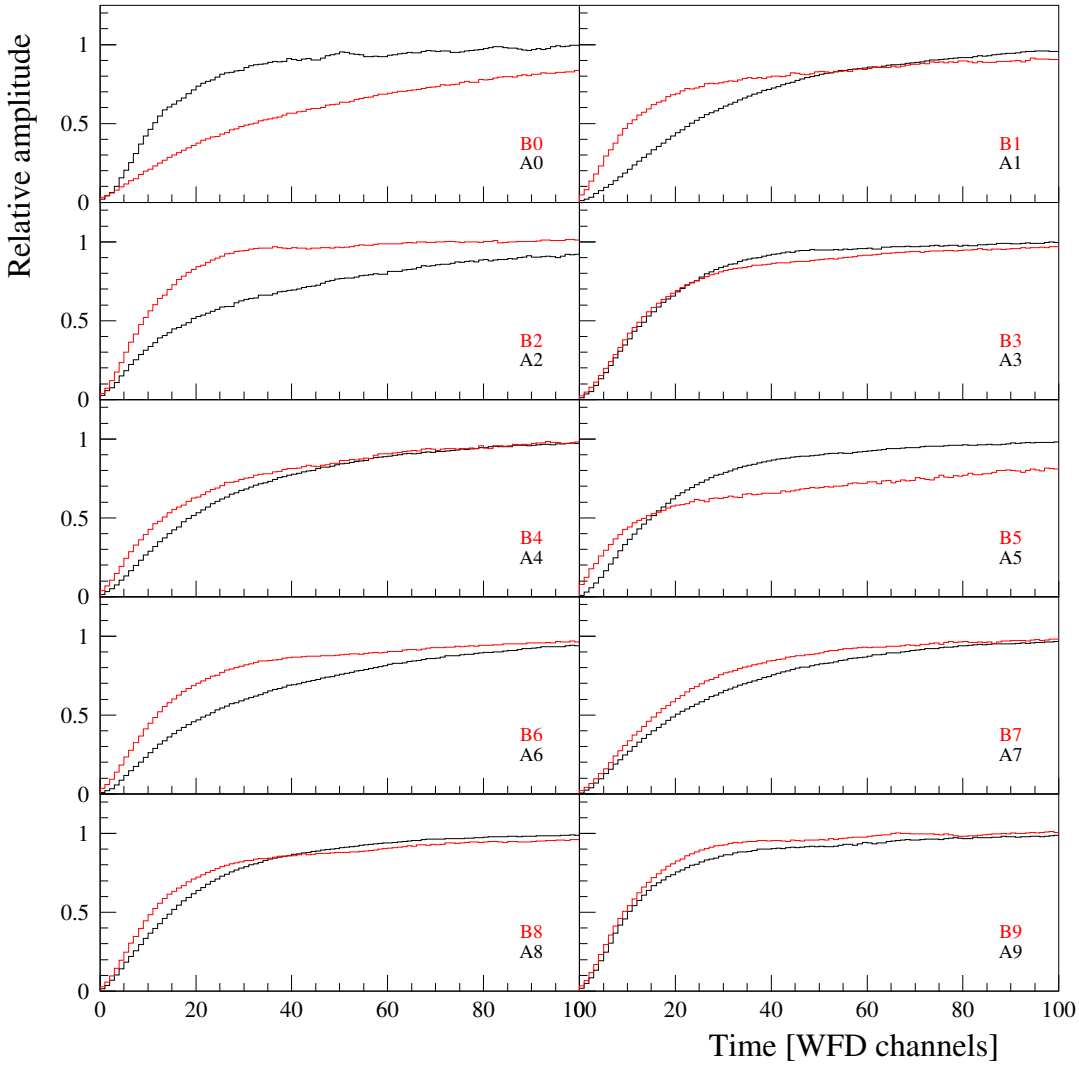

Figure 6.5: Detail of the standard wave forms for all 20 LAAPDs, shown for the first 100 WFD channels (∼7 ns per channel).

The systematic changes of the SWF in time were studied. There are two main LAAPD groups, demonstrated in Fig. 6.6 which shows the variations of the SWF for B1 and B2, as typical representatives of the two groups. Each SWF is produced for each run from the mentioned set of 27 runs. In the first group there are those LAAPDs whose SWF was very stable. This group is represented in Fig. 6.6 by the example of B2. The LAAPDs from the second group, represented by B1, have a SWF which fluctuates with time. In spite of this, it was verified that for these LAAPDs the choice of only one SWF is sufficient. In fact, the changes in time or energy resolution due to differing SWF are minimal. Changes in time and energy calibration represent no problem, since the calibration is performed on a run–by–run basis (see below).

Only the early part of the SWF is used to define a χ^2 (however, the pulse subtraction is performed from the raw–time bin until the *End_point*). The length of this early part has a direct influence on the double–pulse resolution. The probability to detect a muon–decay electron in the same LAAPD as a μp x ray is $\sim 10\%$. In the $2S - 2P$ resonance search,

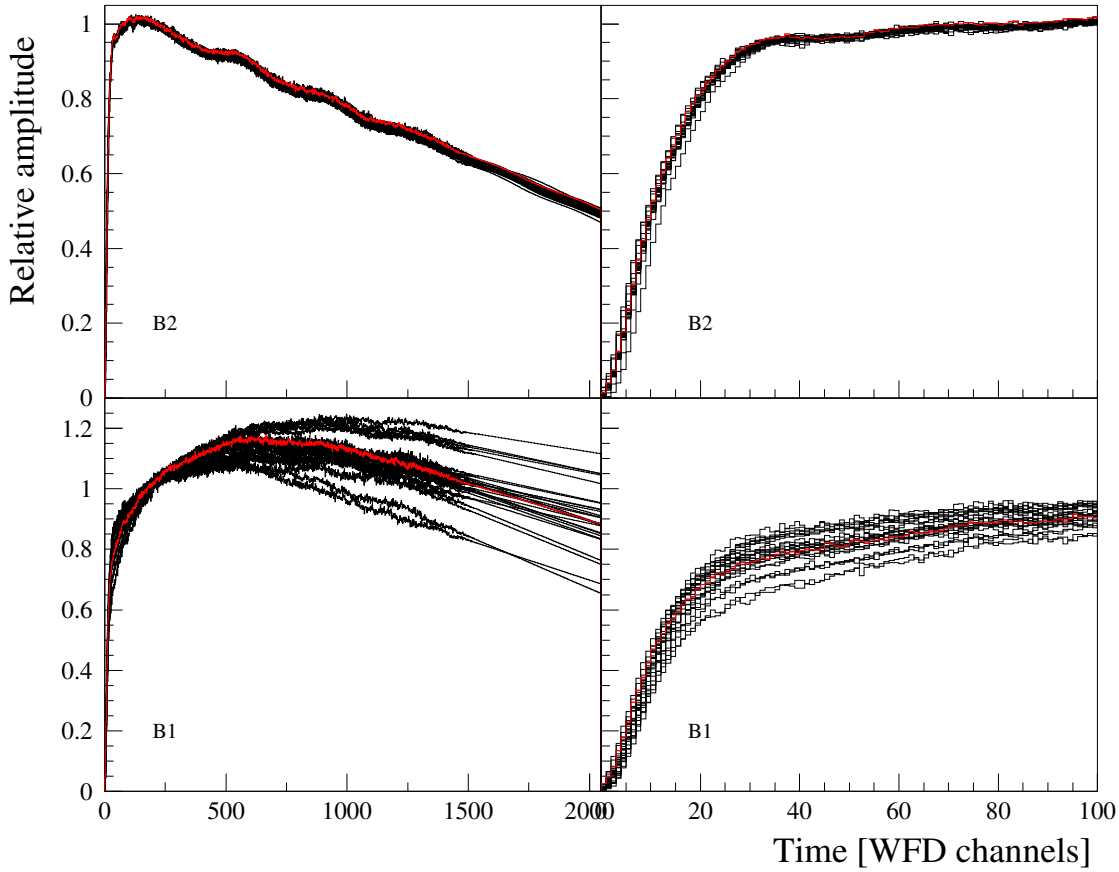

Figure 6.6: Demonstration of the SWF variation during the whole data acquisition period for LAAPDs B2 (top) and B1 (bottom). The SWF are shown in their whole length (left) and in detail for the first 100 bins (right). The SWF shown in red was used in the analysis of all data.

based on the search of rare, delayed 2 keV x rays followed by a muon–decay electron, it is important to collect all possible statistics and to analyze correctly the double pulse events. The SWF is optimized for 2 keV x rays. The fit quality for higher amplitude pulses is not optimum, but this is less important for the $2S - 2P$ experiment. Therefore, this length was set to a minimal value allowing a reasonable fit, *i.e.*, to 40 or 30 channels depending on the LAAPD quality.

For the analysis presented in §7.3, the quality of the energy spectra up to about 10 keV is more important than the double pulse resolution. Therefore, the length of the SWF considered in the χ^2 minimization was increased to 120 channels for all LAAPDs. The deviation of the pulse shape from the SWF increases with pulse amplitude. To eliminate a relatively high contribution of bad quality fits at high energies, a χ^2 cut was introduced (Fig. 6.7) and optimized for all LAAPDs individually.

The analysis of the L_{ON} events is complicated by a pickup disturbance having its origin in the excimer laser discharge (Fig. 6.8). This disturbance has the form of a wave package whose oscillations have a non–negligible amplitude with respect to the amplitude of a 2 keV x–ray signal. A correct treatment of this wave package is crucial for the analysis of laser–induced 2 keV x rays. The timing of the laser induced μp K_α x–rays as well as the wave-package timing are both determined by the laser pulse and therefore they do overlap in the WFD spectra. An approach similar to the one using the SWF for the pulse

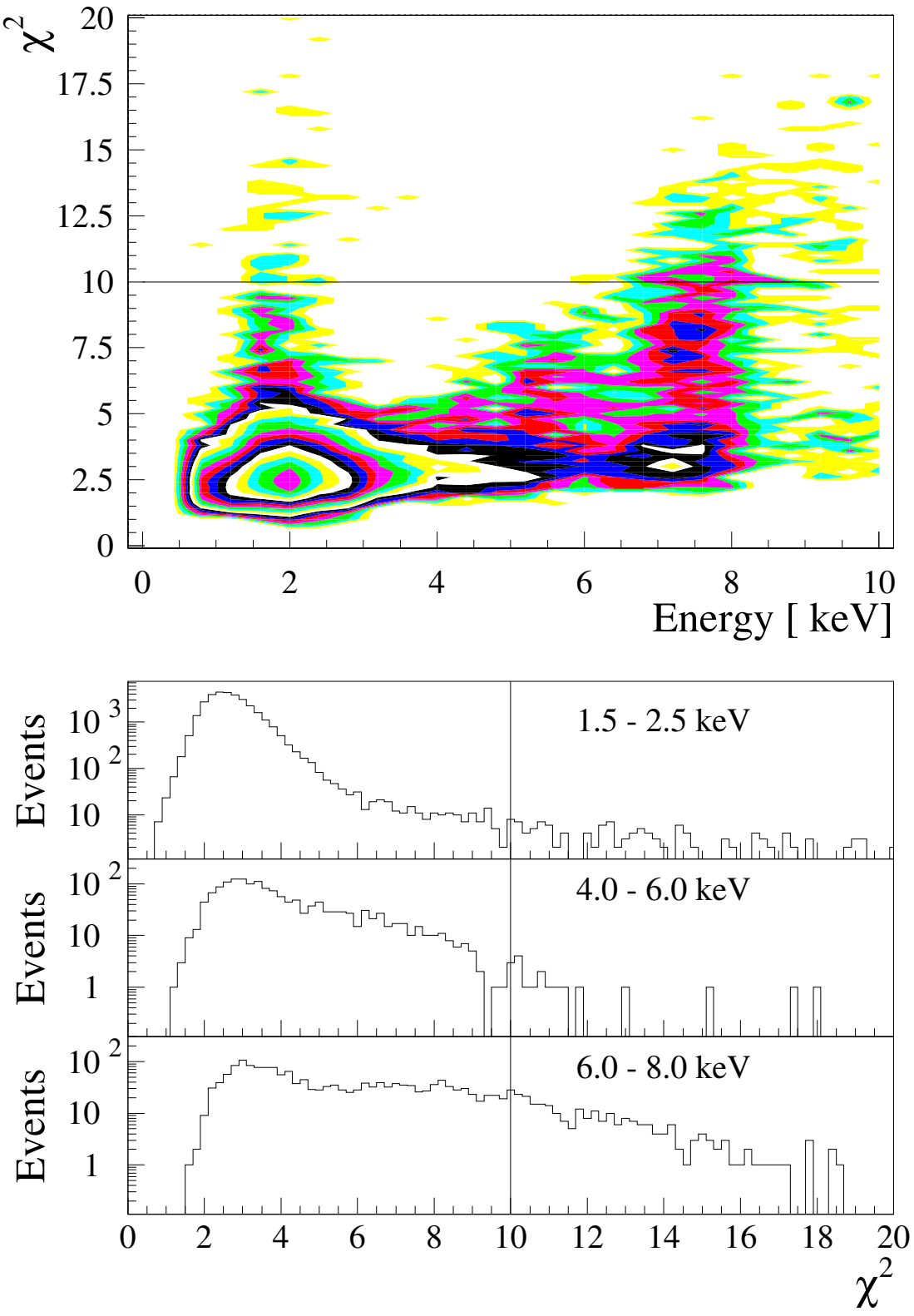

Figure 6.7: Top: Contour plot of the χ^2 versus pulse energy. The contours are in logarithmic scale. The solid line represents the χ^2 cut introduced for some parts of the analysis. Bottom: y–projections of the contour plot given on top for three energy intervals indicated on the plot. The vertical line represents the χ^2 cut.

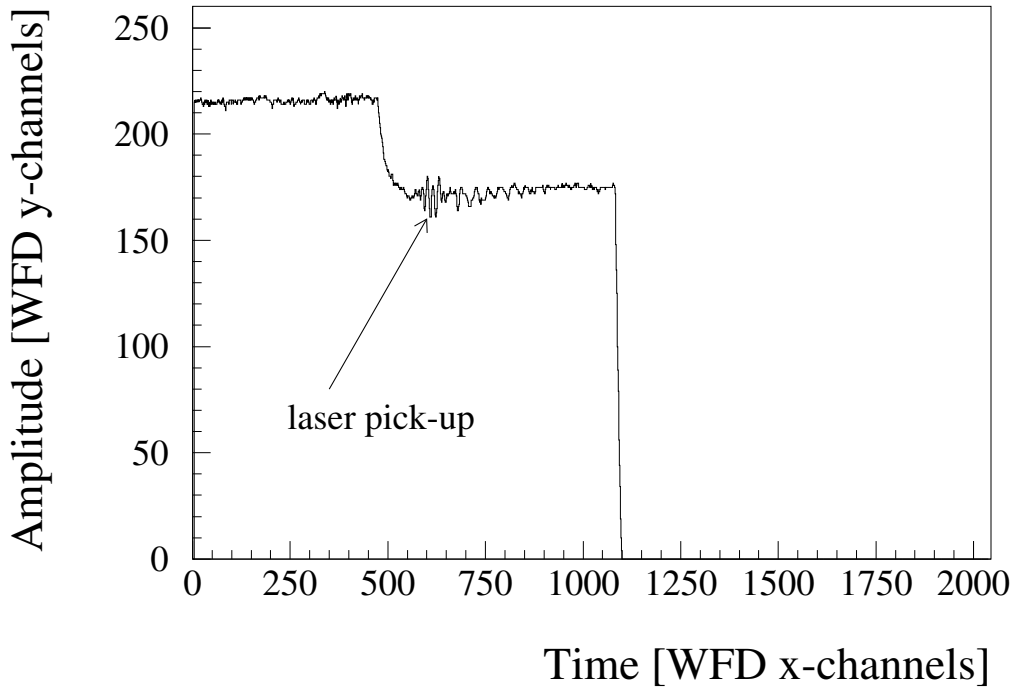

Figure 6.8: Wave form digitizer spectrum with a 1.9 keV μp x ray pulse and an electron. The spectrum is disturbed by a wave package ("wiggle") having its origin in the pick–up due to the excimer–laser discharge.

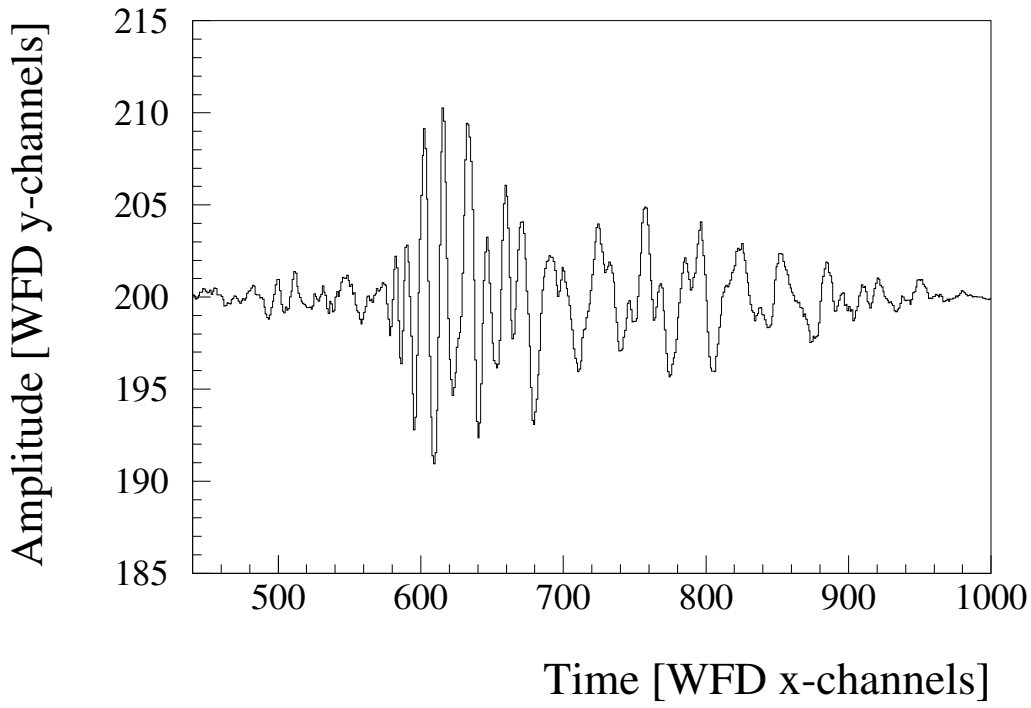

Figure 6.9: A detailed view of an example of the standard wave package used in the analysis of the L_{ON} *events. The origin of this wiggle is in the pick–up due to the excimer–laser discharge.*

subtraction was adopted. A standard wave package was produced for each L_{ON} data run by averaging the wave packages without any superimposed pulses (Fig. 6.9). The relative timing of the wave package was studied; it was found to be strongly correlated with the Dye_2 TDC hits (§§4.3 and 5.2). Therefore, on an event–by–event basis, the Dye_2 TDC hit is used to determine the timing of the standard wave package, which is subtracted from the WFD spectra of the L_{ON} events. After this subtraction, the analysis continues in the usual way as described above.

6.2 Terminology and definitions

The procedure of the data analysis is optimized for the laser experiment. In this section the crucial points in the logic of the analysis are given. The parameters and applied cuts are described in a general way. Their concrete values differ depending on the character of the required spectrum and are mentioned in the sections where the analysis results are presented.

As described in §5.1, a muon trigger opens an event gate (EVG) during which the signals from different detectors are accepted. The logic of the event classification based on the type of signals detected within this gate is described here. This procedure requires calibrated time and energy information for each signal. How the raw times and energies are transformed to calibrated values is described in §§6.3 and 6.4.

Each signal from an electron paddle EP_{left} or EP_{right}, or from the D_3^{hi} detector is considered to be an electron. The group of these three detectors is referred to as electron detectors. In reality such a signal can be produced not only by an electron, but also by gamma rays or by charged particles, not necessarily correlated with the muon triggering the DAQ system. If this is the case, the event may contribute to the background.

LAAPD pulses are considered to be either electrons or x rays, according to the following classification:

1. *LAAPD pulses in coincidence with an electron:*
   If one or several pulses from different LAAPDs are in coincidence with a signal from any of the electron detectors, their origin is attributed to the same electron, which was detected also in the LAAPDs. The width of the coincidence is defined by the parameter Δt_{same}.

2. *LAAPD pulses not in coincidence with an electron:*

   (a) *Single pulse:*
   A single pulse is categorized according to its amplitude. A pulse with an amplitude above the E_x^{low} cut and below the E_x^{hi} cut is considered as an x ray. A pulse with an amplitude above the E_x^{hi} cut is considered to be an electron, detected only in one LAAPD and not in any of the electron detectors. Pulses with an amplitude below the E_x^{low} cut are not considered in the event classification. As will be discussed in §7.2, not all event classes are included in the search for laser–induced 2 keV x rays. Their common feature is that this x ray has to be the first signal of the event. The E_x^{low} cut makes it possible to ignore small amplitude pulses occurring before a delayed 2 keV x ray. The reason for introducing this cut is the existence of signals with amplitudes corresponding to x rays with energies well below 1 keV. However, the absorption layers in front of the LAAPDs exclude the possibility to detect such low–energy

x rays (Fig. 6.24). Hence, the origin of these low amplitude pulses is not really understood. One possible explanation is that they are induced by neutrons abundant at the experimental zone.

(b) *Several pulses in coincidence:*
To this category belong pulses from different LAAPDs which are in coincidence. Again, the width of the coincidence is defined by the parameter Δt_{same}. The physical origin of these pulses cannot be an x ray, but an electron detected in several LAAPDs and not in any of the electron detectors. The amplitudes of all the pulses in coincidence are summed. If the resulting amplitude is above the $E_{\text{e}}^{\text{low}}$ threshold, the event is considered to be an electron. If this amplitude is below the $E_{\text{e}}^{\text{low}}$ threshold, the event is ignored and labeled as a "strange event".

With a small probability, a muon can be captured by a N_2 or O_2 molecule present in the gas target due to a small air leak in our setup (see Appendix B). In this case, several μN or μO x rays (§3.2) are emitted at the same time and they can be detected by several LAAPDs. In the standard analysis, these events are mostly considered to be strange events or they can masquerade as an electron. For a more detailed study of such x–ray events, a different approach is adopted. The parameter Δt_{same} is set to 0 to ensure that these events can be recognized in the classification routine as x rays. More details about the study of these x rays will be discussed in §§6.4 and 6.3.

The outcome of the WFD spectra analysis and the signal sorting described above is a set of signals labeled either as electrons or x–rays. Information about time t_{x} and energy E_{x} of each x ray comes directly from the pulse fitting procedure described in §6.1. The electron time t_{e} is defined either by the pulse fitting procedure or from a TDC hit, depending if the electron was detected in one or several LAAPDs, or in any of the electron detectors. In the case of coincident signals attributed to the detection of the same electron, the electron time t_{e} is defined by the earliest signal, regardless from which detector it originates. There is no general parameter defining the electron energy. The measured electron energies depend on how much energy an electron deposited in a certain detector. If the electron is detected in one or several LAAPDs, the energy $E_{\text{e}}^{\text{APD}}$ is defined by the amplitude of the single pulse or by the sum of the coincident–pulse amplitudes. Energies $E_{\text{e}}^{\text{E}_{\text{l}}}$, $E_{\text{e}}^{\text{E}_{\text{r}}}$, and $E_{\text{e}}^{\text{D}_3}$ are defined by the ADC data if an electron was detected in the electron paddle EP_{left}, EP_{right}, or in the D_3^{hi} detector, respectively.

All x rays and electrons detected within one EVG are ordered in time. Based on this, different event classes are defined, describing the order of x–ray and electron detection. The name of an event class contains letters x and e, standing for an x ray and an electron, respectively. The letters are ordered in time. Table 6.1 gives the relative contributions of the main event classes for the parameter values used in the search for the laser induced 2 keV x rays (§7.2). Physical meaning and acceptance of different event classes in the analysis are described together with the analysis results in Chapter 7.

In order to ensure that an x ray has its origin in a muonic atom and in this way reduce the background, the so called delayed–electron (del_e) cut is introduced. It means that after an x ray, detection of a correlated muon–decay electron is required. Parameters to optimize are the beginning t_1^{dele} and the width Δt^{dele} of a time window, defined with respect to the x ray, in which an electron signal is considered to be due to a muon–decay electron. With an ideal setup detecting all electrons with 100% probability, the efficiency

Table 6.1: Summary of the event classes and their relative contribution to the total data amount. x *and* e *stand for x ray and electron, respectively.* Δt_{same} *= 100 ns,* $E_{\mathrm{x}}^{\mathrm{low}}$ *= 1 keV,* $E_{\mathrm{x}}^{\mathrm{hi}}$ *= 6 keV and* $E_{\mathrm{e}}^{\mathrm{low}}$ *= 6 keV.*

Event class	Relative contribution [%]
xe	12.2
xx	0.1
xee	0.9
xxe	0.1
x	7.6
e	69.6
ee	8.2
eee	0.3
ex	0.2
exe	0.1
Sum	99.3

$\varepsilon^{\mathrm{dele}}$ to detect a muon–decay electron can be expressed as

$$\varepsilon^{\mathrm{dele}}(t_1^{\mathrm{dele}}, \Delta t^{\mathrm{dele}}) = e^{-\lambda t_1^{\mathrm{dele}}} \left(1 - e^{-\lambda \Delta t^{\mathrm{dele}}}\right) , \tag{6.1}$$

where λ is the muon decay constant. The parameter t_1^{dele} must always be bigger than the parameter Δt_{same}. Increasing the width Δt^{dele} increases the probability to detect a muon–decay electron, but also the probability to detect an uncorrelated, in time equally distributed, background event. The spectra in Fig. 6.10 demonstrate and clarify the the parameters t_1^{dele}, Δt^{dele}, and Δt_{same}.

There is also a probability that during an EVG a second muon enters the target, leading to the formation of a μp atom and x ray emission. In the following, such a muon is called *second muon*, while a muon opening the EVG is called *first muon*. The timing of the second muon μp x rays is not correlated with the first, but the second muon, and the probability to detect this x ray is nearly constant during the EVG. This process is a source of dangerous background, since it can mimic a laser induced μp K_α x ray. In order to suppress this effect, a second muon ($\mu^{2\mathrm{nd}}$) cut is introduced.

The time difference between the muon detection in S_1 and the μp x ray emission is independent on the fact if this muon did or did not open an EVG. The time difference $t_{\mathrm{x-S1}}$ is defined by

$$t_{\mathrm{x-S1}} = t_{\mathrm{x}}(2\,\mathrm{keV}) - t_{\mathrm{S1}} , \tag{6.2}$$

where $t_{\mathrm{x}}(2\,\mathrm{keV})$ is the time of a 2 keV x ray from a direct μp cascade and t_{S1} is the time when the muon creating this μp atom was detected by the S_1 detector. For the first muon, t_{S1} is defined by the S_1 TDC and the first hit of the S_1 PTDC (§5.2). The distribution of the $t_{\mathrm{x-S1}}$ time differences is measured by a huge statistics of x rays from the first muon μp atoms and is within the time interval from 440 to 950 ns. The second muon t_{S1} can be recorded by the second or later hit of the S_1 PTDC. Therefore, the time difference defined by Eq. (6.2) is calculated for all x rays and all second and later S_1 PTDC hits. If this time difference is within the interval from 440 to 950 ns and t_{S1} is larger than a time threshold $t_{S1}^{\mu 1}$, the x ray is considered to be due to a second muon stop and the whole event is rejected. The $t_{S1}^{\mu 1}$ threshold is chosen to be later than the time of the after–pulses

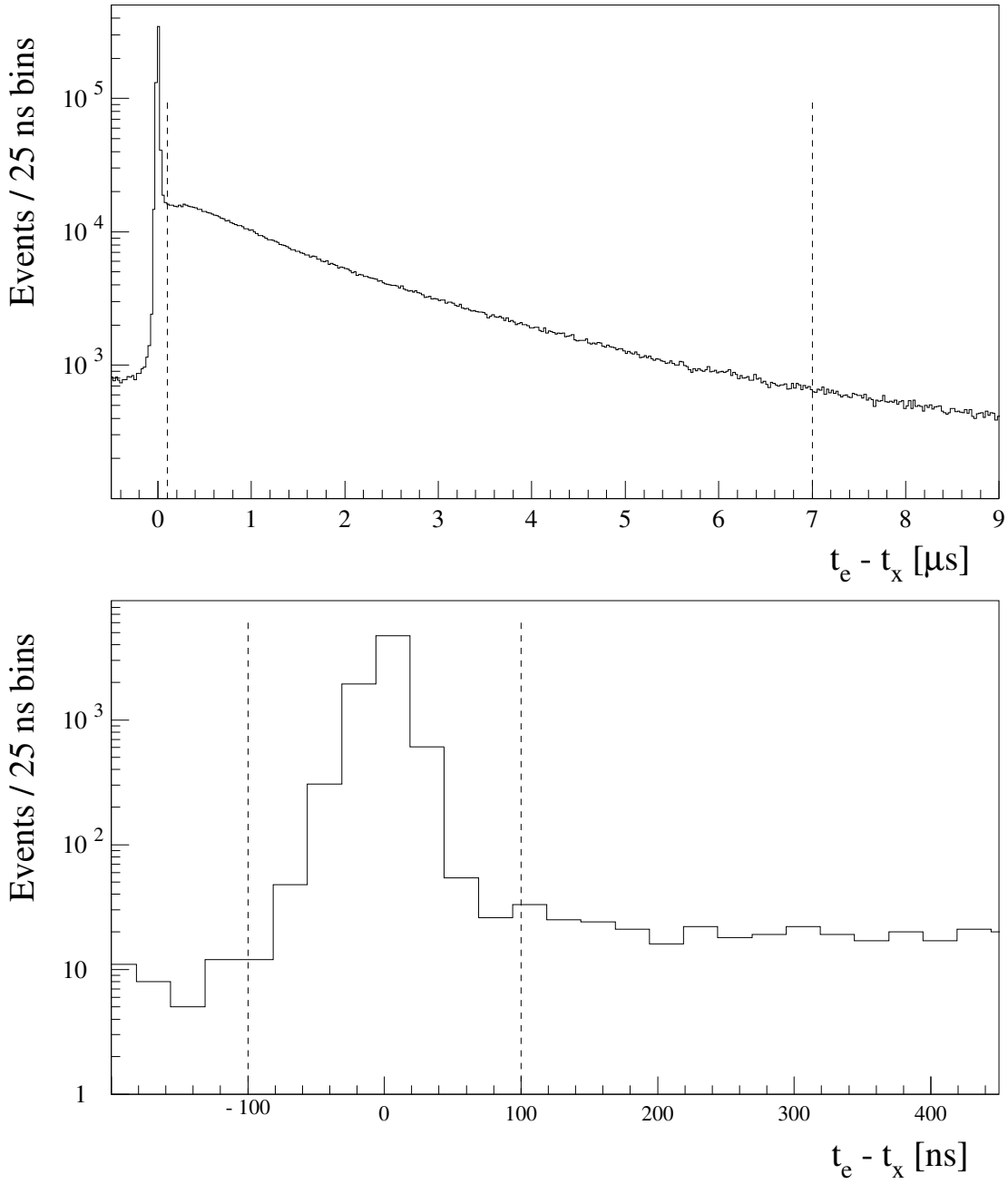

Figure 6.10: For events when both an electron and an x ray were detected, the time difference $t_e - t_x$ is plotted, i.e., the time 0 represents the time of x–ray detection. The spectra are constructed with the parameter Δt_{same}= 0, no del_e *cut is applied. Top: The sharp peak at time 0 is due to the electrons detected at least in two detectors; once also in an LAAPD, where the electron deposited an energy below the E_x^{hi} threshold, and therefore was considered as an x ray. The two dashed lines demonstrate an example of the* del_e *cut time window. The line at 0.1 μs represents the parameter t_1^{dele}, while the distance between the two lines the parameter Δt^{dele}. Bottom: Detail of the peak at time 0 shown only for events with an x ray energy E_x in the interval $1.7 - 2.1$ keV (details about the energy calibration in §6.4) and t_x later than* early *signals due to the 1^{st}–muon stops (details about the time calibration in §6.3.1). The two lines at −100 and 100 ns are to justify the value of the parameter Δt_{same}= 100 ns, used in the standard analysis procedure requiring a strict selection between x rays and electrons (Chapter 7).*

following the majority of the first–muon S_1 pulses. The efficiency of the μ^{2nd} cut is thus given by the S_1 efficiency (about 80%) and is demonstrated in Fig. 6.11. Other details, as the time and energy calibrations and the presence of a 4.9 keV μC peak will be discussed in the following Sections.

Analogous to the S_1 detector, also the S_2 detector could be used. However, this possibility is disabled due to a large excimer–laser pickup noise on the S_2 signal. On the other hand, a possible improvement of the μ^{2nd} cut would be limited by the S_2 muon detection efficiency being about 40%.

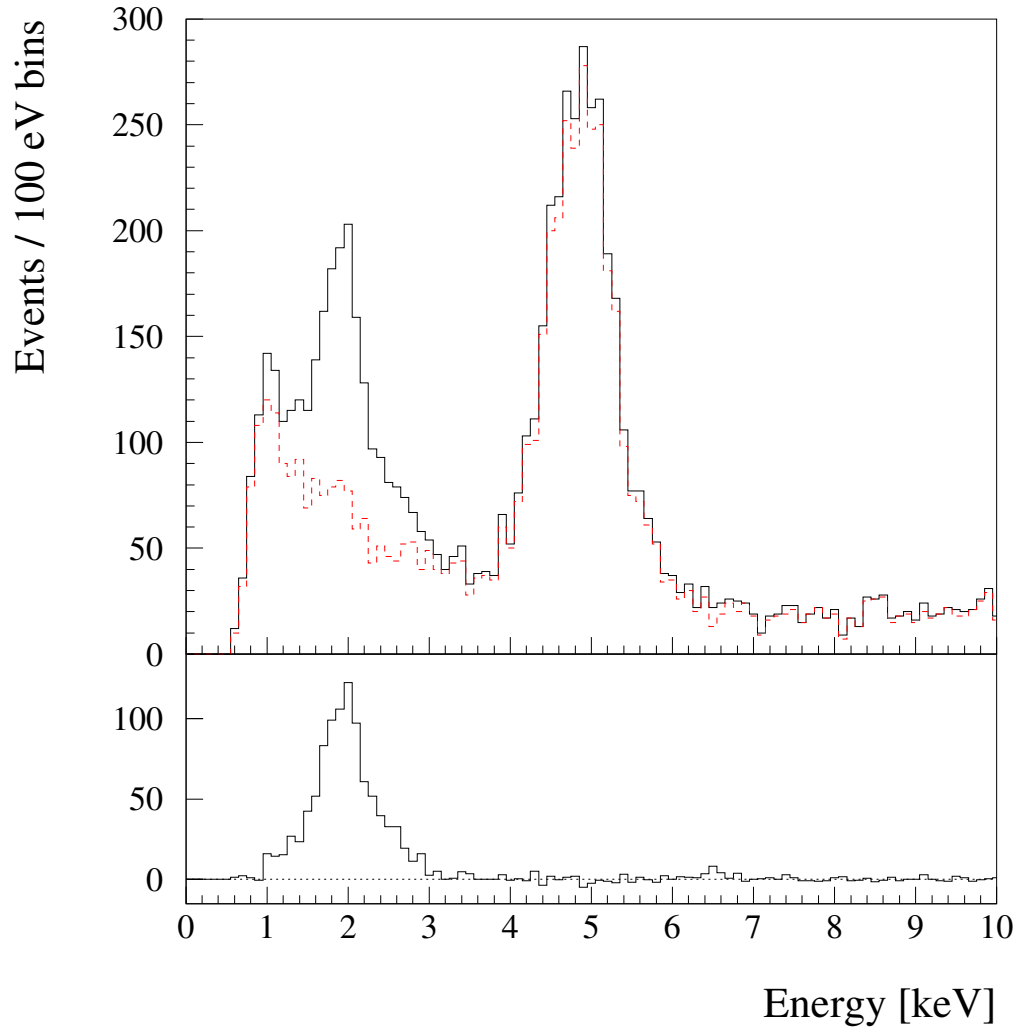

Figure 6.11: Demonstration of the μ^{2nd} cut efficiency. Top: energy spectra of x rays with t_x later than first–muon μp x rays. Each accepted x ray is the first signal within the EVG. The del_e *cut is applied with $t_1^{dele} = 100$ ns, $\Delta t^{dele} = 7$ μs; solid black and dashed red spectrum are without and with the μ^{2nd} cut, respectively. The 2 keV peak is due to the second–muon μp x rays. Bottom: the difference of the black and the red spectra shown in the top part normalized in a way that the 4.9 keV μC peak disappears.*

6.3 Time calibration

6.3.1 Relative and absolute timing of various detectors

The relative timing among the LAAPDs and the electron detectors is defined with respect to the EP_{left} detector. This is possible because some muon–decay electrons create physical coincidences in the LAAPDs and the electron detectors. The 5 Tesla magnetic field forces the electrons to spiral and causes a strong correlation between the A side LAAPDs, and the EP_{left} detector, and between the B side LAAPDs, and the EP_{right} detector (as will be described later, see Fig. 6.27). The following histograms of these time differences are produced:

1. for each A side LAAPD, the time of a large amplitude pulse minus the EP_{left} time,
2. for each B side LAAPD, the time of a large amplitude pulse minus the EP_{right} time,
3. EP_{right}- EP_{left} times.

The peaks in these spectra, which are due to physical coincidences, are fitted by Gaussian functions. For the first two items, a typical FWHM value is about 20 ns, with one extreme case of 37 ns; for the third item, the fitted Gaussian function has a FWHM of 17.5 ns. The LAAPDs and EP_{right} raw times are adjusted by offsets in a way that the peaks in these spectra are centered at zero. This time calibration is done for each run,

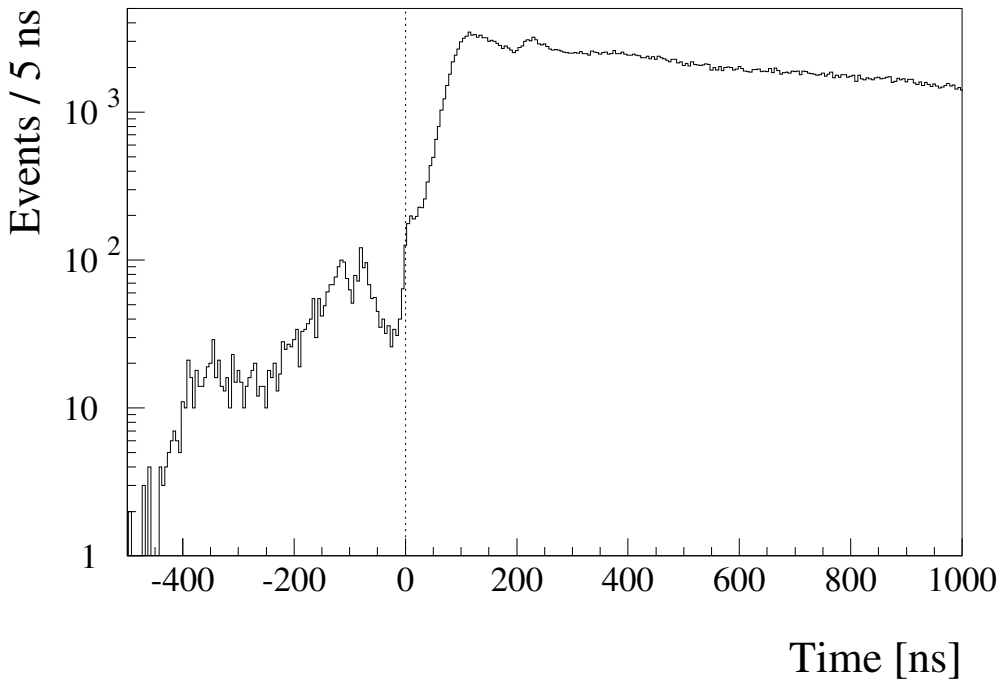

Figure 6.12: Time spectrum of the electrons (event class e) detected in the LAAPDs AB9. The time zero corresponds to the time when the muon is passing the S_2 foil; it can be deduced due to the detection of the muon–decay electrons from the muons stopped in the S_2 foil (sharp edge in the time spectrum marked by a dotted line). The structures at negative times are not fully understood; the origin of the earliest peak can probably be attributed to the muon–decay electrons from the muons stopping in the S_1 foils. The double–peak structure at times ≈100 – 300 ns is due to the muons decaying in flight within the solid angle of the LAAPDs AB9 (§7.1).

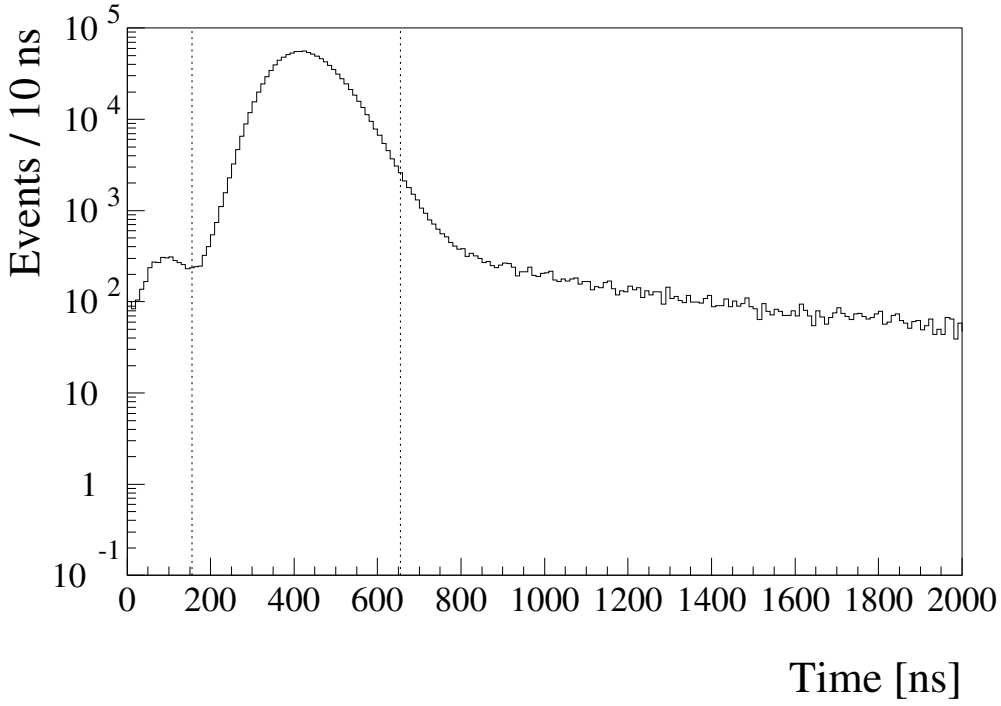

Figure 6.13: Time spectrum of the μp K–series x rays for the sum of the best LAAPDs*(§6.4). No* del_e *cut is applied, each accepted x ray has to be the first signal after the muon trigger. The width of the peak is dominated by the muon stop–time distribution. The two vertical lines show the time interval of early events (t_x from 155 to 655 ns).*

provided it has sufficient statistics in order to perform the fit. For lower statistics runs, the time calibration from the previous high statistics run is adopted.

In order to determine the absolute timing, a time zero has to be defined: it corresponds to the time when a muon is passing the S_2 foil, *i.e.*, the time giving a trigger signal (Fig. 5.1, page 43). The value of the corresponding additional offset for all relatively aligned time spectra is obtained from the LAAPD electron time spectra in which the muon–decay electrons from the muons stopped in the S_2 foil define a sharp edge (Fig. 6.12). The electron time–of–flight from S_2 to LAAPDs AB9 is $1-2$ ns, *i.e.*, negligible. The definition of the absolute timing is important in order to study the slowing down and stop–time distribution of the muons, as described in §7.1. It should be stressed out that the choice of the absolute timing has no influence on the results of the analysis presented in §§7.2 and 7.3. For consistency, all times given in this thesis are corrected for the time zero value (unless explicitly specified the contrary).

Some types of the analysis require studying only signals with specific timing, *e.g.*, with t_x and/or t_e from a certain interval. The concrete values of the applied time cuts are mentioned in the specific sections where the analysis results are described.

Early signals are those with the same timing as x rays from the direct muon cascade. The majority of these early events is represented by the 2 keV first–muon μp x rays. We did not use the term *prompt* because these early signals do not appear immediately after a muon trigger, but only a few hundred nanoseconds later. The width of their time interval is defined by the muon stop time distribution (§7.1) and is about 500 ns. The time cut applied for the early events is therefore from 155 to 655 ns (Fig. 6.13). The term delayed signals is used for the signals which occur later than the early ones, *i.e.*, at times

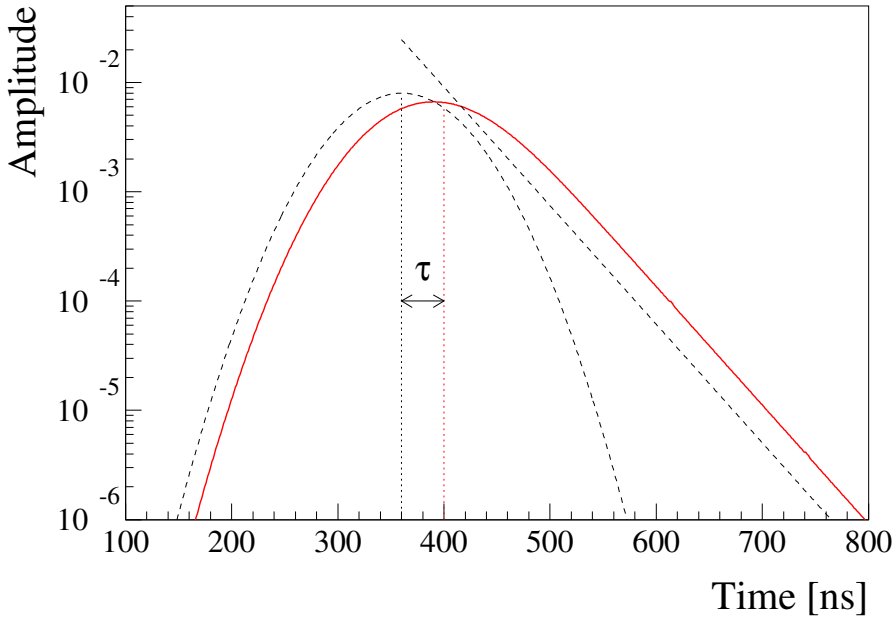

Figure 6.14: Example of a convolution (solid line) of a Gaussian ($c = 360$ ns, $\sigma = 50$ ns) with the Exp function defined in Eq. (6.4) ($\tau = 40$ ns). The original Gaussian and Exp functions are plotted with dashed lines; the position of the Exp function is shifted by +360 ns in order to demonstrate that it defines the right–hand side slope of the convolution. Dotted lines represent the positions of the centers of gravity of the Gaussian and convolution, shifted by the value τ.

when the direct muon cascade is finished.

The early–signal peak present in the μp x–ray time spectra is asymmetric with a tail towards later times (Fig. 6.13). Similar asymmetric structures are present in the majority of the studied time spectra. As fit function of such asymmetric peaks a convolution of two functions f_1 and f_2 is used, defined as:

$$(f_1 \otimes f_2)(t) = \int_{-\infty}^{\infty} f_1(t - t')\ f_2\left(t'\right) \quad dt' \,, \tag{6.3}$$

where t is the time t_x or t_e, depending on which kind of time–spectra is analyzed, and t' is an integration parameter. Both f_1 and f_2 functions are normalized to unity, and therefore also the resulting convolution is normalized to unity.

As the function f_1, an exponential function multiplied by a step function is used:

$$f_1(t;\tau) = Exp\,(t;\tau) = Step(t)\ \frac{1}{\tau}\ \exp\left(-\frac{t}{\tau}\right) , \tag{6.4}$$

where *Step* is defined as

$$Step(t) = 0 \quad (t < 0) \quad \text{and} \quad Step(t) = 1 \quad (t \geq 0)\,. \tag{6.5}$$

A Gaussian with centroid c and standard deviation σ is used as function f_2:

$$f_2 = Gauss(t; c, \sigma) = \frac{1}{\sqrt{2\pi\sigma^2}}\ \exp\left(-\frac{(t-c)^2}{2\sigma^2}\right) . \tag{6.6}$$

In some cases, f_2 is a Gaussian already convoluted with an exponential *Exp*. The parameter values for f_1 and f_2 are given in the sections dedicated to the analysis results.

An example of a convolution of a Gaussian with an Exp exponential is given in Fig. 6.14. The shape of the left–hand side of the convolution is given by the f_2 function, while the right–hand side is dominated by the slope defined by the exponential. The center of gravity cg of a function $f(t)$ defined on a time interval from t_1 to t_2 is

$$cg = \frac{\int_{t_1}^{t_2} t\ f(t)dt}{\int_{t_1}^{t_2} f(t)dt}\,. \tag{6.7}$$

The cg of the convolution is shifted by τ with respect to the cg of the f_2 function, which in case of a Gaussian is equal to its centroid c.

6.3.2 Energy dependence of the LAAPD timing

The relative x–ray timing is checked on the x rays from the direct muon cascade in μN and μO atoms (§3.2, Table 3.3, page 27). The time difference between the x rays from the latest stages of the direct cascade (from the radiative transitions) are of the order of a few ps, *i.e.*, negligibly small. There is an appreciable probability that two or more x rays from the same muonic cascade were detected in the 20 LAAPDs. For a setup with time resolution of several ns, they represent physical coincidences. In the following they are referred to as *coincidence x rays* and their time or energy spectra as *coincidence spectra*. Some details about the method how these x rays are recognized are given in the following section. At this point some notes about their relative timing are given.

There are the three most intense $\Delta n = 1$ transitions with energies below 10 keV both for μN and μO atoms (Table 3.3, page 27). Therefore, six spectra of time differences between the six pairs of *coincidence x rays* (3 pairs for μN and 3 pairs for μO) were constructed. Each spectrum contains one peak. The FWHM of these peaks is in the range from 42 to 52 ns, which corresponds to a σ of $18 - 22$ ns. These are quadratic sums

$$\sigma = \sqrt{\left(\sigma^2(E_{\rm x}^i) + \sigma^2(E_{\rm x}^j)\right)} \tag{6.8}$$

of the corresponding LAAPD time resolutions $\sigma(E_{\rm x}^{i,j})$ at energies $E_{\rm x}^{i,j}$. The resulting values are in the range $\sigma(E_{\rm x}^i) = 12$ to 16 ns (FWHM = 28 to 38 ns), with relatively large statistical uncertainties. It was found that the center of gravity of each peak is shifted from the expected value of zero by several ns (from 5 to 13 ns), depending on the x–ray energy. In spite of the limited statistics of the *coincidence x rays* (with an applied del_e cut, each peak contains about 100 events, with one exception containing 1100 events), a systematic effect can be seen. The results are summarized in Fig. 6.15. Inconsistencies between various pairs on the level of 4 ns are attributed to statistical fluctuations. The precise timing of the LAAPD x–ray signal depends on the x–ray energy. The interaction between an x ray and LAAPD (containing mainly Si) is influenced by the x–ray attenuation length in Si ($\lambda_{\rm Si}$, Eq. (6.15), page 76), which is a function of the x–ray energy and has a discontinuity at 1.839 keV (Si K–edge). This will be discussed in more details in §6.4, since it has an important effect on the peak shape of the x–ray energy spectrum and causes deviations from linearity for the energy calibration.

In practice, only the time differences between the μN$(5 \rightarrow 4)$ line at 3.1 keV and the μp K–series lines at $1.9 - 2.45$ keV are relevant for the data analysis. As an example, $\Delta t(1.9\text{ keV} - 3.1\text{ keV}) = (3 \pm 4)$ ns is deduced from Fig. 6.15.

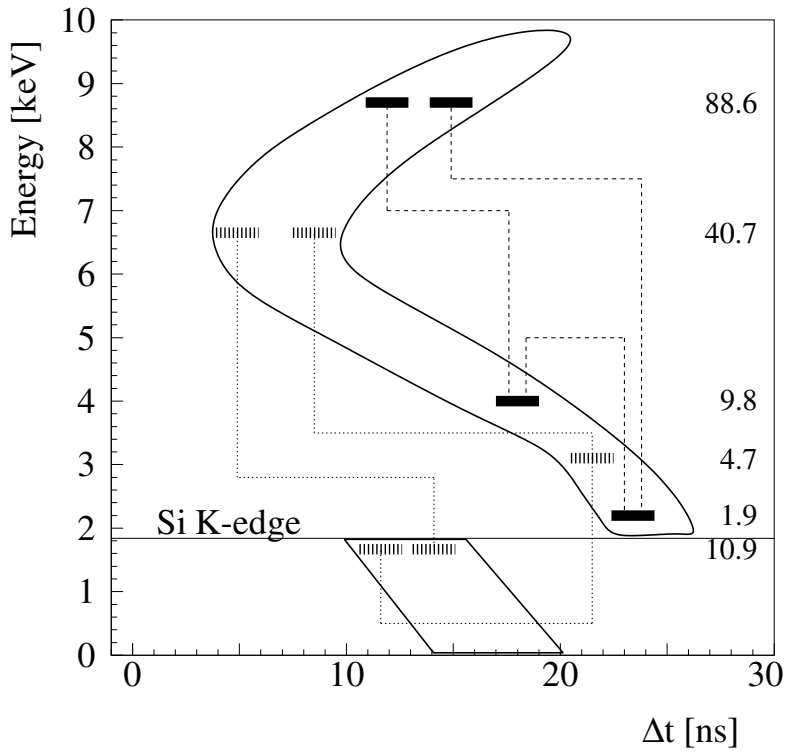

Figure 6.15: The timing of an x–ray signal in the LAAPD depends on the energy of the incident x ray; it is found by studying the time differences between the six pairs (each pair indicated by a dotted line) of μN (striped blocks) and μO (solid blocks) physically coincident x rays. The x–axis indicates the time difference between the times t_x of these x rays, the y–axis shows the x–ray energy. The numbers at the right–hand side are the values of the x–ray attenuation length in Si, λ_{Si}, given in μm. The solid horizontal line at 1.839 keV demonstrates the energy of the K–edge in Si. The intense solid line shows an approximate shape of the newly found systematic effect.

6.3.3 Timing of the LAAPD signals relative to the laser pulse

In the search for the $2S-2P$ resonance it is important to know the time of the laser–pulse arrival in the mirror cavity. For this purpose special calibration data L_{CAL} were taken (§5.3). The timing of the laser pulse, dominated by the internal delay of the excimer laser, was not stable during the data taking period, as demonstrated in Fig. 6.16. Therefore, the laser arrival time has to be defined for each L_{ON} event separately (details in §7.2). For this purpose it is important to determine the Δt_{V_2} time offset between the time when the red laser light used in the calibration measurement (and having the same timing as the 6 μm laser) is detected by an LAAPD and the V_2 TDC signal. For each LAAPD such a time difference spectrum is created and the peak is fitted with a Gaussian function. The laser arrival time t_{laser} is defined as

$$t_{laser} = t_{V_2} + \Delta t_{V_2} \,. \tag{6.9}$$

The Δt_{V_2} delay is therefore obtained for each LAAPD, having a mean value of ~ 770 ns. The average value of t_{V_2} is about 1250 ns (Fig. 6.16). Therefore, the average value of t_{laser} is about (1250+770) = 2020 ns (which is the beginning of the laser time window shown in Fig. 7.15, page 111). For 12 LAAPDs the Δt_{V_2} value differs from the average

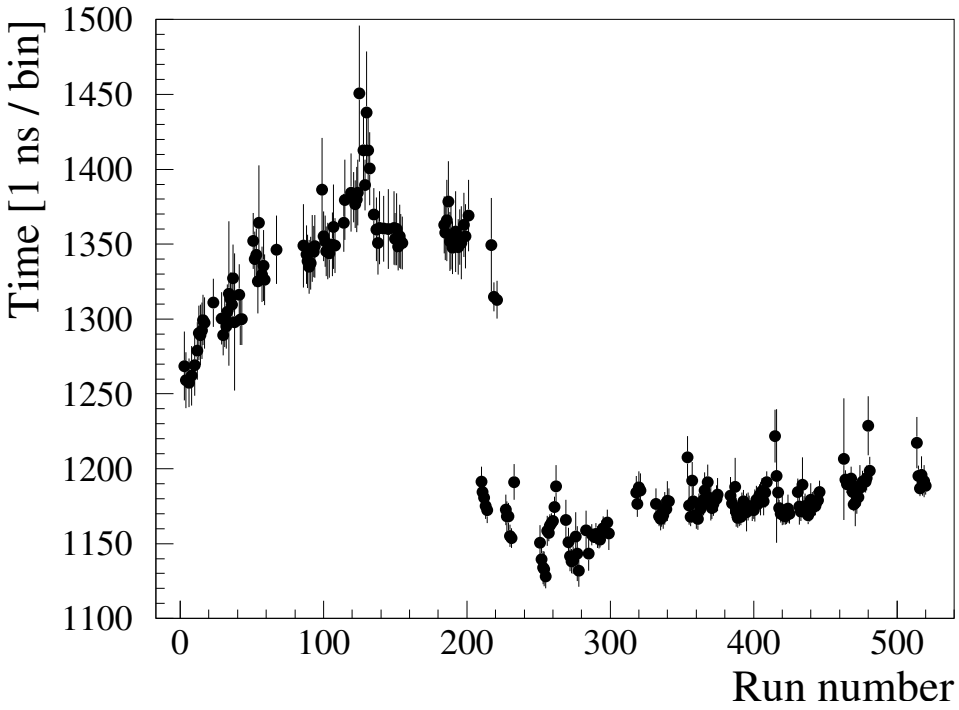

Figure 6.16: Timing of the V_2 *laser signal* (t_{V_2}) *as a function of run number. Each point represents a mean value for one run. In the middle of the data taking period the internal delay of the excimer laser was reduced by* $\sim$ *200 ns.*

value by ± 10 ns, for another six diodes by less than ± 15 ns, and for the remaining two cases it is 18 and 29 ns. The reason why these values are different from zero is that the relative time calibration between the LAAPDs is based on high–amplitude electron signals (as described above in §6.3.1). However, the SWF used to fit the signals with all amplitudes is optimized for 2 keV signals which causes small systematic deviations of the electron times (which are acceptable for the laser experiment).

6.4 LAAPD energy calibration and x ray energy spectra

The LAAPD energy calibration is performed on a run by run basis analogous to the time calibration. Its aim is to determine for each LAAPD the parameters *Slope* and *Offset* in the linear equation

$$E_{\mathrm{x}} = \mathit{Slope} \times A_{\mathrm{WFD}} + \mathit{Offset}\,, \tag{6.10}$$

where A_{WFD} is the pulse amplitude (a number between 0 and 255) and E_{x} is the corresponding x–ray energy expressed in keV.

In the search for laser–induced delayed μp K_α x rays, the energy calibration is based on the early μp K_α x–ray peak. Only the xe event class is considered, with the del_e cut parameters $t_1^{\mathrm{dele}} = 100$ ns, $\Delta t^{\mathrm{dele}} = 7$ μs. The *Offset* parameter is defined to be zero. This calibration is sufficient for the experiment counting the number of x rays with the same E_{x} that is the one of x rays determining the energy calibration. The raw energy spectrum of early signals is fitted in the interval from 1.2 to 4 keV with a function defined as the sum of five peaks (μp K_α, K_β, K_{rest} and μN$(5 \rightarrow 4)$ and $(6 \rightarrow 5)$ lines), together with a flat background.

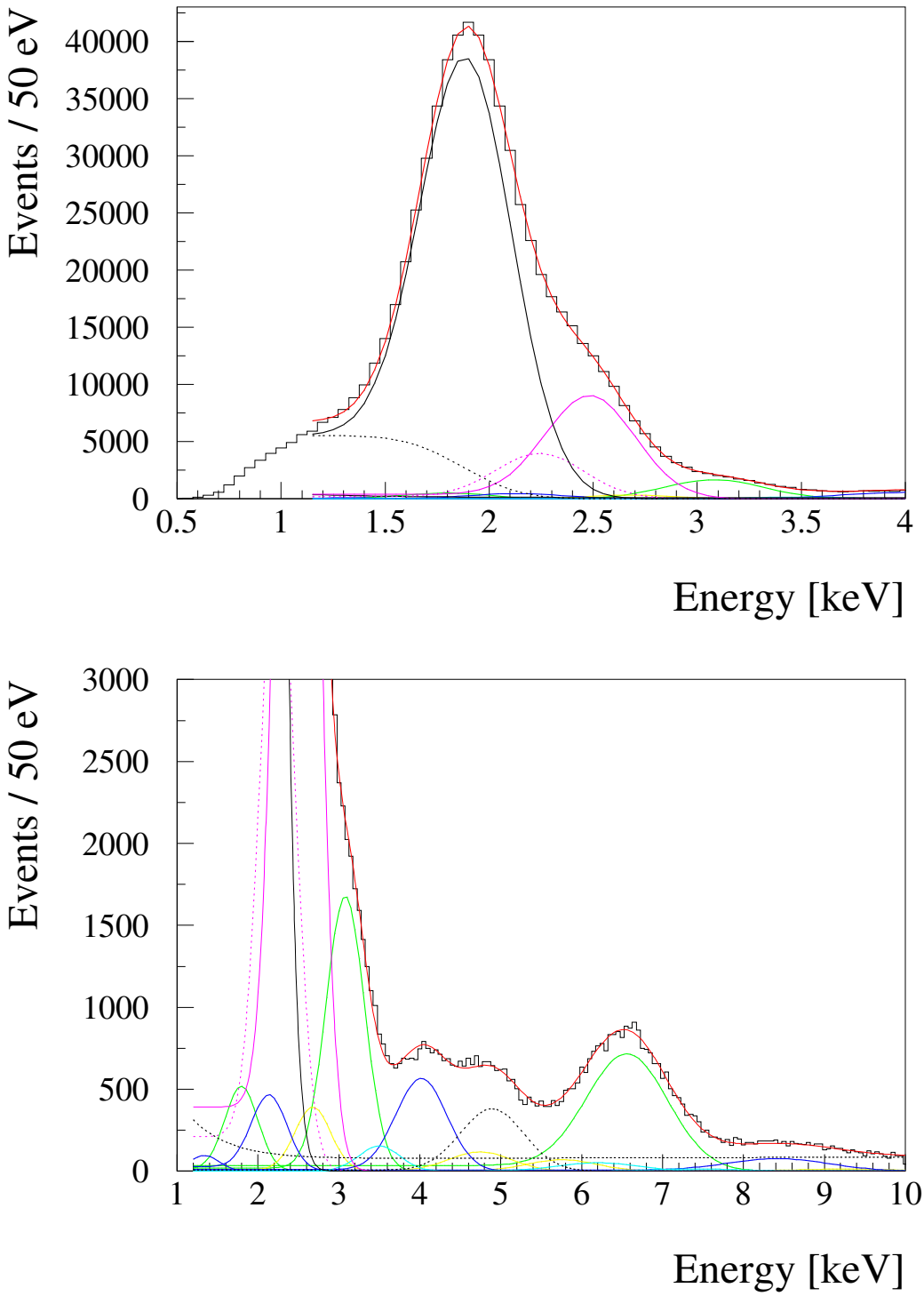

Figure 6.17: Calibrated energy spectrum of the early *signals ($t_x = 155 - 655$ ns) with a* del_e *cut, shown up to 4 keV (top) and with a reduced y–scale up to 10 keV (bottom). Only the* best LAAPDs *(page 73) are considered. The total fit function is in red. Other lines: μp K_α (solid black; its low–energy tail is shown by a black dotted line in top figure), μp K_β (dashed magenta), μp K_{rest} (solid magenta), $\Delta n = 1$ and $\Delta n > 1$ μN transitions (green and yellow, respectively), $\Delta n = 1$ and $\Delta n > 1$ μO transitions (blue and cyan, respectively), μC($4 \rightarrow 3$) (dotted black), background (dashed black).*

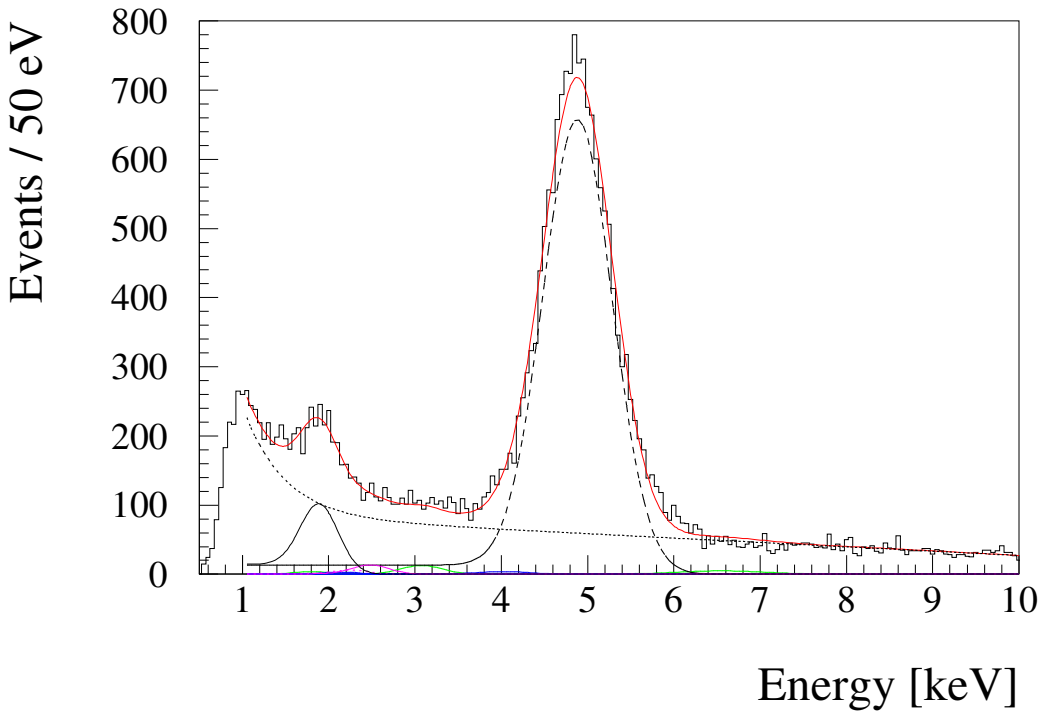

Figure 6.18: Calibrated energy spectrum of the delayed *x rays (t_x from 755 to 1955 ns) with a* del_e *cut. The μ^{2nd} cut is not applied. The total fit function is shown in red. Other lines: μC($4 \rightarrow 3$) (dashed black), μp K_α (solid black), μp K_β and K_{rest} (magenta), μN lines (green), μO lines (blue), background (dotted black).*

For other types of the analysis requiring more precise calibration at energies up to 10 keV, a different method is applied. Introducing the χ^2 cut and a longer fit–part of the SWF as described above in §6.1 improves the quality of the higher energy spectra. The 4.89 keV μC($4 \rightarrow 3$) line is included in the energy calibration and both parameters *Slope* and *Offset* from Eq. (6.9) are determined for each LAAPD. The raw energy spectrum of the early signals is produced and fit in the same way as described above. Additionally, a raw energy spectrum dominated by the μC peak is produced, considering only the delayed signals with a time cut from 755 to 1955 ns. Again, only the xe event class is considered, with the del_e cut parameters $t_1^{dele} = 200$ ns and $\Delta t^{dele} = 3$ μs. This spectrum is fit in the interval from 3 to 6.5 keV with a function defined as the sum of a μC($4 \rightarrow 3$) peak and a flat background.

The calibration was rechecked and refined in several stages during the analysis. The final calibrated energy spectra of the early and delayed x rays fitted up to 10 keV are shown in Figs. 6.17 and 6.18, respectively, for the sum of the best LAAPDs. The term best LAAPDs refers here and below always to the same group of LAAPDs with relatively good energy resolution, namely A3, A4, A6, A7, A8, A9, B2, B6, and B9, which contain about half of all data . Details about the background shape are discussed in §6.7.2. The most relevant results important for the energy calibration are given below in this section.

Each peak in the LAAPD energy spectrum is fitted with a Gaussian and a tail towards lower energies. The parameters for a Gaussian fit are the centroid c and the standard

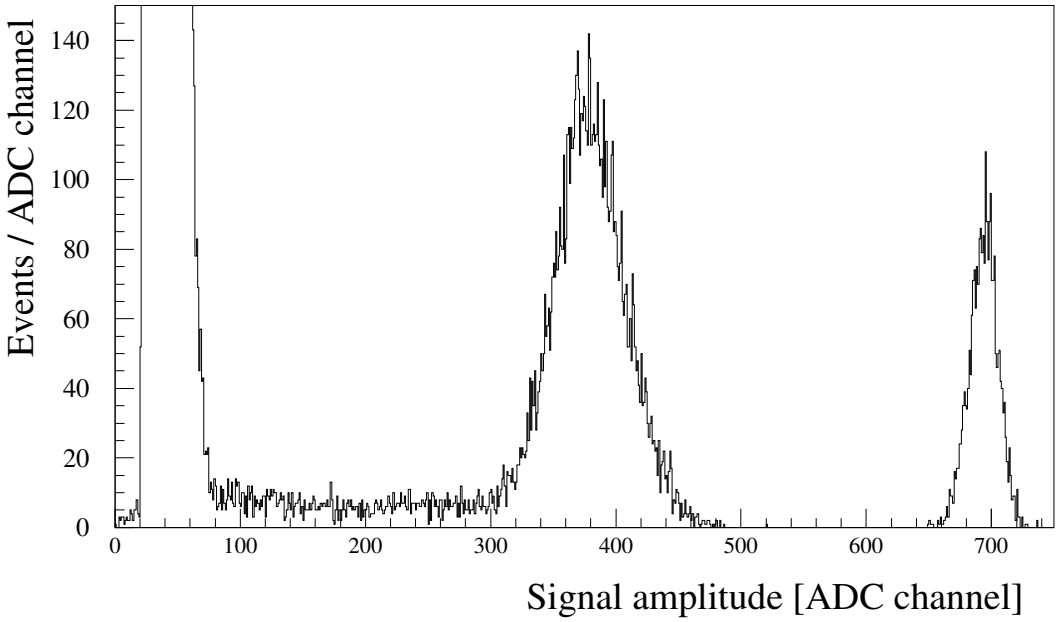

Figure 6.19: Raw energy spectrum for a typical LAAPD from a measurement with a ^{55}Fe source. Note the low–energy tail of the peak in the middle, which is due to 5.9 keV x rays. The noise peak and a peak due to pulses from a pulse generator are visible at the left and right side, respectively.

deviation σ

$$Gauss(E_{\mathrm{x}}; c, \sigma) = \frac{1}{\sqrt{2\pi\sigma^2}} \exp\left(-\frac{(E_{\mathrm{x}} - c)^2}{2\sigma^2}\right) . \tag{6.11}$$

The integral of this Gaussian is normalized to one

$$\int_{-\infty}^{+\infty} Gauss(E_{\mathrm{x}}; c, \sigma) dE_{\mathrm{x}} = 1 . \tag{6.12}$$

The low–energy tail is an intrinsic feature of the LAAPDs and not due to any background, as shown in:

- the background–free spectra in the measurements with the ^{55}Fe source (5.9 keV) (Fig. 6.19);
- the background–subtracted spectra of the μp K–series lines (2 keV) from the second–muon stops as shown in the bottom part of Fig. 6.11.

Its presence is explained by the collection inefficiency of the charge created in the LAAPD by an incident x ray, caused by:

- Charge losses in the front dead layer on the LAAPD surface, in case of low–energy x rays. The width of this layer is on the order of fractions of μm.
- Reduced gain when the x ray is absorbed in the LAAPD drift region, in case of high–energy x rays. The width of the multiplication region is on the order of a few tens of μm.

Not fully understood is the relative height of this tail, its shape, especially towards very low energies, and its dependence on the x–ray energy. In the fitting procedure, the

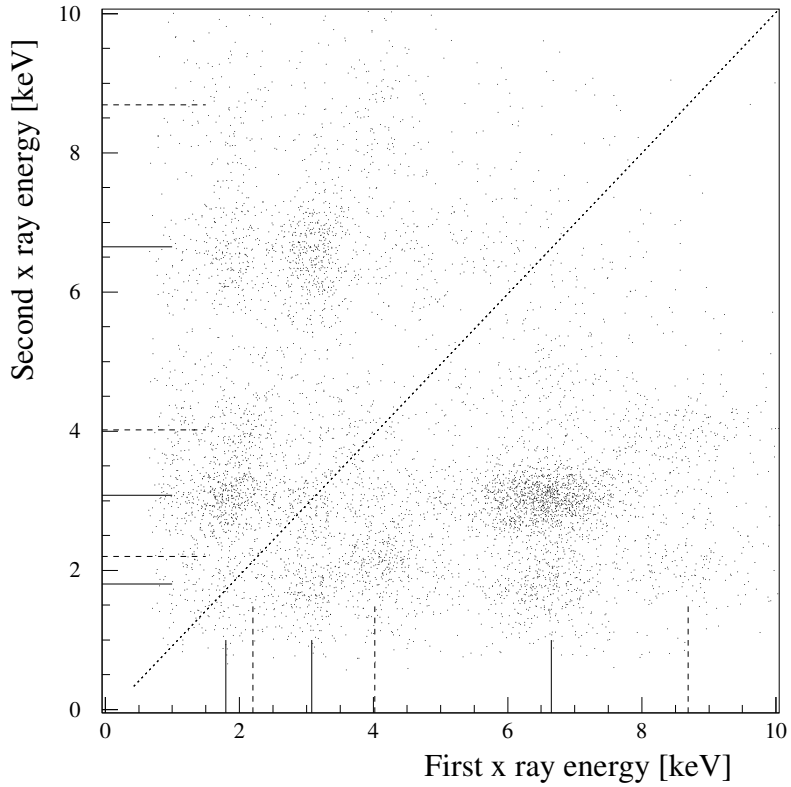

Figure 6.20: 2D energy spectrum where E_x of the first versus E_x of the second x ray from an early*–time x–ray coincidence pair is plotted. The coincidence time width is 30 ns. The* del_e *cut with parameters $t_1^{dele} = 100$ ns and $\Delta t^{dele} = 9$ μs is applied with respect to the first x ray. Intense regions are due to the x rays from radiative transitions in the μN and μO atoms (§3.2). The μN and μO transition energies are indicated by solid and dashed lines, respectively. The asymmetry of this spectrum with respect to the dotted line is due to correlations between t_x and E_x, as discussed in §6.3.*

tail is represented by a Gaussian complementary error function *erfc* defined as

$$erfc(E_x; c, \sigma) = 1 - \int_{-\infty}^{+E_x} Gauss(E_x; c, \sigma) dE_x \,, \tag{6.13}$$

where c and σ are the same parameters as the ones defined by the Gaussian in Eq. (6.11). The shape of the low–energy tail is illustrated for the μp K_α line in the top part of Fig. 6.17. It was tested that the events at ~ 1 keV have precisely the same behaviour as the 2 keV events.

The final fit function for each peak in the x–ray energy spectrum becomes then

$$f(A, r, c, \sigma) = A \ \left(Gauss(E_x; c, \sigma) + r \ erfc(E_x; c, \sigma) \right) \,, \tag{6.14}$$

where A is the Gaussian integral, corresponding to the intensity of the main peak, and r is a factor defining the relative height of the low–energy tail.

As an independent check of the energy calibration, the energy spectra of the coincidence early–time x rays from the radiative transitions in μN and μO atoms are used (§3.2, Table 3.3, page 27). In order to recognize these signals as x rays, the parameter Δt_{same} is set to zero, E_x^{low} to 0.1 keV, E_x^{hi} and E_e^{low} to 30 keV (§6.2). For this analysis only the

best LAAPDs (page 73) are used. The 2D–energy spectrum in Fig. 6.20 shows the energy of the first x ray plotted versus the energy of the second x ray from a coincident pair.

From an analogous 2D spectrum, without any del_e cut, six 1D spectra are produced. The background is only slightly enhanced but the statistics considerably higher in the spectra without the del_e cut. An energy cut is applied in each case on E_{x} of one coincidence x ray, independently if it is the first or the second x ray. The E_{x} of the remaining x ray is then histogrammed. The energy cuts are chosen in order to optimize the probability that histogrammed signals are due to x rays which are in physical coincidence with the μN and μO ($\Delta n = 1$) transition x rays (Figs. 6.21 and 6.22, respectively). The signal fulfilling the energy cut ("main signal") and the histogrammed signal can have different relations:

1. Both signals are due to x rays which are in physical coincidence. The main signal is due to an x ray from
   (a) the desired transition;
   (b) a transition whose main peak is overlapping with the desired transition peak;
   (c) a low–energy tail of an x–ray peak with E_{x} higher than the desired transition energy.
2. Both coincidence signals are due to the same electron detected in two LAAPDs (§6.6).
3. Accidental coincidences.

All six spectra are fitted with a function which is the sum of the peaks and background. The background shape is discussed in §6.7.1. The peaks included in the fit function are due to the x rays from the μN and μO radiative transitions whose yields, with respect to the total yield, are known (Table 3.3, page 27). From these yields, the conditional yields, *i.e.*, the yields when a coincidence with an x ray from a certain transition is required, can be deduced with sufficient precision in order to guide the fit procedure. For example, if an x ray from the $\mu\mathrm{N}(5 \to 4)$ transition is required, it is obvious that the conditional yield of the $\mu\mathrm{N}(6 \to 4)$ transition is zero. However, since the item 1(a) is not the only contribution to the spectra, the intensity of the $\mu\mathrm{N}(6 \to 4)$ peak can be non–zero. All six spectra are fitted following these main ideas:

- The relative amplitudes of the peaks in all spectra should be consistent. If the relative amplitude of a peak is different with respect to other spectra, the change has to be in qualitative agreement with the estimation of the conditional yield.
- The parameters c, σ, and r defined in Eq. (6.14) for each peak individually, have to be the same within one standard deviation for all spectra.
- The dependence of the parameters c, σ, and r on the E_{x} of an incident x ray should be smooth and qualitatively understood.

Of important influence on the energy dependence of these parameters is the x–ray attenuation length λ_{Si} defined as

$$P(d, E_{\mathrm{x}}) = \exp\left(-\frac{d}{\lambda_{\mathrm{Si}}(E_{\mathrm{x}})}\right) , \tag{6.15}$$

where P is the probability that an x ray with energy E_{x} is not absorbed in a silicon layer of width d. The dependence of λ_{Si} on E_{x} (Fig. 6.23) has a characteristic step at

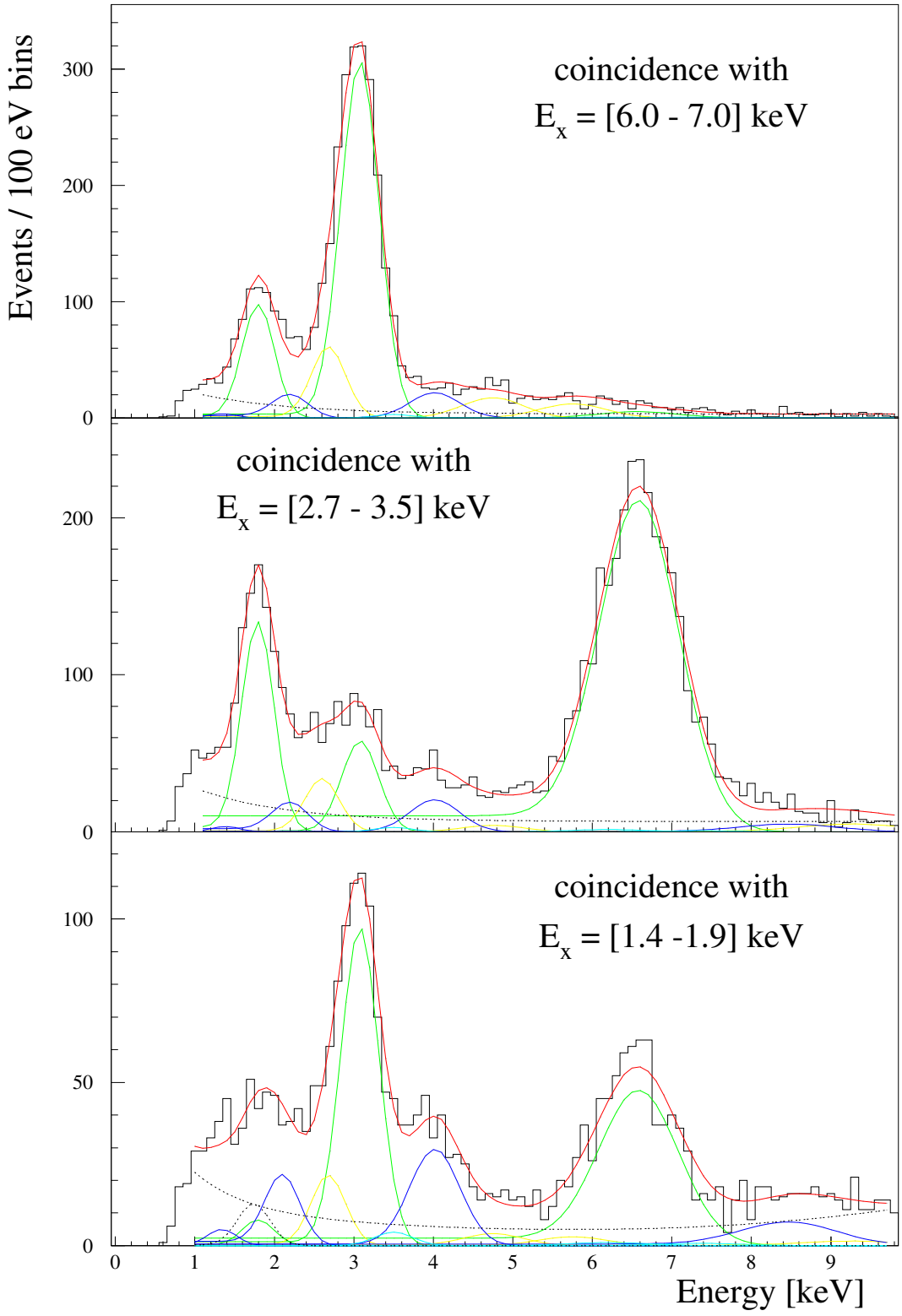

Figure 6.21: Energy spectra of early *x rays which are time–coincident (30 ns) with a signal whose amplitude lies within a certain energy cut. Top: from 6.0 to 7.0 keV (μN(4 → 3) at 6.65 keV). Middle: from 2.7 to 3.5 keV (μN(5 → 4) at 3.08 keV). Bottom: from 1.4 to 1.9 keV (μN(6 → 5) at 1.67 keV). Red: the final fit. Green and yellow: $\Delta n = 1$ and $\Delta n > 1$ μN transitions, respectively. Blue and cyan: $\Delta n = 1$ and $\Delta n > 1$ μO transitions, respectively. Dashed black: continuous background and Si peak (1.74 keV).*

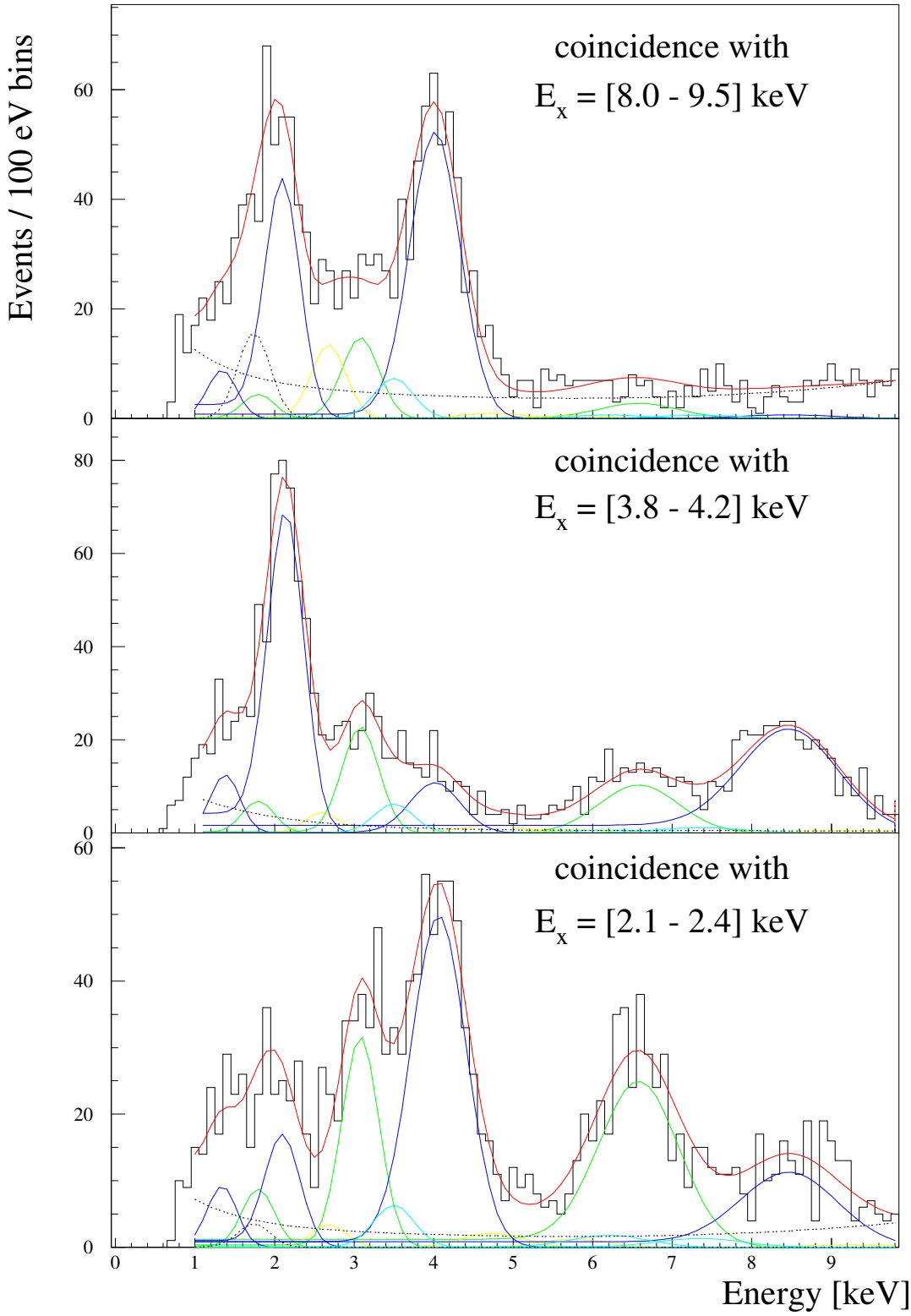

Figure 6.22: Energy spectra of early *x rays which are time–coincident (30 ns) with a signal whose amplitude lies within a certain energy cut. Top: from 8.0 to 9.5 keV (μO($4 \rightarrow 3$) at 8.69 keV). Middle: from 3.8 to 4.2 keV (μO($5 \rightarrow 4$) at 4.02 keV). Bottom: from 2.1 to 2.4 keV (μO($6 \rightarrow 5$) at 2.19 keV). Red: the final fit. Blue and cyan: $\Delta n = 1$ and $\Delta n > 1$ μO transitions, respectively. Green and yellow: $\Delta n = 1$ and $\Delta n > 1$ μN transitions, respectively. Dashed black: continuous background and Si peak (1.74 keV).*

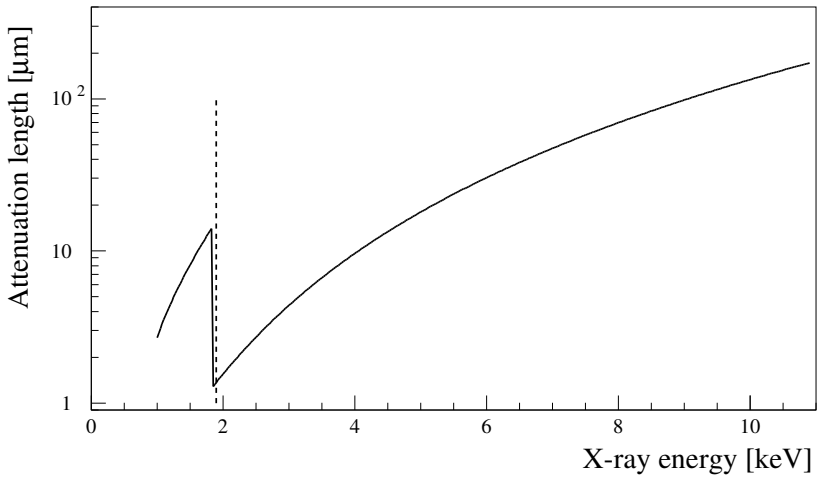

Figure 6.23: Attenuation length λ_{Si} for x rays in Si with the density 2.33 $\mathrm{g \cdot cm^{-3}}$ as a function of the x–ray energy. Note that the dashed line at 1.895 keV, i.e., at the μp K_α x–ray energy, is positioned just above the Si K–edge (1.839 keV).

1.839 keV (Si K–edge) where λ_{Si} changes by an order of magnitude. This is due to the fact that an incident x ray with an energy just above the Si K–edge can ionize silicon K–shell electrons. The μp K_α line, used in the energy calibration, has an energy just above the silicon K–edge. This means that the frontal dead layer of an LAAPD causes a much bigger charge–collection inefficiency in case of the μp K_α x rays in comparison with the 1.67 keV μN line. Since the energy calibration is based on the μp K_α x rays, the relative position of the 1.67 keV $\mu\mathrm{N}(6 \rightarrow 5)$ line is shifted towards higher energies. A small shift of the $\mu\mathrm{O}(6 \rightarrow 5)$ at 2.19 keV line towards lower energies is not understood. However,

Table 6.2: Parameters c, σ (with the FWHM resolution $res = 2.36\,\sigma$), and r defined in Eq. (6.14) for the most intense peaks in the coincidence spectra (Figs. 6.21 and 6.22) and for the μp and μC transitions. E_{x} is the x–ray energy, λ_{Si} the attenuation length in Si. The parameter r corresponds to the relative height of the low–energy tail with respect to the intensity A of the main peak (has no units and is given for 50 eV binning). The relative height of the low–energy tail, when expressed with respect to the height of the main peak (equal to $A/(\sqrt{2\pi}\sigma)$ is given in the last column.

Atom	E_{x} [keV]	λ_{Si} [μm]	c [keV]	σ [keV]	res [%]	r dimensionless	$r\sqrt{2\pi}(\sigma/50\mathrm{eV})$ dimensionless
μN	1.67	10.9	1.79(2)	0.203(3)	28.6(4)	0.002(1)	0.022(10)
μp	1.90	1.4	1.90(0)	0.220(2)	27.3(3)	0.014(3)	0.153(33)
μO	2.19	1.9	2.14(2)	0.220(5)	23.7(5)	0.006(2)	0.061(22)
μp	2.45(2)	2.6	2.48(2)	0.215(2)	20.6(2)	0.005(2)	0.055(22)
μN	3.08	4.7	3.08(1)	0.237(1)	18.1(1)	0.001(1)	0.012(12)
μO	4.02	9.8	4.02(2)	0.315(10)	18.4(6)	0.001(1)	0.016(16)
μC	4.89	16.9	4.89(0)	0.391(4)	18.8(2)	0.001(1)	0.020(20)
μN	6.65	40.7	6.57(3)	0.500(9)	17.7(3)	0.002(1)	0.050(25)
μO	8.69	88.6	8.44(5)	0.625(15)	16.9(4)	0.003(2)	0.085(63)

it should be mentioned that the error on this value is bigger due to the lower statistics of the μO coincidence x rays. A shift towards lower energies which occurs in the case of high–energy x rays is a well known non–linearity effect as described in §4.4.

All information obtained from the study of coincidence spectra, *e.g.*, the energy dependence of parameters c, σ, and r, as well as relative ratios of the peak intensities, were applied in the fit of the early and delayed x ray energy spectra shown in Figs. 6.17 and 6.18, respectively. An overview of the parameters c, σ, and r for the μN and μO ($\Delta n = 1$) transitions, as well as for the μC and μp transitions is given in Table 6.2. A new systematic effect at the Si K–edge energy was found, causing a non–linearity of the energy calibration at low energies and influencing the line shape in the x–ray energy spectra. The charge–collection inefficiency causes a broadening of the main peak as well as an increase of the relative height of the low–energy tail. This effect is strongly pronounced for the μp K_α line due to the small value $\lambda_{Si} = 1.4$ μm. For completeness it should be recalled that a systematic effect at the Si K–edge energy was found also for the timing of x–ray signals, as was demonstrated in §6.3.2.

6.5 X–ray detection efficiency versus energy

Here, the x–ray detection efficiency as a function of the x–ray energy is studied, as far as x–ray absorption in the material in front of the LAAPDs (polypropylene foils and Li sheets) and the intrinsic LAAPD efficiency are considered. The effective thicknesses of different absorption layers take into account an average incident angle of an x ray. The absolute detection efficiencies are not studied, since no influence of the solid angle is accounted for.

X–rays produced inside the hydrogen target can be detected by the LAAPDs and the detection efficiency is influenced mainly by:

1. The absorption in the protective Li sheets with an average thickness $d_{Li} = 175\,\mu$m (9.35×10^{-3} g $\cdot$ cm^{-2}) placed in front of the LAAPDs. The thickness of the foils are not perfectly homogeneous, which may influence the x–ray detection efficiencies of the individual LAAPDs. In addition, lithium reacts strongly with nitrogen. The presence of a small amount of N_2 in the target is proved. Therefore, it is not excluded that locally a thin layer of LiN was created on the Li surface which has a stronger absorption power than pure Li. The effect of such a layer with unknown thickness is treated in the efficiency calculation by introducing a free parameter $d_{Li}^{calc} \geq d_{Li}$ which represents an increased apparent Li width.
2. The absorption in the polypropylene ($\approx (CH_2)_n$) foils. One layer is represented by the target window. Polypropylene foils are placed also at both sides of the Li sheets. The total width of these three foils is $d_{CH_2} = (457 \pm 70) \times 10^{-6}$ g $\cdot$ cm^{-2}. The foils are produced by a stretching procedure and are therefore not very homogeneous. In the calculation of the x–ray absorption in the polypropylene foils only the attenuation length in pure carbon was considered. The corresponding thickness was scaled by a factor 0.85 which is the mass ratio of a C atom to a CH_2 molecule: $d_C = 0.85\, d_{CH_2} = (392 \pm 60) \times 10^{-6}$ g $\cdot$ cm^{-2} $= (1.8 \pm 0.3)$ μm.
3. The absorption in a front dead layer of the LAAPDs. The d_{Si}^1 width of this layer is not well known, being of the order of magnitude of fractions of μm.
4. The probability not to be absorbed in a finite width d_{Si}^2 of the LAAPD drift region, being of the order of few tens of μm.

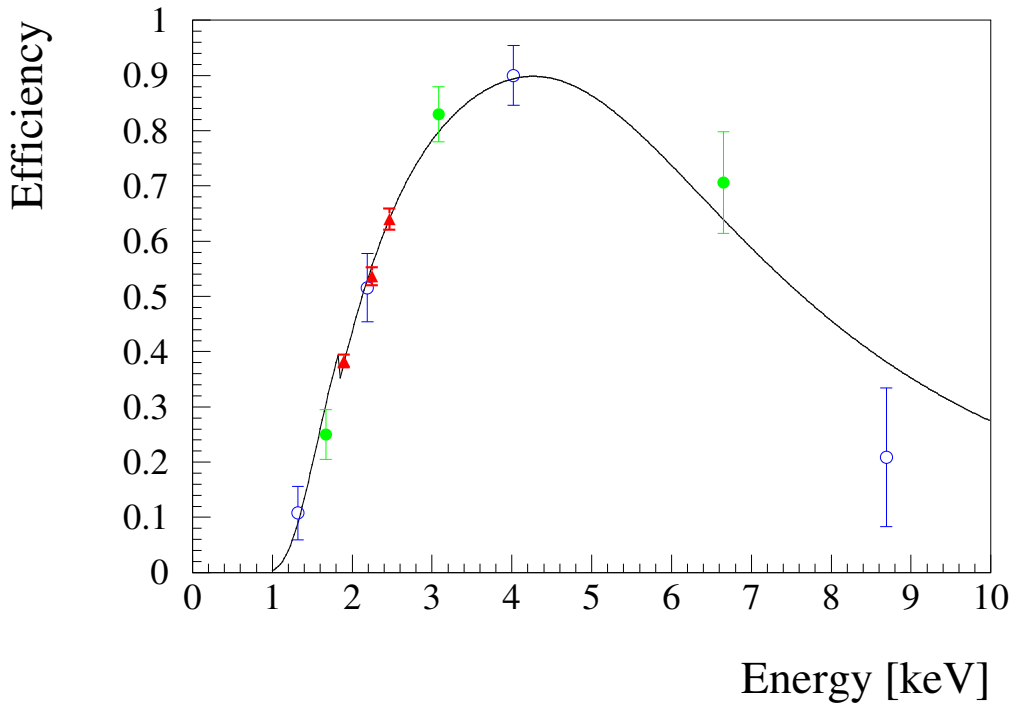

Figure 6.24: Efficiency of the x–ray detection plotted as a function of the x–ray energy. Points: μp K_α, K_β and K_{rest} (red triangles), circular transitions in μN (green full circles), and circular transitions in μO (blue empty circles). The solid curve is the calculated efficiency ε_x when considering the intrinsic LAAPD efficiency, the absorption in the Li sheets, and the polypropylene windows placed in front of the LAAPDs.

The total x–ray detection efficiency ε_x is thus

$$\varepsilon_x = \exp\left(-\frac{d_{\mathrm{Li}}^{\mathrm{calc}}\,\bar{a}}{\lambda_{\mathrm{Li}}}\right)\,\exp\left(-\frac{d_{\mathrm{C}}^{\mathrm{calc}}\,\bar{a}}{\lambda_{\mathrm{C}}}\right)\,\exp\left(-\frac{d_{\mathrm{Si}}^{1}\,\bar{a}}{\lambda_{\mathrm{Si}}}\right)\,\left[1-\exp\left(-\frac{d_{\mathrm{Si}}^{2}\,\bar{a}}{\lambda_{\mathrm{Si}}}\right)\right]\,, \qquad (6.16)$$

where λ_{Li}, λ_{C}, and λ_{Si} are the x–ray attenuation lengths in Li, C, and Si, respectively, which depend on E_{x} [81]. The parameter $\bar{a}$ represents the effect of the angular distribution of the x–rays and was determined by a Monte Carlo simulation [82] to be 1.6 ± 0.05. It corresponds to an average angle $\bar{\alpha} = 51^\circ$ with which the x rays reach the LAAPD surface, according to the relation

$$\bar{a} = \frac{1}{\cos\left(\bar{\alpha}\right)}\,. \qquad (6.17)$$

Equation (6.16) is used to fit the efficiencies determined from the data, considering that the x–ray yields for μp K–lines and for the μN and μO ($\Delta n = 1$) transitions are known. Information about the relative efficiencies come from the fits of the early–time x–ray energy spectra (Fig. 6.17) and from the study of the early–time coincidence spectra (Figs. 6.21 and 6.22). Three sets of relative efficiencies are obtained:

1. $\varepsilon_{\mu\mathrm{N}}^{rel}$ set: relative efficiencies of the μN ($\Delta n = 1$) transitions with respect to the μN($5 \rightarrow 4$) line (0.301, 1.000, and 0.851 for 1.67, 3.08, and 6.65 keV x rays, respectively);
2. $\varepsilon_{\mu\mathrm{O}}^{rel}$ set: relative efficiencies of the μO ($\Delta n = 1$) transitions with respect to the μO($5 \rightarrow 4$) line (0.119, 0.573, 1.000, and 0.232 for 1.32, 2.19, 4.02, and 8.69 keV x rays, respectively);

3. $\varepsilon_{\mu\mathrm{p}}^{rel}$ set: relative efficiencies of the μp K–series lines with respect to the μp $\mathrm{K}_{\mathrm{rest}}$ line (0.609, 0.867, and 1.000 for the K_α, K_β, and $\mathrm{K}_{\mathrm{rest}}$ lines).

Three scaling factors $f_{\mu\mathrm{p}}$, $f_{\mu\mathrm{N}}$, and $f_{\mu\mathrm{O}}$ are defined in the fit procedure:

$$\varepsilon_{\mu\mathrm{p}} = f_{\mu\mathrm{p}} \times \varepsilon_{\mu\mathrm{p}}^{rel} \tag{6.18}$$

$$\varepsilon_{\mu\mathrm{N}} = f_{\mu\mathrm{N}} \times \varepsilon_{\mu\mathrm{N}}^{rel} \tag{6.19}$$

$$\varepsilon_{\mu\mathrm{O}} = f_{\mu\mathrm{O}} \times \varepsilon_{\mu\mathrm{O}}^{rel} \tag{6.20}$$

where $\varepsilon_{\mu\mathrm{p}}$, $\varepsilon_{\mu\mathrm{N}}$, and $\varepsilon_{\mu\mathrm{O}}$ are the sets of efficiencies, as specified at the beginning of this Section.

The best agreement between the data and the ε_x defined in Eq. (6.16) is obtained with the parameter values $d_{\mathrm{Li}}^{\mathrm{calc}} = (200 \pm 20)$ μm, $d_{\mathrm{C}}^{\mathrm{calc}} = (2.1 \pm 0.4)$ μm, $d_{\mathrm{Si}}^{1} = (0.17 \pm 0.05)$ μm, $d_{\mathrm{Si}}^{2} = 27^{+13}_{-5}$ μm, $f_{\mu\mathrm{p}}$=0.64, $f_{\mu\mathrm{N}}$=0.83, $f_{\mu\mathrm{O}}$=0.90, as shown in Fig. 6.24. Parameters $d_{\mathrm{Li}}^{\mathrm{calc}}$ and $d_{\mathrm{C}}^{\mathrm{calc}}$ are strongly correlated; the error of one parameter corresponds to a fixed value of the second parameter. However, a nearly identical efficiency curves can be obtained with $d_{\mathrm{Li}}^{\mathrm{calc}} = 300$ μm (when no polypropylene considered), or with $d_{\mathrm{C}}^{\mathrm{calc}} = 6.5$ μm (when no Li is considered). The resulting d_{Si}^{1} and d_{Si}^{2} values are in agreement with the expected values based on general knowledge about LAAPDs.

6.6 Electron spectra and electron multiplicity

In order to study the LAAPD response to electrons, energy spectra of LAAPD signals in a 30 ns time coincidence with electrons detected by the electron detectors are constructed. An example of such a spectrum is given in Fig. 6.25. There are two energy regions where the electrons preferentially deposit energy: above the threshold $E_{\mathrm{e}}^{\mathrm{APD_{hi}}}$ and below the threshold $E_{\mathrm{e}}^{\mathrm{APD_{low}}}$. Only a small fraction of electrons deposit energy in the interval

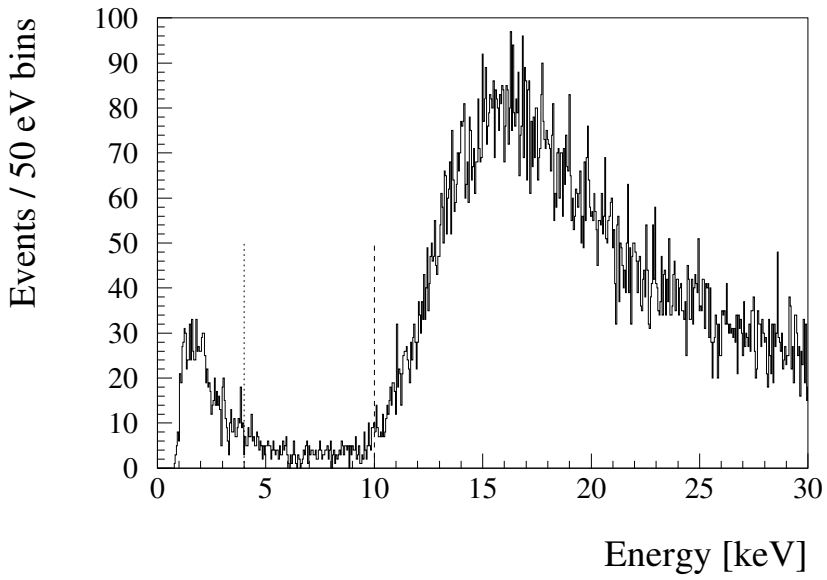

Figure 6.25: An example of an LAAPD electron energy spectrum, measured in the detector A1. Dotted and dashed lines represent the energy thresholds $E_{\mathrm{e}}^{\mathrm{APD_{low}}}$ and $E_{\mathrm{e}}^{\mathrm{APD_{hi}}}$, respectively.

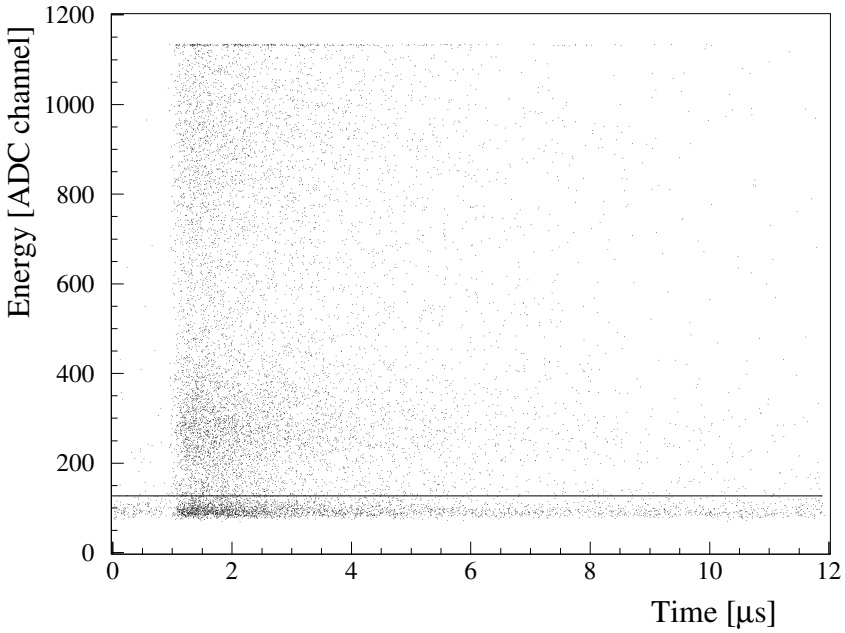

Figure 6.26: 2D spectrum of time t_e versus energy E_e^{El} of electrons detected in EP_{left} *is plotted. The solid horizontal line shows the value of the electron energy threshold* $E_e^{PAD_{thr}}$.

between $E_e^{APD_{low}}$ and $E_e^{APD_{hi}}$. The values chosen for $E_e^{APD_{hi}}$ are in the range from 8 to 14 keV for different diodes. The corresponding electron energy distribution has not a Gaussian shape and is very broad, extending typically from 10 to 40 keV. $E_e^{APD_{low}}$ has a value of $2-4$ keV for all LAAPDs. The shape of the electron energy spectrum is not fully understood. The peak above $E_e^{APD_{hi}}$ represents those cases when an electron deposits energy in the LAAPD drift and multiplication regions. Since the widths of these regions vary for different diodes, also the $E_e^{APD_{hi}}$ value is not unique. A possible explanation for the events at very low energies is that an electron is striking the LAAPD at its inactive thin margin, where only a small part of the created charge is collected, or the APD gain is small. A 0.3 mm wide margin region is sufficient to explain the measured ratio of $5-10\%$ for the number of events below $E_e^{APD_{low}}$ relative to events above $E_e^{APD_{hi}}$.

The 2D–histogram in Fig. 6.26 shows the time t_e versus the energy E_e^{El} of electrons detected in EP_{left} (the analogous spectrum is identical for EP_{right}). The solid line positioned at ADC channel 120 represents the threshold $E_e^{PAD_{thr}}$. Events with energies below this threshold have a higher level of muon–uncorrelated and time–independent background with respect to events with energies above this threshold. In the search for the laser induced events it is important to accumulate all possible statistics. Therefore, in this case no requirement is put on the "paddle" energy of electrons accepted for the del_e cut. However, for the analysis described in §7.3 this cut was applied, and only those EP_{left} and EP_{right} signals were accepted as electrons whose energy is above $E_e^{PAD_{thr}}$. The majority of the muon–correlated events shown in Fig. 6.26 have energies around ADC channel 250. More energy is deposited at high incident angles, or when the electron crosses the plastic scintillator more than once. The excess of events between channels 700 to 1100 is not understood. The events below $E_e^{PAD_{thr}}$ correspond to single–photon detection in the PMT, probably caused by Čerenkov light produced by electrons striking the lucite light–guide but not the scintillator.

As discussed above, the same electron can be detected in several LAAPDs and/or in

Table 6.3: Summary of the contributions of different detectors and their combinations to the total muon–decay electron detection efficiency. $\mathrm{APD_X}$ *is the LAAPD in which the x ray is detected, while* $\mathrm{APD_{\bar{X}}}$ *stands for any other LAAPD. The total probability to detect a muon–decay electron by any detector is 65.4% (within the time cuts* $t_1^{\mathrm{dele}} = 100$ *ns and* $\Delta t^{\mathrm{dele}} = 7$ *μs).*

Detector	M^{tot}	M^{APD}	Contribution [%]
$\mathrm{EP_{left}}$	1	0	15.7
$\mathrm{EP_{right}}$	1	0	15.6
$\mathrm{D_3^{hi}}$	1	0	1.7
$\mathrm{EP_{left}}$ and $\mathrm{EP_{right}}$	2	0	1.7
$\mathrm{APD_X}$	1	1	2.1
$\mathrm{APD_{\bar{X}}}$	1	1	7.5
$\mathrm{APD_{\bar{X}}}$	> 1	> 1	1.8
$\mathrm{APD_X}$ and $\mathrm{APD_{\bar{X}}}$	> 1	> 1	1.3
$\mathrm{EP_{left}}$ and ($\mathrm{APD_X}$ or $\mathrm{APD_{\bar{X}}}$)	> 1	≥ 1	7.2
$\mathrm{EP_{right}}$ and ($\mathrm{APD_X}$ or $\mathrm{APD_{\bar{X}}}$)	> 1	≥ 1	7.7
$\mathrm{D_3^{hi}}$ and (LAAPD or $\mathrm{EP_{left}}$ or $\mathrm{EP_{right}}$)	2	0 or 1	2.0
Other combinations			1.1
Sum			65.4

any of the electron detectors. The total electron multiplicity M^{tot} defines the number of detectors in which an electron is detected, while the LAAPD electron multiplicity M^{APD} gives the number of LAAPDs detecting this electron. The contribution of different detectors to the total electron detection efficiency is studied. The probability to detect a muon–decay electron (within the time cuts $t_1^{\mathrm{dele}} = 100$ ns and $\Delta t^{\mathrm{dele}} = 7$ μs) is 65.4%. An exclusive contribution of the electron detectors is $\sim 35\%$ and of the LAAPDs about $\sim 13\%$; the remaining 18% represent different combinations of the coincident detection by the LAAPDs and any of electron detectors. The contribution of different detectors to the total electron detection efficiency is summarized in Table 6.3.

The correlation between the electron detectors and the LAAPDs is demonstrated in Fig. 6.27. The 5 Tesla magnetic field forces the electrons to spiral and causes a strong correlation between the A side LAAPDs, and the $\mathrm{EP_{left}}$ detector, and between the B side LAAPDs, and the $\mathrm{EP_{right}}$ detector. In contrast, an electron detected in the $\mathrm{D_3^{hi}}$ detector mounted at the downstream side of the target has an equal chance to be detected in A or B side.

The probability that the multiplicity M^{APD} is equal to 1 is very high, *i.e.*, about 50% for the front side LAAPDs, 40% for the middle ones and nearly 70% for the back side diodes. This enhancement for the back side LAAPDs together with the muon–stop distribution (also enhanced for the back side LAAPDs, §7.1), explains the pattern seen in the first row of Fig. 6.27, where it is required that an electron is detected by the electron detectors and $M^{\mathrm{APD}} = 1$.

In contrast, if $M^{\mathrm{APD}} > 4$ is required, the pattern is completely different (second row of Fig. 6.27). If an electron is detected in an LAAPD, the probability to be detected also in another diode is highest for the neighboring LAAPDs and strongly decreases for the more distant diodes from the same side (Fig. 6.28). Therefore, the condition of high multiplicity M^{APD} is fulfilled mostly for the central diodes, as is seen in the lower row of Fig. 6.27. Only the electrons with a small angle between their momentum vector and the beam axis

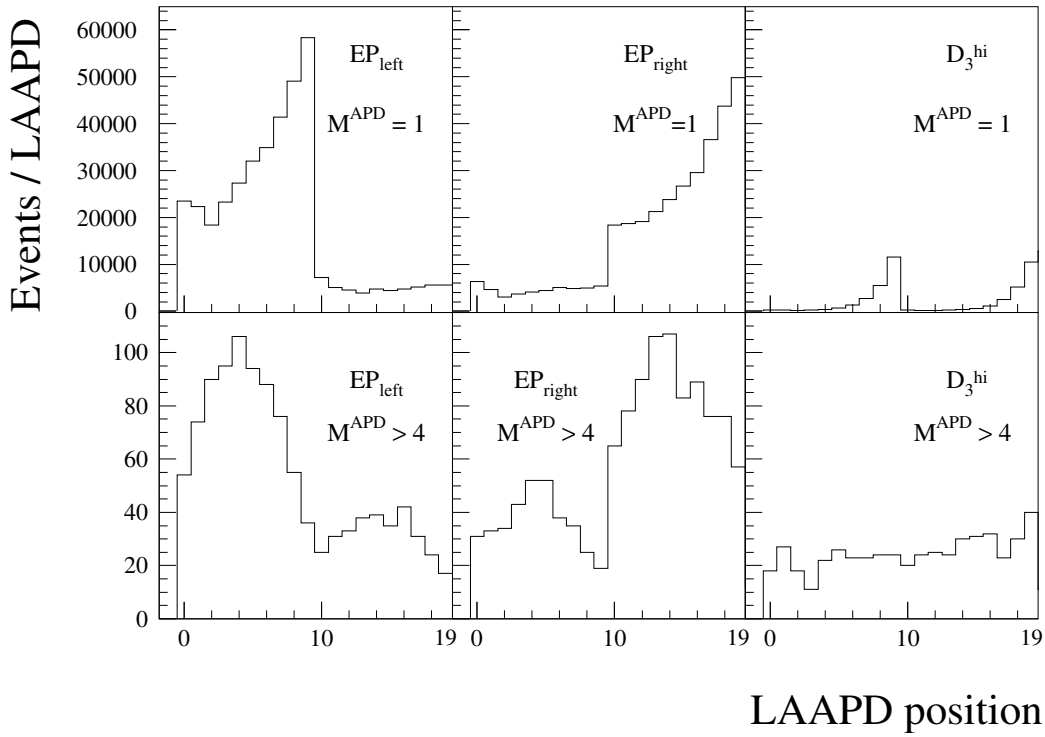

Figure 6.27: Demonstration of the correlations between electron detectors *and LAAPDs from the point of view of electron detection. The number of detected electrons is plotted versus the LAAPD position (0–9: A side, 10–19: B side). Different conditions are required: detection in the* $\mathrm{EP_{left}}$ *(*$\mathrm{EP_{right}}$*) detector for the first (middle) column, and in* $\mathrm{D_3^{hi}}$ *for the last column. The multiplicity conditions* $M^{\mathrm{APD}} = 1$ *and* $M^{\mathrm{APD}} > 4$ *are put for the upper and lower row, respectively. Details in the text.*

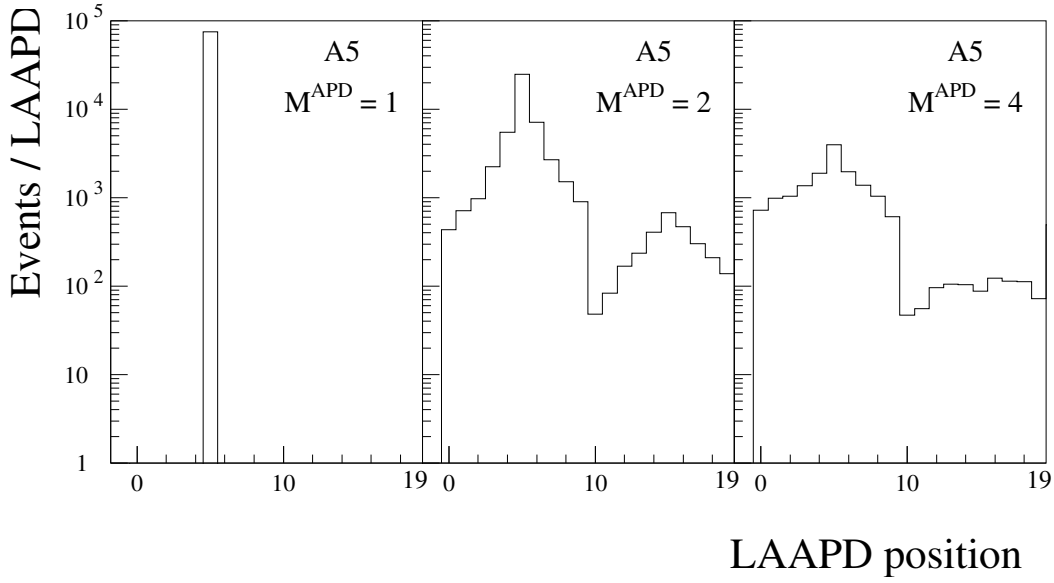

Figure 6.28: Number of detected electrons versus LAAPD position (0–9: A side, 10–19: B side). Detection in A5 is required. The left plot contains about 75 000 events fulfilling the $M^{\mathrm{APD}} = 1$ *condition for the LAAPD multiplicity. The plot in the middle (right) is for the* $M^{\mathrm{APD}} = 2$ *(*$M^{\mathrm{APD}} > 4$*) condition and contains about 50 000 (16 000) events.*

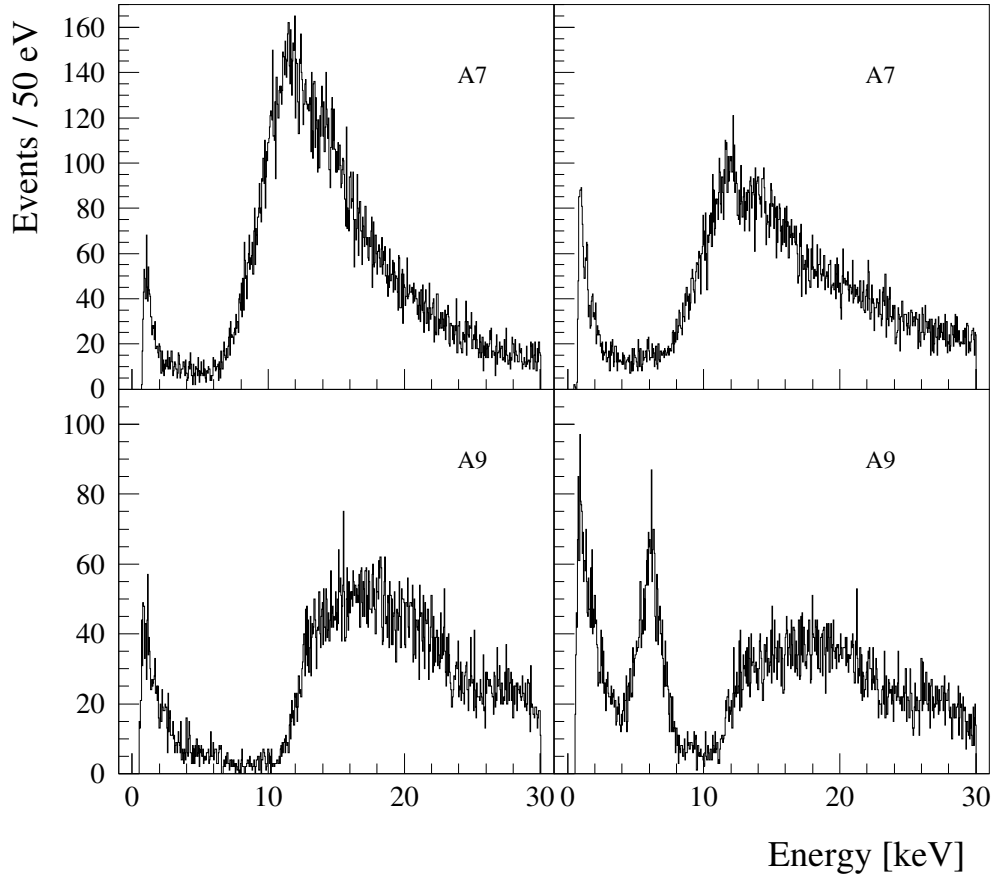

Figure 6.29: Energy spectra of (top) LAAPD A7 and (bottom) A9 for very early times before 155 ns, i.e., before the early *times. (Left) Signals in a 30 ns time–coincidence with electron paddle signals. (Right) Signals which are not in time–coincidence with a signal from any of the* electron detectors*. Note the presence of a Fe fluorescence peak (∼6 keV) for non–coincidence signals in A9.*

can be detected at the very downstream D_3^{hi} detector with $M^{APD} > 4$. This explains the flat distribution in the lower right corner in Fig. 6.27.

The A and B sides are nearly isolated from the point of view of electron detection. For example, if an electron is detected in A5, the probability to be detected in any of the B side diodes is about 20 times lower than the probability to be detected by another A side diode (Fig. 6.28). This is due to the fact that electrons are strongly decelerated in high Z materials such as the cavity mirrors or the Ti–holders of the LAAPDs. Thus, the radius of their spiral decreases and the electrons move away from the solid angle of any LAAPD.

6.7 X–ray energy spectra background

Here, the background determination for x–ray energy spectra with different t_x time cuts is described. This study is performed for the sum of best LAAPDs (page 73), since this LAAPD group is used in the analysis requiring the determination of x–ray energy spectra background. The background relevant for the laser–induced events considering all LAAPDs is described in §7.2.

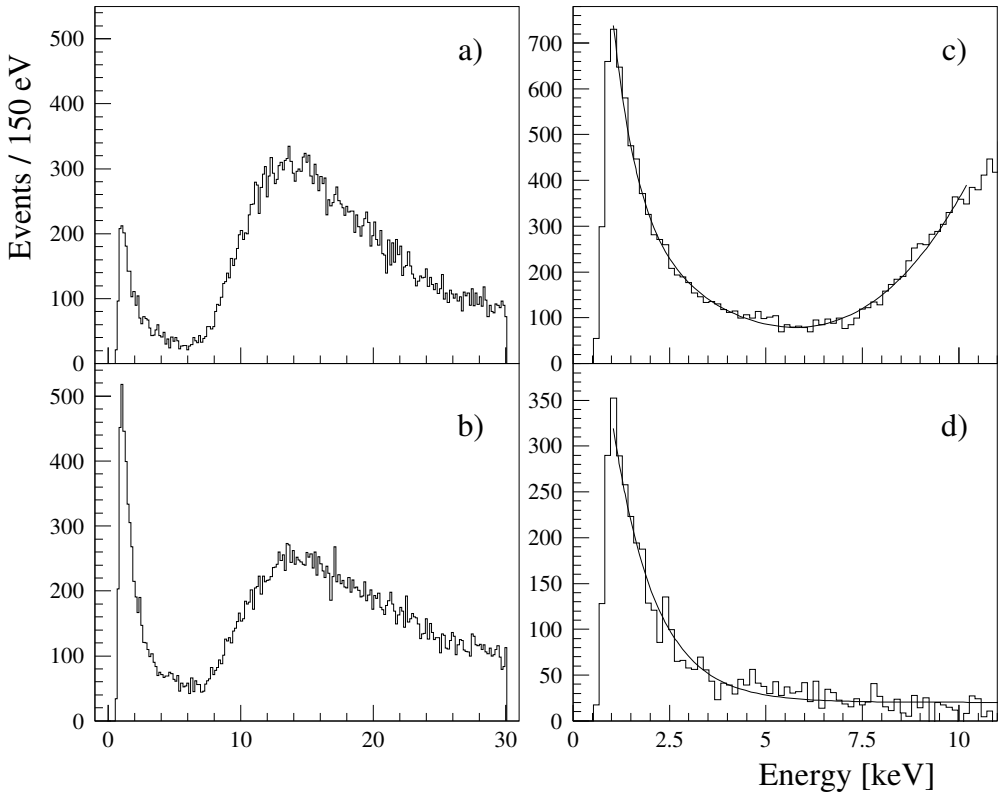

Figure 6.30: LAAPD energy spectra for the sum of best LAAPDs *(page 73) for times after 7.5 μs. (a) Events in a 30 ns time–coincidence with electron paddle signals and (b) events which are not in such a coincidence. (c) Sum of the a) and the b) spectrum together with a fit function $\mathcal{B}^{\mathrm{uncor}}_{\mathrm{e+neu}}$ (up to 10 keV) which represents the shape of the total muon–uncorrelated background. (d) Difference b) − a) spectra together with a fit function $\mathcal{B}^{\mathrm{uncor}}_{\mathrm{neu}}$; spectrum a) is suitably scaled in order to obtain a flat function for energies above $E_{\mathrm{e}}^{\mathrm{APD_{hi}}}$. The fit function $\mathcal{B}^{\mathrm{uncor}}_{\mathrm{neu}}$ represents that particular component of the total muon–uncorrelated background (and therefore of the $\mathcal{B}^{\mathrm{uncor}}_{\mathrm{e+neu}}$ function) whose origin is not due to electrons but probably due to neutrons.*

6.7.1 Background not correlated with the 1^{st}–muons

The signals which are not correlated in time with muons stopping in the gas target are considered as a background. This kind of background is studied

1. at very early times (less than 155 ns, see Fig. 6.13, page 67), *i.e.*, before the time when a muon can be stopped and captured in the gas (Fig. 6.29).
2. at very late times (after 7.5 μs), when the probability that a muon–decay electron is present in the system is at the level of a few percent (Fig. 6.30). In this particular case the $\mu^{2\mathrm{nd}}$ cut is applied, but this cut was optimized to suppress muonic x rays and not electrons from 2^{nd}–muons decaying at later times.

In both cases, the dominant background contribution comes from electrons. For case 1, most of these electrons originate from muons decaying before entering the target. For case 2, there are 2^{nd}–muons stopping and decaying in the target, and partially there are also very late decays of 1^{st}–muons (MUON). The shape of the LAAPD energy spectrum originating from electrons is obtained when considering only LAAPD signals which are in 30 ns coincidence with electrons detected by the electron detectors (page 61). A

characteristic shape of this background is shown in the left part of Fig. 6.29 and in Fig. 6.30 a).

The complementary signals, *i.e.*, those which are not in coincidence (right part of Fig. 6.29 and Fig. 6.30 b), have two components. These two components are explained in the example shown in Fig. 6.30 b) , *i.e.*, the spectrum for the sum of best LAAPDs (page 73). One component comes from those electrons which were not detected by any of electron detectors. It can be assumed that this component has the identical shape as the spectrum shown in Fig. 6.30 a), *i.e.*, the spectrum of events in coincidence with an electron detected in electron detectors. The shape of the second component, which is not correlated with electrons, can be obtained when the coincidence (an therefore electron generated) spectrum shown in Fig. 6.30 a) is subtracted from the non–coincidence spectrum shown in Fig. 6.30 b). The coincidence spectrum is scaled such that the electron peak above the $E_{\mathrm{e}}^{\mathrm{APD_{hi}}}$ is completely eliminated in the difference spectrum. The resulting difference spectrum is shown in Fig. 6.30 d) and peaks towards low energies, in particular below ~ 3 keV. The origin of these events is not completely clear, but could be attributed, for example, to the interaction of neutrons which are abundant in the experimental area.

There are no substantial differences in the shape of the coincident spectra for the early (item 1) and late (item 2) time case. Originating from electrons, it is unimportant if they are correlated to the 1^{st}–MUON or any 2^{nd}–muon. For the non–coincidence spectra, there is a particularity for the backside LAAPDs (page 35) as shown on example of A9 spectrum (Fig. 6.29, bottom right): the very early–time energy spectra (item 1) contain a Fe fluorescence peak coming from the stainless steel holder of the cavity mirror placed close to the back side of the target. The presence of this Fe peak is restricted to very prompt times. In conclusion, there are two classes of time–uncorrelated background: one associated with electrons, with energy spectra as shown in Fig. 6.30 a), the other one probably due to neutrons, with spectra as in Fig. 6.30 d).

In order to determine the shape of the time–uncorrelated background for the best LAAPDs group, the spectra of very late signals (after 7.5 μs, item 2) are considered, since they are not complicated by the presence of Fe–fluorescence.

First, the shape of the total muon–uncorrelated background is considered. Therefore, for the group of best LAAPDs, the coincidence [Fig. 6.30 a)] and non–coincidence [Fig. 6.30 b)] spectra are summed. The resulting spectrum, shown in Fig. 6.30 c), is fitted up to 10 keV with the sum of an exponential and a third–order polynomial. The resulting function which represents the data is

$$\mathcal{B}_{\mathrm{e+neu}}^{\mathrm{uncor}} = 2350\, \exp\left(-\frac{E}{0.66}\right) + 312 - 53.5\, E - 2.6\, E^2 + 0.843\, E^3\,, \qquad (6.21)$$

where E stands for the energy (in keV) of an LAAPD signal.

Second, the difference spectrum shown in Fig. 6.30 d) is also fitted up to 10 keV. The resulting fit function $\mathcal{B}_{\mathrm{neu}}^{\mathrm{uncor}}$ describes the shape of the electron–uncorrelated (and probably neutron–correlated) background for the sum of best LAAPDs:

$$\mathcal{B}_{\mathrm{neu}}^{\mathrm{uncor}} = 776\, \exp\left(-\frac{E}{1.10}\right) + 20.2\,, \qquad (6.22)$$

where E stands again for the energy (in keV) of an LAAPD signal. The form of both functions $\mathcal{B}_{\mathrm{e+neu}}^{\mathrm{uncor}}$ and $\mathcal{B}_{\mathrm{neu}}^{\mathrm{uncor}}$ is purely empirical, *i.e.*, these functions just describe the data. The numerical coefficients have no physical meaning and do not reflect (in an obvious way) the similar shape of both background functions for energies below 5 keV.

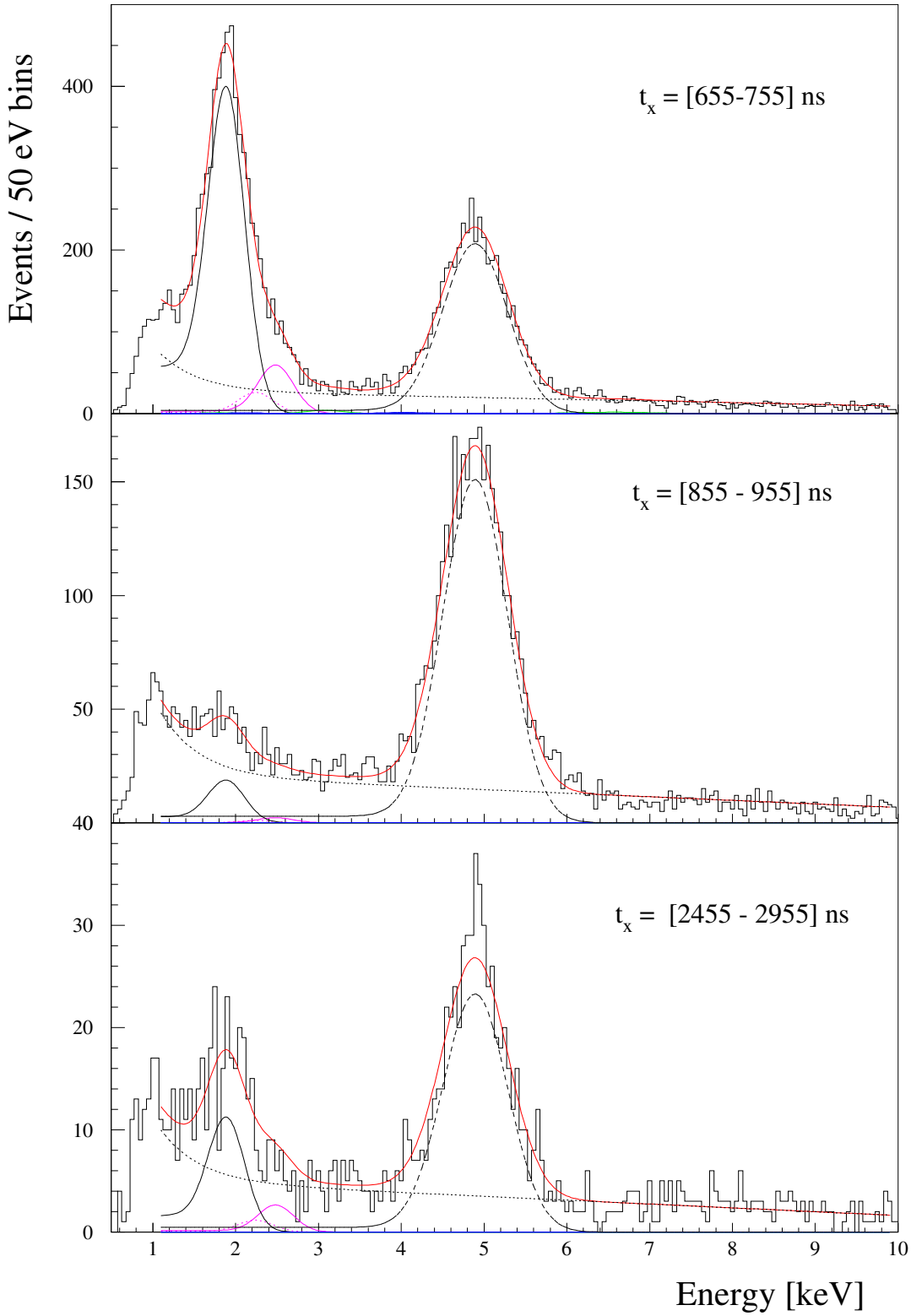

Figure 6.31: X–ray energy spectra (3 out of 19) which were studied in order to deduce the shape of the muon–correlated background, i.e., the function $\mathcal{B}^{\mathrm{cor}}$ (dotted black lines). The applied time cuts are indicated in the plots. The spectra are shown for the sum of best LAAPDs *(page 35). Only the* xe *event class is considered, the* del_e *cut is applied. No $\mu^{2^{\mathrm{nd}}}$ cut is introduced. The 2 keV peaks for the middle and bottom plot are mostly due to the second–muon μp atoms. The final fit function is shown in red. The peak at 4.9 keV is $\mu\mathrm{C}(4 \rightarrow 3)$ transition (dashed black line). The black solid line represents μp K_{α}, while magenta lines μp K_{β} and $\mathrm{K}_{\mathrm{rest}}$ transitions.*

In the fit procedure of the early–time coincidence x–ray spectra (μN and μO transitions) both background shapes described above are applied. First, the background shape in these x–ray coincidence spectra was deduced by comparison of the spectra shown in Figs. 6.21 and 6.22 (therefore with an applied del_e cut) with the analogous spectra in which no del_e cut was applied. Based on this comparison, two groups of coincidence spectra were distinguished. Both groups have in common a background increasing for energies below ∼2 keV, but only for some of them the background level increases also at energies above ∼8 keV. An increase for higher energies is typical for electron energy spectra. The contribution of electron background in x–ray coincidence spectra is enhanced since electrons can be detected in several LAAPDs in coincidence and therefore can fake real x–ray coincidences. Indeed, when E_{x} of the main signal lies below $E_{\mathrm{e}}^{\mathrm{APD_{low}}}$ or above $E_{\mathrm{e}}^{\mathrm{APD_{hi}}}$, *i.e.*, in intervals where electrons preferentially deposit their energy, such a background increase at high energies is observed. Therefore, $\mathcal{B}_{\mathrm{e+neu}}^{\mathrm{uncor}}$ is used to fit the background. As can be seen in Figs. 6.21 and 6.22, the presence of a peak at 1.74 keV from Si–fluorescence had to be allowed in these cases in order to fit the data. When the energy of the main signal lies between $E_{\mathrm{e}}^{\mathrm{APD_{low}}}$ and $E_{\mathrm{e}}^{\mathrm{APD_{hi}}}$, *i.e.*, in the region where electrons do not preferentially deposit their energy, $\mathcal{B}_{\mathrm{neu}}^{\mathrm{uncor}}$ is applied (and no Si peak). In both cases, the background function, when used in the fit, is multiplied by a free scaling factor, and an additional constant background is allowed. The Si peak seems to be present only when electrons contribute to the background on a relevant level, but this correlation is not understood.

6.7.2 Background correlated with the 1^{st}–muons

For x–ray energy spectra whose background is correlated with the muon and muonic atoms another method is applied to extract the background shape. First, a set of x–ray energy spectra with different time cuts applied on the x–ray time is produced. The time interval from 555 to 1455 ns is divided into 9 parts of 100 ns step size, while the interval from 1455 to 6455 ns is divided into ten parts of 500 ns step size. Only the `xe` event class is accepted in these 19 x–ray energy spectra. The parameter Δt_{same} is set to 100 ns, the del_e cut parameters t_1^{dele} and Δt^{dele} to 100 and 5000 ns, respectively, while the $\mu^{2^{\mathrm{nd}}}$ cut is not applied. Each of these 19 x–ray energy spectra is fitted. The energy spectra and resulting fit functions are shown on three examples in Fig. 6.31.

The fit function of each of the 19 x–ray energy spectra is composed of:

1. *muon–correlated background:*
   The background $\mathcal{B}^{\mathrm{cor}}$ is at energies E_{x} below 10 keV as

$$\mathcal{B}^{\mathrm{cor}} = P \ \exp\left(-\frac{E_{\mathrm{x}}}{0.47}\right) + R \ (14.3 - E_{\mathrm{x}}) \ , \tag{6.23}$$

   where P and R are free fit parameters and E_{x} in keV–units. The other parameters given just as numbers were found to describe the data on a satisfactory level. Figure 6.32 shows the dependence of the parameters P and R on time. The function $\mathcal{B}^{\mathrm{cor}}$ was applied also in the fits shown in Figs. 6.17 and 6.18.
2. $\mu\mathrm{C}(4 \rightarrow 3)$ *line:*
   For a majority of the fitted x–ray energy spectra, the $\mu\mathrm{C}(4 \rightarrow 3)$ is the most intense line. The parameters σ and c (Eq. (6.14)) are free if the line amplitude is more than 50 (in 50 eV binning), otherwise they are fixed. The parameter r is fixed and the line intensity A is always a free fit parameter. The time dependence of A is shown in the bottom part of Fig. 6.32.

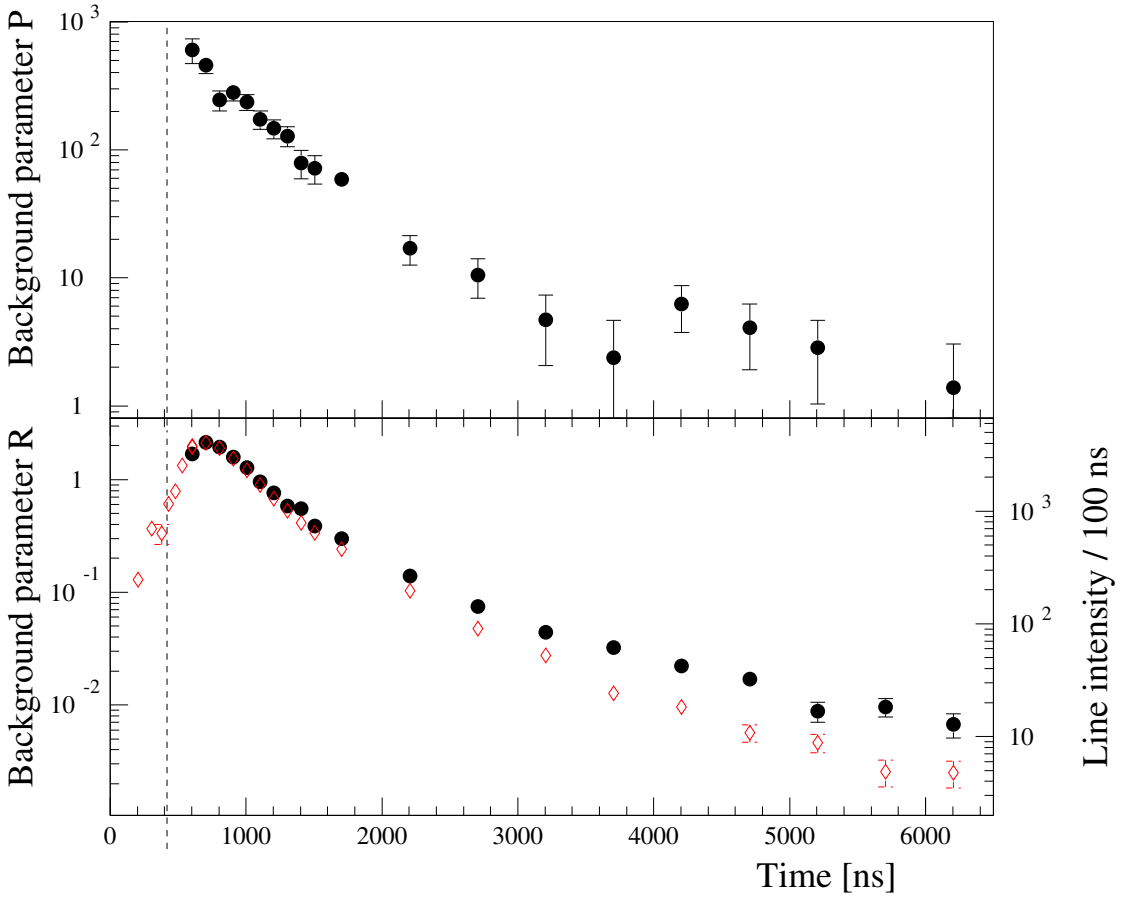

Figure 6.32: Parameters (top) P and (bottom) R of the x–ray energy spectra background $\mathcal{B}^{\rm cor}$ shown as a function of time and normalized to 100 ns (full circles). The μC($4 \rightarrow 3$) line intensity as a function of time, normalized to 100 ns bin size, is given with empty diamonds (right scale, bottom). The dashed vertical line indicates the average time of the μp K_α transition.

As discussed in Chapter 3, the origin of this line is the muon transfer from a μp atom to a C atom present in the polypropylene foils in front of the Li sheets. A μp atom has to drift from the muon stop region at the target center to the target walls, by a distance of 5 mm up to a few cm. The distribution of arrival times (μC deexcitation, empty–diamonds in the bottom part of Fig. 6.32) peaks at 700 ns, *i.e.*, 300 ns later than the μp K–line time distributions (Fig. 6.13), and has a quasi–exponential tail towards later times. A small increase of intensity at very early times (second empty–diamond point in the bottom part of Fig. 6.32) may be due to muon stops in the muon entrance window.

The shape of the μC time dependence is similar to the shape of the time dependency of the parameter R from Eq. (6.23), with exponential time constants of $\sim$ 600 ns at times around 1.5 μs. The parameter P has a similar time–dependence at times above 1 μs. This suggests that the time–correlated, *i.e.*, muon correlated background $\mathcal{B}^{\rm cor}$ originates from muon transfer processes. Only at early times there is some enhancement of the low–energy background (parameter P). The energy dependence of $\mathcal{B}^{\rm cor}$ is not well understood. A possible explanation is that higher energy μC transitions are detected in the LAAPDs at reduced gain or with partial charge

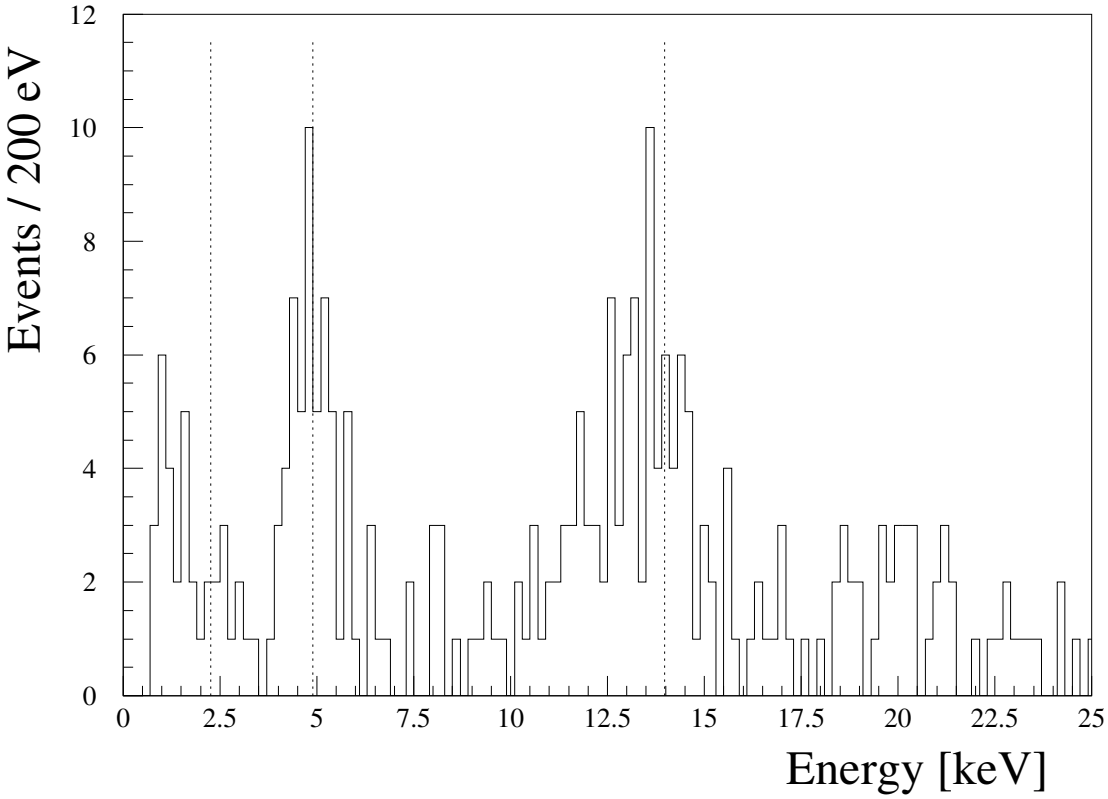

Figure 6.33: Energy spectrum of delayed coincidence x rays (t_x from 755 to 1955 ns, 30 ns coincidence width). The del_e *cut is applied. It is required that the energy E_x of one x ray from the coincidence pair is within one of two intervals: 4.6 to 5.3 keV or 13 to 15 keV. Therefore, this is the energy spectrum of x rays being in coincidence with μC($4 \rightarrow 3$) (4.89 keV) or μC($3 \rightarrow 2$) (13.97 keV) transition x rays. The three vertical lines represent the main μC transition energies. No clear peak is present at 2.26 keV (μC($5 \rightarrow 4$)). The increase towards low energies (below 3 keV) is due the electrons detected in two LAAPDs (the second interval of required energies, i.e., 13 to 15 keV is above the $E_e^{\mathrm{APD_{hi}}}$ threshold).*

collection when the x ray is absorbed in a not fully efficient region of the LAAPD. The presence of a large amount of μC x rays with energies 75 and 89 keV is proved by the detection of an intense μC 4.9 keV line whose yield is about an order of magnitude smaller than the yield of high energy transitions (Table 3.2, page 26). A source of dangerous background, *i.e.*, delayed 2 keV x rays, could be a μC($5 \rightarrow 4$) transition at 2.3 keV. However, its transfer yield is very small, as indicated by calculated yields (Table 3.2) and confirmed by the delayed coincidence spectrum shown in Fig. 6.33.

3. μp *K–series lines:*
   For the three lines μp K_α, K_β and K_{rest}, the only free fit parameters are the total intensity of the K–series and the yield of the K_{rest} line. All other parameters are fixed to the values resulting from the fit of the early–time x–ray energy spectrum (Fig. 6.17). The relative yield of the K_β line with respect to the K_{rest} line is kept constant. The cascade calculations do not predict substantial changes of this ratio in time (Fig. 3.4, page 22), and the energy resolution and in some cases also the low statistics do not allow leaving it free during the fit.

   At late times the major population of μp atoms is due to second–muon stops.

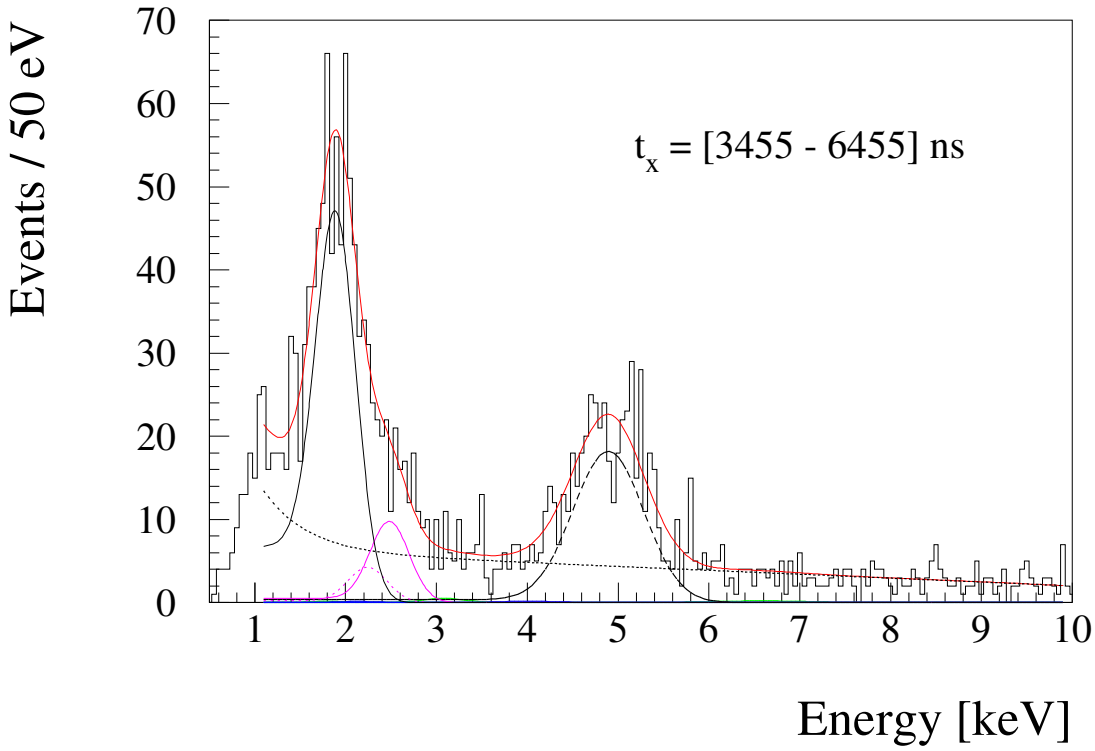

Figure 6.34: The x–ray energy spectrum of very late signals (t_x from about 3.5 to 6.5 μs). The spectrum is shown for the sum of best LAAPDs *(page 35). Only the* xe *event class is considered, the* del_e *cut is applied. No* $\mu^{2^{nd}}$ *cut is introduced: the peaks at 2 keV are only due to the second–muon* μp *atoms. The relative yield of the* μp K_{rest} *line was kept as a free fit parameter: the resulting value is* (16.2 ± 2.0)*%, i.e., within less than one sigma consistent with the yield of 17.8% obtained from the fit of* early *signals (Fig. 6.17). The final fit function is in red. Other lines:* $\mu C(4 \rightarrow 3)$ *(dashed black),* μp K_α *(solid black),* μp K_β *and* K_{rest} *(magenta),* $\mathcal{B}^{cor}$ *background (dotted black).*

The relative yields of the K–series lines are still the same as in the case of the 1^{st}–muon μp atoms, as shown in the fit of the x–ray energy spectrum with large delayed t_x interval from 3.5 to 6.5 μs where the statistics allows the μp K_{rest} yield to vary as a free parameter (Fig. 6.34). Therefore, for the energy spectra with time cuts later than 1455 ns, all yields are fixed to the values obtained from the early time x–energy spectrum (Fig. 6.17). The amplitudes of the K_α and K_{rest} lines as functions of time are discussed in §7.3.

4. μN *and* μO *lines:*
The μN and μO lines have small amplitudes and are fitted in case of the five energy spectra with time cuts below 1055 ns. The only free fit parameter is the $\mu N(5 \rightarrow 4)$ line amplitude at 3 keV. The relative yields in μN and μO are fixed to the values obtained from the fit of the early–time x–ray energy spectra (Fig. 6.17). In case of the energy spectra with later time cuts, the amplitudes of the μN and μO lines are fixed to zero. The amplitude of the $\mu N(5 \rightarrow 4)$ line as a function of time is discussed in §7.3.

Chapter 7

Results and conclusions

7.1 Muon slowing down and stop–time distribution

In order to study how the muons traverse the target, slow down, stop and create muonic atoms, three categories of LAAPD time spectra were produced: time spectra of μp K–series x rays ($\sim$2 keV, Fig. 7.1), time spectra of μN($5 \rightarrow 4$) x rays ($\sim$3 keV, Fig. 7.2), and electron time spectra (Fig. 7.3, fitted functions discussed below in §7.1.1).

For the μp K–series x rays the low–energy cut is in an interval from 1.3 to 1.6 keV. It was chosen individually for each LAAPD in order to accept as few low–energy background events as possible. The upper energy cut was set for all LAAPDs to 2.6 keV in order to accept most of the μp K–series x rays but no μN($5 \rightarrow 4$) x rays.

For the μN($5 \rightarrow 4$) x rays, the low energy cut is set to 3 keV in order to minimize the μp x–rays contribution, the upper one to 4 keV. For LAAPDs with poor energy resolution, some μp x rays were also accepted. In Fig. 7.2, *e.g.*, the higher peak intensity in the B4 spectrum is due to this effect. The energy cuts chosen for both μp and μN x rays are illustrated in Fig. 7.4.

At this point it should be mentioned that the x–ray spectra in Figs. 7.1 and 7.2 represent all the available statistics. However, the peak intensities for different LAAPDs should not be compared here, since they are affected by the fact that not all detectors were properly working throughout the whole data acquisition period. When the relative peak intensities are of importance for the data analysis, only the runs where all 20 LAAPDs worked properly are considered. The del_e cut, *i.e.*, the requirement of detecting a muon–decay electron is not applied mainly due to the following two reasons. First, we did not want to reduce the statistics, especially in the case of the μN x rays. Second, we did not want to influence the relative peak intensities, since the muon–decay electron detection efficiency depends on the LAAPD position.

The signals fulfilling the energy cuts applied in the construction of the μp and μN x–ray time spectra are not exclusively correlated with these muonic atoms. These events can also be part of low–energy tails of higher energy x–ray peaks, they can represent a time–uncorrelated background, or they can be correlated with an electron. To increase the probability that an accepted signal has its origin in a muonic–atom x ray, this signal must be the first one after the muon trigger, and must not be in coincidence with a signal from any of the electron detectors.

The electron time spectra are constructed using a different approach. The energy of an accepted signal has to be above the $E_{\mathrm{e}}^{\mathrm{APD_{hi}}}$ threshold (§6.6) and the time–coincidence with the electron detectors signals is not considered. Also here, an accepted event has to

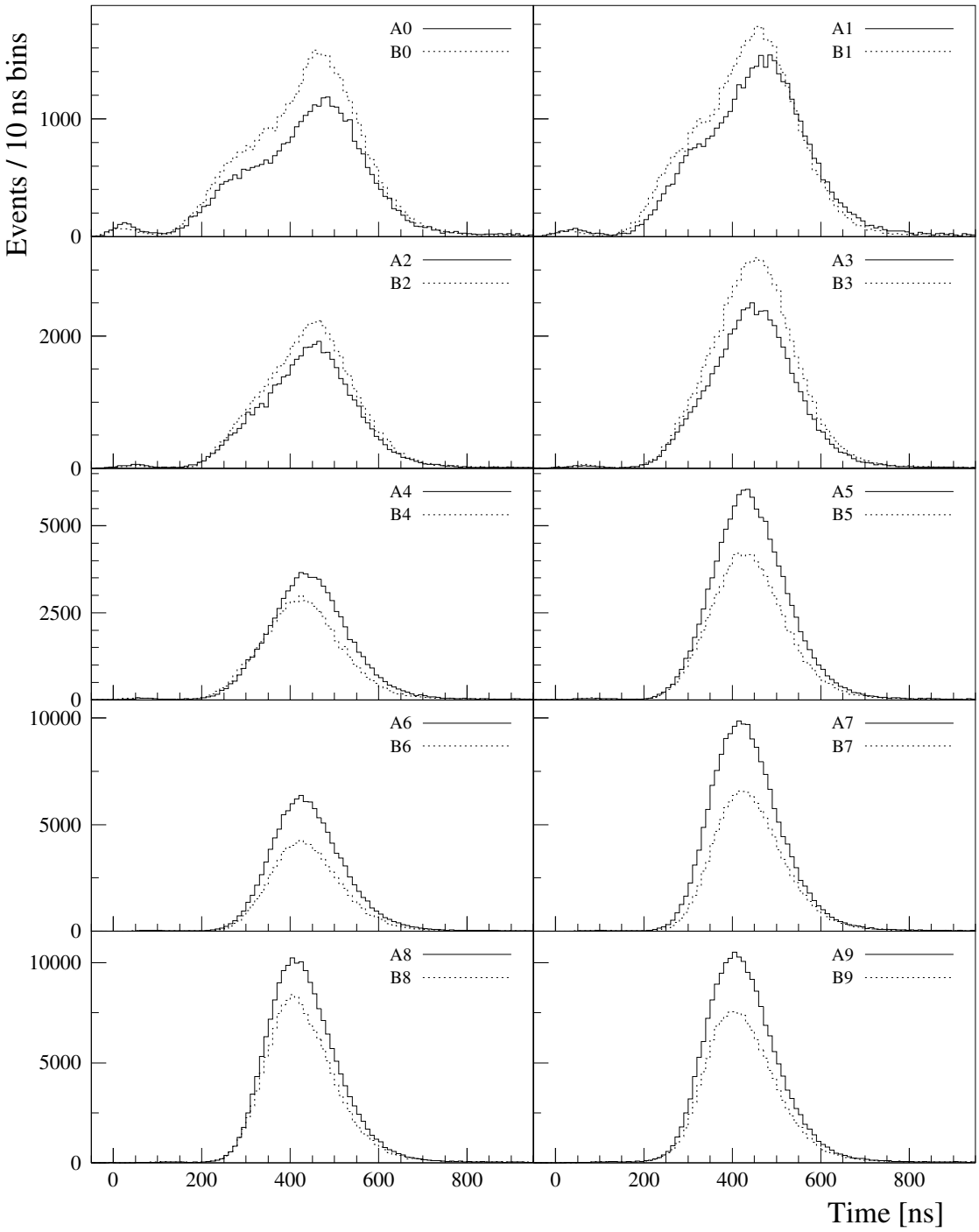

Figure 7.1: LAAPD time spectra of x rays with energies up to 2.6 keV. The low energy cut varies for different LAAPDs due to the different background level and is in the interval from 1.3 to 1.6 keV. Note that the double peak structure is obvious for LAAPDs A0/B0 and is becoming less visible with increasing LAAPD number, i.e., with increased detector distance from the muon entrance window.

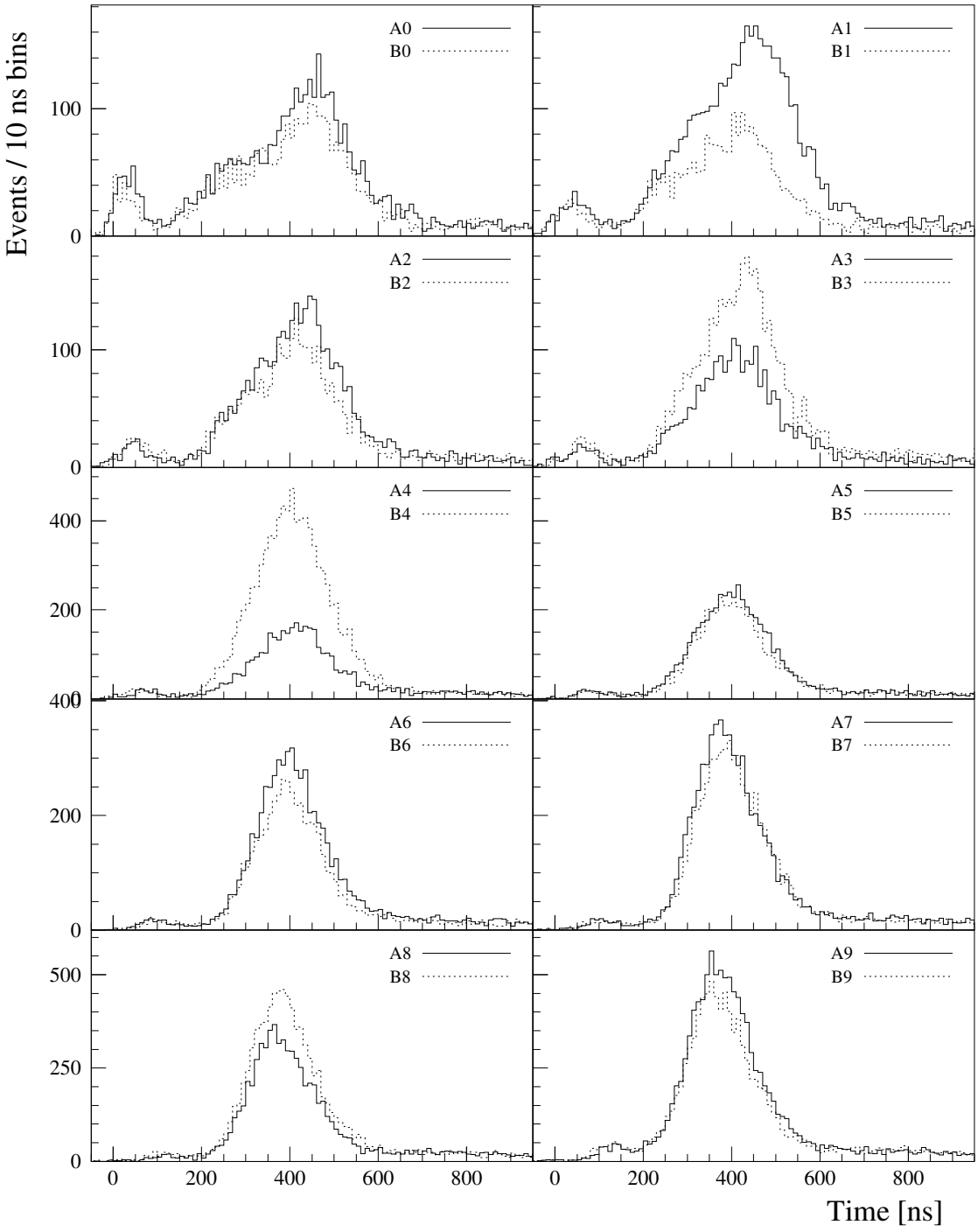

Figure 7.2: LAAPD time spectra of x rays with energies between 3 to 4 keV. Note that the double peak structure is obvious for LAAPDs A0/B0 and is becoming less visible with increasing LAAPD number, i.e., with increased detector distance from the muon entrance window.

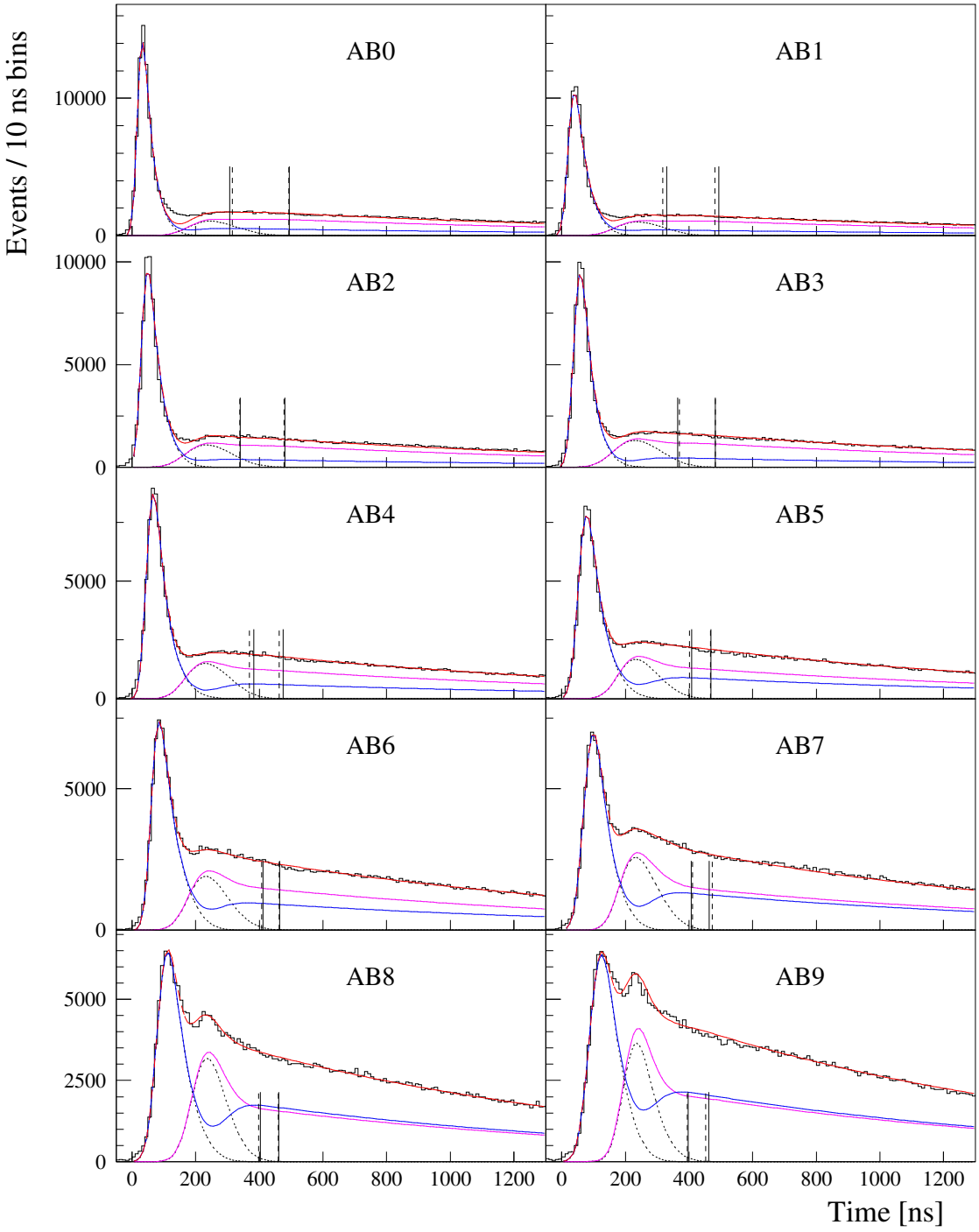

Figure 7.3: LAAPD electron time spectra. Both for the incoming *and* reflected *muons two functions are fitted: one for electrons from muons decaying in flight (dashed black lines) and one for the stopped–muon decay electrons. The upper solid line (red) represents the sum of all four functions. The two lower solid lines represent the two sums of the two functions individually for* incoming *(blue) and* reflected *(magenta) muons. The solid (dashed) vertical lines represent the centers of gravity of peaks in μp x–ray time spectra, i.e., the fit results for the A(B) side LAAPDs. The earlier solid (dashed) line is due to the* incoming *muon stops, while the later solid (dashed) line due to the* reflected *muon stops.*

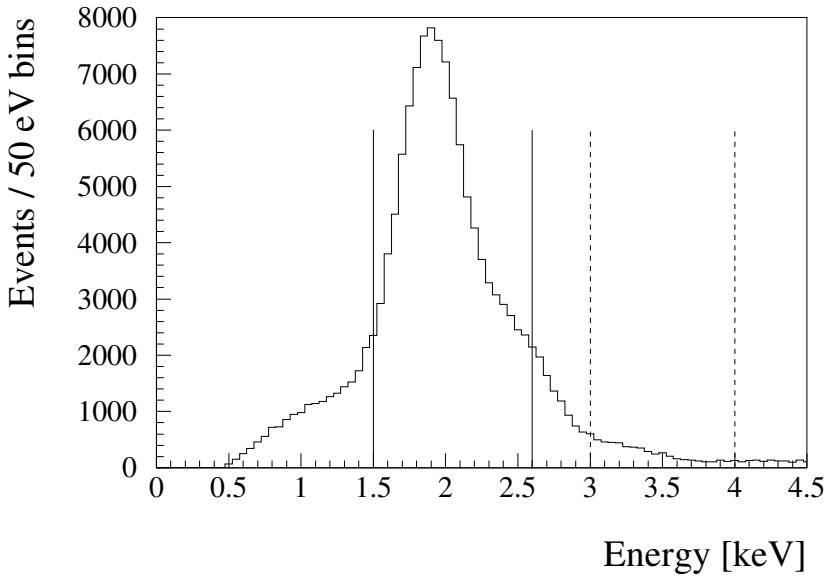

Figure 7.4: X–ray energy spectrum from detector B2 having the best energy resolution of all LAAPDs. The solid and dashed vertical lines represent the energy cuts applied for this LAAPD to construct μp and μN$(5 \rightarrow 4)$ x–ray time spectra, respectively.

be the first one after a muon trigger.

A striking feature in the x–ray time spectra (Figs. 7.1 and 7.2) is a double peak structure, which becomes less pronounced for the backside LAAPDs. The μp K–series peaks are positioned at later times and are slightly broader with respect to the μN$(5 \rightarrow 4)$ x–ray peaks. For simplicity, from now on we will refer to these x rays only as μp and μN x rays.

The electron time spectra (Fig. 7.3) demonstrate a clear double peak structure only in case of the most downstream LAAPDs, *e.g.*, A9/B9 and A8/B8. The first, earlier peak is clearly present in the spectra of all LAAPDs. With increasing LAAPD number, this peak is shifted towards later times, broadened and less pronounced with respect to the continuum part of the spectrum.

7.1.1 Fitting procedure

The fitting procedure is guided by the working hypothesis that the double peak structures present in the time spectra are due to muon reflection from the gold surface covering the LYSO crystal (D_3 detector) placed at the downstream end of the target. The situation is sketched in Fig. 7.5. A muon is entering from the left, and gives a trigger signal when crossing the thin carbon foil inside the first S2 ring held at -3.5 kV (details in §4.1). The second ring is at ground potential and does not contain a foil. Due to this potential difference, the muon is accelerated and gains 3.5 keV energy. The muon then crosses the formvar window where it is slowed, and enters the target vessel filled with 0.6 hPa of hydrogen gas. The relations between muon energy, range, and slowing–down time were given in §3.1.1. When the muon reaches the capture energy $E_{\rm cap}$ (§3.1.1), a μp atom is formed. Muons with lower energies are stopped earlier, muons with higher energies traverse the target and reach the gold surface. The gold acts as a reflector for low–energy muons, modifying their energy and angle distributions. Some of the reflected muons stop

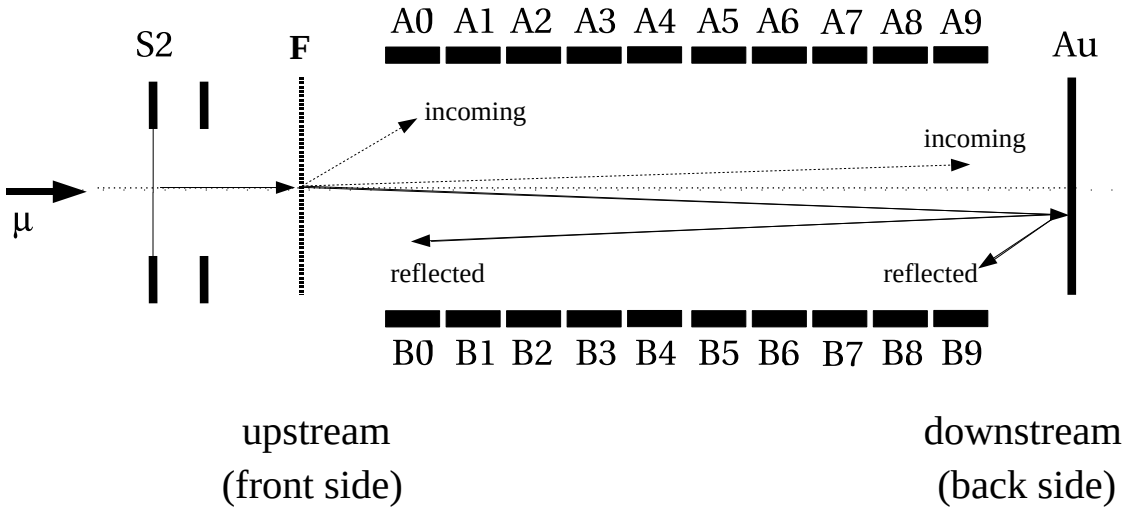

Figure 7.5: A simplified sketch of the setup, including the components essential for the explanation of the x–ray and electron time spectra: two S_2 *rings placed in vacuum, one with and one without a carbon foil, a formvar window F separating the vacuum from 0.6 hPa of hydrogen gas, 20 LAAPDs A(B)0 to 9, and the gold surface at the end of the target. A muon is entering from the left, giving a trigger signal when crossing the* S_2 *foil. Along the muon beam axis, shown by the dotted line, the sketch is approximately in scale; the center–to–center distance of the two adjacent LAAPDS is 16.5 mm. The arrows represent the trajectories of four muon classes:* incoming *muons stopping in front of A0 and A9 (dashed lines in the "upper" part of the target), and* reflected *muons stopping in front of the B9 and B0 (solid lines) in the "bottom" part of the target.*

just after the reflection, the most energetic ones can reach again the front parts of the target. In the following, the muons which do not have enough energy to reach the gold surface will be referred to as incoming muons, while those which are energetic enough to reach the gold surface will be referred to as reflected muons. The extreme cases, namely incoming muons stopping in front of A0 or A9, and reflected muons stopping in front of B9 or B0, are represented by arrows in Fig. 7.5. Fig. 7.6 illustrates the time– and space (along beam axis) evolution of one incoming and one reflected muon (some terms indicated in this Figure are defined below).

7.1.1.1 Fit function for x–ray time spectra

Each x–ray time spectrum is fitted within a time interval from $\sim$ 220 ns to $\sim$ 700 ns. The fitting function is a sum of two peak functions, an earlier and a later one, corresponding to x rays from muonic atoms formed either by incoming or by reflected muons, respectively, and an exponential background. A convolution, Eq. (6.3, page 68) of a Gaussian, Eq. (6.6) with an *Exp* function, Eq. (6.4) is used as a peak fitting function. The centroids and sigmas of both Gaussians are kept free and independent. The same exponential decay constant of the *Exp* function is used for both peaks and it is kept as a free fit parameter. The intensities of both convolutions are also free fit parameters.

Because of the high μp x–rays statistics, it is possible to perform the fit for each LAAPD separately. Fit results for the A0 and A9 spectra with the maximal statistics are

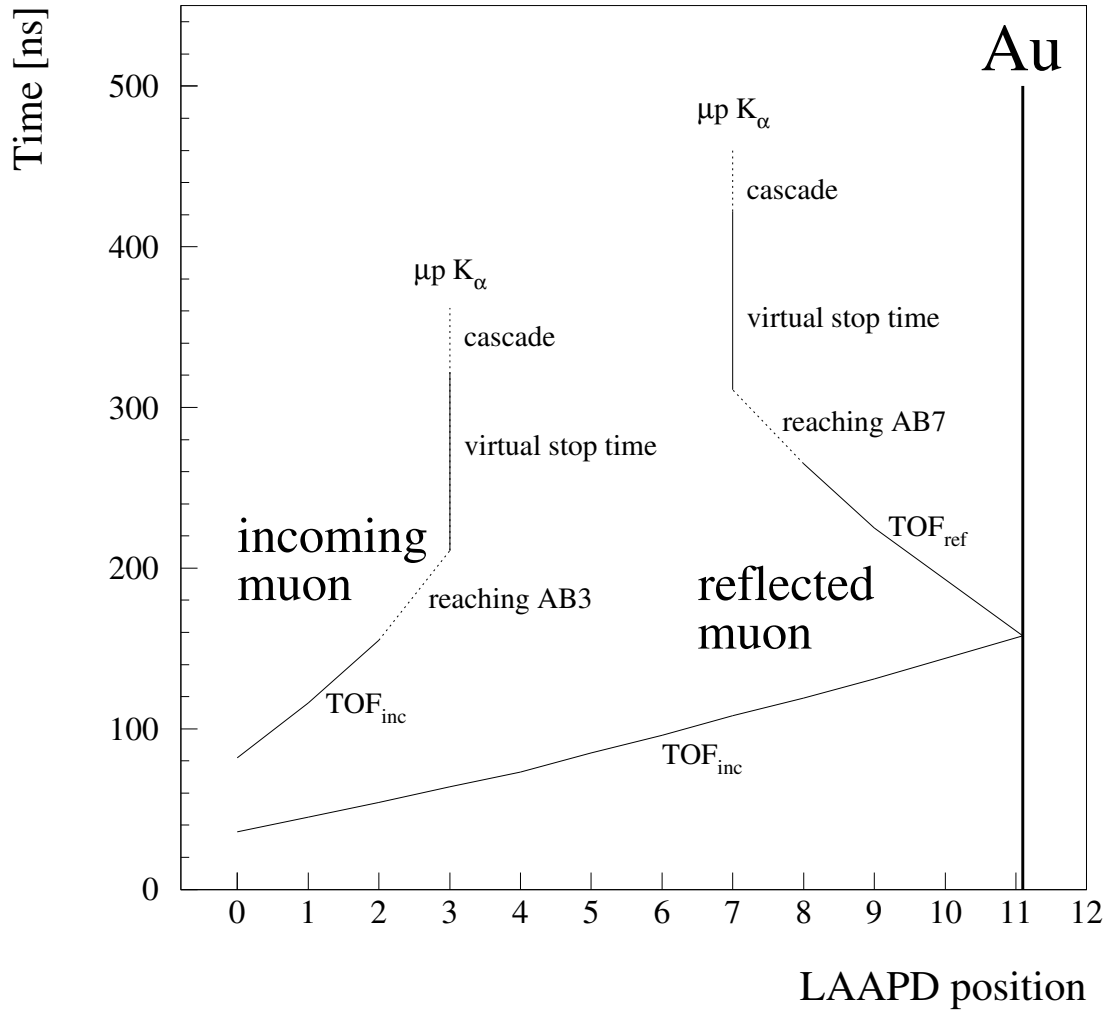

Figure 7.6: History of an incoming *muon stopping in front of LAAPD AB3 and of a* reflected *muon stopping in front of AB7, as considered in the fit and simulation. The x–axis is the coordinate along the beam axis (0–9 corresponds to LAAPD numbers), the y–axis gives the time. The position of the gold surface is indicated. If a muon decayed within the $TOF_{\rm inc}$ ($TOF_{\rm ref}$), the muon–decay electron would contribute to the convolution $Gauss^{\rm TOF} \otimes Exp^{\rm TOF}$ for* incoming *(*reflected*) muons; if a muon decayed at any time when it has already reached a certain LAAPD, the muon–decay electron would contribute to the convolution $erf^{\rm TOF} \times (Gauss^{\rm stop} \otimes Exp^{\rm stop})$. The "virtual stop time" is a time interval when the muon is quasi–stopped and loitering in the vicinity of a particular LAAPD. The 40 ns μp cascade time is also indicated.*

shown in Fig. 7.7. The residuals shown in the plots are defined as

$$\text{residual} = \frac{N(i) - f(i)}{\sqrt{N(i)}}\,, \tag{7.1}$$

where $N(i)$ is the i–bin content of the measured spectrum and $f(i)$ is the i–bin value of the fitting function.

The statistics of the μN x rays is more than an order of magnitude smaller than the μp data and the background shape plays an important role in these fits. The fits for the summed spectra of the LAAPDs AB0, AB1 and AB2 were not stable and had large systematic errors. The dependence of the peak centroids on the LAAPD position is quite

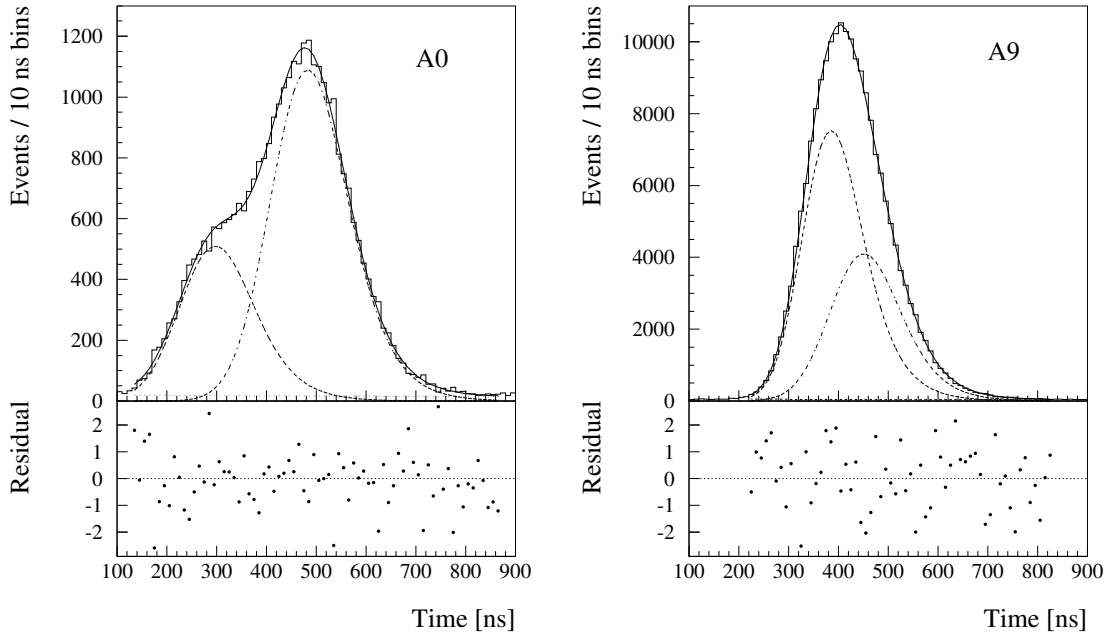

Figure 7.7: Time spectra of the μp x rays (2 keV) from A0 (left) and A9 (right) together with the fit functions (solid line) and corresponding residuals. The two peaks (dotted line) are due to the incoming *and* reflected *muon stops (earlier and later peak, respectively).*

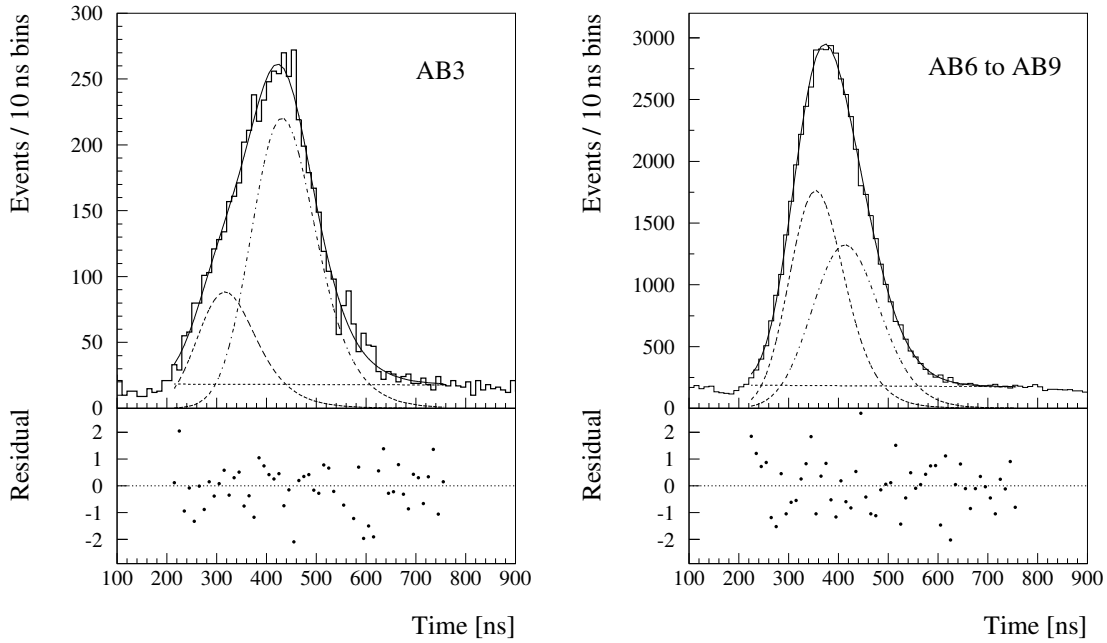

Figure 7.8: Time spectra of the μN$(5 \rightarrow 4)$ x–rays (3 keV) from AB3 (left) and from AB6 to AB9 (right) together with the fit functions (solid line) and corresponding residuals. The two peaks (dotted line) are due to the incoming *and* reflected *muon stops (earlier and later peak, respectively).*

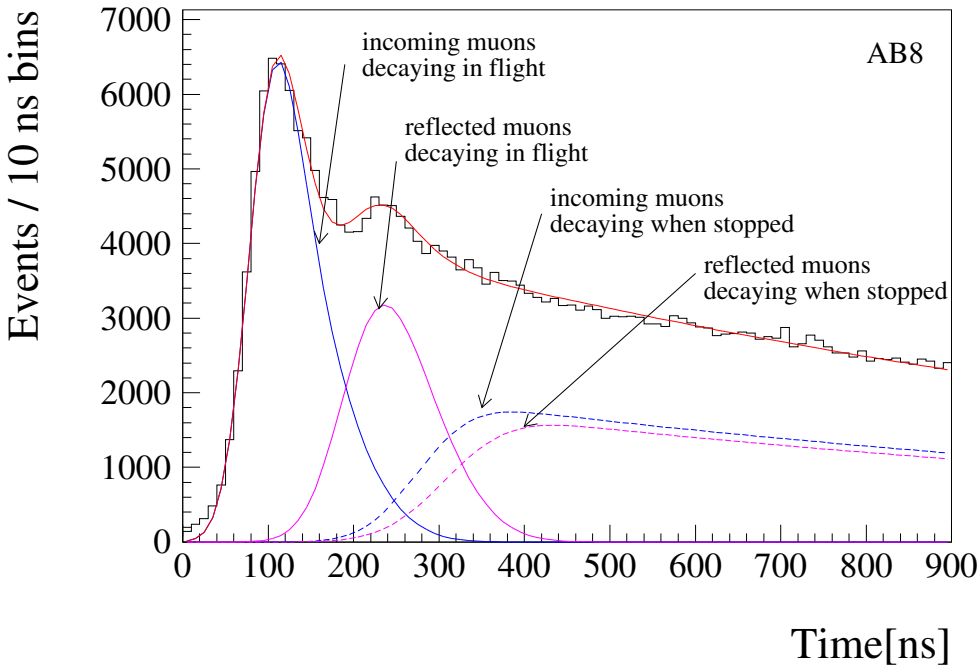

Figure 7.9: Electron time spectrum from AB8 illustrating the four fit functions as described in the text. The total fit function, the sum of all four functions, is shown in red; the functions due to the incoming *and* reflected *muons in blue and magenta, respectively. The peaks due to electrons from muons decaying in flight, i.e., the convolutions* $Gauss^{\mathrm{TOF}} \otimes Exp^{\mathrm{TOF}}$ *are plotted as solid lines. The functions corresponding to the stopped–muon decay electrons, i.e., the convolutions* $erf^{\mathrm{TOF}} \times (Gauss^{\mathrm{stop}} \otimes Exp^{\mathrm{stop}})$ *are plotted as dashed lines.*

large for the front side LAAPDs, as confirmed by the fit results for the μp x rays, and also by the dependency of the mean slowing–down time on the mean range (Fig. 3.2, page 18). Therefore, it is not possible to simply sum the data from LAAPDs AB0, AB1 and AB2. On the other hand, a reasonable fit was obtained for the summed data of AB3 (left side of Fig. 7.8) and of AB5. The energy resolution of B4 is poor and the admixture of μp x rays did not allow a reasonable fit. For the LAAPDs AB6 to AB9, the peak–centroids variation is small. Hence, the data from these detectors were summed and then fitted (right side of Fig. 7.8). To ensure that the fit results of the summed spectrum agree with the fit results of the individual LAAPD spectra, the analogous summed spectrum was fitted also for the μp x rays.

7.1.1.2 Fit function for electron time spectra

The fitting functions for the electron time spectra are more complex, being the sum of four functions, two for both incoming and reflected muons. All functions represent muon–decay electron time spectra, but in one case the decaying muon is in flight and in the other case the muon is stopped near an LAAPD. The four fit functions are demonstrated on example of AB8 in Fig. 7.9.

The clear peaks in the electron time spectra are due to muons decaying in flight. Muons of all classes have to pass in front of A0 and B0, *i.e.*, the LAAPDs closest to the S_2 foil, where the trigger signal is produced. With increasing distance from S_2, the peak width naturally increases. Muons reflected at the gold surface loose a substantial part of their

energy, and a peak due to muon decay in flight following reflection is clearly seen only in the backside LAAPDs. However, a double peak structure in the A0/B0 x–ray time spectra proves that also some reflected muons reach the front part of the target.

As fit function for muon–decay–in–flight electrons a convolution, Eq. (6.3) page 68, of a Gaussian, Eq. (6.6), ($Gauss^{\mathrm{TOF}}$) with an *Exp* function, Eq. (6.4), (Exp^{TOF}) is used. The $Gauss^{\mathrm{TOF}}$ centroid and width, the exponential decay constant of the Exp^{TOF} function, as well as the peak intensity are all free fit parameters for both incoming and reflected muons. The centers of gravity of the $Gauss^{\mathrm{TOF}} \otimes Exp^{\mathrm{TOF}}$ convolutions are referred to as measured time–of–flights (TOF). As discussed above, the categorization incoming and reflected muons is based on the muon kinetic energy. However, a muon with sufficient energy to reach the gold surface and to be reflected, *i.e.*, in our terminology a reflected muon, can also decay before reaching the gold surface ($\mathrm{TOF}_{\mathrm{inc}}$ of a reflected muons in Fig. 7.6). In this case, the muon–decay electron would contribute to the first, earlier peak which in our terminology is due to the incoming muons. For simplicity we keep the terminology as defined above, keeping this effect in mind.

The continuous part of the spectra is due to stopped–muon decay electrons. As a fit function for these electrons again a convolution of a Gaussian $Gauss^{\mathrm{stop}}$ with an *Exp* function Exp^{stop} is used. A discrete distinction between the classes of muon–in–flight and stopped–muon decay electrons is not natural. A smooth overlap of both categories is obtained if the $Gauss^{\mathrm{stop}} \otimes Exp^{\mathrm{stop}}$ convolution is multiplied by the *erf* of the $Gauss^{\mathrm{TOF}}$, defined as:

$$erf^{\mathrm{TOF}}(t_{\mathrm{e}}) = \int_{-\infty}^{+t_{\mathrm{e}}} Gauss^{\mathrm{TOF}}(t_{\mathrm{e}})\, dt_{\mathrm{e}} \tag{7.2}$$

where t_{e} is the electron time.

The results obtained from the x–ray time spectra provide some restrictions to the fit parameters of the $Gauss^{\mathrm{stop}} \otimes Exp^{\mathrm{stop}}$ convolution. The sigma of the $Gauss^{\mathrm{stop}}$ is taken to be the same as the sigma used in the convolution fitting the x–ray time spectrum, both for incoming and reflected muons. The centroids could not be used directly. The peak centroids of the x–ray time spectra represent the time when the muon has already created a muonic atom and x rays were emitted from radiative transitions which dominate the latest parts of the cascade. The time difference between the μp and μN peak is mainly due to the long μp cascade time (§3.2) and can be roughly estimated to be about 40 ns; a more precise value is derived in §7.3.

The case of the stopped–muon decay electron time spectrum is a different situation. A muon with an energy still above the capture energy E_{cap}, but moving only within a small region in front of a particular LAAPD, can be considered as quasi–stopped, loitering muon. This means that the centroids obtained from the μN x–ray fits have to be shifted by a certain amount towards earlier times. This time shift, *i.e.*, the time interval within which a muon is considered to be quasi–stopped and later is referred to as the *virtual stop time*, can be estimated from two points of view. First, during this time the muon can only move within a region covered by the solid angle of one LAAPD. Its range is then of the order of a few cm, which corresponds to slowing–down times of about 100 ns (Fig. 3.2, page 18). Second, a muon remains within a small region, when large angle scattering becomes probable. As shown in Ref. [83], this occurs at muon energies $\sim$ 100–150 eV, which leads again to time shifts of 110 to 140 ns. Consequently, the $Gauss^{\mathrm{stop}}$ centroids were semi–fixed. In practice, the centroids of the 2 keV x–ray time spectra were taken, since it was not possible to fit the 3 keV x–ray time spectra for all LAAPDs. Then, the mean cascade time of 40 ns plus an additional 110 to 120 ns were subtracted. The

Exp^{stop} exponential decay time should ideally be 2.2 μs. In reality, this value is modified by different position– and time–dependent efficiencies of the electron detection. With a simple exponential fitted at later times (data after 1.5 μs), an average value of the decay time of 1.3 μs was obtained, and this value is used as a fixed fit parameter. The integral of the resulting function $erf^{\mathrm{TOF}} \times (Gauss^{\mathrm{stop}} \otimes Exp^{\mathrm{stop}})$ has to be proportional to the number of stopped muons and to the number of x rays. Therefore, the intensity ratio of these functions for incoming and reflected muons is different for each LAAPD and is fixed to the value of the ratio of the incoming to reflected–muon x–ray peak intensities.

The resulting fits of the electron spectra are shown in Fig. 7.3. The best agreement with the data is obtained for the LAAPDs placed in the central parts of the target. For AB0 and 1, there is a clear excess of the data at the times when the peak of the incoming muon–in–flight decay electrons is finishing. This is probably due to a class of slow muons stopping in the front parts of the target, which are not described by our simple model. As the peak of the incoming muon–in–flight decay electrons looses its dominance with increasing LAAPD number, the fitting function suffers from larger systematic errors. The contrary is valid for the fit of the peak due to the reflected muon–in–flight decay electrons, where the systematic error is smaller for the back end LAAPDs, even if its sharpness is not very well reproduced.

7.1.2 Fit results versus simple model

The different assumptions and simplifications used in our fit model, as described above, yield fit results with limited precision. Their uncertainty is in most cases dominated by systematic effects, and this is the reason why no statistical errors are shown in many of the following plots. In any case, our model gives relevant new information on a phenomenological and semi–quantitative level.

The most important fit results are the peak positions, their FWHM and the relative intensities for different LAAPDs. The intensities of the peaks of incoming and reflected muon–in–flight decay electrons versus LAAPD position are shown in Fig. 7.10 (left side). For the incoming muon case, the peak intensity is rather constant; some variations are probably not physical but due to systematic errors of the fit. For a given LAAPD this intensity is proportional to the number of by–passing muons and inversely proportional to their mean velocity. Both this number and velocity decrease downstream and the resulting intensity thus remains about constant. The time difference from the first to the last LAAPD is less than 100 ns, so the intensity variation of the peak due to muon decay is negligible.

The most important effect decreasing the peak intensity could be due to muons stopping in the gas. The fact that this is not observed suggests that the fraction of incoming muons which stop in the target is relatively small with respect to the total number of muons. The intensity of the reflected muon–in–flight decay electron peak is decreasing with increasing distance from the gold. The energy of a reflected muon is smaller and the probability to stop is higher. The FWHM of these peaks (right side of Fig. 7.10) increases with the time of flight, as expected.

The intensities of the μp x–ray peaks versus LAAPD position for incoming and reflected muons are shown in Fig. 7.11. For both incoming and reflected muon stops, the peak intensity increases with LAAPD number. A very small part of the incoming muons is stopped within the region seen by the first LAAPDs. The majority of the incoming muons is stopped at the downstream side of the target, which is seen by the LAAPDs AB6 to

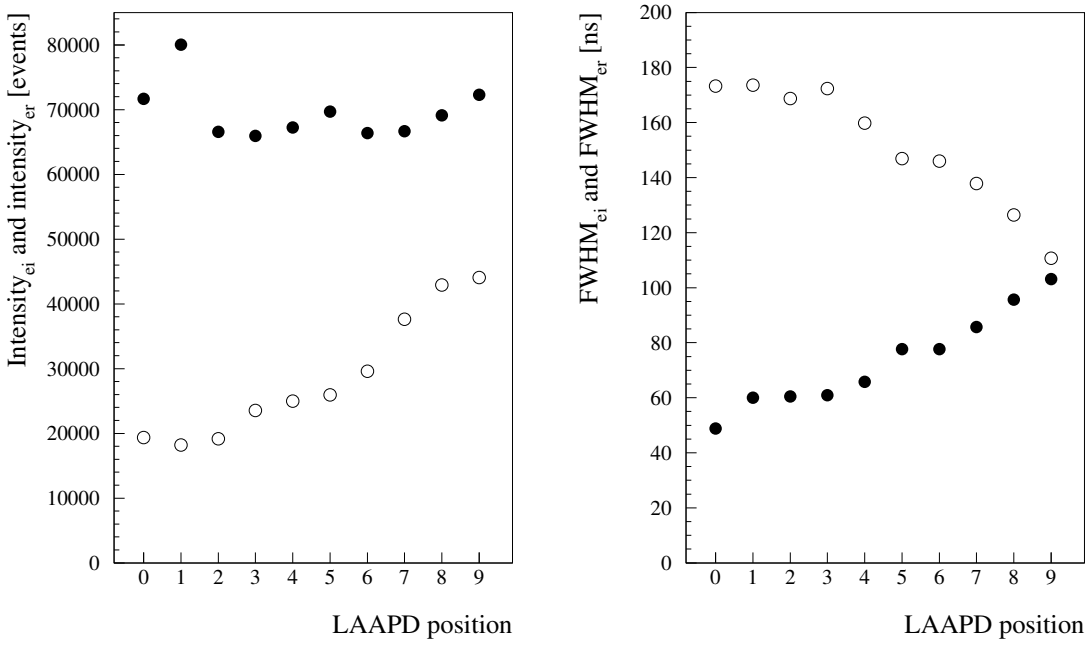

Figure 7.10: Intensities (left) and FWHM (right) of the peaks in the electron time spectra, due to incoming *(full circles) and* reflected *(empty circles) muon–in–flight decay electrons versus LAAPD position. The intensities are for the sum of the A and B side LAAPDs data.*

9. After being reflected at the gold surface, the number of reflected muon stops decreases smoothly. A striking systematic feature is that for the first LAAPDS, the B–side LAAPD peaks have higher intensities, while A–side LAAPD peaks have higher intensities for the back side LAAPDs. This is an indication that the muon beam was up to ∼1 mm misaligned with respect to the target axis.

The ratios of the x–ray peak intensities for reflected to incoming muons are shown in Fig. 7.12, both for μp and μN x rays. At the downstream of the target the number of incoming and reflected–muon stops is equal, while in the upstream the contribution from reflected–muon stops is 2 to 3 times higher.

The FWHM of the x–ray peaks are between 130 and 190 ns. The peaks due to reflected muon stops are in general wider than those due to the incoming muon stops, and the μp x–ray peaks are wider than the μN x ray peaks due to the μp cascade time (see §7.3).

The times of the peak centers of gravity (*cg*'s, as defined in Eq. (6.7), page 69), versus LAAPD position are shown in Fig. 7.13. The *cg*'s of the incoming muon–in–flight decay electron peaks, as well as of the μp and μN x–ray peaks are shown. The lines are the results of a simple simulation of the muon slowing and stopping processes. The simplified geometry indicated in Fig. 7.5 is used in the simulation. Muon time and path along the z–axis (parallel to the muon beam) are simulated. Incoming and reflected muons stopping in front of each LAAPD are considered separately. The muon stopping power in hydrogen gas, shown in Fig. 3.1, page 17, is used. The energy loss in the muon entrance window is calculated by adding the carbon stopping power [84] (92 weight–%) and the hydrogen stopping power (8 weight–%) (assuming that the stopping powers of oxygen and carbon atoms present in the formvar molecule are approximately the same). The parameters of the simulation are the average angles (momentum vector with respect to the beam axis)

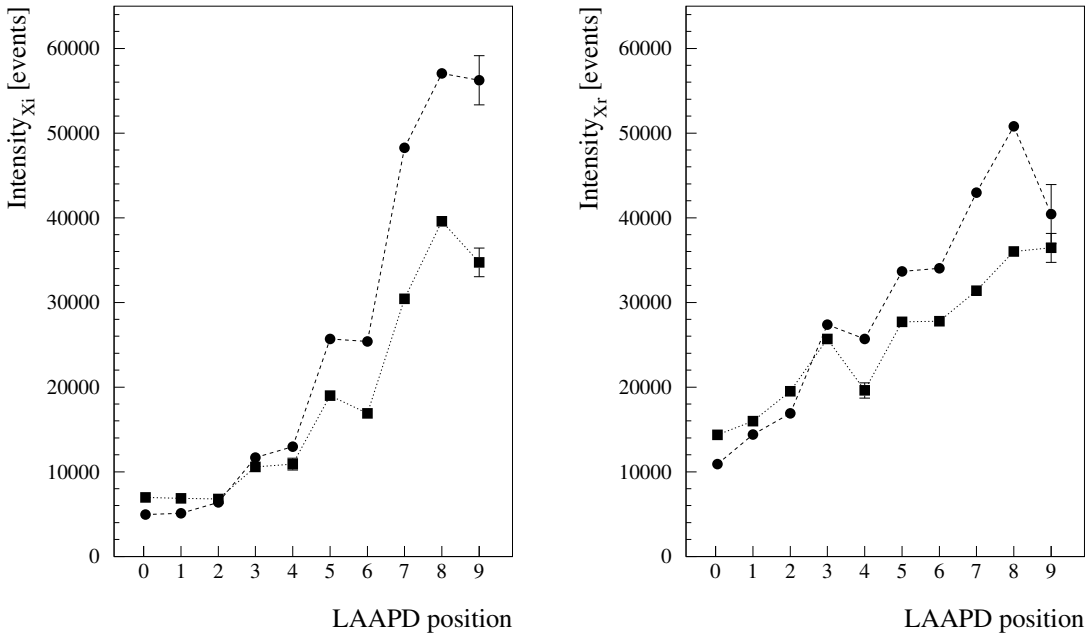

Figure 7.11: Intensity of the first (left) and the second (right) peak in the μp x–ray time spectra, due to incoming *and* reflected *muon stops, respectively, versus LAAPD position. Circles and squares represent A and B side LAAPDs, respectively.*

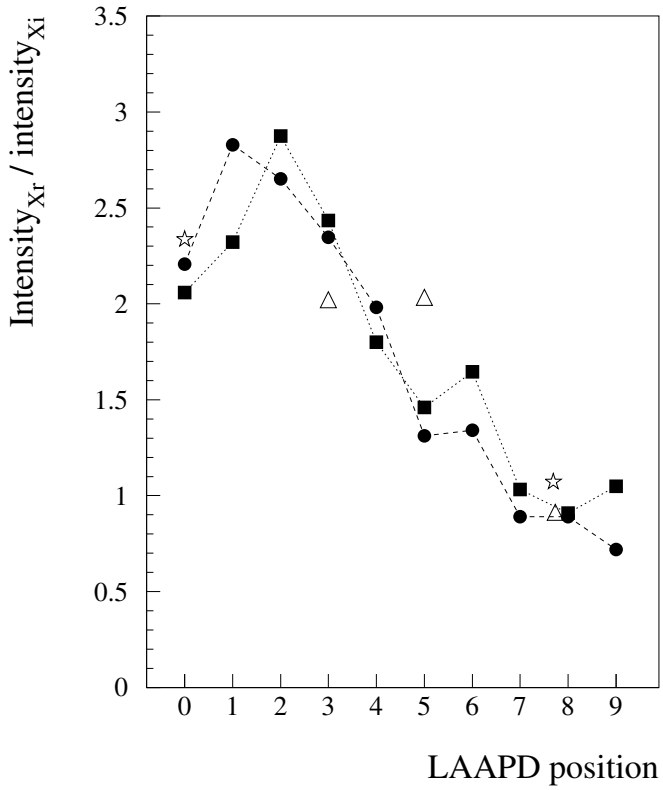

Figure 7.12: X–ray peak intensity ratios of reflected *to* incoming *muons, versus LAAPD position. Circles (A side LAAPDs), squares (B side LAAPDs), stars (summed data from A and B side LAAPDS) represent μp x rays; triangles μN x rays.*

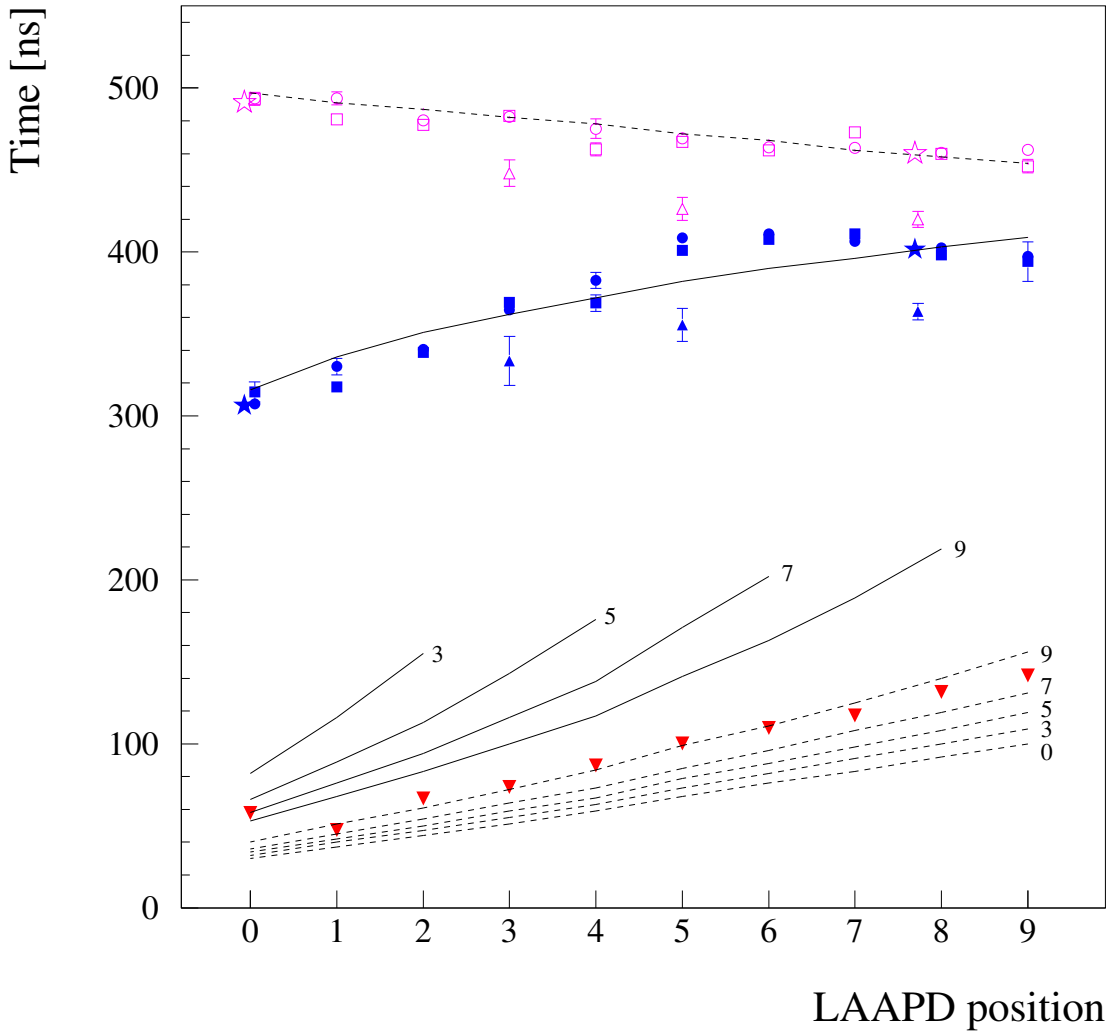

Figure 7.13: Centers of gravity of the fit functions for muon–in–flight decay electrons ($Gauss^{TOF} \otimes Exp^{TOF}$ due to the incoming *muons, measured TOF, red full downward triangles) and for x rays due to* incoming *(blue full symbols) and* reflected *(magenta empty symbols) muon stops versus LAAPD position. Circles, squares and stars represent the A, B and A+B side LAAPDs μp x–ray time spectra, respectively. Upward triangles represent the μN x–ray time spectra. Solid and dashed lines represent the simulations done for the* incoming *and* reflected *muons, respectively. Details in the text (page 109).*

of a certain muon class, the thickness of the formvar window (known only with limited precision), and the energy and angle modification of the reflected muons at the gold surface. In order to obtain the best agreement with the fit, the thickness of the formvar window is assumed to be 4.7 μg cm^{-2}, somewhat more than its nominal thickness of $(2 \pm 1)\,\mu$g cm^{-2} claimed by the manufacturer [82]. The mean angle in the vacuum is assumed to be 25°. The measured x–ray times from incoming muons stopping in the front parts of the target make it necessary to consider large angle scattering in the formvar foil. For incoming muons stopping in front of LAAPDs 0 to 9, the angle is thus assumed to decrease smoothly from 67 to 25 degrees. For all reflected muons an angle of 30 degrees is supposed before they reach the gold surface. After the reflection, large angles are considered for muons stopping in the back side of the target (60 degrees for A9/B9). For muons reaching

the more frontal target parts, the angle is smoothly diminished to 20 degrees at A0/B0. The energy distribution of the muons after the gold reflection is not known. An empirical model function

$$E_{\mathrm{Au}}^{\mathrm{out}} \approx 0.43\, E_{\mathrm{Au}}^{\mathrm{in}} + 165\,\mathrm{eV} \tag{7.3}$$

is used where $E_{\mathrm{Au}}^{\mathrm{in}}$ and $E_{\mathrm{Au}}^{\mathrm{out}}$ are the muon energies (in eV) before and after the reflection. The so–called virtual stop time (page 104), discussed above, is 111 ns, corresponding to a residual range of 3.1 cm and a muon energy of 104 eV. The average μp cascade time is taken to be 40 ns.

The calculated μp x–ray times for incoming and reflected muons are shown in Fig. 7.13 by the solid and dashed lines, respectively. The set of solid and dashed lines marked by a number are the time of flights ($\mathrm{TOF_{inc}}$, Fig. 7.6) for incoming and reflected muons, respectively; the number refers to the LAAPD in front of which the muon with the particular kinetic energy stopped. For the reflected muons the time of flight $\mathrm{TOF_{ref}}$ (Fig. 7.6) is not shown. The measured time–of–flights are not supposed to agree with any of the simulated curves in the lower part of the Fig. 7.13, but rather with a suitably weighted superposition of these curves, a task which is beyond the limits of the present simple simulation model. The measured μp x–ray times agree both for incoming and reflected muons quite satisfactory with the corresponding calculated curves (upper part of the Fig. 7.13). This indicates that at least the mean values of the peaks in the time spectra are well reproduced by our model.

The initial muon energy for time zero, *i.e.*, just at the exit of the S_2 foil, results from the simulation using the parameters given above. For incoming muons stopping in front of the LAAPDs 0 to 9, this energy increases from 50 to 450 eV. For the reflected muons this energy depends strongly on the function defining the energy loss in gold. Taking into account Eq. (7.3), it varies from 3550 to 3950 eV for LAAPDs 9 to 0, respectively. The initial energies of the reflected muons reaching the front parts of the target are obviously higher than the energies of the muons stopping at the back side. Table 7.1 summarizes the energies of the incoming and reflected muons stopping in front of LAAPDs 0, 3, 6, and 9, namely the energies at time zero, at the entrance and the exit of the formvar window

Table 7.1: Calculated energies, given in eV, of the incoming *and* reflected *muons stopping in front of LAAPDs A(B) 0, 3, 6, and 9, respectively.* E_{S2}, $E_{\mathrm{formvar}}^{\mathrm{in}}$, $E_{\mathrm{formvar}}^{\mathrm{out}}$ *are the energies with which the muon is exiting the S2 foil, entering and exiting the muon entrance window, respectively.* $E_{\mathrm{Au}}^{\mathrm{in}}$ *and* $E_{\mathrm{Au}}^{\mathrm{out}}$ *are the energies just before and after the gold reflection.*

Incoming Muons					
LAAPD	E_{S2}	$E_{\mathrm{formvar}}^{\mathrm{in}}$	$E_{\mathrm{formvar}}^{\mathrm{out}}$		
0	50	3550	530		
3	65	3570	830		
6	240	3740	1090		
9	450	3950	1300		
Reflected Muons					
LAAPD	E_{S2}	$E_{\mathrm{formvar}}^{\mathrm{in}}$	$E_{\mathrm{formvar}}^{\mathrm{out}}$	$E_{\mathrm{Au}}^{\mathrm{in}}$	$E_{\mathrm{Au}}^{\mathrm{out}}$
9	2110	5610	2460	550	400
6	3420	6920	3510	1290	720
3	4360	7860	4290	1920	990
0	5180	8680	5010	2520	1240

for both incoming and reflected muons; for the reflected muons the energies before and after the gold reflection are also listed. From the agreement of the simulation with the data and from the intensity ratios shown in Fig. 7.12 it can be concluded that more than 60%, and probably as much as 80%, of the muons reaching the gold surface are reflected, loosing about half of their energy. To obtain more precise values about this reflectivity would need further experimental and theoretical investigation, but this was not the aim of our experiment.

7.2 Search for the μp$(2S-2P)$ resonance line

The aim of the μp$(2S)$ Lamb shift experiment, *i.e.*, a 30 ppm measurement of the μp$(2S-2P)$ resonance line, was described in Chapter 2. Particular details of the analysis, not described in the more general Chapter 6, together with the results and their discussion are given here.

The data from all 20 LAAPDs are used in the search of the laser induced μp K_α x rays, *i.e.*, not only the group of best LAAPDs. Only the L_{ON} data which contain L_{ON} and L_{OFF} events (§5.3) were considered: the L_{OFF} events are used for background studies, the L_{ON} events for the search of laser induced μp K_α x rays. The L_{ON} events represent ∼30% of the L_{ON} data. In total, nearly 1.1 million K–line x rays were detected. Energy and time calibrations are in detail described in §§6.4 and 6.3, respectively. The appropriate energy cuts for the μp K_α x rays were studied, and the values applied are shown in Fig. 7.14. The low–energy cut is in the interval from 1.3 to 1.6 keV, chosen for each LAAPD individually in order to accept as few low–energy background signals as possible, the level for which varied for each detector. The upper–energy cut is set for all LAAPDs at 2.6 keV which

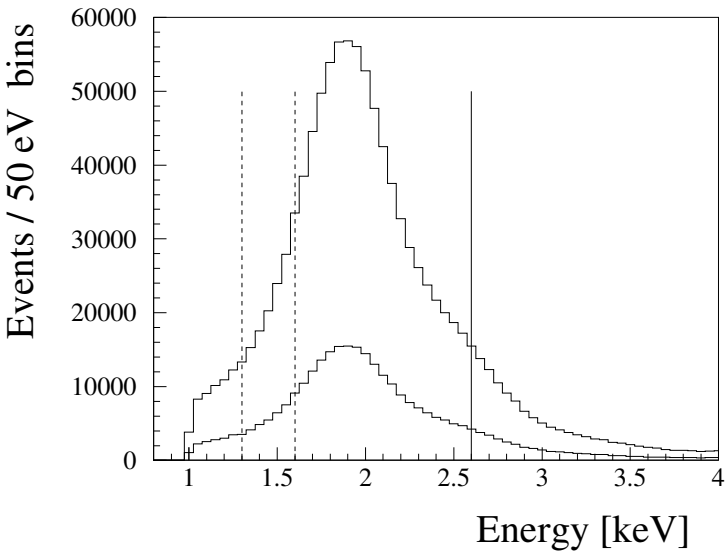

Figure 7.14: Two energy spectra of the x rays from the xe *event class, summed for all 20 LAAPDs. The higher statistics histogram shows all* L_{ON} *data (*L_{ON} *and* L_{OFF} *events). About 30% of the data included in this peak are due to the* L_{ON} *events, shown separately as the lower–statistics spectrum. The* del_e *cut is applied to both spectra. The vertical lines indicate the energy cuts used in the search of the laser induced* μp K_α *x rays. The two dashed lines represent the spread of the low–energy cut for different LAAPDs, while the solid line marks the high–energy cut common for all diodes.*

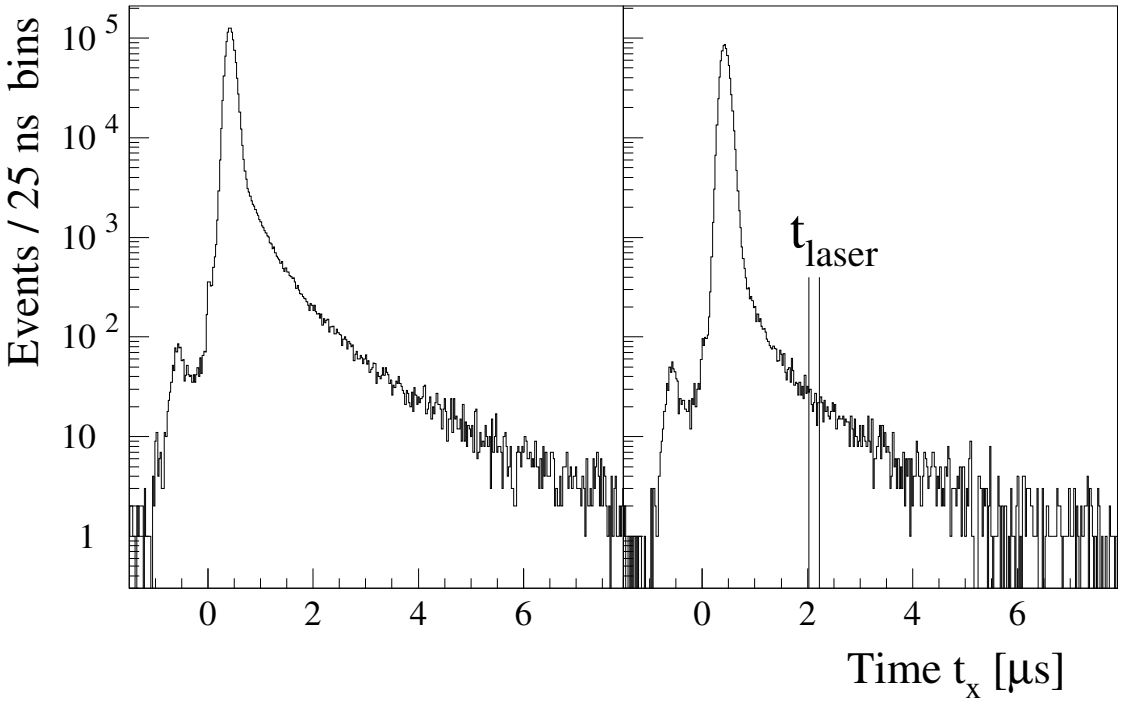

Figure 7.15: Time spectra of the x rays from the xe *event class, summed for all 20 LAAPDs and both* L_{ON} *and* L_{OFF} *events. The* del_e *and* $\mu^{2^{nd}}$ *cuts are applied. (Left) All x–ray energies are accepted. (Right) Only the signals fulfilling the* μp K_α *energy cut are considered. The two vertical lines demonstrate the approximate position of the time window in which the laser induced x rays were expected. It is approximate because the laser arrival time varied from event to event and thus had to be considered for each event individually.*

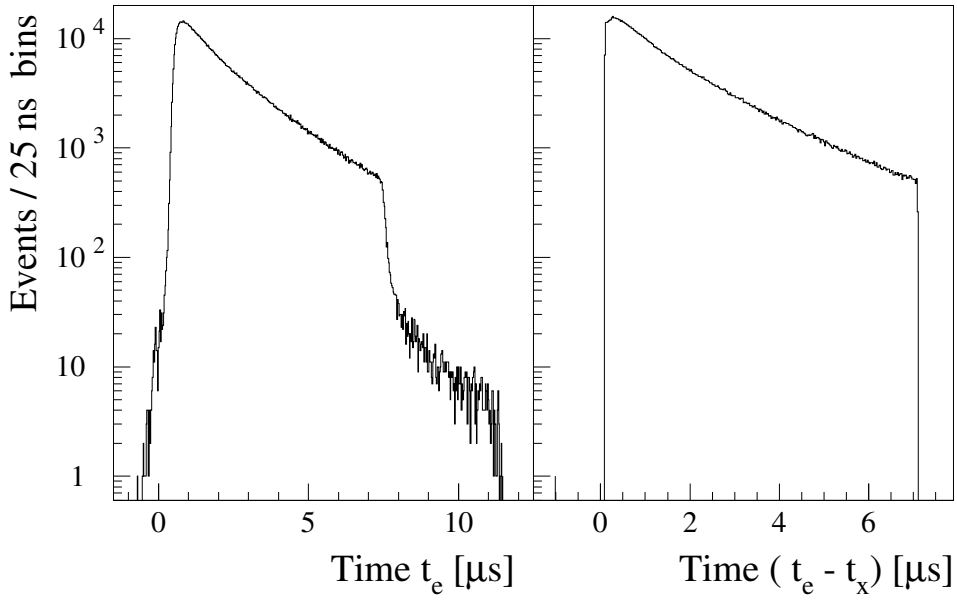

Figure 7.16: Time spectra of all electrons from the xe *event class, summed for both* L_{ON} *and* L_{OFF} *events. (Left) Spectrum of the time* t_e*. The edge at times from* $\sim$ *7.5 to 8.0* μs *is due to the* del_e *cut. (Right) Time zero is defined by the x–ray time* t_x*, i.e., the time difference* $(t_e - t_x)$ *is histogrammed. The* del_e *cut with the parameters* $t_1^{dele} = 0.1$ μs *and* $\Delta t^{dele} = 7$ μs *causes the sharp limits in this spectrum.*

includes most of the 1.9 keV x–ray signals even for LAAPDs with poor energy resolution. The energy cuts were set asymmetrically with respect to the 1.9 keV K_α line because the relevant background (at delayed t_x) increases towards lower energies (c.f., bottom part of Fig. 6.31, page 89). In the rest of this Section, x rays within these energy cuts will be referred to as the signals with the μp K_α energy cut. The parameter Δt_{same} is set to 100 ns, as justified in the bottom part of Fig. 6.10, page 64. In order to accept as many LAAPD signals due to muon–decay electrons as possible, the parameters E_x^{hi} and E_e^{low} (§6.2) were set to 6.0 keV. A lower value could not be used because of the relatively abundant $\mu C(4 \rightarrow 3)$ x rays having an energy of 4.895 keV (bottom part of Fig. 6.32, page 91). The del_e cut is applied with the parameter t_1^{dele} set to 100 ns, *i.e.*, the same value as used for Δt_{same}. Due to the categorization of the event classes (Table 6.1, page 63), making a reasonable preselection of the "good events", it is possible to use a large time window for the del_e cut by setting the parameter Δt^{dele} to 7 μs (Fig. 6.10, page 64). The μ^{2nd} cut is also applied.

The xe event class represents $\sim 92\%$ of the events accepted for the analysis when the mentioned cuts are applied. The remaining part of the accepted data is dominated by the xee event class ($\sim 7\%$). The rest, less than 1%, is the contribution of the xx category. In the following, all three categories are described in order to justify this choice in the search for the resonance line. The contribution of early μp x rays (first signal) followed by a muon–decay electron (second signal) is dominant for all three categories. The level of the delayed background, *i.e.*, the number of delayed signals in the time window from 1.5 to 3.5 μs normalized to the number of the early signals (from 0.155 to 0.655 μs, c.f. Fig. 6.13, page 67), was studied for the x rays (for all three categories, always the first signal) fulfilling the μp K_α energy cut. For the xe, xee and xx category this ratio is (2.44, 1.26, and 1.40) $\times 10^{-3}$, respectively. It should be stressed that this ratio is used only to compare the background level of the three categories and cannot be directly used as the background level for the laser induced events. The 2 μs time interval of the delayed events is chosen in order to increase the statistical precision; the laser time window is only 200 ns wide, as will be discussed later on in this Section.

The xe category is dominated by events when the first signal is due to a μp K–line x ray and the second signal due to a muon–decay electron. The del_e cut is applied on the time difference $t_e - t_x$. The x–ray energy and time spectra are shown in Figs. 7.14 and 7.15, respectively, while the electron time spectra are shown in Fig. 7.16. The $(t_e - t_x)$ spectrum shows a 20%–increase for the first 300 ns and then an exponential behaviour with a time constant of approximately 1.3 μs. This deviation from the expected value of 2.2 μs (muon lifetime) is due to an increase of the solid angle for electron detection when the μp$(1S)$ atoms drift to the target walls where μC atoms are formed (2 μs lifetime), or μZn/μSe atoms ($\sim$ 200 ns lifetime) when the laser cavity mirrors are hit. The short muon lifetime in those higher–Z materials reduces the number of muon–decay electrons detected at times $(t_e - t_x)$ larger than 0.5 μs. The apparent lifetime of 1.3 μs is therefore not to be considered as "muon lifetime" but rather as a time–dependent reduction of the number of available muons which could decay to electrons.

There is a not negligible probability that after the μp x ray and the muon–decay electron detection, another signal is detected; to recall, the length of the EVG gate is 12 μs which is long compared to the muon lifetime of 2.2 μs. This "third" signal is usually not correlated with the muon causing the $S_1 \cdot S_2 \cdot \bar{D}_3$ trigger and is mainly due to electrons. Its origin can be correlated, *e.g.*, with the decay of another muon, which could enter the system within the EVG gate, and was most probably not recognized by the μ^{2nd} cut (either

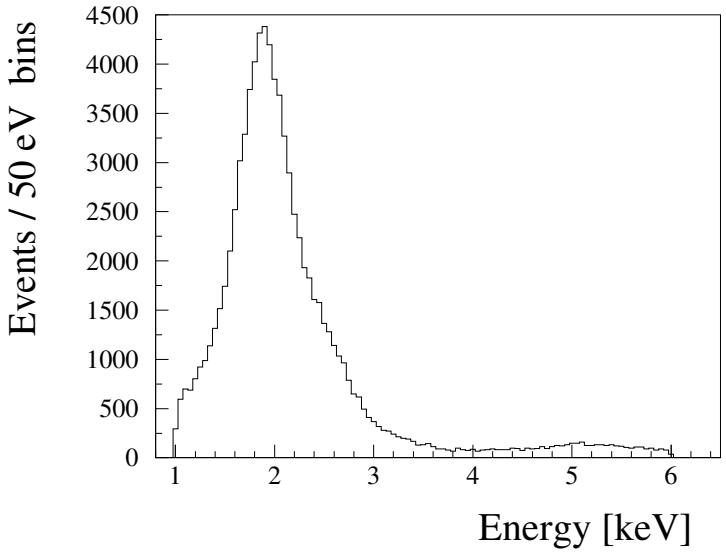

Figure 7.17: Energy spectrum of the x rays from the xee *event class, summed for all 20 LAAPDs and both* L_{ON} *and* L_{OFF} *events. The* del_e *cut is applied. The large peak is due to the* μp *K–series x rays. The small peak around 5 keV is due to the* $\mu C(4 \rightarrow 3)$ *transition.*

it was not detected by the S_1 detector, or did not produce a μp x ray, or such an x ray was not detected). If this happens after the detection of both the μp x ray and the electron from the first muon decay, there is no reason to reject such an event. The xee event class represents this case. The x–ray energy spectrum in Fig. 7.17 proves that the majority of x rays from this event class originates from μp atoms. The time spectra of all three signals are shown in Fig. 7.18. In the x–ray time spectrum, there is a dominant peak at early times, due to the μp x rays from the direct muon cascade. The first–electron time spectrum has the same characteristics as the electron time spectrum from the xe event class (Fig. 7.16) and confirms that the first electron is correlated with the first muon. Therefore, the del_e cut is applied with respect to the first–electron time. The second–electron time spectrum is flat, proving that the second electron is not correlated with the first muon.

The energy and time spectra of the signals from the xx event class, shown in Figs. 7.19 and 7.20, respectively, clearly demonstrate the origin of both signals. While the first signal is mainly due to μp x rays, the second signal has the characteristics of muon–correlated electrons measured in a LAAPD. Indeed, the second signal is, in the majority of cases, not due to an x ray, but due to a muon–decay electron depositing in a LAAPD an energy lower than the E_x^{hi} threshold (set to 6 keV). Therefore, the xx case is an analogous to the xe event class. Here, however, the electron was not detected by any of the electron detectors, but only by a LAAPD.

In the search for the $2S-2P$ resonance, the events from the xe, xee and xx classes were summed. As demonstrated in Fig. 6.16, page 71, the timing of the laser pulse with respect to the trigger signal was not stable (in the middle of the data acquisition period the internal delay of the excimer laser was successfully reduced by ~ 200 ns). As a consequence for the analysis, it was necessary to define a laser time window individually for each L_{ON} event. The start of the laser time window t_{laser} (the time when the 6 μm laser light arrived at the mirror cavity) is defined relative to the timing of the V_2 signals, detected for each L_{ON} event. The time calibration of the V_2 TDC signals is described in §6.3. To recall, it

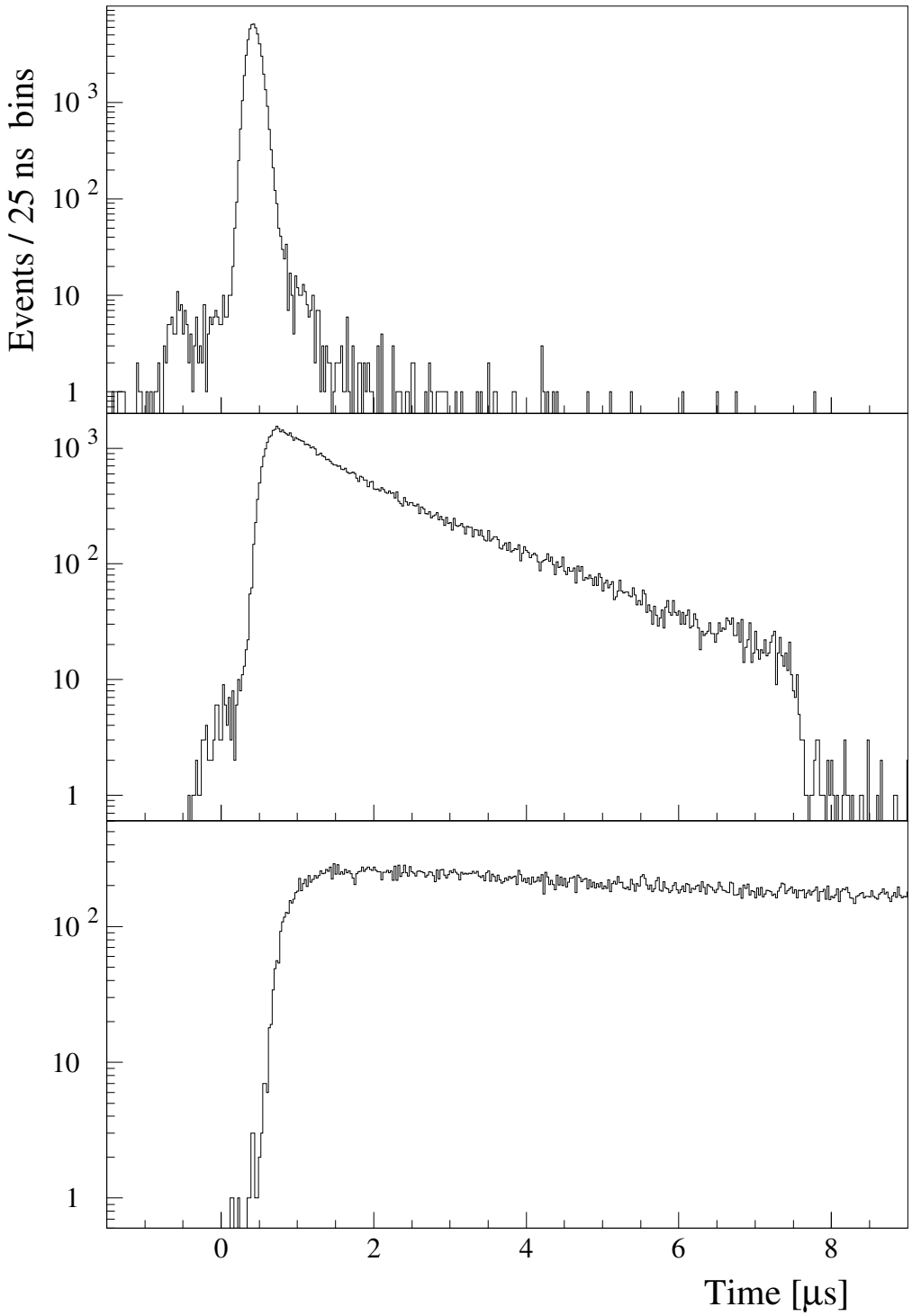

Figure 7.18: Time spectra of the signals from the `xee` *event class, summed for all 20 LAAPDs and both* L_{ON} *and* L_{OFF} *events. Top: Time spectrum of the x rays fulfilling the* μp K_α *energy cut. Middle: Time spectrum of the first electron, being a decay electron of the muon creating the* μp *atom (of which the* K_α *x ray was detected, top spectrum). The edge at times from* $\sim$ *7.5 to 8.0* μs *is due to the* del_e *cut. Bottom: The time spectrum of the second electron signal. Its almost flatness confirms that the second electron is not correlated with the first muon.*

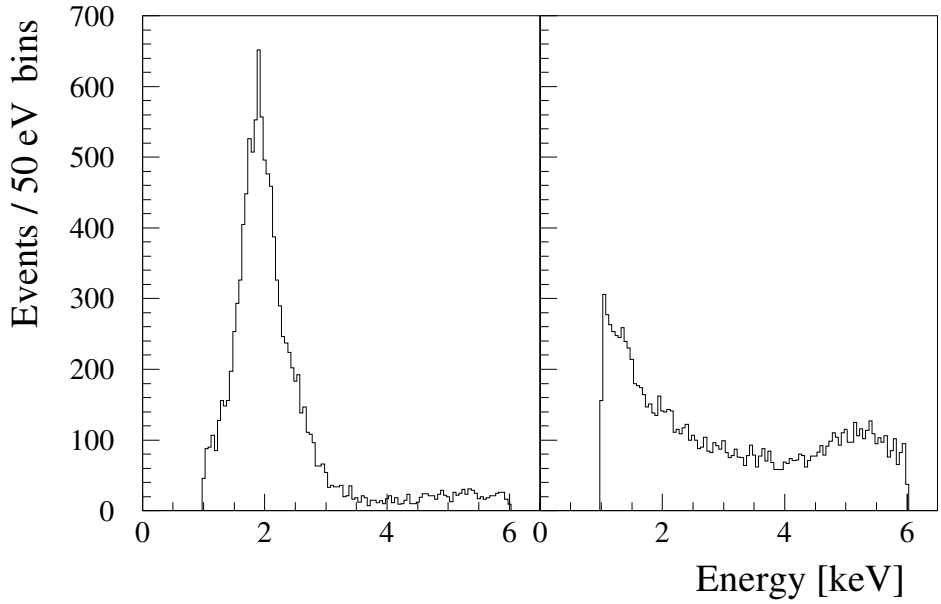

Figure 7.19: Energy spectra of the signals from the xx *event class, summed for all 20 LAAPDs and both* L_{ON} *and* L_{OFF} *events. Left: Energy spectrum of the first signal, dominated by the peak due to* μp *K–line x rays. Right: Energy spectrum of the second signal from the* xx *class. It has a continuous shape with the same characteristics as the low–energy part of the LAAPD electron energy spectrum in Fig. 6.25. Therefore, the second signal from the* xx *event class is mainly due to electrons depositing in an LAAPD an energy lower than the* E_x^{hi} *threshold (set to 6 keV). The small peak at* ~ 5 *keV is due to* $\mu C(4 \rightarrow 3)$ *x rays.*

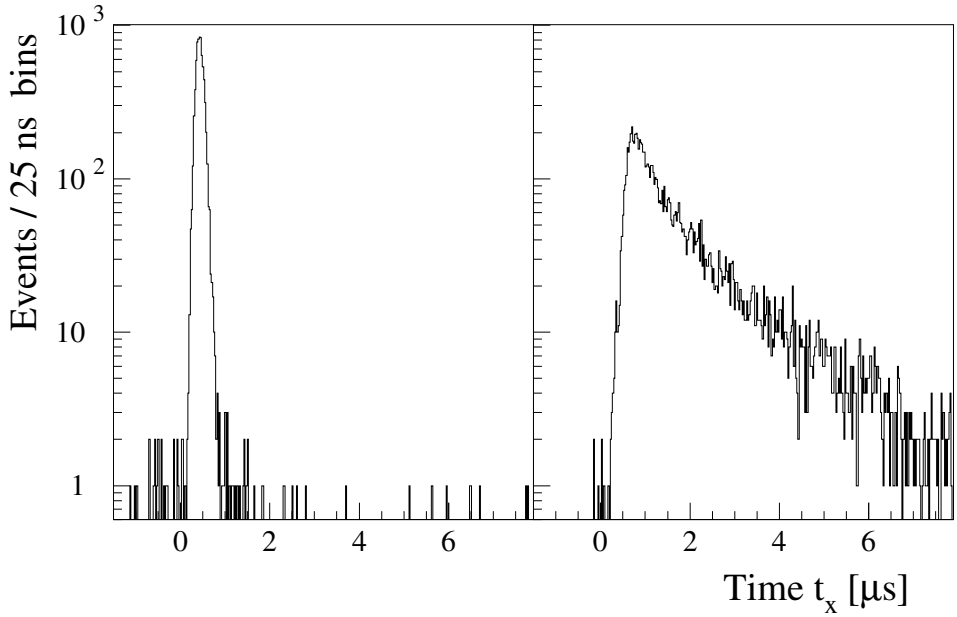

Figure 7.20: Time spectra of the signals from the xx *event class, summed for all 20 LAAPDs and both* L_{ON} *and* L_{OFF} *events. Left: Time spectrum of the first signal, characterized by the peak of the* early μp *x rays. The* μp K_α *energy cut is applied. Right: Time spectrum of the second signal. It has the same characteristics as the previous correlated–electron time spectra (left part of Fig. 7.16, or middle part of Fig. 7.18).*

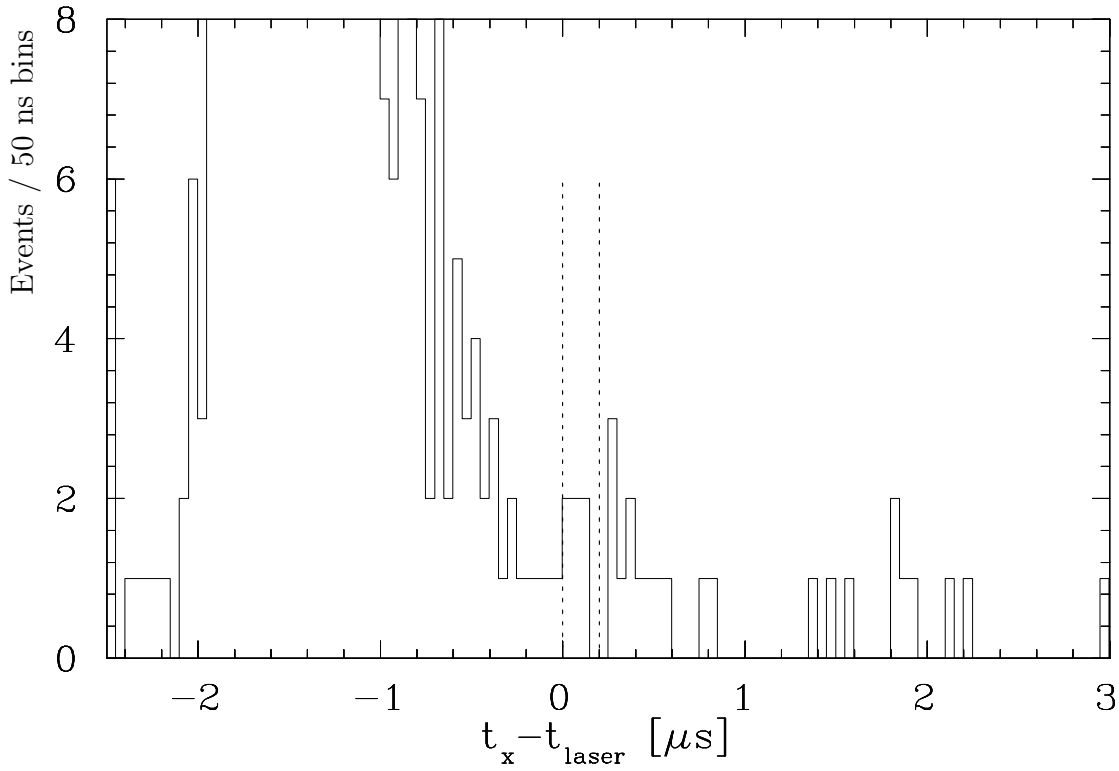

Figure 7.21: An example of a "shifted" time spectrum of the x rays with the μp K_α energy cut (50 ns/bin) for L_{ON} data from all LAAPDs, measured for one particular laser wavelength, corresponding to FP = 282 843. Time zero represents the time of the laser arrival to the mirror cavity. The two dotted vertical lines show the 200 ns wide time window in which the search of the laser induced μp K_α x rays was performed. The number of the early *x rays in this spectrum is* 2.1×10^4.

is based on the determination of the relative time offsets Δt_{V_2}between the time when the red laser light used in the calibration measurement (and having the same timing as the 6 μm laser) is detected by an LAAPD and the V_2 TDC signal. For each L_{ON} event, the x–ray time t_x, the V_2 time t_{V_2} and the relative offset Δt_{V_2} (different for each LAAPD) are known. It is therefore possible to construct the so called "shifted" time spectra with the time $\tilde{t}_x$ defined as

$$\tilde{t}_x = t_x - t_{laser} = t_x - (t_{V_2} + \Delta t_{V_2}) \tag{7.4}$$

where the time zero is defined by the laser arrival time t_{laser}. Such a shifted time spectrum is constructed for the x rays fulfilling the μp K_α energy cut separately for each laser wavelength (each FP fringe value). An example of such a spectrum is given in Fig. 7.21 for FP=282 843. Laser induced μp K_α x rays were searched for in a time window from $\tilde{t}_x = 0$ to $\tilde{t}_x = 200$ ns. The width of 200 ns is chosen according to the light confinement time of the mirror cavity of $\sim$ 145 ns (Fig. 4.11, page 40). Figure 7.22 shows the measured number of events in this laser time window, normalized to the number of early events, for each laser wavelength.

It is important to estimate the number of background events in the laser time window. This has to be done individually for each FP, since the internal laser delay was not constant,

while the delayed background has an exponential shape (Fig. 7.15), and the measuring time for each FP was different. The background of delayed 2 keV x rays is a superposition of several effects:

1. μp($1S$) atoms drift within typically 1 μs into the window foils ($(CH_2)_n$) of the gas target. After muon transfer, some μC x-rays are emitted at 5 keV and higher energies, with tails in the LAAPD energy spectrum down to 2 keV. The muon lifetime in carbon is still of the order of 2 μs.
2. In some cases, a signal within the μp K_α energy cut is uncorrelated to the first muon (*e.g.* neutron–induced), whereas the electron originates from the decay of that muon.
3. In other cases, a signal within the μp K_α energy cut is caused by bremsstrahlung from muon decay and is thus correlated, whereas the electron is uncorrelated.
4. There is a small component where the x-ray as well as the electron are uncorrelated to the first incoming muon, corresponding to a flat component. This effect is mostly caused by second muons entering the gas target without triggering S_1.

No significant difference is found when the analogous spectra of L_{ON} and L_{OFF} events are compared. It is therefore assumed that the background has the same shape in both cases, so that the large statistics accumulated for L_{OFF} events can be used for a precise determination of the background in L_{ON} events. The delayed background $\mathcal{B}$ in the unshifted x–ray time spectrum of L_{OFF} events (μp K_α energy cut applied), summed for all three event categories, can be fit by a sum of two exponential functions and a constant background:

$$\mathcal{B}(t_x) = A \left[\exp\left(\frac{-t_x}{0.96\,\mu s}\right) + 14.1 \exp\left(\frac{-t_x}{0.31\,\mu s}\right) + 0.0074 \right], \tag{7.5}$$

where A is the amplitude optimized for the data and studied for different bin widths. This equation is a purely empirical fit, and no attempt was made to disentangle the background types 1–4 which have different time slopes. Additional distortion of $\mathcal{B}(t_x)$ originates from radiative quenching of μp($2S$) atoms (with ∼150 ns lifetime) and the time–dependent efficiency of the μ^{2nd} cut. In turns out that $\mathcal{B}(t_x)$ is composed of several exponentials with different time constants, but for our purpose the parametrization chosen for Eq. (7.5) is sufficient.

The total number of early signals in the fitted spectrum is 565 220. For each run (data file) an average value of the V_2 time t_{V_2} is calculated, and the background $\mathcal{B}(t_x)$ is transformed to the function $\mathcal{B}(\tilde{t}_x)$, using the average t_{V_2} and Δt_{V_2} values (Eq. (7.4)). The integrated background in the time window from $\tilde{t}_x = 0$ to $\tilde{t}_x = 200$ ns is calculated and then scaled according to the number of L_{ON} early signals in the studied run. The background from all runs with the same laser wavelength is summed. The resulting ratio of background signals (in the $\tilde{t}_x = 0$ to $\tilde{t}_x = 200$ ns time window) normalized to the number of early signals varies between 2.5×10^{-4} and 3.0×10^{-4} for the different laser wavelengths (see Fig. 7.22). Averaged over all wavelengths, the ratio is $(2.8 \pm 0.2) \times 10^{-4}$.

The expected rate for laser–induced x rays (on resonance), relative to the early signals, can be calculated as the product of the following numbers:

1. *relative population of the slow* $2S$*–component* (0.011 ± 0.002);
2. *occupation probability of the* $F = 1$ *hyperfine level* (0.75);
3. $2S - 2P$ *transition probability in the mirror cavity* (0.30 ± 0.06)
   This probability contains three factors. First, the transition probability for the

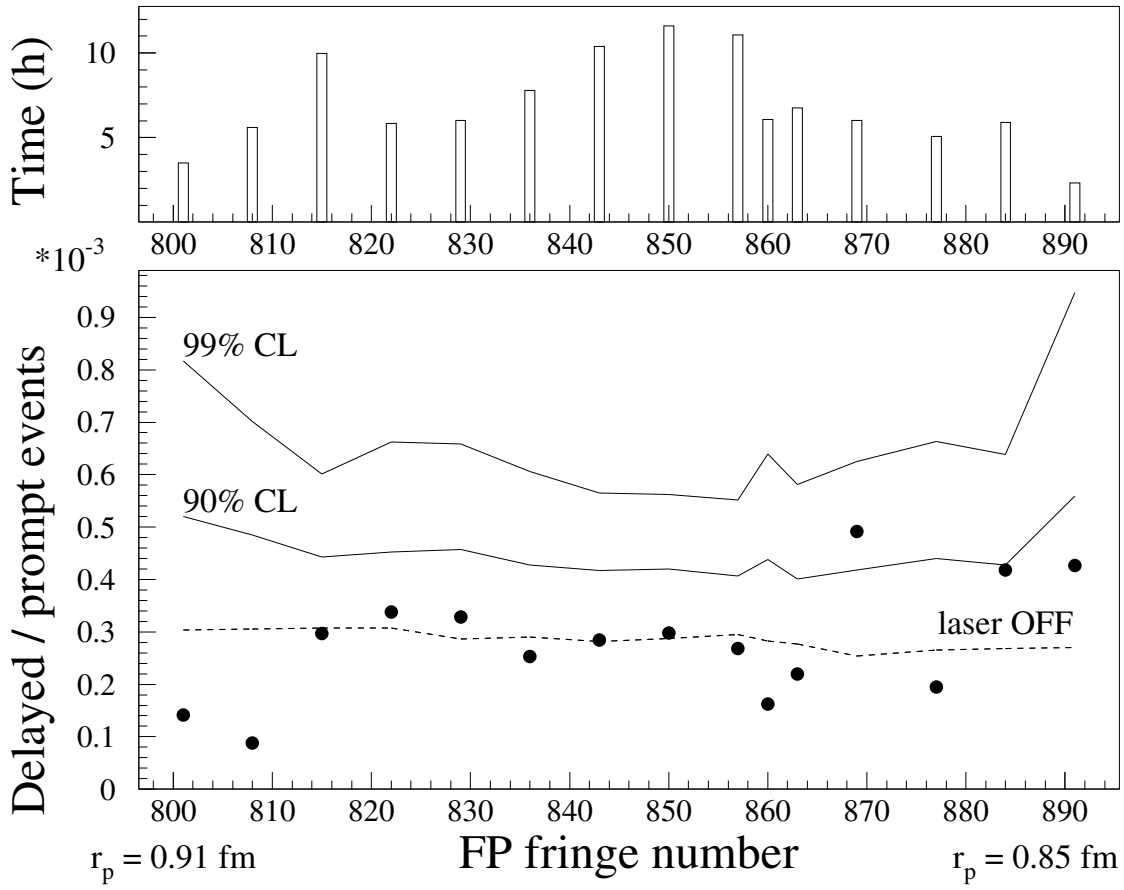

Figure 7.22: Result of the search for the $2S-2P$ resonance line. Black dots are the number of measured events in the 200 ns wide laser time window normalized to the number of early *events. The FP fringe number (with an offset of 282 000) is a measure for the laser wavelength. The scanned region corresponds to rms proton charge radii in the interval from 0.85 to 0.91 fm. The dashed line shows the expected number of background events. The confidence levels are for the hypothesis that only background is present, calculated with the Poisson distribution function. The upper plot shows the approximate measuring time per FP value (real measuring time corrected for beam– and laser–intensities fluctuations).*

average laser–pulse energy of 0.2 mJ at the exit of the Raman cell is approximately $1-1/e = 0.63$. The laser light is uniformly distributed in the mirror cavity approximately 20 ns after the $t_{\rm laser}$ entrance time. The transition probability in the remaining $200-20 = 180$ ns, considering the measured (140 ± 10) ns light decay time in the cavity, is thus $1-\exp(-180/140) \approx 0.7$. Finally, the light losses due to the sub optimally filled cavity were about 25%. In total, $0.63\times0.7\times(1.00-0.25) \approx 0.3$.

4. *$2S$-survival probability* (0.32 ± 0.06)
   $\exp(-1.52\,\mu{\rm s}/1.32\,\mu{\rm s}) = 0.32$, where 1.52 μs is the average delay time of the laser arrival with respect to the early signals, and (1.32 ± 0.24) μs is the lifetime of the slow $\mu{\rm p}(2S)$ component at the employed hydrogen pressure of 0.6 hPa.
5. *drift factor* (0.45 ± 0.10)
   The probability that the $\mu{\rm p}(2S)$ atom did not drift out of the laser–irradiated volume before the laser light arrived is estimated to be $f_{\rm drift} = 0.45$. This number was determined by a Monte Carlo calculation, using the elastic cross sections calculated

by T. S. Jensen [85]. The uncertainty of $f_{\rm drift}$ was estimated using different assumptions for the calculation of these cross sections.

The resulting ratio for the number of expected laser–induced μp K_α x rays (on resonance), relative to the number of early signals, is thus $0.011 \times 0.75 \times 0.3 \times 0.32 \times 0.45 = (3.6 \pm 1.5) \times 10^{-4}$. Therefore, the expected ratio of effect to background (based on the calculated effect and the measured background) is $3.6 \times 10^{-4}/2.8 \times 10^{-4} = 1.3$, *i.e.*, around unity.

The final result of the 2003 run is shown in Fig. 7.22. The number of $L_{\rm ON}$ signals measured in the laser time window divided by the number of early $L_{\rm ON}$ signals is plotted for each wavelength (shown in units of the FP fringe number). In this way, the number of delayed events is normalized to the true number of useful laser shots at this wavelength. The expected number of background events, normalized similarly, is shown as the dotted line "laser OFF". The lines "90% CL" and "99% CL" indicate the 90 and 99% confidence levels for the hypothesis that the data contains only background. The confidence levels are calculated for a Poisson statistical distribution with the expected number of background events as mean value. The top graph shows the approximate measurement time for each wavelength.

No resonance is seen in Fig. 7.22. Such a line is expected to have an amplitude of 3.6×10^{-4}, as discussed above, and a full–width at half–maximum of 14 in units of FP fringe numbers, *i.e.*, at least two data points should be higher than the average. On the other hand, the line amplitude may be as low as $\sim 2 \times 10^{-4}$, and the statistics are too low to exclude the existence of a resonance effect in the wavelength range of our measurements. It can be concluded that the statistics are too low to make any positive or negative statement.

About 2000/hour of the $L_{\rm ON}$ early μp x rays were detected. The rate expected for laser events on resonance is therefore $\sim$ (2000/h $\times(3.6 \times 10^{-4})) = (0.7 \pm 0.3)$/h which is insufficient for the search of the resonance line. There are three main factors which lowered the rate of expected good laser–induced events to a value smaller than expected. A factor 2 was lost because a lithium foil had to be installed in front of the LAAPDs in order to protect them from alpha particles emitted by the ThF_4 dielectric coating of the laser cavity mirrors (§4.4). Another loss–factor of at least 2 is caused by the too long internal delay of the excimer lasers (§4.3). The additional drift loss factor $f_{\rm drift}$, as discussed just above, was found only recently. These effects reduced the rate of good events from 4/hour to less than 1/hour which is too low for the limited measuring time of $5 - 10$ hours per wavelength.

7.3 Lifetime and population of the μp$(2S)$ state

The aim of the analysis described in this section is to extract new information about

- the cascade time in the μp atom (§3.1.2)
- the population and lifetime of the fast component of the μp$(2S)$ state (§3.1.3)

The analysis is based on an analysis of the following three highly–correlated spectra:

1. time spectrum of the μN$(5 \rightarrow 4)$ x rays (3.1 keV),
2. time spectrum of the μp $K_{\rm rest}$ line (2.4 keV),
3. time spectrum of the μp K_α line (1.9 keV).

The method by which these spectra are deduced from the data is described in §7.3.1. The details about the appropriate fit functions and fitting procedure are given in §7.3.2, while the final results are discussed in §7.3.3. The basic ideas of the analysis are, firstly, that the μN time spectrum corresponds to the times when the muonic atoms (μN or μp) are formed (*i.e.*, the muon slowing down times, from passing S_2 until atomic capture). The μN cascade time is negligibly short ($\sim 10^{-10}$ s, §3.2). Second, the μp K–lines have the same time distributions but convoluted by their cascade time distributions (not necessarily similar for K_α and K_{rest}). Third, radiative quenching of $2S$ states (Eq. (3.20), page 24) would show up in the K_α but not in the μp K_{rest} spectrum.

7.3.1 Time spectra of the μN and μp x rays

It is crucial that the background level in the three spectra mentioned above is minimized. There are various classes of background, *e.g.*, x rays correlated to muon decay or to $\mu p \rightarrow \mu C$ transfer processes, which have different time distributions and contribute with unknown relative weights to the three time spectra. Formerly employed cuts, as *e.g.*, energy or del_e cuts (see Chapter 6), are not sufficient to reduce the background to an acceptable level.

Here, an indirect construction of these spectra is chosen. First, several energy spectra of the x rays fulfilling different t_x cut conditions are produced and fitted. As common conditions, only the xe event class is accepted, with the parameters $\Delta t_{same} = 100$ ns, $t_1^{dele} = 100$ ns, $\Delta t^{dele} = 5000$ ns, and the μ^{2nd} cut not applied. Only the summed energy spectra of the group of the best LAAPDs (defined on page 73) are taken into account. The intensities of the μN and μp lines for a given t_x interval are obtained as fit results. The desired time spectra are obtained by plotting these amplitudes versus time.

In total, 26 energy spectra are produced and fitted:

1. t_x *from 155 to 255 ns:*
   For this time interval only one energy spectrum is produced and fitted (Fig. 7.23, top). As background shape $\mathcal{B}_{neu}^{uncor}$ is used (Eq. (6.22), page 88), scaled with a free amplitude. In addition to the free fit parameters described in item 2, also the μp K_β yield, and the intensities of the $\mu N(6 \rightarrow 5)$ and $\mu O(5 \rightarrow 3)$ lines are fitted as free parameters.
2. t_x *from 255 to 555 ns:*
   Five x–ray energy spectra are constructed: the first 100 ns of this time interval, *i.e.* 255 to 355 ns, represent the time cut of the first spectrum and the remaining part (355 to 550 ns) is divided in four 50 ns wide bins. These five energy spectra are the ones with the highest statistics representing the majority of the early x rays. Thus, the influence of the background shape on the fit result is minimal for all 5 spectra. In the bottom part of Fig. 7.23 a typical example is shown. In the fit there are five free parameters, namely
   (a) total intensity of the μp K–complex,
   (b) relative intensity of the μp K_{rest} line,
   (c) $\mu C(4 \rightarrow 3)$ peak intensity,
   (d) $\mu N(5 \rightarrow 4)$ peak intensity,
   (e) energy–constant background level, which was allowed in addition to the muon–correlated background $\mathcal{B}^{cor}$ (Eq. (6.23), page 90) whose parameters P and R were extrapolated following the trend of their time–dependence, as shown in Fig. 6.32, page 91.

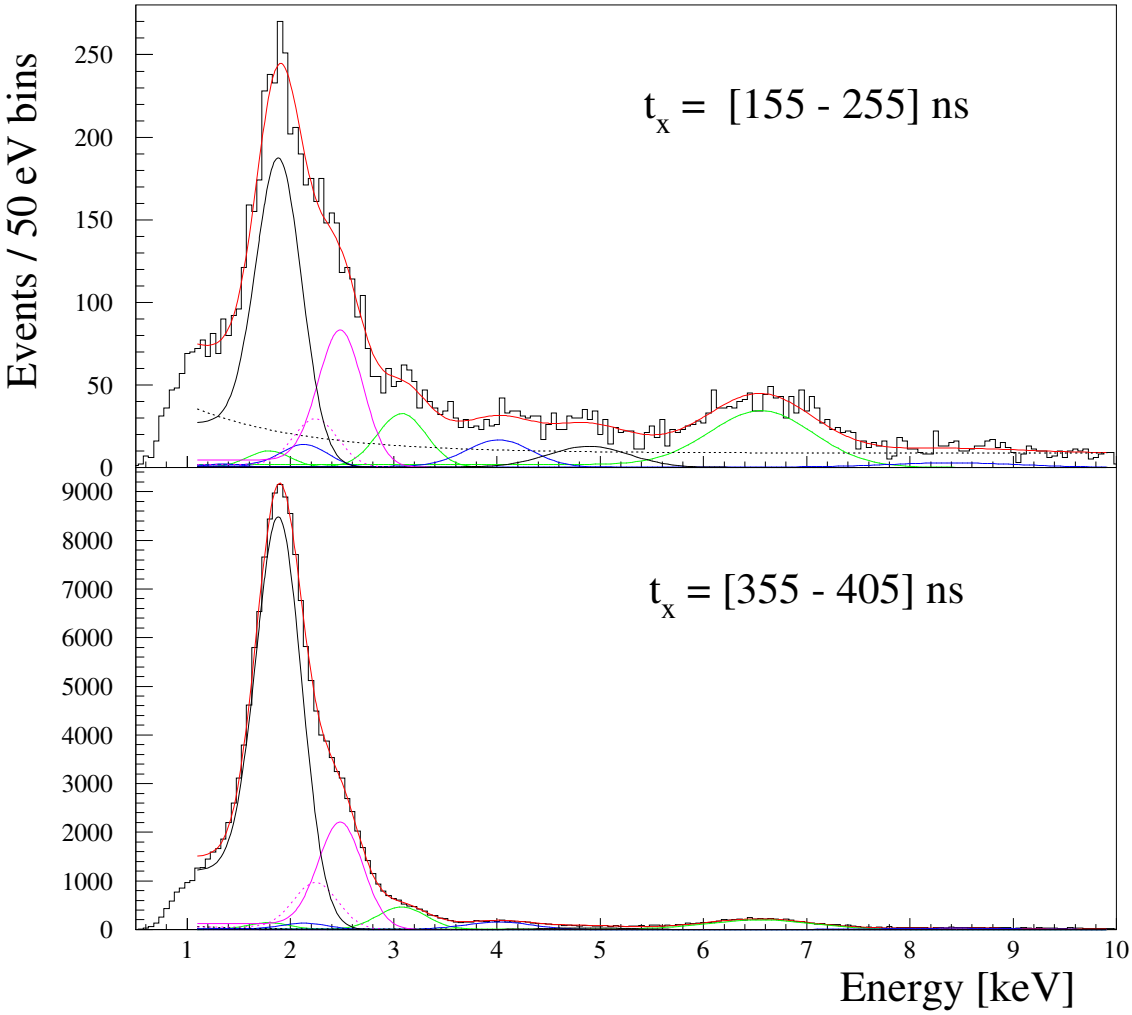

Figure 7.23: X–ray energy spectra (2 out of 26) with different t_x–time cuts (as indicated in the plots), studied in order to obtain the time distribution of the μp and μN x rays. The spectra are shown for the sum of best LAAPDs. *Only the* xe *event class is considered, the* del_e *cut is applied. No* $\mu^{2^{nd}}$ *cut is applied. The final fit function is shown in red. Other lines: (solid black) μp K_α, (magenta) μp K_β (dashed) and K_{rest} (solid), (green) μN lines, (blue) μO lines. The black dotted line in the top spectrum is the muon–correlated background $\mathcal{B}^{cor}$. The $\mu C(4 \rightarrow 3)$ peak at 4.9 keV (black line in the top spectrum) is probably due to the muon capture in C atoms in the target window.*

The parameters c, σ, and r of all peaks are fixed as given in Table 6.2, page 79. The relative intensities of the μp K_β line are fixed with respect to the K_{rest} line (I_β/I_{rest} = 0.43). The relative yields of the μN and μO transitions not mentioned above are also fixed to the values resulting from the fit of the early x–ray energy spectra shown in Fig. 6.17, page 72.

3. t_x *from 555 to 6455 ns:*
The corresponding 19 x–ray energy spectra (3 of them shown in Fig. 6.31, page 89) and the fit procedure are described in §6.7.2 at the point where the background $\mathcal{B}^{cor}$ is defined. (Another energy spectrum of x rays with t_x within this time interval (t_x from 3455 to 6455 ns) was discussed in Fig. 6.34, page 93.)

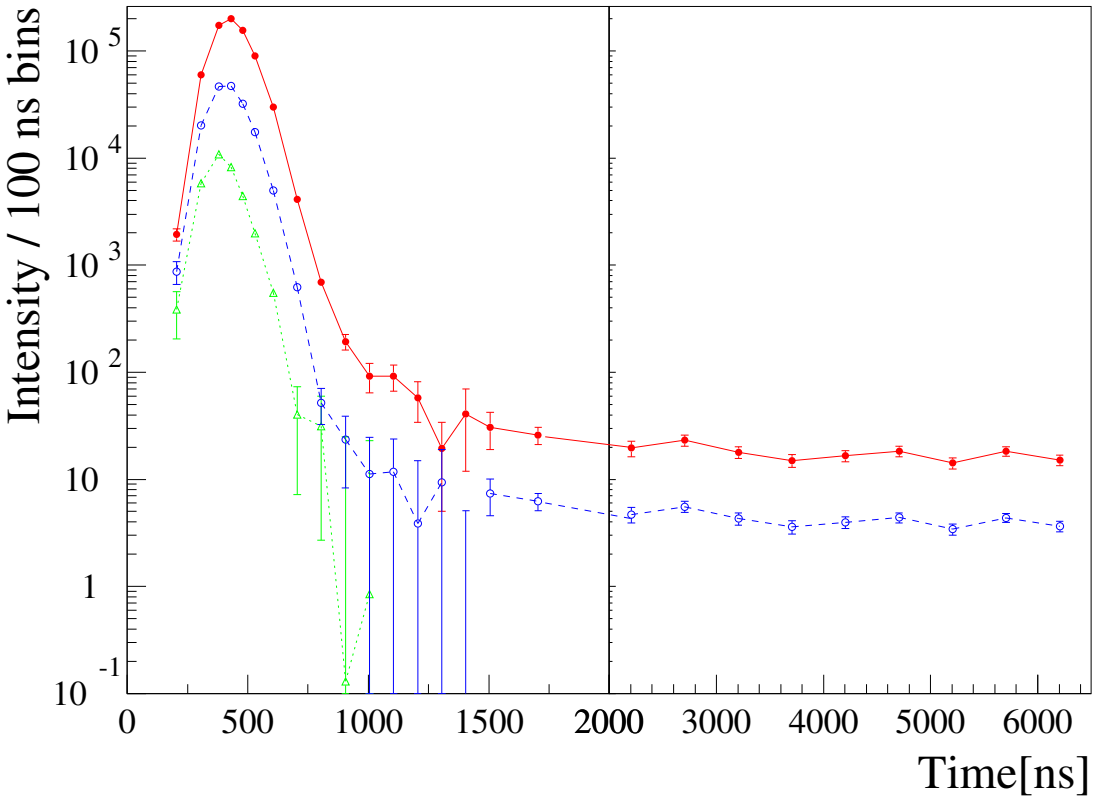

Figure 7.24: Intensities of the μp K_α (red full circles, solid line), μp K_{rest} (blue empty circles, dashed line), and $\mu N(5 \rightarrow 4)$ transition (green triangles, dotted line) plotted as functions of time. The data are from the group of the best LAAPDs. *Where the error bars are not visible, the errors are too small to be plotted in log y–scale. The time bins are 50, 100, and 500 ns wide (c.f. text), and the points are plotted at the middle of each time interval.*

The resulting time spectra of the $\mu N(5 \rightarrow 4)$ and μp K_{rest} and K_α lines are shown in Fig. 7.24. The time of each data point corresponds to the middle of the corresponding time interval. The error of each point is the error resulting from the fit of the corresponding energy spectrum. Only in case of the first point (item 1, t_x from 155 to 255 ns) the error resulting from the fit of the energy spectra is enlarged by a factor three. First, this is due to the uncertainty of the background shape. In addition, the relative peak intensities can be biased by additional systematic errors due to the correlations between t_x and E_x as described in §6.3.2. The final results do not significantly depend on this first point.

7.3.2 Fitting procedure

A basic fit function used in the fit of all three spectra is defined as

$$\mathcal{F}(t_x) = A_j \, Exp\,(t_x;\tau_{stop}) \otimes \left[\frac{1}{1+a_{ri}} \, Gauss^i\left(t_x; c_j, \sigma_j^i\right) + \frac{a_{ri}}{1+a_{ri}} \, Gauss^r\left(t_x; c_j + \Delta t, \sigma_j^r\right) \right], \tag{7.6}$$

which is a function of the x–ray time t_x and has 7 parameters

$$\mathcal{F}(t_x) = \mathcal{F}(t_x; A_j, a_{ri}, \tau_{stop}, c_j, \Delta t, \sigma_j^i, \sigma_j^r)\,. \tag{7.7}$$

A double peak structure of the x ray time spectra due to the incoming and reflected muons was shown in §7.1. In the $\mathcal{F}(t_{\mathrm{x}})$ function, this fact is reflected by the sum of two *Gauss* functions (Eq. (6.6), page 68). The indices i and r refer to the incoming and reflected muons, while the indexes $j = 1, 2, 3$ refer to the parameters defined for the μN$(5 \rightarrow 4)$, μp $\mathrm{K_{rest}}$ and K_α time spectra, respectively. Parameters c_j and σ_j^i are centroid and sigma of the incoming–muons $Gauss^i$, respectively. The reflected–muons $Gauss^r$ has a centroid which is shifted by Δt with respect to c_j and a sigma σ_j^r. Parameter A_j is the sum of A_j^i and A_j^r, *i.e.*, the intensities of the peaks due to the incoming and reflected–muons, respectively. The ratio a_{ri} is defined as

$$a_{\mathrm{ri}} = \frac{A_j^r}{A_j^i}\,. \tag{7.8}$$

It is required that the intensity ratio a_{ri} as well as the time difference Δt are the same for all three spectra. The *Gauss* functions are convoluted with the $Exp(t_{\mathrm{x}}; \tau_{\mathrm{stop}})$ function as defined in Eqs. (6.3) and (6.4), page 68. The parameter τ_{stop} is common for all three spectra since it phenomenologically describes the muon–stop time distribution and no differences between hydrogen and nitrogen atoms are assumed (§3.2). The parameters σ_j^i and σ_j^r reflect the muon–stop time distribution as well as the LAAPD time resolution. Variance σ_j^r is larger than σ_j^i due to the larger angular spread of the muons after the reflection at the gold surface (§7.1). To first order, the standard deviations for incoming (reflected) muon stops have the same value for all three spectra. However, small differences (ξ_{21} and ξ_{32}) are allowed, mainly due to the dependency of the time resolution on the x–ray energy (§6.3.2):

$$\left(\sigma_2^{i(r)}\right)^2 = \left(\sigma_1^{i(r)}\right)^2 + (\xi_{21})^2\,, \tag{7.9}$$

$$\left(\sigma_3^{i(r)}\right)^2 = \left(\sigma_2^{i(r)}\right)^2 + (\xi_{32})^2\,. \tag{7.10}$$

In all three spectra, the main background source is due to second–muon stops. The $\mu^{2^{\mathrm{nd}}}$ cut is not applied by purpose, since it is not possible to apply it for $t_{\mathrm{x}} < 1100$ ns (§6.2). However, a more than 5 μs long time interval (from ≈ 2 to 7 μs) is dominated nearly exclusively by the second–muon stop x rays. It thus allows us to determine the background with high precision and to extrapolate its shape also for the times before 2 μs. The background from second muons is in principle independent on time (constant). However, if an x ray or, more likely, an electron correlated to the first muon was measured, it is not possible to record any event of the xe class (both x–ray and electron correlated to second–muon) at later times. The efficiency to detect delayed xe events from second muons thus decreases according to the time distribution of the first electron, measured as the $(t_{\mathrm{e}} - t_{\mathrm{x}})$ distribution (see §7.2). Adopting its characteristic time constant $\tau_{\mathrm{first}} = 1300$ ns, the background shape is defined as a sum of an exponential function and a constant, muon–uncorrelated background P_j^{hor}

$$\mathcal{B}_j(t_{\mathrm{x}}) = P_j^{\mathrm{exp}} \exp\left(-\frac{t_{\mathrm{x}}}{\tau_{\mathrm{first}}}\right) + P_j^{\mathrm{hor}}\,, \tag{7.11}$$

The parameters P_j^{exp} and P_j^{hor} are free fit parameters in case of the two μp x–ray time spectra. In case of the μN x–ray time spectrum, it is not possible to fit them freely; in the fit of the energy–spectra with delayed time cuts, the intensity of the μN transitions is very small compared to the background and is set to zero in the energy fit (§7.3.1). However,

the ratio of μN to μp x rays has to be the same for the first and the second muon stops. Therefore, the background parameters of the μp K_{rest} time spectrum are used for μN, properly scaled by a factor 0.199 which is the intensity ratio of the $\mu N(5 \rightarrow 4)$ to the μp K_{rest} lines.

The final fit functions $\mathcal{C}_j^{tot}(t_x)$ of the three x–ray time spectra are:

1. $\mu N(5 \rightarrow 4)$ *time spectrum:*

$$\mathcal{C}_1^{tot}(t_x) = \mathcal{C}_1(t_x) + \mathcal{B}_1(t_x)\,, \tag{7.12}$$

$$\mathcal{C}_1(t_x) = \mathcal{F}(t_x; A_1, a_{ri}, \tau_{stop}, c_1, \Delta t, \sigma_1^i, \sigma_1^r)\,. \tag{7.13}$$

The shape of this time spectrum is determined by the muon–stop time distribution and by the x–ray time resolution, since the muon cascade time is considered to be zero. The center of gravity cg_1 (Eq. (6.7), page 69) of the incoming–muon peak is shifted by τ_{stop} with respect to the $Gauss^i$ centroid c_1:

$$cg_1 = c_1 + \tau_{stop}\,. \tag{7.14}$$

For the reflected–muon $Gauss^r$, both the centroid and the center of gravity are shifted by Δt. The resulting fit of the $\mu N(5 \rightarrow 4)$ time spectrum is shown in Fig. 7.25. The residuals shown at the bottom are defined in Eq. (7.1), page 101.

2. μp K_{rest} *time spectrum:*

$$\mathcal{C}_2^{tot}(t_x) = \mathcal{C}_2(t_x) + \mathcal{B}_2(t_x)\,, \tag{7.15}$$

$$\mathcal{C}_2(t_x) = Exp\left(t_x; \tau_{cas}^{\mu p}\right) \otimes \mathcal{F}(t_x; A_2, a_{ri}, \tau_{stop}, c_2, \Delta t, \sigma_2^i, \sigma_2^r)\,. \tag{7.16}$$

Here, the $\mathcal{F}(t_x)$ function is convoluted with an exponential with decay constant $\tau_{cas}^{\mu p}$ (§3.1.2). The center of gravity cg_2 of the incoming–muon peak is shifted with respect to the $Gauss^i$ centroid c_2:

$$cg_2 = c_2 + \tau_{stop} + \tau_{cas}^{\mu p}\,. \tag{7.17}$$

For the reflected–muon $Gauss^r$, both the centroid and the center of gravity are shifted by Δt. The resulting fit of the μp K_{rest} time spectrum is shown in Fig. 7.26 for the first 2 μs.

3. μp K_α *time spectrum:*

$$\mathcal{C}_3^{tot}(t_x) = \mathcal{C}_3(t_x) + \mathcal{C}_{2S}^{fast}(t_x) + \mathcal{B}_3(t_x)\,. \tag{7.18}$$

$\mathcal{C}_3(t_x)$ is defined analogously as for the μp K_{rest} line

$$\mathcal{C}_3(t_x) = Exp\,(t_x; \tau_{cas}^{\mu p}) \otimes \mathcal{F}(t_x; A_3, a_{ri}, \tau_{stop}, c_3, \Delta t, \sigma_3^i, \sigma_3^r) \tag{7.19}$$

and also analogously

$$cg_3 = c_3 + \tau_{stop} + \tau_{cas}^{\mu p}\,. \tag{7.20}$$

In addition, the function $\mathcal{C}_{2S}^{fast}(t_x)$ is defined as

$$\mathcal{C}_{2S}^{fast}(t_x) = \tilde{P}_{2S}^{fast}\; Exp\left(t_x; \tau_{2S}^{fast}\right) \otimes \left[Exp\,(t_x; \tau_{cas}^{\mu p}) \otimes \mathcal{F}(t_x; A_3, a_{ri}, \tau_{stop}, c_2, \Delta t, \sigma_3^i, \sigma_3^r)\right]\,, \tag{7.21}$$

where τ_{2S}^{fast} is the lifetime of the fast $\mu p(2S)$ component defined in §3.1.3. $\tilde{P}_{2S}^{fast}$ is the population of the fast $\mu p(2S)$ component normalized with respect to A_3. The *Gauss*

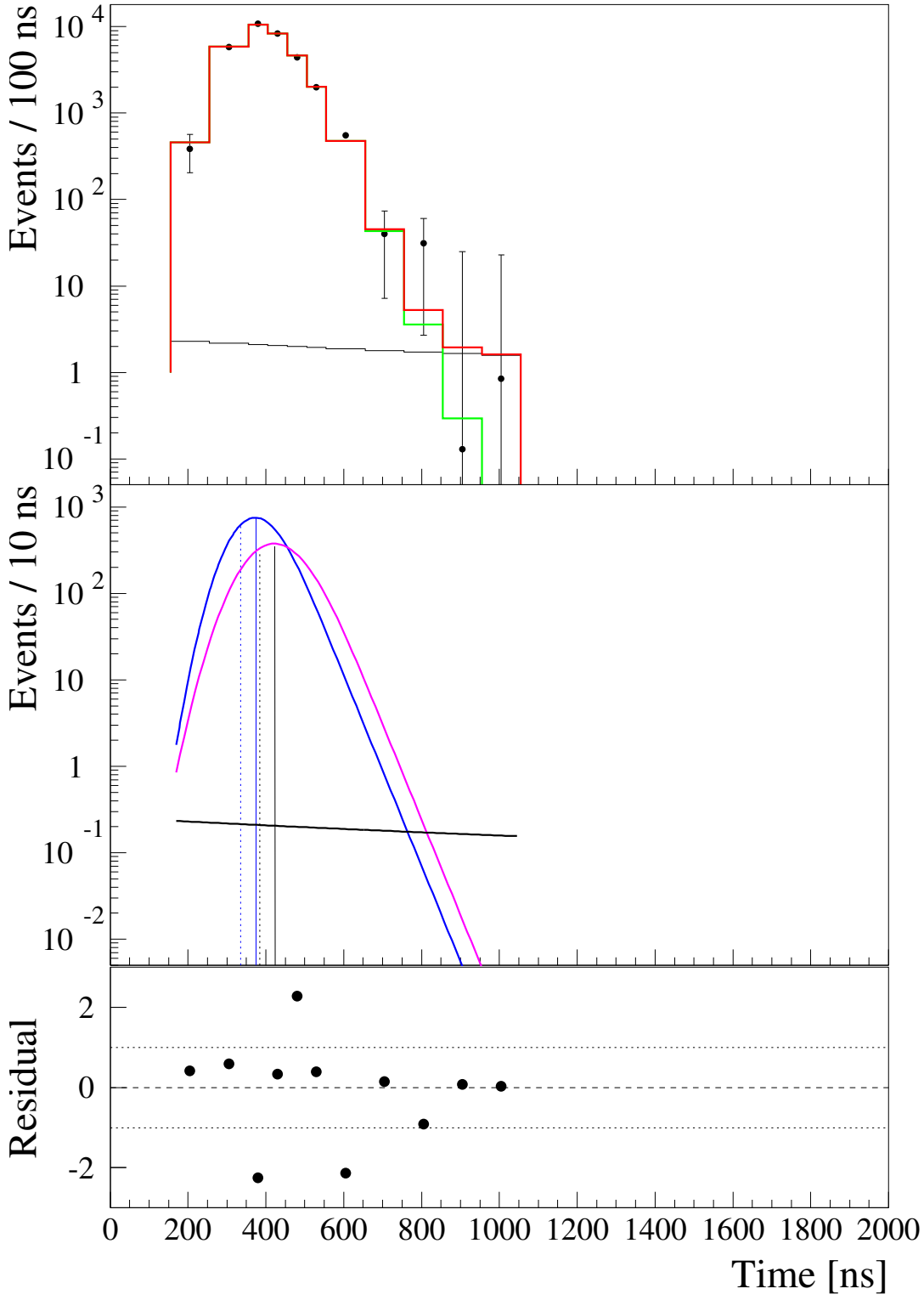

Figure 7.25: Top: time spectrum of the μN$(5 \rightarrow 4)$ transition x rays. The function $\mathcal{C}_1^{\mathrm{tot}}(t_{\mathrm{x}})$ (red) is a sum of the peak $\mathcal{C}_1(t_{\mathrm{x}})$ (green) and the background $\mathcal{B}_1(t_{\mathrm{x}})$ (black) (which is due to the same μN transition from second–muon stops). Middle: convolutions defining the green fit function above; blue and magenta are due to the incoming *and* reflected*–muon stops, respectively. The black line is a background. The dashed and solid vertical lines show the positions of the $Gauss^{i(r)}$ centroids and the centers of gravity cg of the convolutions, respectively. The cg is shifted by τ_{stop} with respect to the Gauss centroid. Bottom: residuals of the fit.*

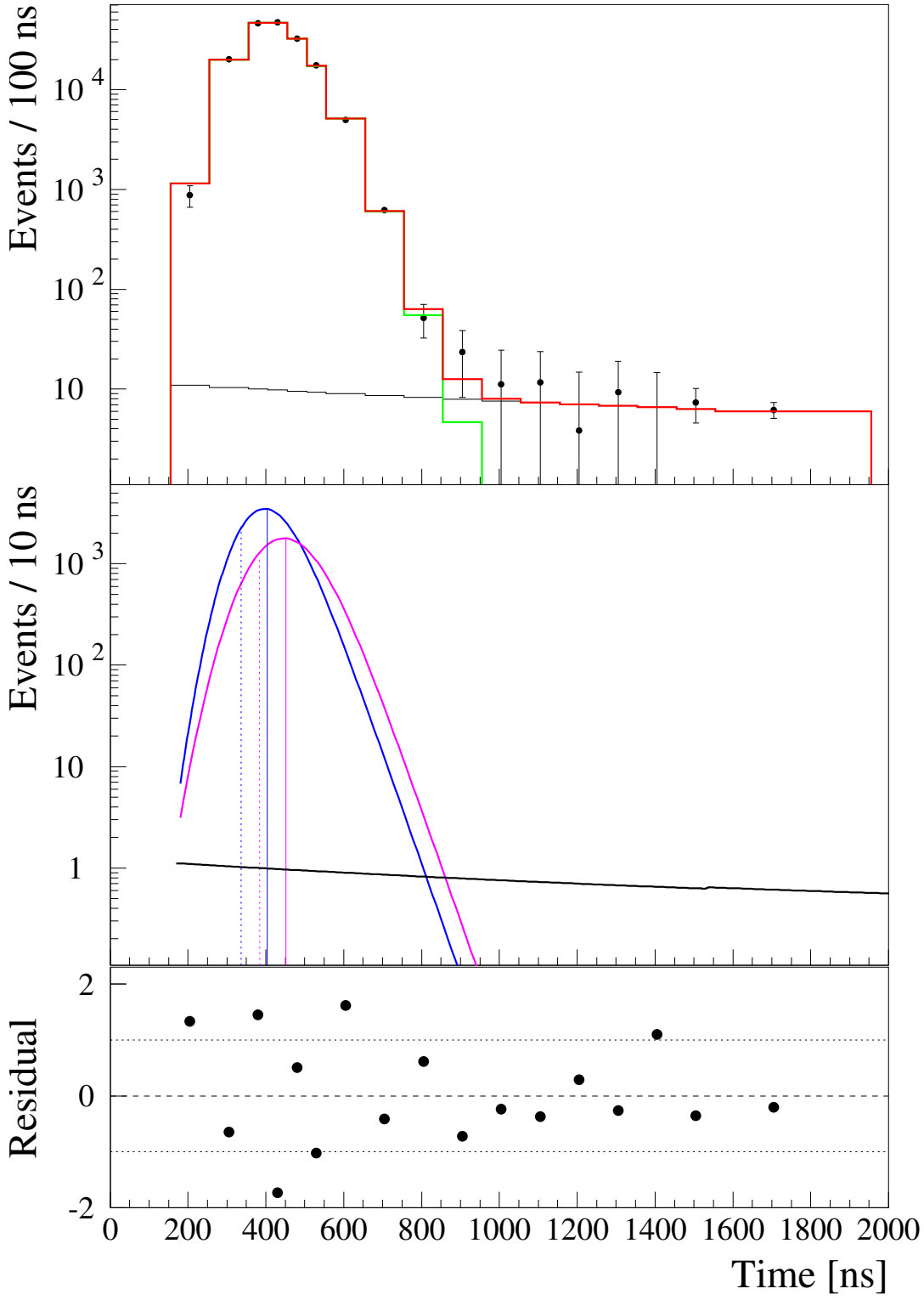

Figure 7.26: Top: time spectrum of the μp K_{rest} line. The function $\mathcal{C}_2^{tot}(t_x)$ (red) is a sum of the peak $\mathcal{C}_2(t_x)$ (green) and the background $\mathcal{B}_2(t_x)$ (black) (which is due to the second–muon μp K_{rest}). Middle: convolutions defining the green fit function above; blue and magenta are due to the incoming *and* reflected*–muon stops, respectively. The black line is a background. The dashed and solid vertical lines show the positions of the $Gauss^{i(r)}$ centroids and the centers of gravity of the convolutions, respectively. The cg is shifted by $(\tau_{stop} + \tau_{cas}^{\mu p})$ with respect to the Gauss centroid. Bottom: residuals of the fit.*

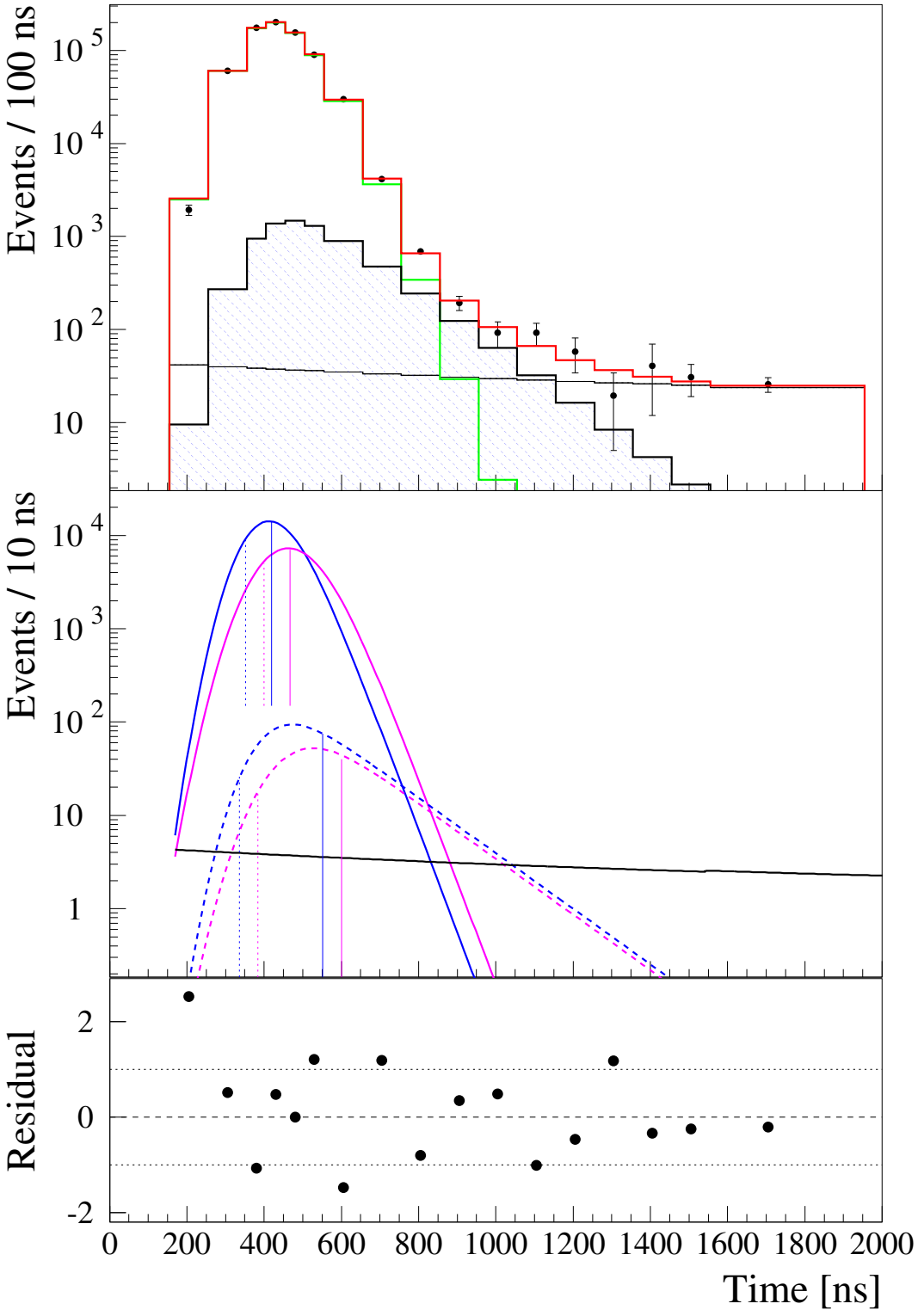

Figure 7.27: Top: time spectrum of the μp K_α line. The function $C_3^{tot}(t_x)$ (red) has contributions from the direct cascade $C_3(t_x)$ (green), from the μp(2S) fast component $C_{2S}^{fast}(t_x)$ (dotted area), and from the background $B_3(t_x)$ (black) (which is due to the second–muon μp K_α). Middle: convolutions due to the incoming *(blue) and* reflected *(magenta) muon stops. Solid curves: contributions to $C_3(t_x)$. Dashed curves: contributions to $C_{2S}^{fast}(t_x)$. The dashed and solid vertical lines show the positions of the Gauss$^{i(r)}$ centroids and the centers of gravity of the final convolutions, respectively. Bottom: residuals of the fit.*

centroids of this function are c_2 and $c_2 + \Delta t$, as in case of the μp K_{rest} line. This is because the $\mu p(2S)$ level is populated mainly via the non–circular transitions whose timing behaviour is closer to that of the non–circular K_{rest} line than to the circular K_α line (§3.1.2). The center of gravity of the incoming–muon $\mu p(2S)$ convolution is

$$cg_{2S} = c_2 + \tau_{\rm stop} + \tau_{\rm cas}^{\mu p} + \tau_{\rm 2S}^{\rm fast} \tag{7.22}$$

and again, the *Gauss* centroid and the convolution center of gravity for the reflected–muon case are shifted by Δt. The fit of the μp K_α line time spectrum is shown in Fig. 7.27.

The fit functions $\mathcal{C}_j^{\rm tot}(t_{\rm x})$ are numerically integrated for each of the 26 time intervals (§7.3.1), and χ–squared values χ_j^2 are determined for the three time spectra shown in Fig. 7.24.

The three $\mathcal{C}_j^{\rm tot}(t_{\rm x})$ fit functions contain 12 convolutions in total and have several common parameters. No common fit of all three functions with all parameters allowed as free fit parameters is performed. Instead, all three spectra are fitted separately with the aim of keeping the values of $a_{\rm ri}$ and Δt the same for all of them and not to allow big differences among the parameters σ_j^i and σ_j^r. In addition, some other simplifications are taken into account. The parameter $\tau_{\rm stop}$ is the one which enters all three fit functions and whose value could have an important systematic effect on the final value of the parameters of interest. Different values of this parameter are therefore tested for all three time spectra. In the fitting procedure, $\tau_{\rm stop}$ is fixed and the other parameters are optimized in order to satisfy the requirements as described above. In practice, also the parameters $\sigma_{2,3}^{i,r}$ are fixed in the fitting procedure, so that the number of convolutions needed to be calculated are substantially reduced. A large set of different values for $\sigma_{2,3}^{i,r}$ is used in the fitting procedure, in order to study the correlations among all parameters and to estimate the systematic errors, which have to be added to the errors of the fit with some parameters fixed.

7.3.3 Fit results and discussion

The best fit is obtained for a value $\tau_{\rm stop} = 40$ ns; a summary of the values of all parameters for the best fit is given in Table 7.2. The errors of the most relevant parameters will be discussed below. For comparison, Table 7.3 summarizes the values of $\tau_{\rm cas}^{\mu p}$, $\tilde{P}_{\rm 2S}^{\rm fast}$, and $\tau_{\rm 2S}^{\rm fast}$ optimized for $\tau_{\rm stop} = 36$, 40, and 44 ns. $\chi^2_{\rm tot}$ is the sum of the three χ_j^2 of the fits of the individual spectra. χ^2_{tot} for the fit with $\tau_{\rm stop} = 40$ ns lies not in the middle of the two other $\chi^2_{\rm tot}$ values. Hence, the real optimum value may be (39.2 ± 1.3) ns. However, since the total error of the parameters of interest is much bigger than a possible improvement due to a re-optimization of the fit for a corrected $\tau_{\rm stop}$ value, this is not done.

An optimum value of 8 ns was found for both parameters ξ_{21} and ξ_{32} defined in Eqs. (7.9) and (7.10). The study of the energy dependence of the LAAPD x–ray times (§6.3.2, page 69) has shown that the time resolution depends on $E_{\rm x}$ and is spread within the interval from 12 to 16 ns for x–ray energies below 10 keV. Therefore, the quadratic differences among the time resolutions of x–rays with different energies can reach up to $\sqrt{16^2 - 12^2} \sim 11$ ns. The ξ_{21} value can therefore be explained by a better time resolution of 3.1 keV x rays with respect to 2.4 keV x–rays. This effect can have a small influence also on the ξ_{32} value. In this case, however, an important contribution can also be due to the K_α cascade time distribution (its build–up character was shown in Fig. 3.4, page 22), as discussed in §3.1.2.

Table 7.2: Summary of the parameters of the functions $\mathcal{C}_j^{\rm tot}(t_{\rm x})$, $j = 1, 2, 3$, for the best fit obtained for the μN$(5 \to 4)$ ($j = 1$), the μp $\rm K_{rest}$ ($j = 2$), and the $\rm K_\alpha$ ($j = 3$) x–ray time spectra.

Parameter	μN$(5 \to 4)$ $j = 1$	μp $\rm K_{rest}$ $j = 2$	μp $\rm K_\alpha$ $j = 3$	Units
$\tau_{\rm stop}$	40.0	40.0	40.0	ns
c_j	334.8	336.3	352.1	ns
cg_j	374.8	403.6	419.4	ns
Δt	48.0	48.0	48.0	ns
σ_j^i	55.42	56.0	56.57	ns
σ_j^r	69.54	70.0	70.46	ns
a	0.6	0.6	0.6	—
A_j	19 611	98 597	403 312	events
$\tau_{\rm cas}^{\mu p}$	—	27.3	27.3	ns
$\tilde{P}_{\rm 2S}^{\rm fast}$	—	—	1.17	%
$\tau_{\rm 2S}^{\rm fast}$	—	—	148.4	ns
$P_j^{\rm exp}$	4.9	129	470	per 10 ns binning
$P_j^{\rm hor}$	1.4	37	155	events / per 10 ns

Important results are the time differences between the parameters c_j having a small contribution due to the dependence of $t_{\rm x}$ on $E_{\rm x}$ as described in §6.3. When corrected for this systematic effect which amounts to $\Delta t_{\rm x}(2.4\ \text{keV} - 3.1\ \text{keV}) = (2 \pm 3)$ ns (Fig. 6.15, page 70) the resulting time difference is

$$\Delta t_{21} = c_2 - c_1 - \Delta t_{\rm x}(2.4\,\text{keV} - 3.1\,\text{keV}) = (0 \pm 4)\,\text{ns} \tag{7.23}$$

i.e., compatible with zero. The error includes the uncertainties $\sigma(c_j) \approx 2$ ns resulting from the fit. Therefore, a possible negative offset of the $\rm K_{rest}$ time distribution, as discussed in §3.1.2, is not observed. However, the parameter c_3 is positioned 15.8 ns later than c_2.

Table 7.3: Comparison of the $\tau_{\rm cas}^{\mu p}$, $\tilde{P}_{\rm 2S}^{\rm fast}$ and $\tau_{\rm 2S}^{\rm fast}$ parameter values optimized for different values of the parameter $\tau_{\rm stop}$.

Parameter	Value			Units
$\tau_{\rm stop}$	36	40	44	ns
$\tau_{\rm cas}^{\mu p}$	29.8	27.3	23.9	ns
$\tau_{\rm 2S}^{\rm fast}$	120.2	148.4	124.3	ns
$\tilde{P}_{\rm 2S}^{\rm fast}$	1.26	1.17	1.53	%
χ_1^2	15.96	16.60	20.39	for 11 data points
χ_2^2	22.53	21.36	24.78	for 26 data points
χ_3^2	30.19	24.24	31.82	for 26 data points
$\chi_{\rm tot}^2$	68.68	62.20	76.99	for 63 data points
χ_1^2/DOF	1.77	1.84	2.26	for DOF = 9
χ_2^2/DOF	1.07	1.02	1.18	for DOF = 21
χ_3^2/DOF	1.51	1.21	1.59	for DOF = 20
$\chi_{\rm tot}^2$/DOF	1.37	1.24	1.54	for DOF = 50

The time difference

$$\Delta t_{32} = c_3 - c_2 - \Delta t_{\mathrm{x}}(1.9\,\mathrm{keV} - 2.4\,\mathrm{keV}) = (15 \pm 4)\,\mathrm{ns} \tag{7.24}$$

(when corrected for the systematic shift Δt_{x}(1.9 keV - 2.4 keV) = (1 ± 3) ns, Fig. 6.15, page 70) is dominated by intrinsic differences in the muon cascade correlated with the μp K_α and $\mathrm{K}_{\mathrm{rest}}$ lines (§3.1.2, Fig. 3.4 on page 22).

- $\mu\mathrm{p}(2S)$ **cascade time**

The parameter $\tau_{\mathrm{cas}}^{\mu p}$ is mostly correlated with the parameters τ_{stop}, $\sigma_{2(3)}^{i}$, $\sigma_{2(3)}^{r}$, and ξ_{12}. The $\tau_{\mathrm{cas}}^{\mu p}$ statistical error, resulting from the fit procedure in which the above mentioned parameters are fixed, is in the order of 1 ns. An additional systematic error has to be however considered. The contribution of this systematic error was determined by studying the $\tau_{\mathrm{cas}}^{\mu p}$ dependency on a large set of different values of the above mentioned parameters. The resulting $\tau_{\mathrm{cas}}^{\mu p}$ value is

$$\tau_{\mathrm{cas}}^{\mu p} = (28 \pm 5)\,\mathrm{ns}\,, \tag{7.25}$$

where the error includes both statistical and systematic contributions. This value is $2-3$ times less than the calculated values of $50-80$ ns (for different n_{i} values, §3.1.2, Fig. 3.4, page 22). This is an indication that not all cascade processes are treated correctly in the present cascade model.

The parameter $\tau_{\mathrm{cas}}^{\mu p}$ characterizes the exponential tail of the μp K–line cascade time distributions. However, in the K_α case, there is an average time shift corresponding to an average K_α cascade time $T_{\mathrm{cas}}^{\mathrm{K}_\alpha}$ of

$$T_{\mathrm{cas}}^{\mathrm{K}_\alpha} = \tau_{\mathrm{cas}}^{\mu p} + \Delta t_{21} + \Delta t_{32} = (43 \pm 7)\,\mathrm{ns}\,. \tag{7.26}$$

The corresponding average time shift for $\mathrm{K}_{\mathrm{rest}}$ is

$$T_{\mathrm{cas}}^{\mathrm{K}_{\mathrm{rest}}} = \tau_{\mathrm{cas}}^{\mu p} + \Delta t_{21} = (28 \pm 6)\,\mathrm{ns}\,. \tag{7.27}$$

Considering the K–yields (Table 3.1, page 21), the resulting mean μp cascade time is

$$T_{\mathrm{cas}}^{\mu \mathrm{p}} = (39 \pm 7)\,\mathrm{ns}\,. \tag{7.28}$$

This value corresponds to the average cascade time of 40 ns applied in §7.1.

- $\mu\mathrm{p}(2S)$ **lifetime and population**

The resulting values and the errors of the parameters characterizing the fast component of the $\mu\mathrm{p}(2S)$ are

$$\tilde{P}_{2\mathrm{S}}^{\mathrm{fast}} = (1.17 \pm (0.22)_{\mathrm{stat}} \pm (0.1)_{\mathrm{syst}})\,\% = (1.17 \pm 0.24)\,\%\,, \tag{7.29}$$

$$\tau_{2\mathrm{S}}^{\mathrm{fast}} = (148 \pm (20)_{\mathrm{stat}} \pm (8)_{\mathrm{syst}})\ \mathrm{ns} = (148 \pm 22)\ \mathrm{ns}\,. \tag{7.30}$$

The statistical errors result from a fit with the parameters τ_{stop}, σ_3^i, σ_3^r, and ξ_{32} fixed. The systematic errors were determined by studying the $\tilde{P}_{2\mathrm{S}}^{\mathrm{fast}}$ and $\tau_{2\mathrm{S}}^{\mathrm{fast}}$ dependency on a large set of different values of the above mentioned parameters. The 1σ and 2σ confidence level regions for $\tilde{P}_{2\mathrm{S}}^{\mathrm{fast}}$ and $\tau_{2\mathrm{S}}^{\mathrm{fast}}$ resulting from the μp K_α time spectra are shown in Fig. 7.28; they are calculated in a way that in addition to $\tilde{P}_{2\mathrm{S}}^{\mathrm{fast}}$ and $\tau_{2\mathrm{S}}^{\mathrm{fast}}$, the parameters A_3, c_3, P_3^{exp}, and P_3^{hor} are kept free in the $\mathcal{C}_3^{\mathrm{tot}}(t_{\mathrm{x}})$ fit function.

The calculation of the fast component time distribution shown in Fig. 3.6 on page 25 [49], was based on the cross sections calculated by T. S. Jensen [53] and assumes that one H_2 molecule has to be considered as two H atoms. The resulting lifetime for this distribution is 120 ns. If one H_2 molecule is treated as one H atom, the resulting lifetime turns out to be about twice as much [85]. A good agreement between our measured τ_{2S}^{fast}–value and calculation can thus be obtained when one H_2 molecule is treated as 1.8 H atoms.

The population $\tilde{P}_{2S}^{fast}$ is normalized with respect to the K_α line and includes the weak effect of muon decay; the correlation with P_{2S}^{fast} defined in §3.1.3 can therefore be expressed as:

$$P_{2S}^{fast} = \tilde{P}_{2S}^{fast} \; \frac{Y_{K_\alpha}}{(1 + P_{2S}^{slow})} \; \frac{\lambda_{tot}}{\lambda_{tot} - \lambda_\mu} \; , \tag{7.31}$$

where λ_{tot} is given by

$$\lambda_{tot} = \frac{1}{\tau_{2S}^{fast}} = \lambda_{quench} + \lambda_\mu \; , \tag{7.32}$$

Y_{K_α} is the μp K_α yield (Table 3.1, page 21), $P_{2S}^{slow} \approx 1\%$ the population of the slow $2S$ component, λ_μ the muon decay rate (both defined in §3.1.3, page 23), and λ_{quench} the quenching rate of the fast $2S$ component. The resulting P_{2S}^{fast} value becomes then

$$P_{2S}^{fast} = (1.02 \pm 0.21)\% \; . \tag{7.33}$$

In order to corroborate the fact that the fast $\mu p(2S)$ component is observed, two set of fits are performed:

1. The μp K_{rest} time spectrum is fitted with a function which includes a $2S$–tail (as $\mathcal{C}_3^{tot}(t_x)$), however with parameters c_2, σ_2^i, and σ_2^r fixed. Free fit parameters are the background parameters, the amplitude of $Gauss^i$, and $\tilde{P}_{2S}^{fast}$ (in this case normalized to the amplitude A_2). The parameter τ_{2S}^{fast} is fixed to different values between 25 to 240 ns, in steps of 25 ns. The resulting $\tilde{P}_{2S}^{fast}$ values turns out to be consistent with zero (as shown in Fig. 7.28), thus confirming that only the μp K_α line contributes to the fast $\mu p(2S)$ component.
2. The μp K_α spectrum is fitted assuming $\tilde{P}_{2S}^{fast} = 0$. The fit is performed with fixed values of τ_{stop}, σ_3^i, and σ_3^r; the peak amplitude A_3, the centroid c_3, as well as Δt, a, and $\tau_{cas}^{\mu p}$ are kept free. It is then not possible to obtain a reasonable fit. The χ_3^2 value found is 59.7 with a dominant contribution from the points defining the $\mu p(2S)$ tail. The increase of χ_3^2 by 35.5 excludes the assumption $\tilde{P}_{2S}^{fast} = 0$ by 6 standard deviations.

Therefore, it can be stated that the measurement of the fast $\mu p(2S)$ component is confirmed. It is its first direct experimental observation even if the existence of this fast $\mu p(2S)$ component was predicted already a long time ago (Kodosky and Leon, Ref. [54]). As discussed in §3.1.3, the initial population P_{2S} of $\mu p(2S)$ atoms is $P_{2S} = (2.49 \pm 0.17)\%$ at 0.6 hPa H_2 gas pressure. The slow $\mu p(2S)$ component P_{2S}^{slow} was measured to be $(1.1 \pm 0.2)\%$ [45]. Based on the relation given in Eq. (3.17), page 23, a new independent value $P_{2S}^{slow} = P_{2S} - P_{2S}^{fast} = (1.47 \pm 0.27)\%$ can thus be deduced for the population of the slow $2S$ component, the population on which is based our laser experiment.

The new results about the $2S$–lifetime and –population have to be considered as preliminary for the following reasons:

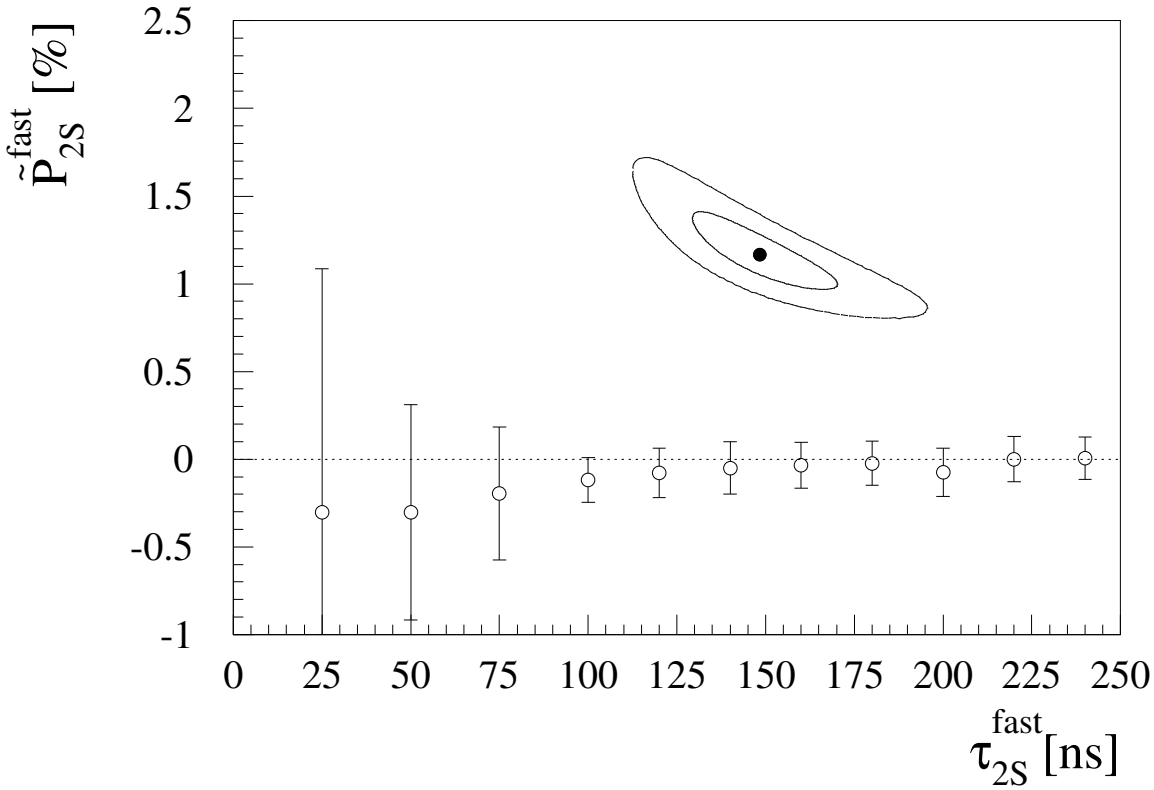

Figure 7.28: Relative population $\tilde{P}_{2S}^{fast}$ (normalized to A_3) of the fast $\mu p(2S)$ component plotted versus its lifetime τ_{2S}^{fast}. The full circle represents the result of the fit; the ellipsoids represent 1σ and 2σ confidence level regions. Empty circles are analogous results for μp K_{rest} for different fixed τ_{2S}^{fast} values (in this case, $\tilde{P}_{2S}^{fast}$ is normalized to A_2). The horizontal dotted line corresponds to $P_{2S}^{fast} = 0\%$. A full explanation is given in the text.

- there may be systematic effects on the time slope of radiative $2S$–quenching because some of the $\mu p(2S)$ atoms reach the target walls before being quenched (or slowed below the $2S - 2P$ threshold energy). In addition, there are small time–dependent variations for detecting μp–K x rays because of the same drift effect. The careful investigation of these effects will need a complete reanalysis on the basis of all existing knowledge about the relevant elastic and inelastic cross sections for $2S$–collisions, which depend on the μp kinetic energy. The previously measured kinetic energy distributions will be a basis for an elaborate Monte Carlo code which will simulate the experimental situation.

- These effects may also lead to some deviation of the observed delayed K_α transitions (due to $2S$ quenching) from a pure exponential.

It will be a major task to treat these effects in all necessary details, which is well beyond the topic of the present thesis. However, it is not expected that the results presented here will be changed substantially.

Appendix A

Abbreviations

This chapter lists abbreviations used through the thesis. A separation was made between electronics and physics abbreviations. Only electronic objects of major importance are described in Table A.1. Electronics modules which were only used in Chapter 5 are not shown here but directly defined in Table 5.1, page 45.

Table A.1: Abbreviations for electronic devices and companies.

Abbreviation	Meaning
ADC	Analog to Digital Converter
API	Advanced Photonix, Inc. (company)
DAQ	Data Acquisition
OR	Output Register
PSI	Paul Scherrer Institute
PTDC	Pipeline Time–to–Digital Converter
RMD	Radiation Monitoring Devices, Inc. (company)
TDC	Time–to–Digital Converter
WFD	Wave Form Digitizer

A list of apparatus is given in Table A.2, whereas physics terms as well as names used during the analysis are defined in Table A.3.

Table A.2: Abbreviations referring to the apparatus.

Abbreviation	Meaning
CR	Counting Room
CT	Cyclotron Trap
FP	Fabry – Perot
LAAPD	Large Area Avalanche Photodiode
LH	Laser Hut
LYSO	Lutetium Yttrium Orthosilicate
MEC	Muon Extraction Channel
PSC	Phase Space Compression
Ti:Sa laser	Titanium – Sapphire laser

Table A.3: Frequently used physics abbreviations.

Abbreviation	Meaning
CM	Center of Mass frame
cw	continuous wave
DC offset	Direct Current offset
DOF	Degrees Of Freedom
hfs	hyperfine splitting
K_α	$2P \rightarrow 1S$ transition
K_β	$3P \rightarrow 1S$ transition
K_{rest}	$nP \rightarrow 1S$ transitions, $n > 3$
LAB	Laboratory frame
μC	muonic carbon atom
μN	muonic nitrogen atom
μO	muonic oxygen atom
μp	muonic hydrogen atom
$(\mu p)^*$	muonic hydrogen atom in an excited state
QCD	Quantum Chromodynamics
QED	Quantum Electrodynamics
QM	Quantum Mechanics
r_p	proton root–mean–square charge radius
rms	root–mean–square
SWF	Standard Wave Form
SWP	Standard Wave Package
TOF	Time–Of–Flight
VP	Vacuum Polarization

Appendix B

Air and water concentrations in the H_2 gas target

The determination of the air and H_2O concentrations is given here. The total number N_x of formed μp, μN, and μO atoms is calculated from the relation

$$N_x = \frac{N_i^{det}}{\varepsilon_i \, Y_i} \tag{B.1}$$

where the index x stands for μp, μN, or μO atoms, and the index i for the μp–K_α, μN($5 \rightarrow 4$), and μO($5 \rightarrow 4$) transitions. The number of detected x rays N_x^{det} from the corresponding transition results from the fit of the x–ray energy spectrum of the early signals from the best LAAPDs (Fig. 6.17, page 72). The transition yields Y_i are given in Chapter 3. The detection efficiencies ε_i (§6.5) take into account the x–ray absorption in the material in front of the LAAPDs (polypropylene foils and Li sheets) and the intrinsic LAAPD efficiency; they do not consider solid angles. The resulting numbers of formed muonic atoms, *i.e.*, the number of atoms which would be detected by the best LAAPDs if they had 100% efficiency and the transition yields were 1, are: $N_{\mu p} = 1.26 \times 10^6$, $N_{\mu N} = 3.37 \times 10^4$, and $N_{\mu O} = 1.49 \times 10^4$.

The ratio of the N_2 to H_2 partial pressures $p(N_2)/p(H_2)$ can be calculated if the ratio $A_\mu(N_2, H_2)$ of the muon–capture rate by N_2 and H_2 molecules is known. A measured value $A_\mu(N_2, H_2) = 8 \pm 1$ follows from [86]. A π^- capture rate ratio $A_\pi(N_2, H_2) = 6.6 \pm 0.3$ is given in [87]. Since the π^- and μ^- capture rates are not expected to differ, we adopt a value $A_\mu(N_2, H_2) = 7 \pm 1$. The resulting partial–pressure ratio is

$$\frac{p(N_2)}{p(H_2)} = \frac{N_{\mu N}}{N_{\mu p}} \cdot \frac{1}{A_\mu(N_2, H_2)} = (3.2 \pm 0.5) \times 10^{-3} \, . \tag{B.2}$$

Considering the relative contribution of N_2 molecules in air (78%), the relation between N_2 and air partial pressures becomes

$$p(\text{air}) = 1.28 \, p(N_2) \, . \tag{B.3}$$

Therefore,

$$\frac{p(\text{air})}{p(H_2)} = (4.1 \pm 0.6) \times 10^{-3} \approx (0.4 \pm 0.1)\% \, , \tag{B.4}$$

which corresponds to $p(\text{air}) = (2.5 \pm 0.4) \times 10^{-3}$ hPa for our H_2 gas target.

The partial water pressure, $p(H_2O)$, can be estimated from the ratio of the number of formed μN and μO atoms, based on the relation

$$\frac{N_{\mu O}}{N_{\mu N}} = \frac{p(O_2)}{p(N_2)} A_\mu(O,N) + \frac{p(H_2O)}{p(N_2)} A_\mu(H_2O, N_2) \tag{B.5}$$

and assuming that each μ^- captured by a water molecule will form a μO atom. The ratio of the partial pressures $p(O_2)$ and $p(N_2)$ is given by the air composition (0.21/0.78). The two A_μ ratios can be estimated from the models for muon capture in gas compounds. The relation $A_\mu(Z,H) \propto (Z^{1/3} - 1)$ is suggested for gas mixtures in reference [88], which is for low Z in rough agreement with the simple Fermi–Teller rule $A_\mu(Z,H) \approx Z$ [89] (Z being an atom/molecule with charge Z). Considering

$$A_\mu(Z_1, Z_2) = \frac{A_\mu(Z_1, H)}{A_\mu(Z_2, H)}\,, \tag{B.6}$$

the ratios A_μ needed in Eq. (B.5) can be deduced as $A_\mu(O,N) = 1.1 \pm 0.15$ and $A_\mu(H_2O, N_2) = 0.7 \pm 0.2$. Using these values and solving Eq. (B.5) for p_{H_2O}, we obtain

$$p(H_2O) \approx (4 \pm 2) \times 10^{-4}\,\mathrm{hPa}\,, \tag{B.7}$$

so that

$$\frac{p(H_2O)}{p(H_2)} \approx (0.07 \pm 0.03)\%\,. \tag{B.8}$$

The water present in our gas target originated mostly from the outgasing of plastic materials like O–rings.

References

[1] H. Hellwig et al. *Measurement of the unperturbed hydrogen hyperfine transition frequency*. IEEE Trans. Instrum. Meas. **19** (1970), 200–209.

[2] W. E. Lamb and R. C. Retherford. *Fine structure of the hydrogen atom by a microwave method*. Phys. Rev. **72** (1947), 241–243.

[3] H. A. Bethe. *The electromagnetic shift of energy levels*. Phys. Rev. Lett. **91** (1947), 339–341.

[4] K. Pachucki and U. D. Jentschura. *Two-loop Bethe-logarithm correction in hydrogenlike atoms*. Phys. Rev. Lett. **91** (2003), 113005.

[5] M. I. Eides, H. Grotch, and V. A. Shelyuto. *Theory of light hydrogenlike atoms*. Phys. Rep. **342** (2001), 63–261.

[6] K. Pachucki. *Theory of the Lamb shift in muonic hydrogen*. Phys. Rev. A **53** (1996), 2092–2100.

[7] E. Borie and G. A. Rinker. *The energy levels of muonic atoms*. Rev. Mod. Phys. **54** (1982), 67–118.

[8] J. R. Sapirstein and D. R. Yennie. *Theory of hydrogenic bound states*. In T. Kinoshita, editor, *Quantum electrodynamics*, volume 7, pages 560–672. World Scientific, Singapore, 1990.

[9] S. G. Karshenboim. *What do we actually know about the proton radius*. Can. J. Phys. **77** (1999), 241–266.

[10] K. Pachucki. *Proton structure effects in muonic hydrogen*. Phys. Rev. A **60** (1999), 3593–3598.

[11] T. Kinoshita and M. Nio. *Sixth–order vacuum–polarization contribution to the Lamb shift of the muonic hydrogen*. Phys. Rev. Lett. **82** (1999), 3240–3243.

[12] P. Indelicato et al. *Aspects of QED in the framework of exotic atoms*. In P. Kienle et al., editors, *Proceedings of the Int. Workshop on Exotic Atoms (EXA02)*, pages 61–70. Austrian Acad. of Science, Vienna, 2003.

[13] A. Veitia and K. Pachucki. *Nuclear recoil effects in antiprotonic and muonic atoms*. Phys. Rev. A **69** (2004), 042501.

[14] E. Borie. *Lamb shift in muonic hydrogen*. Phys. Rev. A **71** (2005), 032508.

[15] A.P. Martynenko. *2S Hyperfine splitting of muonic hydrogen.* Phys. Rev. A **71** (2005), 022506.

[16] J. L. Friar, M. Martorell, and D. W. L. Sprung. *Hadronic vacuum polarization and the Lamb shift.* Phys. Rev. A **59** (1999), 4061–4063.

[17] S.A. Srartsev et al. *Corrections for nuclear polarizability to the energy of s levels in light atoms and μ^- mesic molecules.* Yad. Fiz. **23** (1976), 1233–1243. [Sov. J. Nucl. Phys. **23**, 1233–1243, (1976)].

[18] K. Pachucki and S. G. Karshenboim. *Higher–order recoil corrections to energy levels of two–body systems.* Phys. Rev. A **60** (1999), 2792–2798.

[19] R. Rosenfelder. *Proton polarization shifts in electronic and muonic hydrogen.* Phys. Lett. B **463** (1999), 317–322.

[20] R. N. Faustov and A. P. Martynenko. *Proton polarizability contribution to the hydrogen hyperfine splitting.* Phys. Atom. Nucl. **65** (2002), 265–270.

[21] E. Borie and G.A. Rinker. *Improved calculation of the muonic-helium Lamb shift.* Phys. Rev. A **18** (1978), 324–327.

[22] P. J. Mohr and B. N. Taylor. *CODATA recommended values of the fundamental physical constants: 2002.* Rev. Mod. Phys. **77** (2005), 1–107.

[23] I. Sick. *On the rms–radius of the proton.* Phys. Lett. B **576** (2003), 62–67.

[24] B. de Beauvoir et al. *Metrology of the hydrogen an deyterium atoms: Determination of the Rydberg constant and Lamb shifts.* Eur. Phys. J. D **12** (2000), 61–93.

[25] V. A. Yerokhin, P. Indelicato, and V. M. Shabaev. *Two–loop self-energy correction in high-Z hydrogenlike atoms.* Phys. Rev. Lett. **91** (2003), 073001.

[26] R. Pohl et al. *Observation of the molecular quenching of $\mu p(2S)$ atoms.* Hyp. Interact. **138** (2001), 35–40.

[27] H. Anderhub et al. *Measurement of the K–line intensity ratios in muonic hydrogen between 0.25 and 150 torr gas pressures.* Phys. Lett. B **143** (1984), 65–68.

[28] H. Anderhub et al. *Search for the metastable 2s state in muonic hydrogen.* Phys. Lett. B **71** (1977), 443–445.

[29] P. O. Egan et al. *Search for long–lived 2S muonic hydrogen in H_2 gas.* Phys. Rev. A **23** (1981), 1152–1163.

[30] J. S. Cohen. *Slowing down and capture of negative muons by hydrogen: classical-trajectory Monte Carlo calculation.* Phys. Rev. A **27** (1983), 167–179.

[31] P. Hauser, F. Kottmann, C. Lüchinger, and R. Schaeren. *Slowing down of negative muons in gaseous H_2 and determination of the stopping power.* In L. A. Schaller and C. Petitjean, editors, *Muonic Atoms and Molecules*, pages 235–241. Birkhäuser Verlag, Basel, 1993. [Proceedings of the Int. Workshop on Muonic Atoms and Molecules, Ascona].

[32] M. Agnello et al. *Antiproton slowing down in H_2 and He and evidence of nuclear stopping power.* Phys. Rev. Lett. **74** (1995), 371–374.

[33] F. J. Hartmann et al. *Experiments with low–energy muons.* Hyp. Interact. **101/102** (1996), 623–632.

[34] G. Schiwietz et al. *Comprehensive analysis of the stopping power of antiprotons and negative muons in He and H_2 gas target.* J. Phys. B **29** (1996), 307–321.

[35] R. Schmidt et al. *Measurement of the Barkas effect in hydrogen.* Eur. Phys. J. D **3** (1998), 119–122.

[36] C. Varelas and J. P. Biersack. *Reflection of energetic particles from atomic and ionic chains in single crystal.* Nucl. Instrum. Methods **79** (1970), 213–218.

[37] F. Kottmann et al. *Kinetic energy of exotic H atoms at formation and cascade.* Hyp. Interact. **119** (1999), 3–10.

[38] T. S. Jensen. *Atomic cascade in light exotic atoms.* PhD thesis, University of Zuerich, Switzerland, 2002.

[39] M. Leon and H. A. Bethe. *Negative meson absorption in liquid hydrogen.* Phys. Rev. **127** (1962), 636–647.

[40] V. E. Markushin. *Atomic cascade in muonic hydrogen and the problem of kinetic–energy distribution in the ground state.* Phys. Rev. A **50** (1994), 1137–1143.

[41] E. Borie and M. Leon. *X–ray yields in protonium and mesic hydrogen.* Phys. Rev. A **21** (1980), 1460–1468.

[42] V. E. Markushin. *Light μ^- atoms in liquid and gaseous hydrogen and deuterium.* Zh. Eksp. Teor. Fiz. **80** (1981), 35–48. [Sov. Phys. JETP **53**, 16–22 (1981)].

[43] V. E. Markushin. *Cascade in muonic and pionic atoms with Z=1.* Hyp. Interact. **119** (1999), 11–21.

[44] D. J. Abbott et al. *Diffusion of muonic deuterium and hydrogen atoms.* Phys. Rev. A **55** (1997), 214–229.

[45] R. Pohl. *Investigation of the long–lived metastable 2S state in muonic hydrogen.* PhD thesis, Swiss Federal Institute of Technology (ETHZ), Switzerland, 2001. (unpublished).

[46] T. S. Jensen and V. E. Markushin. *Collisional deexcitation of exotic hydrogen atoms in highly excited states II. Cascade calculations.* Eur. Phys. J. D **21** (2002), 271–283.

[47] M. Bregant et al. *Measurement of the K X–ray intensity ratios in muonic hydrogen at low gas densities.* Phys. Lett. A **241** (1998), 344–350.

[48] B. Lauss et al. *X–ray emission during the muonic cascade in hydrogen.* Phys. Rev. Lett. **80** (1998), 3041–3044.

[49] T. S. Jensen. Private communication.

[50] J. Shapiro and G. Breit. *Metastability of 2s states of hydrogenic atoms.* Phys. Rev. **113** (1959), 179–181.

[51] A. Bertin, A. Vacchi, and A. Vitale. *On the initial population of the 2s metastable state in muonic hydrogen and deuterium.* Lett. Nuovo Cimento **18** (1977), 277–282.

[52] G. Carboni and G. Fiorentini. *On the collision quenching of the 2S–state of muonic hydrogen.* Nuovo Cimento B **39** (1977), 281–291.

[53] T. S. Jensen and V. E. Markushin. *Collisional quenching of the 2S state of muonic hydrogen.* nucl–ph Preprint **0001009** (2000).

[54] G. Kodosky and M. Leon. *On the metastability of the 2s state of muonic hydrogen.* Nuovo Cimento B **1** (1971), 41–47.

[55] P. Froelich and A. Flores-Riveros. *Effects of intramolecular dynamics on nuclear fusion rates and sticking from resonant states of the molecular ion $dt\mu$.* Phys. Rev. Lett. **70** (1993), 1595–1598.

[56] J. Wallenius, S. Jonsell, Y. Kino, and P. Froelich. *Muonic atom deexcitation via formation of metastable molecular states, in light of experimental verification.* Hyp. Interact. **138** (2001), 285–288.

[57] R. O. Mueller, V. W. Hughes, H. Rosenthal, and C. S. Wu. *Collision quenching of the metastable 2S state of muonic hydrogen and the muonic helium ion.* Phys. Rev. A **11** (1975), 1175–1186.

[58] J. S. Cohen and J. N. Bardsley. *Radiative collisional quenching of metastable muonic hydrogen $p\mu^-(2s)$ and the metastable muonic helium ion $\alpha\mu^-(2s)$.* Phys. Rev. A **23** (1981), 46–51.

[59] L. I. Men'shikov and L. I. Ponomarev. *Quasiresonance charge exchange of hydrogen isotopes mesic atoms in excited states.* Z. Phys. D **2** (1986), 1–13.

[60] J. A. Böcklin. *Suche nach dem metastabilen 2S-Zustand im myonischen Wasserstoff bei tiefen Gasdrucken.* PhD thesis, ETHZ, Switzerland, 1982. (unpublished).

[61] R. Engfer, H. Schneuwly, J. L. Vuilleumier, H. K. Walter, and A. Zehnder. *Charge-distribution parameters, isotope shifts, isomer shifts, and magnetic hyperfine constants from muonic atoms.* At. Data and Nucl. Data Tables **14** (1974), 509–597.

[62] F. Mulhauser. Private communication.

[63] G. Holzwarth and H. J. Pfeiffer. *The muonic X–ray cascade in fluorine following the μ^- transfer from hydrogen.* Z. Phys. A **272** (1975), 311–313.

[64] V. R. Akylas and P. Vogel. *Muonic atom cascade program.* Comp. Phys. Comm. **15** (1978), 291–302.

[65] G. Fiorentini and G. Torelli. *Muon transfer to heavy atom. A probe for the study of the μp_{2s} system.* Nuovo Cimento A **36** (1976), 317–329.

[66] P. Hauser, K. Kirch, F. Kottmann, and L. M. Simons. *Absolute x–ray yields of light muonic atoms.* Nucl. Instrum. Methods Phys. Res. A **411** (1998), 389–395.

[67] K. Kirch et al. *Muonic cascades in isolated low-Z atoms and molecules.* Phys. Rev. A **59** (1999), 3375–3385.

[68] `http://www.psi.ch/forschung/benutzerlabor_e.shtml`.

[69] A. Antognini et al. *Powerful fast triggerable 6 μm laser for the muonic Lamb shift experiment.* Optics Communications **253** (2005), 362–374.

[70] F. Mulhauser, L. Ludhova, and P. Knowles. *LAAPD's and Related Electronics Study.* University of Fribourg, 2002. (unpublished).

[71] P. deCecco et al. *A new method to produce a negative muon beam of keV energies.* Nucl. Instrum. Methods Phys. Res. A **394** (1997), 287–294.

[72] F. Kottmann et al. *The muonic hydrogen Lamb shift experiment at PSI.* In P. Kienle, J. Marton, and J. Zmeskal, editors, *Exotic Atoms — Future Perspectives*, pages 159–166. Austrian Academy of Sciences Press, Vienna (Austria), 2003. [Proceedings of the Int. Workshop on Exotic Atoms — Future perspectives].

[73] D. Taqqu. *Phase space compression of low energy muon beams.* Z. Phys. C **56** (1992), s250–s254.

[74] M. Mühlbauer et al. *Frictional cooling: experimental results.* Hyp. Interact. **119** (1999), 305–310.

[75] P. Rabinowitz, B. N. Perry, and N. Levinos. *A continuously tunable sequential Stokes Raman laser.* IEEE J. Quant. Electr. **22** (1986), 797–802.

[76] *LeCroy Corporation.* 700 Chestnut Ridge Road, Chestnut Ridge, NY 10977-6499, USA.

[77] *ORTEC - PerkinElmer.* 801 S. Illinois Ave., Oak Ridge, TN 37831-0895, USA.

[78] S. Dhawan. Developed at Physics Department, Yale University, New Haven, CT 06520–8121, USA.

[79] *Rutherford Appleton Laboratory.* Chilton, Didcot, Oxfordshire, OX11 0QX, England.

[80] *CAEN S.p.A.* Via Vetraia, 11, 55049 - Viareggio (LU) - ITALY.

[81] `http://www.cxro.lbl.gov/optical_constants/atten2.html`.

[82] A. Antognini. Private communication.

[83] M. Wälchli. *Abbremsung negativer Myonen und Bildung von myonischem Wasserstoff in H_2–Gas unterhalb 1 Torr.* PhD thesis, ETHZ Zurich, Switzerland, 1981. (unpublished).

[84] S. P. Møller et al. *Antiproton stopping at low energies: Confirmation of velocity-proportional stopping power.* Phys. Rev. Lett. **88** (2002), 193201.

[85] D. Taqqu. Private communication.

[86] Y. A. Thalmann et al. *Muon transfer from excited states of hydrogen and deuterium to nitrogen, neon and argon.* Phys. Rev. A **57** (1998), 1713–1720.

[87] V. I. Petrukhin and V. M. Suvorov. *Study of atomic capture and transfer of π^- mesons in mixtures of hydrogen with other gases.* Zh. Eksp. Teor. Fiz. **70** (1976), 1145–1151. [Sov. Phys. JETP **43**, 595–598 (1976)].

[88] D. Horváth and F. Entezami. *On the models of Coulomb capture of negative particles.* Nucl. Phys. A **407** (1983), 297–308.

[89] E. Fermi and E. Teller. *The capture of negative mesotrons in matter.* Phys. Rev. **72** (1947), 399–408.

Curriculum Vitae Livia Ludhova

Full name:	Livia Ludhova
Birth date:	March 6th 1973
Birth place:	Bratislava, Slovakia
Nationality:	Slovak
Languages:	Slovak: mother tongue Czech: fully fluent English: principal language Italian: fluent German: communication ability French: communication ability Russian: passive knowledge

Education

since 2001:	Graduate student in physics, University of Fribourg, Switzerland
1996–2001:	Undergraduate student in physics, Comenius University, Bratislava, Slovakia Graduated in 2001 as **M. A. (master of arts) in physics** Diploma thesis: *Kaonic nitrogen measurement at the e^+e^- collider DAΦNE, Frascati, Italy (with the DEAR collaboration)*
1996–1999:	Graduate student in geology, Comenius University, Bratislava, Slovakia Graduated in 1999 as **Ph. D. (philosophiae doctor) in petrology** Doctoral thesis: *Reconstruction of Variscan P–T–t path of metapelites in the crystalline complex of Western and High Tatra Mts., Western Carpathians, Slovakia*
1991–1996:	Undergraduate student in geology, Comenius University, Bratislava, Slovakia Graduated in 1996 as **M. A. (master of arts) in geology** Diploma thesis: *P–T–t (pressure–temperature–time) path reconstruction of the high–grade metapelites from the upper tectonic unit, the Western Tatra Mts. crystalline complex, Western Carpathians, Slovakia*

Scholarships, Grants, and Awards

2000–2004:	Transnational Access To Research Infrastructure (TARI) I.N.F.N. — Laboratori Nazionali di Frascati (project numbers 5, 15, 24, and 40)
2000–2001:	Scholarship from the Institute for Medium Energy Physics (IMEP), Austrian Academy of Sciences, Vienna
2000:	Scholarship from the Slovak Ministry of Education to support the cooperation between Slovakia and Austria (IMEP, Austrian Academy of Sciences, Vienna)
1999:	Award of the dean of the Faculty of Natural Sciences, Comenius University, Bratislava, Slovakia
1998:	Comenius University grant UK/3865/98 for young researchers
1997:	Comenius University grant UK/1516/97 for young researchers

List of Publications and Presentations in Physics

a) Scientific Papers:

1. L. Ludhova, F.D. Amaro, A. Antognini, F. Biraben, J.M.R. Cardoso, C.A.N. Conde, D.S. Covita, A. Dax, S. Dhawan, L.M.P. Fernandes, T.W. Hänsch, V.W. Hughes, O. Huot, P. Indelicato, L. Julien, P.E. Knowles, F. Kottmann, Y.-W. Liu, C.M.B. Monteiro, F. Mulhauser, F. New, R. Pohl, P. Rabinowitz, J.M.F. dos Santos, L.A. Schaller, D. Taqqu, J.F.C.A. Veloso: **Planar LAAPDs: Temperature Dependence, Performance, and Application in Low Energy X–ray Spectroscopy**, Nucl. Instrum. Methods Phys. Res. A **540** (2005) 169–179.
2. A. Antognini, F.D. Amaro, F. Biraben, J.M.R. Cardoso, C.A.N. Conde, A. Dax, S. Dhawan, L.M.P. Fernandes, T.W. Hänsch, F.J. Hartmann, V.-W. Hughes, O. Huot, P. Indelicato, L. Julien, P.E. Knowles, F. Kottmann, Y.-W. Liu, L. Ludhova, C.M.B. Monteiro, F. Mulhauser, F. Nez, R. Pohl, P. Rabinowitz, J.M.F. dos Santos, L.A. Schaller, C. Schwob, D. Taqqu, and J.F.C.A. Veloso: **Powerful fast triggerable 6 μm laser for the muonic Lamb shift experiment** Optics Communications **253** (2005) 362–374.
3. G. Beer, A.M. Bragadireanu, M. Cargnelli, C. Curceanu–Petrascu, J.-P. Egger, H. Fuhrmann, C. Guaraldo, M. Iliescu, T. Ishiwatari, K. Itahashi, M. Iwasaki, P. Kienle, T. Koike, B. Lauss, V. Lucherini, L. Ludhova, J. Marton, F. Mulhauser, T. Ponta, L.A. Schaller, R. Seki, D.L. Sirghi, F. Sirghi, and J. Zmeskal: **Measurement of the Kaonic Hydrogen X–Ray Spectrum**, Phys. Rev. Lett. **94** (2005) 212302.
4. T. Ishiwatari, G. Beer, A.M. Bragadireanu, M. Cargnelli, C. Curceanu (Petrascu), J.-P. Egger, H. Fuhrmann, C. Guaraldo, P. Kienle, T. Koike, M. Iliescu, K. Itahashi, M. Iwasaki, B. Lauss, V. Lucherini, L. Ludhova, J. Marton, F. Mulhauser, T. Ponta, L.A. Schaller, R. Seki, D.L. Sirghi, F. Sirghi, P. Strasser, and J. Zmeskal: **Kaonic nitrogen X–ray transition yields in a gaseous target**, Phys. Lett. B **593** (2004) 48–54.
5. L.M.P. Fernandes, A. Antognini, M. Boucher, O. Huot, P.E. Knowles, F. Kottmann, L. Ludhova, F. Mulhauser, R. Pohl, J.M.F. dos Santos, D. Taqqu,and J.F.C.A. Veloso: **Behaviour of Large–Area Avalanche Photodiodes under intense Magnetic Fields for VUV– Visible– and x–ray photon detection**, Nucl. Instrum. Methods Phys. Res. A **498** (2003) 362–368.
6. G. Beer, A.M. Bragadireanu, W. Breunlich, M. Cargnelli, C. Curceanu (Petrascu), J.-P. Egger, H. Fuhrmann, C. Guaraldo, M. Giersch, M. Iliescu, T. Ishiwatari, K. Itahashi, B. Lauss, V. Lucherini, L. Ludhova, J. Marton, F. Mulhauser, T. Ponta, A.C. Sanderson, L.A. Schaller, D.L. Sirghi, F. Sirghi, and J. Zmeskal: **A new method to obtain a precise value of the mass of the charged kaon**, Phys. Lett. B **535** (2002) 52–58.

b) Refereed Conference Proceedings:

1. M. Cargnelli, G. Beer, A.M. Bragadireanu, C. Curceanu(Petrascu), J.-P. Egger, H. Fuhrmann, C. Guaraldo, M. Iliescu, T. Ishiwatari, K. Itahashi, M. Iwasaki, P. Kienle, T. Koike, B. Lauss, V. Lucherini, L. Ludhova, J. Marton, F. Mulhauser, T. Ponta, L.A. Schaller, R. Seki, D.L. Sirghi, F. Sirghi, and J. Zmeskal: **Kaonic hydrogen measurement with DEAR at DAΦNE**. Int. Journ. of Mod. Phys. A **20** (2005) 341. *Proceedings of MESON2004, Cracow, Poland, June 2004.*

2. J. Zmeskal, G. Beer, A.M. Bragadireanu, M. Cargnelli, C. Curceanu, J.-P. Egger, H. Fuhrmann, C. Guaraldo, M. Iliescu, T. Ishiwatari, K. Itahashi, M. Iwasaki, P. Kienle, T. Koike, B. Lauss, V. Lucherini, L. Ludhova, J. Marton, F. Mulhauser, T. Ponta, L.A. Schaller, R. Seki, D.L. Sirghi, F. Sirghi: **The DEAR experiment — first results on kaonic hydrogen**, Nucl. Phys. A **754** (2005) 369c. *Proceedings of HYP2003, Newport News, USA, October 2003.*

3. L.M.P. Fernandes, J.A.M. Lopes, J.M.F. dos Santos, P.E. Knowles, L. Ludhova, F. Mulhauser, F. Kottmann, R. Pohl and D. Taqqu: **LAAPD Low Temperature Performance in X-Ray and Visible-Light Detection**, Trans. Nucl. Sci. **51(4)** (2004) 1575. *Proceedings IEEE Nuclear Science Symposium and Medical Imaging Conference, October 2003, Portland, USA.*

4. L.M.P. Fernandes, A. Antognini, M. Boucher, C.A.N. Conde, O. Huot, P.E. Knowles, F. Kottmann, L. Ludhova, F. Mulhauser, R. Pohl, J.M.F. dos Santos, L.A. Schaller, D. Taqqu, and J.F.C.A. Veloso: **Application of large-area avalanche photodiodes to X-ray spectrometry of muonic atoms**, Spectrochimica Acta Part B: Atomic Spectroscopy **58** (2003) 2255–2260. *Proceedings TXRF 2002 – 9th Conference on Total Reflection X–ray Fluorescence Analysis and Related Methods, September 2002, Madeira Island, Portugal.*

5. M. Boucher, O. Huot, P. Knowles, L. Ludhova, F. Mulhauser, L.A. Schaller, C.A.N. Conde, J.M.F. Dos Santos, L.M.P. Fernandes, J.F.C.A. Veloso, F. Kottmann, A. Antognini, R. Pohl, and D. Taqqu: **Large Area APDs for low energy x–ray detection in intense magnetic fields**, Nucl. Instrum. Methods Phys. Res. A, **505** (2003) 136–139. *Proceedings of 10th Symposium on Radiation Measurements and Applications, May 2002, Ann Arbor, USA.*

c) Talks Presented at Conferences:

1. **Planar LAAPDs: Temperature Dependence, Performance, and Application in Low Energy X-Ray Spectroscopy** presented at the 2004 IEEE Nuclear Science Symposium (NSS), session N32, "New Solid State Detectors II", Rome, Italy, October 20^{th} 2004.

2. **A precise measurement of the proton charge radius: why and how**, presented at the International Nuclear Physics Conference, INPC2004, Göteborg (Sweden), June 28^{th} 2004.

3. **Lamb shift measurement in muonic hydrogen**, presented at the Swiss Physical Society Meeting, Basel (Switzerland) March 21^{th} 2003.

d) Conference Proceedings:

1. A. Antognini, F.D. Amaro, F. Biraben, J.M.R. Cardoso, C.A.N. Conde, A. Dax, S. Dhawan, L.M.P. Fernandes, T.W.Hänsch, F.J. Hartmann, V.-W. Hughes, O. Huot, P. Indelicato, L. Julien, P.E. Knowles, F. Kottmann, Y.-W. Liu, L. Ludhova, C.M.B. Monteiro, F. Mulhauser, F. Nez, R. Pohl, P. Rabinowitz, J.M.F. dos Santos, L.A. Schaller, C. Schwob, D. Taqqu, J.F.C.A. Veloso: **The 2S Lamb shift in muonic hydrogen and the proton rms charge radius**, (LEAP05, Int. Conf. on the the Low Energy Antiproton Physics, Bonn–Jülich, Germany, May 2005).

2. R. Pohl, A. Antognini, F.D. Amaro, F. Biraben, J.M.R. Cardoso, C.A.N. Conde, A. Dax, S. Dhawan, L.M.P. Fernandes, T.W.Hänsch, F.J. Hartmann, V.-W. Hughes, O. Huot, P. Indelicato, L. Julien, P.E. Knowles, F. Kottmann, Y.-W. Liu, L. Ludhova, C.M.B. Monteiro, F. Mulhauser, F. Nez, P. Rabinowitz, J.M.F. dos Santos, L.A. Schaller, C. Schwob, D. Taqqu, J.F.C.A. Veloso: **The muonic hydrogen Lamb shift experiment**, Proceedings of International Workshop on Exotic Atoms, Vienna, Austria, February 2005.

3. R. Pohl, A. Antognini, F.D. Amaro, F. Biraben, J.M.R. Cardoso, C.A.N. Conde, A. Dax, S. Dhawan, L.M.P. Fernandes, T.W.Hänsch, F.J. Hartmann, V.-W. Hughes, O. Huot, P. Indelicato, L. Julien, P.E. Knowles, F. Kottmann, Y.-W. Liu, L. Ludhova, C.M.B. Monteiro, F. Mulhauser, F. Nez, P. Rabinowitz, J.M.F. dos Santos, L.A. Schaller, C. Schwob, D. Taqqu, J.F.C.A. Veloso: **The muonic hydrogen Lamb shift experiment**, Proceedings of the Hydrogen Atom III - International Conference on Precision Physics of Simple Atomic Systems, Mangaratiba, Rio de Janeiro, Brasil, August 2004, pub. in Can. J. Phys. **83** (2005) 339.

4. G. Beer, A.M. Bragadireanu, M. Cargnelli, C. Curceanu (Petrascu), J.-P. Egger, H. Fuhrman, C. Guaraldo, M. Iliescu, T. Ishiwatari, K. Itahashi, M. Iwasaki, P. Kienle, B. Lauss, V. Lucherini, L. Ludhova, J. Marton, F. Mulhauser, T. Ponta, L.A. Schaller, R. Seki, D. Sirghi, F. Sirghi, P. Strasser, J. Zmeskal: **DEAR - Kaonic Hydrogen: First Results**, Proceedings of the workshop "HadAtom03", Trento, Italy, October 2003, arXiv.org:hep-ph/0401204, p. 31. (Preprints ECT*-04-01, HISKP-TH-04/02).

5. W. Amir, A. Antognini, F. Biraben, M. Boucher, C.A.N. Conde, A. Dax, S. Dhawan, L.M.P. Fernandes, T.W. Hänsch, F.J. Hartmann, V.W. Hughes, O. Huot, P. Indelicato, L. Julien, S. Kazamias, P. Knowles, F. Kottmann, Y.-W. Liu, J. Lopez, L. Ludhova, C. Monteiro, F. Mulhauser, F. Nez, R. Pohl, P. Rabinowitz, J.M.F. dos Santos, L.A. Schaller, J.-T. Shy, D. Taqqu, J.F.C.A. Veloso: **Towards the most precise test of bound state QED**, Proceedings of the workshop "HadAtom03", Trento, Italy, October 2003, arXiv.org:hep-ph/0401204, p. 41. (Preprints ECT*-04-01, HISKP-TH-04/02).

6. C. Curceanu (Petrascu) et al. (DEAR/SIDDHARTA Collaborations): **DEAR and SIDDHARTA: present and future precision measurements on kaonic hydrogen and kaonic deuterium**, Proceedings of the "XLII International Winter Meeting on Nuclear Physics" Bormio, Italy, January–February 2004.

7. C. Guaraldo, G. Beer, A.M. Bragadireanu, M. Cargnelli, C. Curceanu (Petrascu), J.–P. Egger, H. Fuhrman, M. Iliescu, T. Ishiwatari, K. Itahashi, M. Iwasaki, B. Lauss, V. Lucherini, L. Ludhova, J. Marton, F. Mulhauser, T. Ponta, L.A. Schaller, R. Seki, D. Sirghi, F. Sirghi, P. Strasser, and J. Zmeskal: **First results on kaonic hydrogen from DEAR at DAΦNE**, Proceedings of the "4th International Conference on Perspectives in Hadronic Physics", Miramare-Trieste, Italy, May 2003, Eur. Phys. J. A **19** (2004), s01, 185–188.

8. M. Cargnelli, G. Beer, A.M. Bragadireanu, C. Curceanu (Petrascu), J.–P. Egger, H. Fuhrmann, C. Guaraldo, M. Iliescu, T. Ishiwatari, K. Itahashi, M. Iwasaki, P. Kienle, B. Lauss, V. Lucherini, L. Ludhova, J. Marton, F. Mulhauser, T. Ponta, L.A. Schaller, R. Seki, D. Sirghi, F. Sirghi, P. Strasser, and J. Zmeskal: **DEAR - Kaonic Hydrogen: First Results**, 4th International Workshop on CHIRAL DYNAMICS 2003 Theory and Experiment, Bonn, Germany, September 2003.

9. C. Curceanu (Petrascu), G. Beer, A.M. Bragadireanu, M. Cargnelli, J.–P. Egger, H. Fuhrmann, C. Guaraldo, M. Iliescu, T. Ishiwatari, K. Itahashi, M. Iwasaki, B. Lauss, V. Lucherini, L. Ludhova, J. Marton, F. Mulhauser, T. Ponta, L.A. Schaller, R. Seki, D. Sirghi, F. Sirghi, P. Strasser, and J. Zmeskal: **Last results from the DEAR experiment at DAΦNE**, Proceedings of "HADRON SPECTROSCOPY", 10^{th} International Conference on Hadron Spectroscopy, Aschaffenburg, Germany, August–September 2003.

10. C. Curceanu (Petrascu) et al. (DEAR Collaboration): **Kaonic nitrogen and hydrogen from DEAR**, Proceedings of the "XLI International Winter Meeting on Nuclear Physics" Bormio, Italy, January–February 2003, published in Ricerca Scientifica ed Educatione Permanente, Universita' degli studi di Milano, Supplemento N. **120**, (2003), 21–27.

11. F. Kottmann, A. Antognini, F. Biraben, M. Boucher, C.A.N. Conde, A. Dax, S. Dhawan, L.M.P. Fernandez, T.W. Hänsch, F.J. Hartmann, V.W. Hughes, O. Huot, P. Indelicato, L. Julien, P. Knowles, Y.-W. Liu, J. Lopes, L. Ludhova, C. Monteiro, F. Mulhauser, F. Nez, R. Pohl, P. Rabinowitz, J.M.F. dos Santos, L.A. Schaller, J.-T. Shy, D. Taqqu, J.F.C.A. Veloso: **The muonic hydrogen Lamb shift experiment at PSI**, Proceedings of International Workshop on Exotic Atoms, Vienna, Austria, November 2002, Austrian Academy of Sciences Press, Vienna, Austria, ed. by P. Kienle, J. Marton, and J. Zmeskal, (2003) 159.

12. J. Zmeskal et al. (DEAR Collaboration): **The DEAR experiment**, (Proceedings of the "EXA 2002 - International Workshop on Exotic Atoms - Future Perspectives"), Vienna, Austria, November 2002, Austrian Academy of Sciences Press eds by P. Kienle, J. Marton, and J. Zmeskal (2003), 113–125.

13. M. Cargnelli, G. Beer, A.M. Bragadireanu, C. Curceanu (Petrascu), J.–P. Egger, H. Fuhrmann, M. Giersch, C. Guaraldo, M. Iliescu, T. Ishiwatari, K. Itahashi, M. Iwasaki, P. Kienle, B. Lauss, V. Lucherini, L. Ludhova, J. Marton, F. Mulhauser, T. Ponta, L.A. Schaller, R. Seki, D. Sirghi, F. Sirghi, and J. Zmeskal: **Kaonic Hydrogen - Status of the DEAR Experiment**, Progress of Theoretical Physics Supplement 149, 240–246, 2003, YITP-RCNP workshop on Chiral Restoration in Nuclear Medium, Yukawa Institute for Theoretical Physics, Kyoto University, October 2002.

14. C. Guaraldo et al. (DEAR Collaboration): **Recent results from DEAR at DAFNE**, Proceedings of the "Workshop on Hadronic Atoms - HadAtom 02", Bern, Switzerland, October 2002.

15. M. Iliescu, G. Beer, A.M. Bragadireanu, M. Cargnelli, C. Curceanu (Petrascu), J.–P. Egger, H. Fuhrmann, C. Guaraldo, M. Iliescu, T. Ishiwatari, K. Itahashi, M. Iwasaki, B. Lauss, V. Lucherini, L. Ludhova, J. Marton, F. Mulhauser, T. Ponta, L.A. Schaller, R. Seki, D. Sirghi, F. Sirghi, and J. Zmeskal: **Exotic atoms production with DEAR at DAΦNE**, Proceedings of the 7th International Workshop on Production, Properties and Interaction of Mesons, MESON 2002, cracow, Poland, May 2002.

16. C. Curceanu (Petrascu) et al. (DEAR Collaboration), **The first measurement of kaonic nitrogen with DEAR at DAΦNE**, Proceedings of the "Workshop on Hadronic Atoms - HadAtom 01", Switzerland, Bern, October 2001.

List of Publications and Presentations in Geology

a) Scientific Papers:

1. M. Nemcok, J. Nemcok, M. Wojtaszek, L. Ludhova, N. Oszczypko, W.J. Sercombe, M. Cieszkowski, Z. Paul, M.P. Coward, and A. Slaczka: **Reconstruction of Cretaceous rifts incorporated in the Outer West Carpathian wedge by balancing**, Marine and Petroleum Geology **18** (2001) 39–64.
2. M. Janak, V. Hurai, L. Ludhova, E.E. Horn, R. Thomas, and Majzlan: **Nitrogen-bearing fluids, brines and carbonate liquids in Variscan migmatites of the Tatra Mountains, Western Carpathians - heritage of high-pressure metamorphism**, European Journal of Mineralogy **12** (2000) 1283–1300.
3. M. Nemcok, J. Nemcok, M. Wojtaszek, L. Ludhova, R.A. Klecker, W.J. Sercombe, M.P. Coward, and J.F. Keith: **Results of 2D balancing along 20 degrees and 21 degrees 30' longitude and pseudo-3D in the Smilno tectonic window: Implications for shortening mechanisms of the West Carpathian accretionary wedge**, Geologica Carpathica **51**, 5 (2000) 281–300.
4. M. Janak, V. Hurai, L. Ludhova, and R. Thomas: **Partial melting and retrogression during exhumation of high-grade metapelites, the Tatra Mountains, Western Carpathians**, Physics and Chemistry of the Earth - Part A. Solid Earth and Geodesy **24**, 3 (1999) 289–294.
5. M. Janak, V. Hurai, L. Ludhova, P.J. O'Brien and E.E. Horn: **Dehydration melting and devolatilzation during exhumation of high-grade metapelites: the Tatra Mountains, Western Carpathians**, Journal of Metamorphic Geology **17** (1999) 379–396.
6. L. Ludhova and M. Janak: **Phase relations and P-T path of cordierite-bearing migmatites, Western Tatra Mountains, Western Carpathians**, Geologica Carpathica **50**,4 (1999) 283–293.

b) Talks Presented at Conferences:

1. **Decompression and exhumation of a Variscan orogenic root in the Tatra Mountains, Western Carpathians: evidence from high–grade metapelites**, presented at International Geological Conference - Carpathian Geology, Smolenice, Slovakia, October 12^{th} 1999.
2. **P-T path reconstruction of the high-grade metapelites, the Tatra Mts., Western Carpathians**, presented at Carpathian–Balkan Geological Association XVI Congress, Vienna, Austria, August 31^{th} 1998.
3. **Cordierit - new mineral from the crystalline complex of the Tatra Mts.**, presented at the Meeting in memory of Prof. J. Kamenicky: Petrology, mineralogy and geochemistry of magmatic and metamorphic processes, Bratislava, Slovakia, November 11^{th} 1997.

d) Conference Proceedings:

1. P. Nemcok, T. Dilov, E. Marton, P. Krzywiec, M. Wojtaszek, L. Ludhova, J. Grabowski, R.A. Klecker, W.J. Sercombe, and M.P. Coward: **Tertiary development of the Polish part of the Carpathian accretionary wedge: insights from deformed balanced cross sections, paleostress and paleomagnetic analyses**, Vijesti, 2000, Vol. **37**, 3 Special Issue 90, PANCARDI 2000, Dubrovnik, Croatia, October 2000)
2. L. Ludhova: **P–T path reconstruction of the high-grade metapelites of upper–tectonic unit from the Tatra. Mts. crystalline complex** (In Slovak), Mineralia Slovaca–Geovestnik, Vol.**30**, 3 (1998) 13.
3. L. Ludhova and M. Janak: **P–T path reconstruction of the high–grade metapelites, the Tatra Mts., Western Carpathians**, Carpathian–Balkan Geological Association XVI Congress, Vienna, Austria, August–September 1998, 346.
4. V. Hurai, M. Janak and L. Ludhova: **Partial melting and retrogression during exhumation of high grade metapelites, the Tatra Mts., Western Carpathians**, European Geophysical Society XXII, Annales Geophysicae, Suppl. I to Vol. **16** (1998) 184, Nice, France, April 1998.
5. M. Nemcok, J. Nemcok, M. Wojtaszek, L. Ludhova, N. Oszczypko, W.J. Sercombe, M. Cieszkowski, Z. Paul, M.P. Coward, and A. Slaczka: **Reconstruction of Cretaceous rifts incorporated in the Outer West Carpathian wedge by balancing**, Przeg. Geol. Vol. **45**, 10/2 (1997) 1093.

Ich versichere, dass ich diese Arbeit selbstständig und ohne unerlaubte Hilfe verfasst und keine anderen als die angegebenen Quellen und Hilfsmittel benutzt sowie Zitate kenntlich gemacht habe.

1700 Fribourg (Switzerland), October 2005

Livia Ludhova